The Effect of Iron and Aluminum Substitution on the Physical Properties of Bridgmanite in Earth's Mantle

by

Britany L. Kulka

A Dissertation Presented in Partial Fulfillment

of the Requirement for the Degree

Doctor of Philosophy in Earth Sciences

St Edmund Hall

UNIVERSITY OF OXFORD

September 2025

ACKNOWLEDGEMENTS

I would like to begin by thanking my advisors, Hauke Marquardt and Andrew Walker, for their support and guidance throughout my degree. I am also grateful to my college advisor, Claire Nichols, for her encouragement and support, particularly during challenging moments. My thanks extend to Jon Wade, Director for his guidance during my time at Oxford. I appreciate the support from members of the department, including Stephenie Lechki, Viktoria Trautner, Estell Ledoux, and Niccolo Satta. Additionally, I would like to thank my college St Edmund Hall. A special thanks to my examiners Oliver Lord (University of Bristol) and David Pyle (University of Oxford) for their time and effort towards my viva and dissertation.

This work was funded by the European Research Council and made my time at Oxford possible. I also acknowledge the support of the University of Oxford Advanced Research Computing (ARC) facility. A significant portion of my research was made possible by Bayreuth Geoinstitute (BGI) in Bayreuth, Germany, and would like to thank Dan Frost, Tony Withers, Raphael Njul, Ulrike Trenz, and Lianjie Man. Many thanks to the beamline scientists at Diamond Light Source, Egor Komets, and at Elektronen-Synchrotron (DESY) in Hamburg, Germany, Hanns-Peter Liermann and Nico Giordano, for their support during my experiments.

I would also like to thank the individuals I worked with at Arizona State University: Claire Richardson, Mara Karageozian, Byeongkwan Ko, Kara Brugman, Kurt Leinenweber, Christy Till, and Sang-Heon Dan Shim, for their ongoing support.

An earnest thank you to my parents for their encouragement to pursue this degree abroad.

Finally, I would like to thank my best friend and husband, Jonathan Dolinschi. Providing endless support not only through my research but through everything life threw our way. Thank you will never be enough.

ABSTRACT

Using a combination of *in situ* high-pressure X-ray diffraction (XRD), density functional theory (DFT) calculations, and thermodynamic modeling, this work explores the influence of Fe and Al substitution on the elastic and thermodynamic properties of bridgmanite, a key mineral in the Earth's lower mantle. The results indicate that Fe and Al substitutions significantly affect bridgmanite's compressibility and stiffness. DFT calculations show that increasing Fe and Al content leads to a decrease in bulk modulus (K_0) under ambient conditions, suggesting a more compressible lattice. However, high-temperature calculations reveal that the softening effect diminishes at elevated temperatures, with the $(Mg_{0.75},Fe_{0.25})(Si_{0.75},Al_{0.25})O_3$ (FeAl25) composition becoming stiffer than the other studied compositions at temperatures above 1000 K. Experimental XRD data on sintered polycrystalline bridgmanite, in contrast, suggest an increase in K_0 with higher Fe and Al content at static conditions, possibly due to extrinsic factors such as sample heterogeneity and grain size. Thermodynamic modeling using Perple_X predicts that increasing Fe-Al content stabilizes bridgmanite over a broader range of pressure-temperature conditions, particularly in deeper mantle regions. The modeling also suggests that Fe-Al substitutions could alter seismic velocities and V_p/V_s ratios, contributing to seismic anomalies such as those observed in Large Low Shear Velocity Provinces (LLSVPs) and Ultra-Low Velocity Zones (ULVZs).

Contents

List of Figures

List of Tables

Chapter 1
Introduction

1.1 Evolutionary History of Earth's Interior

The Earth, like other planets in our solar system, accreted from a solar nebula of gas and dust at 4.5 Ga (Wood *et al.*, 2006; Canup, 2008). This process had great implications for the initial and evolving structure of Earth's interior, which over billions of years has transformed to its present state (Rubie *et al.*, 2011; Halliday and Canup, 2023). This nebula originated from the remnants of a supernova explosion, rich in elements like hydrogen, helium, and heavier elements. Over time, these elements began to coalesce due to gravity, initiating the process of accretion (Rubie *et al.*, 2011). Accretion is a process in which solid particles collide and stick together, growing into larger and larger bodies (Halliday and Canup, 2023). In the densest areas of the solar nebula, tiny dust grains started to stick together, forming planetesimals and protoplanets over millions of years (Halliday and Canup, 2023). Through this process, the early Earth began to take shape.

Proto-earth, still among a dense field of debris, continued to attract and collide with other bodies (Bonsor *et al.*, 2015). Many of these high-energy impacts resulted in substantial heating, along with gravitational energy from ongoing accretion, leading to the radioactive decay of long and short lived radioisotopes, and the melting and differentiation of the Earth's interior. The differentiation process would be crucial in forming the internal layers of the Earth with heavier elements like iron and nickel sinking towards the center due to gravity, forming the Earth's core, and lighter elements and compounds moved towards the surface, creating a primitive mantle and crust. Simultaneously, the intense heat caused volatile substances (H, O, N, etc.) to be degassed from the interior, contributing to the early atmosphere and, later, the hydrosphere once the Earth

cooled enough for water to condense.

Over geologic time, the Earth's interior evolved to its present day layered structure, each layer characterized by distinct composition and physical properties (Carter *et al.*, 2015). The outermost crust is divided into continental and oceanic regions and hosts tectonic plates, often described as being driven by deeper mantle convection. Recognizing the plates as part of this convection process highlights the fundamental role of Earth's interior in shaping its surface. Below the crust, the mantle is composed of dense, hot silicate rock that flows on geologic timescales. Deeper still is the iron-rich core, with a liquid outer region generating Earth's magnetic field and a solid inner region that crystallized as the planet cooled (Wilson *et al.*, 2025). These internal processes remain dynamic, driving plate tectonics, volcanic activity, and many surface processes that shape the global environment (Foley *et al.*, 2014; Korenaga, 2010).

1.2 Overview of Earth's Interior and the Mantle

Earth's interior is composed of three primary layers: the crust, the mantle, and the core. The crust, constituting less than 1% of Earth's mass, can be as thin as 5 km beneath the oceans or as thick as 70 km beneath continents. Below it lies the mantle, which comprises about 67% of Earth's mass and extends to roughly 2,900 km depth (Garnero and McNamara, 2008). The mantle is generally divided into the upper mantle and lower mantle, with a transition zone between 410 and 660 km. This zone is marked by pressure-induced mineral transformations (e.g., olivine to wadsleyite to ringwoodite to bridgmanite), highlighting the strong links between mineral stability and Earth's layered seismic structure (Ringwood, 1991).

Figure 1.1 shows a PREM 1-D seismic velocity reference model (Dziewonski and Anderson, 1981), emphasizing how velocities (both V_p and V_s) and density evolve with depth. These profiles

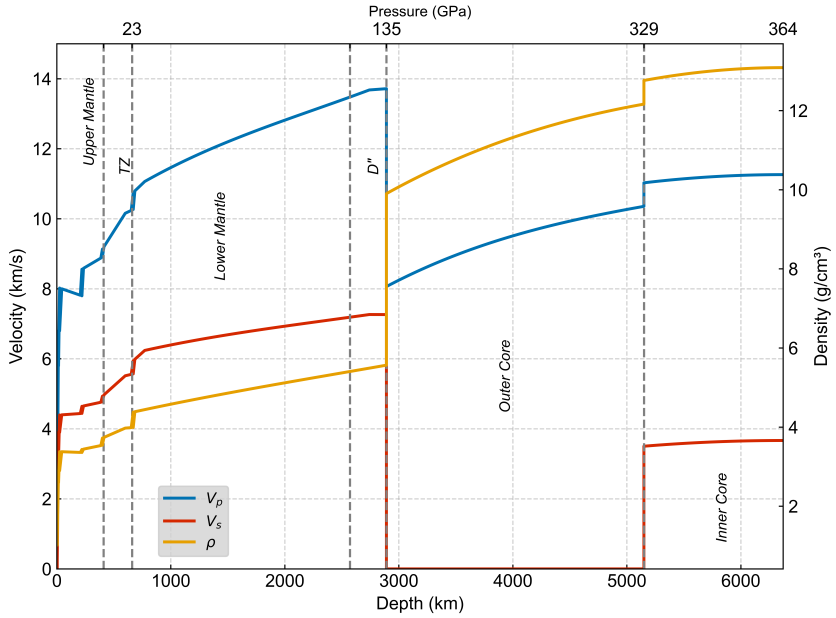

Figure 1.1: PREM-based seismic velocity profile (solid lines) (Dziewonski and Anderson, 1981), illustrating how velocity and density vary with depth. The figure highlights transitions from the upper mantle, through the transition zone (TZ), into the lower mantle, and ultimately into the liquid outer core and solid inner core.

help visualize where mineralogical changes that are driven by increases in pressure and temperature can lead to seismic and compositional boundaries. Notably, the lower mantle extends from 660 km to the core-mantle boundary (CMB) at 2,900 km, exposing materials to pressures of 25-135 GPa and temperatures well above 2,000 K (Garnero, 2000; Garnero and McNamara, 2008).

1.3 Focusing on Earth's Lower Mantle

The lower mantle constitutes the largest volume within Earth's interior and its pressure–temperature regime leads to phase assemblages dominated by bridgmanite ($MgSiO_3$) with Fe and Al substitutions), ferropericlase $\big((Mg,Fe)O\big)$, calcium silicate perovskite ($CaSiO_3$), and at greater depths, post-perovskite (the high-pressure polymorph of bridgmanite) (Murakami *et al.*, 2004; Hirose *et al.*, 2006; Murakami *et al.*, 2012). These identifications are based on high-pressure

experiments and first-principles modeling of pyrolitic compositions, which, when combined with seismic velocity and density profiles, demonstrate that these stoichiometries and structures provide the best match to observed lower-mantle properties (Dziewonski and Anderson, 1981). High-pressure phase transitions, iron spin transitions, and chemical heterogeneities all further influence the physical properties of this region, linking it to surface processes through mantle convection (Hager *et al.*, 1985).

Understanding the mineralogy of the lower mantle first requires choosing a bulk compositional reference. Following most modern mantle convection and mineral physics studies, a pyrolitic composition is used, which is an olivine-rich mixture (roughly 60% peridotite + 40% basalt) that reproduces the 410 km and 660 km seismic discontinuities and matches the density profile of the transition zone and lower mantle (Anderson, 1989; Ringwood, 1962, 1975; Irifune, 1987; McDonough and Sun, 1995; Workman and Hart, 2005). Alternative bulk models, particularly those with a slightly higher SiO_2 content whether from a mechanically mixed basaltic component or an intrinsically silica-enriched lower mantle can satisfy the same transition-zone constraints while increasing the bridgmanite fraction at depths $\gtrsim$ 1000 km (Ballmer *et al.*, 2016; Stixrude and Lithgow-Bertelloni, 2011). These possibilities should be also considered when interpreting seismic and geodynamic observations. Nevertheless, the pyrolite reference such as from provides the most internally consistent framework for this thesis, whose focus is on bridgmanite.

Bridgmanite $(Mg,Fe)(Si,Al,Fe)O_3$, is the most abundant mineral in the lower mantle, accounting for approximately 70–93% of this region by volume depending on the chemistry, making it the most prevalent mineral in the Earth. This estimate arises from high-pressure experimental studies of pyrolitic bulk compositions, first-principles and thermodynamic modeling of mineral stability, and comparisons with seismic velocity and density profiles, all of which indicate that

a bridgmanite-dominated assemblage best matches lower-mantle properties (Irifune *et al.*, 1994; Hirose, 2002; Stixrude and Lithgow-Bertelloni, 2005, 2011; Dziewonski and Anderson, 1981; Murakami *et al.*, 2012; Irifune *et al.*, 2010; Huang *et al.*, 2021b; Zhu *et al.*, 2020). Its crystal structure is orthorhombic perovskite (space group Pnma), and it is capable of incorporating a wide range of chemical substitutions, particularly Fe (both Fe^{2+} and Fe^{3+}) and Al. These substitutions strongly influence physical properties such as seismic velocities, density, elasticity, and phase stability, making bridgmanite central to models of Earth's interior.

Bridgmanite was first synthesized experimentally under high-pressure, high-temperature conditions in the 1970s, but it was not formally recognized as a mineral until its natural occurrence was confirmed in a shocked Tenham meteorite (Sharp *et al.*, 1997; Tschauner *et al.*, 2014). In 2014, the International Mineralogical Association approved the name bridgmanite in honor of Percy W. Bridgman, a pioneer of high-pressure physics and Nobel laureate, whose work laid the foundations for modern high-pressure mineral physics (Tschauner *et al.*, 2014).

Alongside bridgmanite, ferropericlase $\big((Mg,Fe)O\big)$ and calcium silicate perovskite ($CaSiO_3$) are important lower mantle phases. However, the mineralogy of this region is further complicated by the presence of hydrogen, variable iron oxidation states, and other compositional effects, making the lower mantle a primary focus of experimental and computational studies of elasticity, spin transitions, and phase equilibria (Anderson, 1989; Bindi *et al.*, 2020; Marquardt and Thomson, 2020; Ishii *et al.*, 2022).

Figure 1.2 outlines major mineral phases in Earth's mantle, including the transition zone (TZ) and the lower mantle, which is largely bridgmanite (i.e., perovskite) plus ferropericlase. The post-perovskite transition occurring near the D″ layer can help explain certain seismic uncertainties and may link to large, thermochemical structures such as large low shear-wave velocity provinces

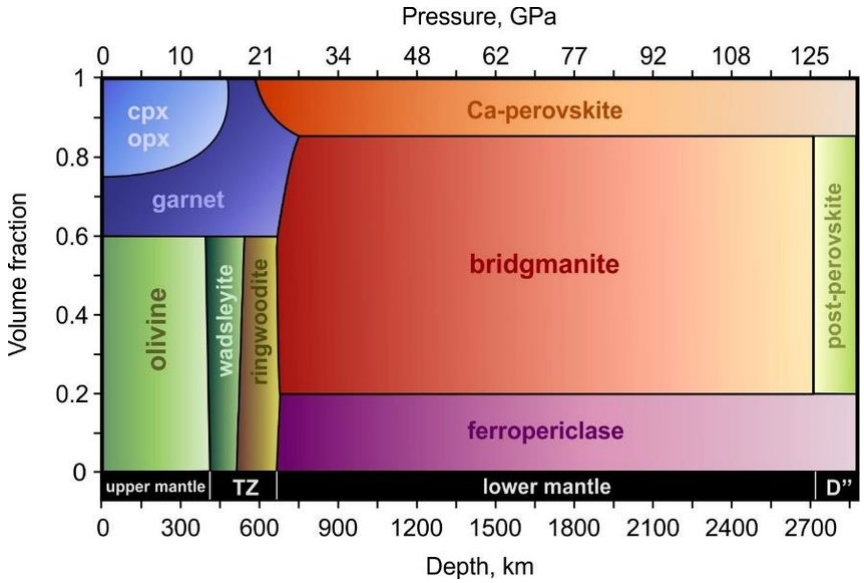

Figure 1.2: Phase diagram of Earth's mantle minerals with a pyrolite composition (Table 1.1), illustrating the relationships between depth (km), pressure (GPa), and volume fraction. The diagram is divided into sections representing the upper mantle, transition zone (TZ), lower mantle, and D″ layer. Figure from Boioli *et al.* (2018).

(LLSVPs) (Garnero and McNamara, 2008; Cottaar and Lekic, 2016). However, transition from bridgmanite to post-perovskite might not be a simple phase transition due to the highly non-linear mantle adiabat in the thermal boundary layer above the core-mantle boundary. A Pv-Ppv double-crossing which is where bridgmanite transforms to post-perovskite and then reverts back to bridgmanite along certain geotherms, introduces significant uncertainty when interpreting seismic discontinuities in the lowermost mantle (Hernlund *et al.*, 2015).

1.3.1 Bridgmanite's Structure, Composition, and Physical Properties

Understanding bridgmanite's orthorhombic distorted perovskite structure (ABX_3) is essential for interpreting geophysical observations such as seismic velocities, density profiles, and mantle convection patterns (Figure 1.3) (Brodholt, 2000; Murakami *et al.*, 2004; Kawai and Tsuchiya, 2009; Tsuchiya *et al.*, 2004). The relatively large, flexible A-site hosts Mg^{2+} or Fe^{2+}, the B-site consists

of octahedrally coordinated Si^{4+}, Al^{3+}, or Fe^{3+}, and X is O^{2-}. Because bridgmanite dominates the lower mantle, even subtle Fe/Al substitutions that modify its elasticity and deformation behavior can translate into measurable changes in viscosity, flow geometry, and seismic anisotropy, thereby shaping our understanding of mantle dynamics and thermal evolution (Tsujino *et al.*, 2016; Couper *et al.*, 2020; Chandler *et al.*, 2021; Fu *et al.*, 2019).

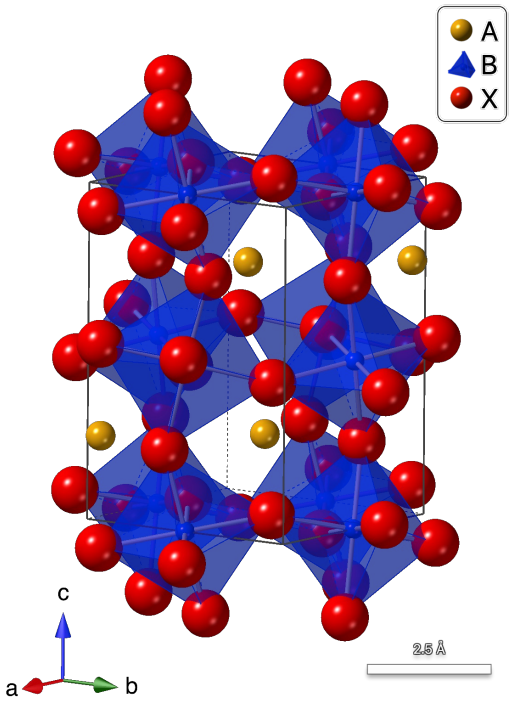

Figure 1.3: Illustration of an orthorhombic perovskite structure, showing the arrangement of the ions within the unit cell. The orange spheres (A) are located at twelve-coordinate sites, while the smaller blue spheres (B) occupy the centers of the octahedra formed by the red spheres (X). The octahedra share corners to create an extended three-dimensional network. The gray lines show the orthorhombic unit cell. Figure generated using CrystalMaker (CrystalMaker, 2023).

The Mg end-member of bridgmanite places Mg^{2+} in the 12-fold coordinated A-site and Si^{4+} in the octahedral B-site, with SiO_6 octahedra linked by oxygen anions. Iron can substitute at either site: ferrous Fe^{2+} predominantly occupies the A-site, whereas ferric Fe^{3+} partitions between both A- and B-sites, with a slight preference for the latter (McCammon, 1997; Burns,

1993). Aluminum (Al^{3+}) also substitutes for Si^{4+} in the B-site, but to maintain charge balance these trivalent cations enter through coupled substitutions such as $Si_B^{4+} + Mg_A^{2+} \rightarrow Al_B^{3+} + Fe_A^{3+}$ or $2\,Si_B^{4+} \rightarrow Al_B^{3+} + Fe_B^{3+}$. These charge-coupled substitutions are well documented as the dominant mechanisms by which Fe^{3+} and Al^{3+} are incorporated into bridgmanite (Catalli *et al.*, 2010; Muir and Brodholt, 2016).

These multivalent substitutions modify cation-oxygen bond lengths, crystal-field environments, and the spin state of iron, producing measurable shifts in density, elasticity, and seismic wave speeds (Burns, 1993; Mao *et al.*, 2017; Nakatsuka *et al.*, 2021; Catalli *et al.*, 2010; Lin *et al.*, 2013; Shukla and Wentzcovitch, 2016; Shukla *et al.*, 2015; Badro *et al.*, 2004; McCammon *et al.*, 2004; Huang *et al.*, 2015; Ballaran *et al.*, 2012; Kurnosov *et al.*, 2017; Li *et al.*, 2018; Huang *et al.*, 2021a). A detailed characterization of Fe-Al-bearing bridgmanite is therefore essential for constraining lower-mantle composition, dynamics, and the interpretation of deep-Earth seismic observations.

Experimental Investigations of Bridgmanite

Much of the experimental and theoretical work to date has focused on the Mg end-member perovskite, bridgmanite ($MgSiO_3$), to establish a baseline for how the crystal responds to high-pressure and high-temperature conditions. Determining elastic moduli (i.e., a material's incompressibility) especially the bulk modulus (K_0), is fundamental to modeling lower mantle composition and interpreting seismic profiles. Different measurement techniques such as X-ray diffraction, Brillouin spectroscopy, and ultrasonic measurements, each explore elastic properties in distinct ways and may entail systematic differences. For example, the choice of equation of state (EOS) (e.g., 3rd-order Birch-Murnaghan (BM3), Vinet) which describes the state of a material by linking its

thermodynamic properties, primarily pressure (P), volume (V), and temperature (T) which can lead to variations in the determined K_0. Figure 1.4 shows reported K_0 for $MgSiO_3$, and demonstrates that K_0 can vary by up to 5–6% without uncertainty (247–261 GPa) when using a 2nd-order Birch-Murnaghan (BM2) equation of state (EOS). Additionally, when iron and/or aluminum are substituted into $MgSiO_3$, the moduli shift further, reflecting the complexities of modeling the lower mantle.

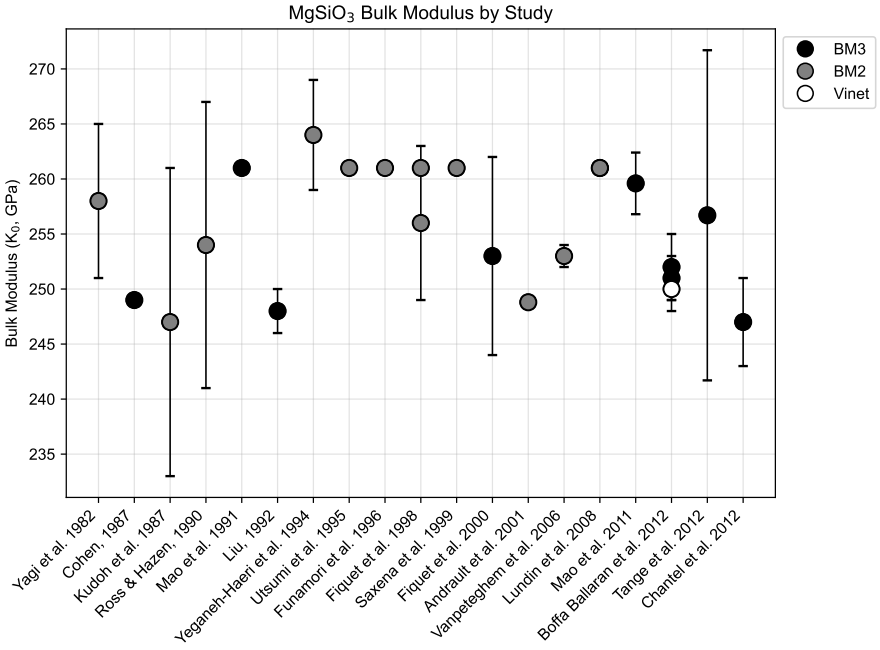

Figure 1.4: Reported isothermal bulk moduli (K_0 GPa) for $MgSiO_3$ bridgmanite from experimental studies (e.g. XRD, ultrasonic, Brillouin), categorized by the type of equation of state (EOS) used: 3rd-order Birch-Murnaghan (BM3), 2nd-order Birch-Murnaghan (BM2), and Vinet. Each point represents a study, with the horizontal axis listing studies chronologically by author/year, and the vertical axis showing the corresponding K_0 values. K_0 errors are included if the study reported them (Yagi *et al.*, 1982; Kudoh *et al.*, 1987; Cohen, 1987; Ross and Hazen, 1990; Mao *et al.*, 1991; Liu, 1992; Yeganeh-Haeri, 1994; Utsumi *et al.*, 1995; Funamori *et al.*, 1996; Jackson and Rigden, 1996; Fiquet *et al.*, 1998; Saxena *et al.*, 1999; Andrault *et al.*, 2001; Vanpeteghem *et al.*, 2006a; Lundin *et al.*, 2008; Mao *et al.*, 2011; Ballaran *et al.*, 2012; Tange *et al.*, 2012; Chantel *et al.*, 2012).

1.3.2 Iron Spin Transitions in the Lower Mantle

The spin transition of iron (Fe) in lower-mantle minerals, particularly bridgmanite and ferropericlase, illustrates the entangled association of crystal-field effects, electron configurations, and extreme geophysical conditions (Catalli *et al.*, 2010; Mao *et al.*, 2015). Crystal-field splitting is the difference in energy between the d-orbitals of a transition metal ion when it is surrounded by a crystal field of ligands. In a free ion, all five d-orbitals have the same energy (they are "degenerate"), but this changes when ligands form a coordination complex around the metal ion. The energy difference created by this process is known as the crystal-field splitting energy, or Δ. The magnitude of Δ determines the resulting electron configurations, magnetic properties, and colors of transition metal complexes (Figure 1.5).

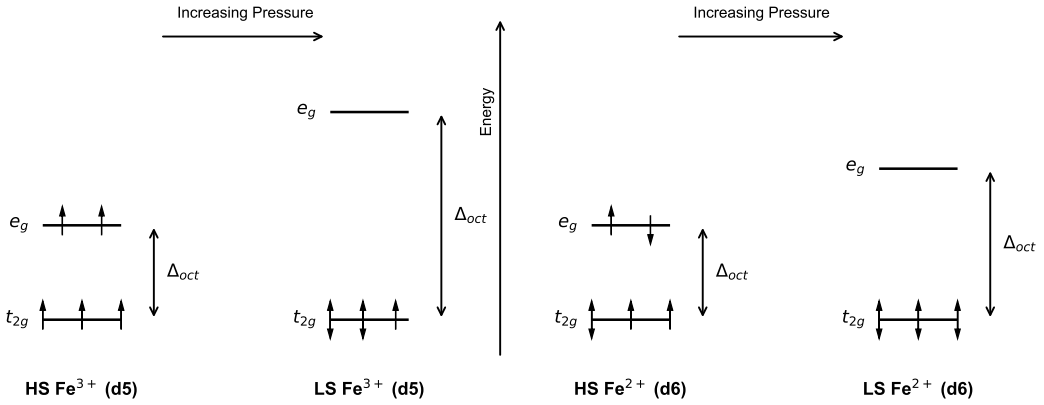

Figure 1.5: Electron configurations of Fe^{3+} ($3d^5$) (left column) and Fe^{2+} ($3d^6$) (right column) in high-spin (HS) (top row) and low-spin (LS) (bottom row) states. $Delta$ is the energy difference created by this process is known as the crystal-field splitting energy. The two sets of d-orbitals (e_g and t_{2g}) formed by the splitting of the five degenerate d-orbitals of a transition metal in an octahedral coordination. Differences in electron occupancy and pairing lead to distinct magnetic and volumetric behavior under high pressures.

Iron in bridgmanite can exist as Fe^{2+} or Fe^{3+}, each of which can transition from a high-spin (HS) state, where electrons occupy higher-energy orbitals singly, to a low-spin (LS) state, where

pairing of electrons is preferred. In general, the LS configuration is favored under sufficiently high pressures because crystal-field splitting increases, making it energetically more advantageous for electrons to occupy the lower-energy orbitals (Lin *et al.*, 2007; Lyubutin *et al.*, 2013; Hsu *et al.*, 2011; Zhu *et al.*, 2020).

A defining result of the HS-LS transition is the reduction in the ionic radius of Fe that accompanies electron pairing. As the Fe ion itself shrinks, the volume of the crystallographic site it occupies contracts, typically producing a measurable decrease in unit-cell volume (Badro *et al.*, 2003; Lin *et al.*, 2005; Hsu *et al.*, 2012). Consequently, density and elastic moduli change, altering seismic wave propagation. Regions undergoing spin transitions can therefore appear as velocity anomalies in tomography (i.e., 2-D or 3-D images of the subsurface) (Lin *et al.*, 2007; Lundin *et al.*, 2008; Mao *et al.*, 2011). This linkage between mineral physics and observed wave-speed variations helps relate deep-Earth composition and structure to geophysical observations (Okuda *et al.*, 2019; Catalli *et al.*, 2011; Fujino *et al.*, 2013; Huang *et al.*, 2015; Badro *et al.*, 2003).

Geodynamic models that explicitly incorporate the depth-dependent HS-LS transition show that the associated density increase modifies buoyancy forces and can reshape mantle flow and thermochemical convection (Bower *et al.*, 2009; Tsuchiya, 2003; Wentzcovitch *et al.*, 2009). Such effects are relevant when interpreting large low-shear-velocity provinces (LLSVPs) and ultra-low-velocity zones (ULVZs), where thermal and compositional anomalies may coincide with spin transitions (Huang *et al.*, 2015; Shahnas *et al.*, 2017; Huang *et al.*, 2015; Vilella *et al.*, 2021; Muir and Brodholt, 2020).

Moreover, spin transitions can influence mantle rheology. Laboratory studies on (Mg,Fe)O indicate that a HS $\rightarrow$ LS change can suppress point-defect diffusion and therefore raise viscosity (Ammann *et al.*, 2011; Saha *et al.*, 2011), suggesting a comparable but less-constrained effect in

Fe-bearing bridgmanite.

Although Fe^{2+} displays a more conventional HS-LS transition pattern, Fe^{3+} exhibits additional complexity because of its half-filled $3d^5$ electron configuration. In principle, this configuration is inherently stable. However, strong crystal fields created by strong ligands and high pressures in the lower mantle can induce partial pairing or changes in bonding that still influence physical properties (Mao *et al.*, 2017; Liu *et al.*, 2018). In this context, the crystal field refers to the electrostatic potential generated by the surrounding anions, which lifts the degeneracy of the Fe $3d$ orbitals into lower-energy (t_{2g}) and higher-energy (e_g) subsets. The strength of this splitting depends on the geometry and size of the cation site, as well as the pressure-temperature conditions, and it governs whether electrons occupy the higher orbitals unpaired (high-spin, HS) or pair in the lower orbitals (low-spin, LS).

Achieving an LS configuration for Fe^{3+} ($3d^5$) requires a sufficiently strong crystal field, which can be provided by the high-pressure environment of the lower mantle or by incorporation into crystallographic sites with small volumes and high symmetry, such as the octahedral site in bridgmanite (Burns, 1993; Kuzmann *et al.*, 2021). Even in the absence of a sharp spin transition, gradual changes in spin state can significantly influence the density, compressibility, and electronic structure of Fe-bearing minerals (Badro *et al.*, 2004; Catalli *et al.*, 2009a; Kupenko *et al.*, 2014).

Figure 1.5 compares the high-spin and low-spin electron configurations for Fe^{2+} and Fe^{3+}, illustrating how different numbers of unpaired electrons translate into distinct magnetic and volumetric behaviors. The significance of this transition lies not merely in the electronic rearrangement itself but in the macroscopic effects that result. As pressure and temperature increase through the lower mantle, both Fe valence states can undergo changes, thereby modifying local seismic wave speeds and influencing the geodynamic behavior of the Earth's deep interior (Lin *et al.*, 2013).

1.3.3 Deep Mantle Heterogeneities

Large Low Shear-Wave Velocity Provinces (LLSVPs)

Among the most notable lower-mantle features are the large low shear-wave velocity provinces (LLSVPs), observed beneath Africa and the Pacific. These structures, which can be as wide as 5000 km and extend up to 1000 km in height from the base of the mantle (Su *et al.*, 1994; Dziewonski *et al.*, 2010; Garnero *et al.*, 2016), exhibit lower V_s (by 2–4%) with only small anomalies in V_p compared to the surrounding mantle. They may represent chemically distinct domains, thermal anomalies, or both (McNamara, 2019; Deschamps *et al.*, 2012). Possible origins include the accumulation of subducted oceanic crust, dense Fe-rich basalt, or remnants of primordial Fe-rich mantle reservoirs (Christensen and Hofmann, 1994; Hofmann, 1997). Their influence on mantle convection is profound, potentially generating plume instabilities and affecting slab descent (Courtillot *et al.*, 2003; Van der Hilst *et al.*, 1997).

Trampert *et al.* (2004) used tomography to infer chemical anomalies throughout the mantle, finding that LLSVPs are denser and have distinct bulk compositions that are likely enriched in Fe and Si but depleted in Mg. They suggest that the observed V_p and V_s anomalies are better explained by chemical heterogeneities than by temperature variations alone. Similarly, Deschamps *et al.* (2012) proposed that LLSVPs are enriched in FeO (10–12 wt%), possibly from accumulated MORB-like basalt or primordial reservoir material, implying that LLSVPs could be compositional piles formed by dynamic mixing and segregation. Recent studies such as Vilella *et al.* (2021) further constrains these compositional and dynamical interpretations, reinforcing the notion that LLSVPs are chemically distinct regions of the mantle.

The compositional traits listed in Table 1.1 summarize the most widely supported chemical

Table 1.1: LLSVP compositional traits per compositional component (weight percent) compared to a pyrolite composition (Anderson, 1989).

Component	Pyrolite (wt%)	Trend vs Pyrolite
FeO	7.80	↑ (10-15 wt%)
MgO	38.10	↓
Al_2O_3	4.60	↑ or baseline
CaO	3.10	Slight ↑
SiO_2	45.10	Slight ↑

distinctions between LLSVPs and ambient pyrolitic mantle, as inferred from thermodynamic interpretations and geophysical modeling. The most consistent finding is an enrichment in FeO, typically ranging from 10-15 wt%, which is required to explain both the observed reduction in V_s and the inferred density increase within LLSVPs (Trampert *et al.*, 2004; Deschamps *et al.*, 2012; Ballmer *et al.*, 2017). The corresponding decrease in MgO reflects the chemical substitution of Fe for Mg in silicate minerals such as bridgmanite and ferropericlase, a process that lowers shear velocity and increases density. Slight enrichment in Al_2O_3 and CaO is consistent with contributions from recycled basaltic material, which stabilizes aluminous and calcium-bearing phases at lower mantle conditions (Deschamps *et al.*, 2012). A modest increase in SiO_2 is also plausible, particularly in models involving the accumulation of eclogitic or basaltic material, which is naturally more silica-rich than pyrolite (Ballmer *et al.*, 2017). Together, these trends describe a composition that is both denser and seismically slower, especially in V_s, than the surrounding lower mantle, thereby offering a chemically consistent explanation for the seismic and dynamic properties of LLSVPs.

These structures are of particular interest because their thermo-chemical properties strongly influence mantle convection, plume dynamics, and heat transport across the core–mantle boundary (Steinberger and Torsvik, 2012). By acting as dense, stable reservoirs, LLSVPs may organize large-scale mantle flow, control the initiation and location of plumes, and help explain the clustering

of hotspots and large igneous provinces at the surface. If they are primordial, they represent long-lived reservoirs preserved since Earth's differentiation. If dominated by recycled crust, they record the efficiency of subduction and mantle mixing through time. In either case, understanding their origin and stability is key to linking deep mantle dynamics with Earth's thermal and tectonic evolution.

Ultra-Low Velocity Zones (ULVZs)

Ultra-low velocity zones (ULVZs) lie near the core-mantle boundary (CMB) (Cottaar and Romanowicz, 2012). They exhibit seismic velocities markedly lower than the surrounding mantle material, suggesting the presence of partial melt or strong compositional contrasts, including high iron content or hydrated phases (Muir and Brodholt, 2020; Hernlund *et al.*, 2015; Williams and Garnero, 1996; Garnero and McNamara, 2008; Anderson, 1977). Some ULVZs are located at the edges of LLSVPs, implying a link between these distinct structures and deeper thermochemical processes (Garnero and McNamara, 2008; McNamara, 2019). These zones are thought to be enriched in iron, which has a great influence on the heat and mass exchange at the CMB (Hernlund *et al.*, 2015). Although their extent is relatively small compared to LLSVPs, ULVZs may be critical in understanding heat flow from the core, the generation of hotspots, and the interactions between the solid mantle and partially molten domains (McNamara, 2019; Li *et al.*, 2025, 2022).

The Post-Perovskite Phase Transition

The perovskite to post-perovskite (Pv–Ppv) transition is strongly influenced by both thermal and compositional effects. A key parameter is the Clapeyron slope, which describes the rate at which the equilibrium pressure of the transition changes with temperature (dP/dT). For the Pv–Ppv boundary this slope is generally positive, meaning that higher temperatures require higher

pressures (greater depths) for post-perovskite to be stable (Tateno *et al.*, 2005; Murakami *et al.*, 2005; Tsuchiya *et al.*, 2004).

The occurrence of a Pv–Ppv double crossing refers to cases where a geotherm intersects this phase boundary twice, first entering the Ppv stability field with increasing depth, and then re-entering the Pv field at greater depth. This produces a thin or discontinuous Ppv layer within an otherwise bridgmanite-dominated mantle, a scenario expected along relatively cool geotherms such as near subducted slabs (Hernlund and Houser, 2008; Hernlund and Bonati, 2019).

The position of the Pv–Ppv boundary is also highly sensitive to composition. Incorporation of Fe and Al alters the relative stability fields of Pv and Ppv by changing their free energies and elastic properties. In general, Al^{3+} and Fe^{3+} tend to stabilize bridgmanite, shifting the Pv–Ppv boundary to higher pressures, whereas Fe^{2+} may favor post-perovskite under some conditions (Dubrovinsky *et al.*, 2001; Kurnosov *et al.*, 2017; Muir and Brodholt, 2020). Such effects imply that chemical heterogeneity in the lowermost mantle contributes to lateral variations in the depth and thickness of the Ppv region.

These combined thermal and compositional controls can generate complex mineralogical layering, promote lateral heterogeneities at the core–mantle boundary, and contribute to seismic scatter and the D″ discontinuity (Hirose *et al.*, 2006; Oganov and Ono, 2004). Moreover, the latent heat associated with repeated Pv–Ppv transitions, coupled with rheological and elastic changes, may impact mantle convection, slab stagnation, and chemical mixing at the base of the mantle (Samuel and Tosi, 2012; Tackley, 2012; Dannberg *et al.*, 2023; Komabayashi *et al.*, 2008; Nakagawa and Tackley, 2014).

1.4 Dissertation Chapter Overview

This section provides a brief summary of the central data chapters. Chapter 2 outlines the experimental and computational techniques used throughout the dissertation, including diamond anvil cell (DAC) experiments, synchrotron X-ray diffraction, and density functional theory (DFT) modeling. These methods form the foundation for the data acquisition and interpretation in subsequent chapters.

Chapter 3: Elastic Behavior of Sintered Polycrystalline Fe-Al-bearing Bridgmanite at High Pressures. *In situ* synchrotron X-ray diffraction experiments conducted in DACs were used to study sintered polycrystalline bridgmanite samples $MgSiO_3$, $Mg_{0.83}Fe_{0.17}Si_{0.91}Al_{0.09}O_3$, and $Mg_{0.68}Fe_{0.32}Si_{0.70}Al_{0.30}O_3$ up to 90 GPa at 300 K. Samples were gas-loaded with helium, neon, or argon, and some runs used metallic-glass gasket inserts to suppress rhenium diffraction. Diffraction-based volume data were fit to third-order Birch-Murnaghan, second-order Birch-Murnaghan, and Vinet equations of state. The Fe-Al-free endmember exhibits K_0 = 255 GPa (K_0' = 4.35), while the Fe-Al-rich sample shows K_0 = 304 GPa (K_0' = 3.05), indicating aluminum's stiffening effect. Helium-loaded runs revealed anomalous behavior between 40 and 55 GPa likely due to infiltration along grain boundaries. Finite-strain and lattice-ratio analyses showed minimal anisotropy ($<1.3\%$) to 90 GPa.

Chapter 4: Elastic Properties of Metastable Fe-Al Majoritic Garnet up to 83 GPa at 300 K. Although bridgmanite was synthesized in a multi-anvil press at 25 GPa and 1800 K, the recovered sample adopted a garnet structure. FIB-prepared disks of $Mg_{0.68}Fe_{0.32}Si_{0.70}Al_{0.30}O_3$ were loaded with argon, Pt markers, and ruby spheres into a DAC for synchrotron XRD at PETRA III. Diffraction patterns from 19.6 to 83.4 GPa show the garnet phase remains stable throughout. Third-order Birch-Murnaghan fits support a cubic model to 35 GPa, while a tetragonal distortion better models data

above 45 GPa. Bulk moduli (230–240 GPa) are consistent with prior studies. Strain-pressure plots and bulk modulus derivatives suggest structural distortions or spin transitions near 24, 50–55, and 75–78 GPa. Compared to the Mg-endmember, Fe-Al substitution increases volume, reduces stiffness, and induces anisotropic compression.

Chapter 5: *Ab Initio* DFT Calculations on Fe-Al-Bridgmanite from 0 to 140 GPa at 0 K. First-principles DFT calculations were performed using CASTEP (PBEsol functional) for $MgSiO_3$, FeAl25, and FeAl50 compositions. Energy cutoffs (800–1100 eV) and k-point meshes were selected for robust convergence. Optimized structures at 5 GPa intervals yielded pressure-volume P–V data fit with third-order Birch-Murnaghan EOS. Fe-Al substitution systematically increased zero-pressure volume and decreased bulk modulus (K_0 = 243.4 GPa to 234.1 GPa), while K_0' remained nearly constant (3.90). Anisotropic lattice contractions were strongest along the a-axis and weakest along the b-axis. These static (0 K) simulations offer a reference for evaluating temperature effects and reinforce the compositional control on elastic behavior.

Chapter 6: *Ab Initio* DFT Calculations at High Temperatures. Density functional theory (DFT) calculations combined with lattice dynamics within the quasi-harmonic approximation (QHA) calculations extended the 0 K DFT models from Chapter 5 to high temperatures (300–3600 K) and pressures (0–140 GPa) for $MgSiO_3$, FeAl25, and FeAl50. Using Helmholtz free energy surfaces, temperature-dependent bulk moduli, thermal expansion coefficients, Grüneisen parameters, and thermal pressures were derived. All compositions show expected thermal softening, but with distinct trends. FeAl50 exhibits the lowest stiffness and highest thermal expansivity, while FeAl25 shows unexpectedly low expansion and relatively high stiffness due to Fe-Al cation pairing.

Concluding Remarks. Taken together, these chapters show that iron and aluminum substitution plays a critical role in modifying the elastic and thermodynamic behavior of bridgmanite and

other mantle minerals. The findings provide additional constraints on the composition-property relationships relevant to seismic interpretations and geodynamic modeling of Earth's deep interior which is done using Perple_X thermodynamic modeling. The thesis concludes with a synthesis of these insights and suggests future experimental and theoretical directions to better resolve the behavior of deep mantle materials.

Chapter 2
Materials and Methodology

In this chapter, the materials and methodology used in this thesis to investigate the behavior of Fe-Al-bearing bridgmanite under extreme conditions are presented. The design and operation of high-pressure tools (including the large volume press and diamond anvil cell) are described first, followed by the characterization techniques (SEM-EDS and XRD) that enable precise analysis of materials at pressures and temperatures equivalent to Earth's deep mantle. Density functional theory (DFT) calculations are then introduced to provide a quantum mechanical framework for interpreting the material's behavior, and the equations of state (EOS) used to model its compression and thermal response are explained. Thermodynamic modeling over a broad pressure–temperature range allows comparisons between experimental data and theoretical predictions, refining understanding of mineral stability and seismic properties. These methods are used in this investigation for sample preparation and analysis but also directly connect to the thesis goals of understanding how iron and aluminum substitution in bridgmanite change the elastic parameters and interpreting the structure–property relationships in deep Earth materials.

2.1 Large Volume Press (LVP)

The large volume press (LVP), also known as the multi-anvil press or apparatus, generates high pressures using anvils (Liebermann, 2011). In materials science and geology, these presses are used to synthesize and study minerals and phases at extreme pressures and temperatures. The LVP's principle follows from the relationship $P = F/A$, where P is pressure, F is force, and A is the area over which force is applied (Halliday *et al.*, 2013).

Force is exerted on an octahedral cell assembly containing the sample material (Liebermann, 2011). Two types of anvils are employed: first-stage and second-stage anvils. This study used a Kawai-type LVP operating on a 6-8 system (Irifune, 2024), consisting of six first-stage anvils and eight second-stage anvils. A hydraulic ram drives the six first-stage anvils, which compress the eight second-stage anvils, and these in turn compress the octahedral cell assembly (Figure 2.1).

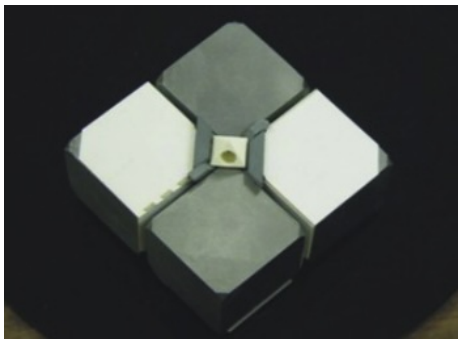

Figure 2.1: Four of the eight 2nd-stage tungsten carbide anvils with the octahedral cell assembly in the center and pyrophyllite gaskets keeping the assembly in place. Image credit: Dr. Kurt Leinenweber, Arizona State University, AZ, USA

The maximum pressure achievable in an LVP depends primarily on the press tonnage and the anvil material. For example, with a 7/3 assembly, a 250-ton press can reach 10 GPa, a 1000-ton press up to 25 GPa, and a 5000-ton press beyond 100 GPa. This study employed two presses at the Bayreuth Geoinstitute (BGI), Germany: a 1000-ton Hymag and a 1200-ton Sumitomo, both used exclusively for sample synthesis prior to diamond anvil cell experiments.

The anvil material and grade also strongly influence maximum pressure (Kunimoto *et al.*, 2016). Common choices include tungsten carbide (WC), sintered polycrystalline diamond, and boron nitride (BN). WC anvils of two grades (i.e., Fujiloy TF05 and Hawedia HA06) are used here. Their mechanical properties (Vickers hardness, Rockwell hardness, and compressional strength) are summarized in Appendix Table B.1 (Ishii *et al.*, 2016). In practice, the HA06 anvils achieved pressures of 25 GPa, while TF05 anvils reached 27 GPa.

2.2 Scanning Electron Microscope with Energy Dispersive X-ray Spectroscopy (SEM-EDS)

Scanning electron microscope with energy dispersive X-ray spectroscopy (SEM-EDS) is used to analyze sample compositions and grain sizes before experiments. An SEM employs a focused electron beam that interacts with atoms in the sample, showing microstructures such as grain size (Fitzgerald *et al.*, 1968). Attached energy dispersive X-ray spectroscopy (EDS) analyzes elemental composition based on the characteristic energies of emitted X-rays (Shindo *et al.*, 2002). This emission results from an electron beam ejecting an inner-shell electron, followed by an electron from a higher-energy shell filling the vacancy, releasing an X-ray diagnostic of the element (Figure 2.2).

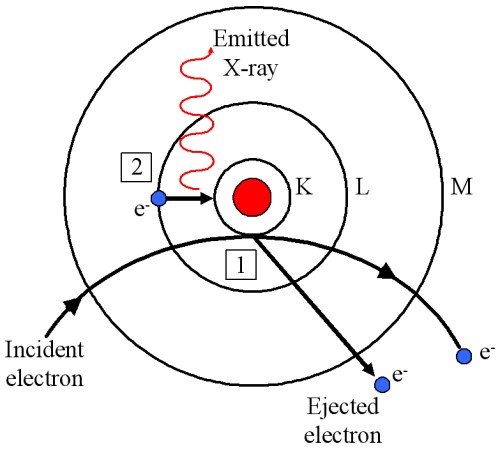

Figure 2.2: Illustration of X-ray emission in EDS. Concentric circles depict electron shells (K, L, M). The incident electron (1) ejects an inner-shell electron, creating a vacancy that is filled by an outer-shell electron (2). This transition emits an X-ray characteristic of the element. Figure adapted from McAneney (2006).

The EDS detector (Oxford Instruments) measures energies and intensities of these emitted X-rays to determine elemental composition and concentration. Data can be presented as spectra, quantitative analyses, or elemental maps. However, because electron and X-ray penetration is

typically limited to the near-surface region (on the order of hundreds of nanometers to a few micrometers, depending on accelerating voltage, sample composition, and density), the analysis provides detailed but localized chemical information. The SEM-EDS (SEM, LEO1530) used for this work is located at Bayreuth Geoinstitute (BGI) in Bayreuth, Germany.

2.3 Diamond Anvil Cell (DAC)

The diamond anvil cell (DAC) is designed to investigate materials under extreme conditions such as those in planetary interiors (Figure A.1) (Eremets, 1996; Li *et al.*, 2018). Two truncated diamond tips called culets, form a minimal surface area that supports extreme pressures based on $P = F/A$, as described in Section 2.1. Diamond, the hardest known natural substance (Callister Jr and Rethwisch, 2020), can withstand high pressures and is transparent across a wide spectrum of electromagnetic waves (including X-rays), enabling *in situ* sample characterization (Figure 2.3).

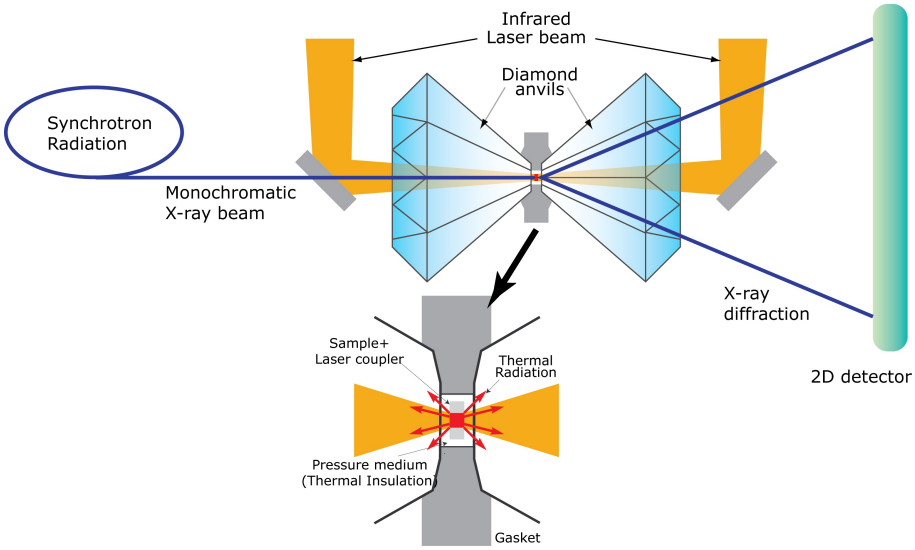

Figure 2.3: Schematic diagram of X-ray diffraction in a diamond anvil cell. Image credit: Dr. Sang-Heon Dan Shim, Arizona State University, AZ, USA.

For this study, standard diamonds that have culets with 200 μm diameters are used by gluing

the table side of the diamond to anvils referred to as seats, one make of tungsten carbide (WC) and the other is of boron nitride (BN). A rhenium gasket that sits between the diamonds is pre-indented to 20–40 μm thickness and has a drilled circular sample chamber. Two types of sample chambers are prepared and used in this study, (1) a 110–120 μm hole laser-drilled into the indented gasket served as the sample chamber; (2) a larger hole (150–165 μm) is initially drilled to place a $Fe_{0.79}Si_{0.07}B_{0.14}$ metallic glass disc provided by Egor Komets (Dong *et al.*, 2022), then trimmed to 110–120 μm. The metallic glass helped reduce rhenium peaks in the X-ray diffraction patterns.

Samples synthesized using an LVP and polished by a technician at BGI are prepared for DAC loading by using a focused ion beam (FIB) to cut 10 μm-thick discs with 30 μm diameter and are loaded either by hand or with a micro-manipulator (Microsupport Axis Pro SS) at Diamond Light Source or Deutsches Elektronen Synchrotron.

Gold (Au) and ruby (Al_2O_3) are added as pressure markers. Figure 2.4 shows a loaded DAC sample chamber before gas loading. To maintain hydrostatic pressure, a super pressure medium is loaded at the beamline (Mills *et al.*, 1980). A gas-pressure membrane and jacket is also employed to allow *in situ* control of DAC pressure through the use of a PACE 5000 pressure controller at Diamond Light Source or at Deutsches Elektronen Synchrotron.

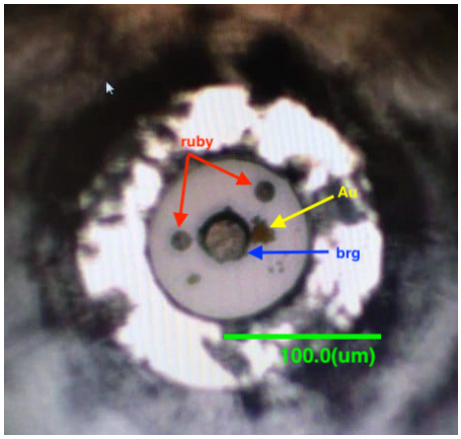

Figure 2.4: DAC sample chamber loaded with a sample disc (brg), ruby spheres, and gold (Au) powder before being closed and gas loaded.

2.4 X-ray Diffraction (XRD)

X-ray diffraction (XRD) is a technique used to determine and identify the atomic structure of crystalline materials. When X-rays interact with a crystalline sample, they are elastically scattered (diffracted) by the electron clouds associated with the atoms in the lattice. Because crystals are composed of periodically arranged atoms that form lattice planes, X-rays incident at specific angles undergo constructive interference, resulting in diffraction cones.

The diffracted intensity is from the constructive interference of scattering from the atoms, which reflects the spatial distribution of electron density and varies with both scattering angle and X-ray wavelength (Cullity and Stock, 2014). The positions and intensities of these peaks provide information about the atomic arrangement and electron density within the crystal.

The most fundamental equation in XRD is Bragg's Law, shown in Equation 2.1, which defines the conditions under which constructive interference occurs (Bragg and Bragg, 1913; Cullity and Stock, 2014). Here (Equation 2.1), n is a positive integer (order of reflection), λ is the wavelength of the incident X-ray beam, d is the interplanar spacing, and θ is the angle between the incident

beam and the lattice plane normal.

$$2d \sin \theta = n\lambda \tag{2.1}$$

Figure 2.5 illustrates the geometry of Bragg's Law, showing incident beams (IB1 and IB2) and diffracted beams (RB1 and RB2) interacting with lattice planes.

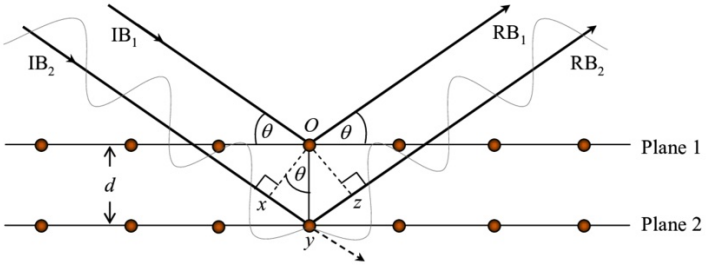

Figure 2.5: Schematic representation of X-ray Diffraction illustrating Bragg's Law (Equation 2.1). "Plane 1" and "Plane 2" are the lattice planes of the crystal structure, with red circles symbolizing atoms within the lattice. "IB1" and "IB2" represent the incident X-ray beams, while "RB1" and "RB2" depict the corresponding diffracted X-ray beams. Source: Thomas (2006)

Bragg's Law is a geometric simplification that treats atomic planes as idealized "mirrors" reflecting X-rays and yields only the condition for diffraction-peak positions. A more exact treatment uses the structure factor, which sums the contributions of electron density from all atoms in the unit cell. In Equation 2.2, f_j is the atomic scattering factor (proportional to the number of electrons in atom j), (x_j, y_j, z_j) are its fractional coordinates, and (hkl) are the Miller indices of the diffracting plane. The structure factor thus defines the scattering amplitude associated with each reflection and links it directly to the crystal's electron-density distribution. In practice, however, the observed diffraction profile is not determined by the structure factor alone, but by its convolution with instrument parameters such as the incident beam profile and detector response, which govern peak intensities and shapes.

$$F(h,k,l) = \sum_j f_j e^{(2\pi i\,(hx_j+ky_j+lz_j))} \tag{2.2}$$

In this study, synchrotron-based *in situ* XRD data are collected at the I15 - Extreme Conditions beamline of Diamond Light Source (Diamond) (Oxfordshire, England) and P02.2 - Extreme Conditions beamline of Deutsches Elektronen Synchrotron (DESY) (Hamburg, Germany). A monochromatic X-ray beam, either 29.2 keV ($\lambda = 0.4246$ Å) or 40.0 keV ($\lambda = 0.3100$ Å), is precisely aligned with the sample contained in the diamond anvil cell (DAC) using stage motors (Figure 2.3). At Diamond, a 2-D Pilatus3 X CdTe 2M detector recorded the resulting diffraction patterns, and at DESY, either a Perkin Elmer (XRD1621) or a GaAs LAMBDA detector is used.

By analyzing the resulting diffraction peaks and referencing the known X-ray wavelength (Å) or beam energy (keV), the *d*-spacing (Å) of each set of lattice planes is determined, providing phase identification. The detector collects these diffraction cones as two-dimensional patterns, each ring corresponding to a specific d-spacing value. The rings' radii decrease as d-spacing becomes smaller, and the center of the image corresponds to the direct beam. Software such as Dioptas (Prescher and Prakapenka, 2015) integrates the 2-D rings into 1-D diffraction patterns and subtracts background for further analysis with techniques like Rietveld refinement (Rietveld, 1969; Young, 1993) or PeakPo analysis software (Shim, 2017) (Section 2.4.1).

In single-crystal diffraction, a well-oriented crystal produces sharp diffraction spots, because only those reciprocal-lattice points that intersect the Ewald sphere at a given orientation satisfy Bragg's law (Cullity and Stock, 2014; Ewald and Ewald, 1923). Each spot corresponds to a specific set of lattice planes at a defined Bragg angle (θ).

In powder diffraction, the sample contains a large number of randomly oriented crystallites.

For any set of planes with spacing d, Bragg's law is satisfied at the same 2θ, but with many different azimuthal orientations (ϕ) around the diffraction cone. On a 2-D detector this produces continuous Debye–Scherrer rings rather than discrete spots (Debye and Scherrer, 1916).

The powder-type patterns used in this thesis are obtained from *in situ* DAC experiments on sintered polycrystalline samples. These conditions are well suited for phase identification at extreme pressure and temperature, as the complete Debye–Scherrer rings provide effective powder averaging without requiring sample rotation.

2.4.1 XRD Analysis in this Thesis

It is important to acknowledge the limitations and uncertainties inherent to XRD analysis. For instance, peak overlap in complex multi-phase systems and micro-strain (i.e., small, non-uniform distortions of interatomic spacings caused by defects, dislocations, or stress fields, which introduce a distribution of d-spacings rather than a single value and thereby broaden diffraction peaks) within the crystal lattice can lead to peak broadening. These often require additional analysis or complementary techniques for a comprehensive understanding. Additionally, spotty XRD rings arising from crystalline size effects or sample behavior under extreme conditions can make Rietveld refinement impractical, since the uneven intensity distribution complicates peak fitting and leads to unreliable refinement results (e.g., false minima). However, within the high-pressure research, XRD serves as a technique for understanding phase transitions, equations of state, and the behavior of materials under extreme conditions like those found in the Earth's mantle.

XRD data in this study often exhibited significant peak broadening, incomplete rings, or high noise, which made Rietveld refinement difficult. Due to this, Rietveld refinement is done only on XRD collected at ambient conditions (i.e., V_0).

Peak fitting for all data was performed using pseudo-Voigt functions, which parameterize the peak center, integrated intensity, peak width, and mixing parameter η that controls the relative contributions of Gaussian and Lorentzian peak broadening (Thompson *et al.*, 1987). The PeakPo software (Shim, 2017) was used to extract peak positions ($2\theta_0$), integrated intensities (A), and peak widths, from which d-spacings were calculated via Bragg's Law.

Prior to fitting, raw diffraction images were processed in Dioptas (Prescher and Prakapenka, 2015) to perform detector calibration and background subtraction. Detector calibration was carried out using standard materials (e.g., CeO_2 or LaB_6), allowing the geometric parameters (sample-to-detector distance, detector tilt/rotation, and beam center) to be refined. Background subtraction was applied to remove scattering from diamonds, gasket, and air paths, which is especially important for weak sample peaks.

The instrument parameter function, describing peak broadening from the optics and detector, was incorporated during fitting, ensuring that peak widths reflect both instrumental and sample contributions. For spotty diffraction rings, often caused by grain growth or preferred orientation at high pressure and temperature, intensity variations were noted but peak positions could still be extracted reliably. These effects limit the use of Rietveld refinement but do not strongly bias the determination of lattice parameters, since volumes depend primarily on accurate peak positions rather than intensities.

The `UCFit` feature in PeakPo then refined the lattice parameters by least-squares minimization (Equation 2.3), where d_{hkl}^{obs} is the observed spacing for Miller indices (hkl) and d_{hkl}^{calc} is the calculated spacing from the chosen crystal symmetry.

$$S = \sum_{hkl} \left[d_{hkl}^{\mathrm{obs}} - d_{hkl}^{\mathrm{calc}} \right]^2 \tag{2.3}$$

The least-squares minimization allows adjusting of the lattice parameters and angles, to reduce the discrepancy between observed and calculated spacings. This method provides a phase fitting for lower-quality diffraction patterns (i.e. high noise, poor background, and partial peak overlap).

2.5 Density Functional Theory (DFT) Calculations

Density functional theory (DFT) is a quantum mechanical method used to calculate the electronic structure of many-body systems, including atoms, molecules, and solids (Sholl and Steckel, 2022). In this study, DFT is used to determine the electronic and structural properties of bridgmanite. Developed from the work of Hohenberg, Kohn, and Sham (Hohenberg and Kohn, 1964; Hohenberg *et al.*, 1990; Kohn and Sham, 1965), DFT is based on the principle that a system's ground-state properties (i.e., 0 K) are uniquely determined by its electron density, $\rho(\mathbf{r})$.

By using the electron density as the central quantity and introducing Kohn–Sham orbitals, which are fictitious single-electron wavefunctions that reproduce the exact ground-state electron density, DFT allows us to treat each electron as moving in an effective potential rather than the full many-electron wavefunction. This greatly reduces computational effort, since $\rho(\mathbf{r})$ is always a three-dimensional function regardless of electron number. The main difficulty in DFT is in describing electron–electron interactions, in particular the exchange–correlation functional, which accounts for quantum mechanical effects of exchange (arising from the Pauli exclusion principle) and correlation (arising from the instantaneous interactions between electrons) that go beyond simple electrostatics.

In the Kohn–Sham formulation of DFT, the many-electron problem is organized into a set of

single-electron equations (Equation 2.4) (Car and Parrinello, 1985).

$$\left(-\frac{\hbar^2}{2m}\nabla^2 + V_{\text{eff}}(\mathbf{r})\right)\psi_i(\mathbf{r}) = \varepsilon_i\psi_i(\mathbf{r}), \tag{2.4}$$

Here, the index i runs over each occupied Kohn–Sham orbital, which is a fictitious single-electron wavefunction introduced to reproduce the exact ground-state electron density. The first term on the left-hand side, $-\frac{\hbar^2}{2m}\nabla^2$, is the kinetic energy operator of the electron, where $\hbar$ is the reduced Planck constant, m is the electron mass, and ∇^2 is the Laplacian operator that measures the curvature of the orbital in space. The quantity ε_i on the right-hand side is the energy eigenvalue associated with orbital $\psi_i(\mathbf{r})$.

The second term, $V_{\text{eff}}(\mathbf{r})$, acts as the effective potential energy experienced by each electron. It is composed of three contributions,

$$V_{\text{eff}}(\mathbf{r}) = V_{\text{ext}}(\mathbf{r}) + V_{\text{H}}(\mathbf{r}) + V_{\text{xc}}(\mathbf{r}), \tag{2.5}$$

where $V_{\text{ext}}(\mathbf{r})$ is the external potential arising from the positively charged atomic nuclei, and $V_{\text{H}}(\mathbf{r})$ is the Hartree potential that represents the classical Coulomb interaction between the electron at position $\mathbf{r}$ and the full spatial distribution of all other electrons. Explicitly, the Hartree potential is given by

$$V_{\text{H}}(\mathbf{r}) = \int \frac{\rho(\mathbf{r}')}{|\mathbf{r} - \mathbf{r}'|}\, d\mathbf{r}', \tag{2.6}$$

which describes the mean electrostatic field generated by the total electron density $\rho(\mathbf{r})$. The third contribution, $V_{\text{xc}}(\mathbf{r})$, is the exchange–correlation potential. This term incorporates the effects that cannot be described by either the external potential or the classical electrostatic interaction alone.

Specifically, the exchange part accounts for the antisymmetry of the many-electron wavefunction enforced by the Pauli exclusion principle, while the correlation part accounts for the tendency of electrons to avoid each other due to instantaneous Coulomb repulsion beyond the mean-field description. Formally, the exchange–correlation potential is defined as the functional derivative of the exchange–correlation energy with respect to the electron density,

$$V_{\mathrm{xc}}(\mathbf{r}) = \frac{\delta E_{\mathrm{xc}}[\rho]}{\delta \rho(\mathbf{r})}. \tag{2.7}$$

The total electron density is obtained from the Kohn–Sham orbitals according to Equation 2.8,

$$\rho(\mathbf{r}) = \sum_{i}^{\text{occupied}} |\psi_i(\mathbf{r})|^2 . \tag{2.8}$$

Since the Hartree potential $V_{\mathrm{H}}(\mathbf{r})$ [Equation 2.6] and the exchange–correlation potential $V_{\mathrm{xc}}(\mathbf{r})$ [Equation 2.7] are explicit functionals of the electron density, the effective potential itself depends on $\rho(\mathbf{r})$,

$$V_{\mathrm{eff}}(\mathbf{r})[\rho] = V_{\mathrm{ext}}(\mathbf{r}) + V_{\mathrm{H}}[\rho](\mathbf{r}) + V_{\mathrm{xc}}[\rho](\mathbf{r}). \tag{2.9}$$

Equations 2.4, 2.8, and 2.9 together define the self-consistent Kohn–Sham scheme: an initial guess for $\rho(\mathbf{r})$ is used to construct $V_{\mathrm{eff}}(\mathbf{r})$, which determines new orbitals $\psi_i(\mathbf{r})$ and thus a new electron density. This cycle is repeated until the input and output densities agree within a chosen tolerance.

2.5.1 Exchange-Correlation Functionals

One challenge in DFT is accurately approximating the exchange–correlation energy. The earliest widely used approach was the Local Density Approximation (LDA), which assumes that

at each point in space the exchange–correlation energy density can be approximated by that of a homogeneous electron gas with the same local density $\rho(\mathbf{r})$. In this way, the system is not treated as globally uniform, but rather each infinitesimal volume element is modeled as if it were part of a uniform electron gas. This approach is computationally efficient and works surprisingly well for many materials, but its accuracy decreases in systems where the electron density changes rapidly in space, since it neglects density gradients and other nonlocal effects (Sahni *et al.*, 1988).

Generalized Gradient Approximations (GGAs) refine LDA by accounting not only for the density but also for its spatial gradient, $\nabla\rho(\mathbf{r})$ (Ziesche *et al.*, 1998; Perdew, 2013). The Perdew–Burke–Ernzerhof (PBE) functional is one widely used GGA that often provides improved results over LDA, particularly for structural properties (Sholl and Steckel, 2022; Perdew *et al.*, 1996). For crystalline solids, the PBEsol functional (Perdew *et al.*, 2008) was developed to restore the correct second-order gradient expansion for exchange in slowly varying densities, which makes it better suited for equilibrium properties of solids such as lattice constants and bulk moduli. This improvement comes at the expense of somewhat less accurate atomization energies compared to PBE, but it significantly enhances predictions of condensed-phase structural parameters. Like other GGAs, however, PBEsol still underestimates electronic band gaps. Figure 2.6 shows the difference in three different functionals (LDA, PBE, and PBEsol) to highlight the impact the functional has on a pressure–volume curve. In this thesis, the PBEsol functional is employed for calculations involving bridgmanite.

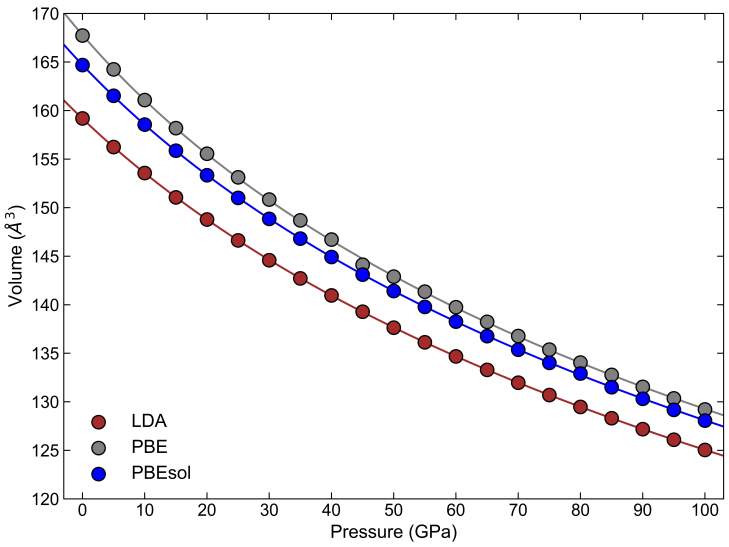

Figure 2.6: Three different functionals calculated on $MgSiO_3$ at 0 K without any pressure correction to show the difference the choice of a functional has on the same composition and structure. Brown circles represent LDA. Gray circles represent PBE. Blue circles represent PBEsol. Curves are BM3-EOS fits for the functional of the corresponding color.

2.5.2 DFT for Periodic Systems and Application to Bridgmanite

DFT can be efficiently applied to periodic solids (e.g., minerals like bridgmanite) by employing a plane-wave basis set. In this approach, the electronic wavefunctions are expanded as a sum of plane waves, $\exp(i\mathbf{G}\cdot\mathbf{r})$, where $\mathbf{G}$ are reciprocal lattice vectors of the crystal. Each plane wave has an associated kinetic energy, $\frac{\hbar^2|\mathbf{G}|^2}{2m}$, so the set of all possible plane waves is infinite. To make the calculation tractable, only plane waves with kinetic energies below a chosen cutoff value, E_{cut}, are included in the expansion. A higher cutoff includes more plane waves with shorter wavelengths, which improves the accuracy of the wavefunction representation but also increases computational cost. In this sense, the "energy cutoff" defines how finely the electronic wavefunctions can be resolved in space.

The efficiency of this approach relies on Bloch's theorem, which states that electrons in a periodic potential (e.g., a crystal lattice) have wave functions that can be expressed as a plane wave

modulated by a function with the same periodicity as the lattice (Segall *et al.*, 2002). This theorem justifies the use of plane waves for describing electronic states in solids and allows for a compact representation of the wave functions in reciprocal space, which is the Fourier-transformed space associated with the crystal lattice. In reciprocal space, points correspond to wavevectors rather than real-space positions, and the periodicity of the lattice in real space translates into a discrete grid of reciprocal lattice vectors.

Sampling of the Brillouin zone is performed at discrete *k*-points, where each *k*-point corresponds to a specific wavevector in reciprocal space. The k-point meshes are selected to ensure sufficiently dense and symmetry consistent sampling of the Brillouin zone, with the mesh density scaled to the reciprocal-lattice dimensions to achieve convergence in energies, stresses, and structural parameters. For example, in orthorhombic bridgmanite (i.e., perovskite), the lower symmetry and anisotropic lattice metrics require a directionally weighted Monkhorst–Pack grid to maintain balanced sampling and reliable elastic-property predictions. Because Bloch's theorem reduces the problem of electrons in a periodic crystal to the first Brillouin zone, the electronic structure can be reconstructed by evaluating the wavefunctions at a finite grid of *k*-points rather than over all possible wavevectors. A denser *k*-point mesh provides a more accurate description of the electronic states, particularly for properties sensitive to the Fermi surface, but also increases the computational cost. To ensure reliable results, both the plane-wave energy cutoff and the density of the *k*-point grid are systematically *converged*, meaning they are gradually increased until the quantities of interest (such as total energy, forces, or stress) change by less than a specified tolerance. Convergence thresholds used in this thesis are in the documentation for CASTEP (CASTEP Developers Group, 2024).

To further reduce computational complexity in plane-wave calculations, pseudopotentials

are introduced. In an all-electron description, the true potential near each nucleus is very steep, and the corresponding core electron wavefunctions oscillate rapidly in space. Representing these oscillations accurately would require an impractically large number of plane waves (i.e., a very high energy cutoff). Pseudopotentials replace the true all-electron potential with a smoother effective potential that reproduces the same scattering properties for the chemically relevant valence electrons, while eliminating the need to explicitly describe the tightly bound core states (Car and Parrinello, 1985). This smoothing reduces the number of plane waves required, thereby lowering the plane-wave cutoff and computational cost, without significant loss of accuracy for structural and energetic properties. Such an approach is particularly important for transition-metal-bearing silicates like bridgmanite, where the presence of heavy elements would otherwise demand prohibitively high cutoffs.

Once the computational parameters are set, geometry optimization ("structure relaxation") seeks the configuration of atoms and cell parameters that minimizes the total energy of the system. For bridgmanite, this procedure is required for accurately capturing its equilibrium crystal structure, which then provides a solid foundation for analyzing other properties such as elastic constants, phonon frequencies, and electronic behavior. Figure 2.7 illustrates the workflow of a DFT calculation performed in this study.

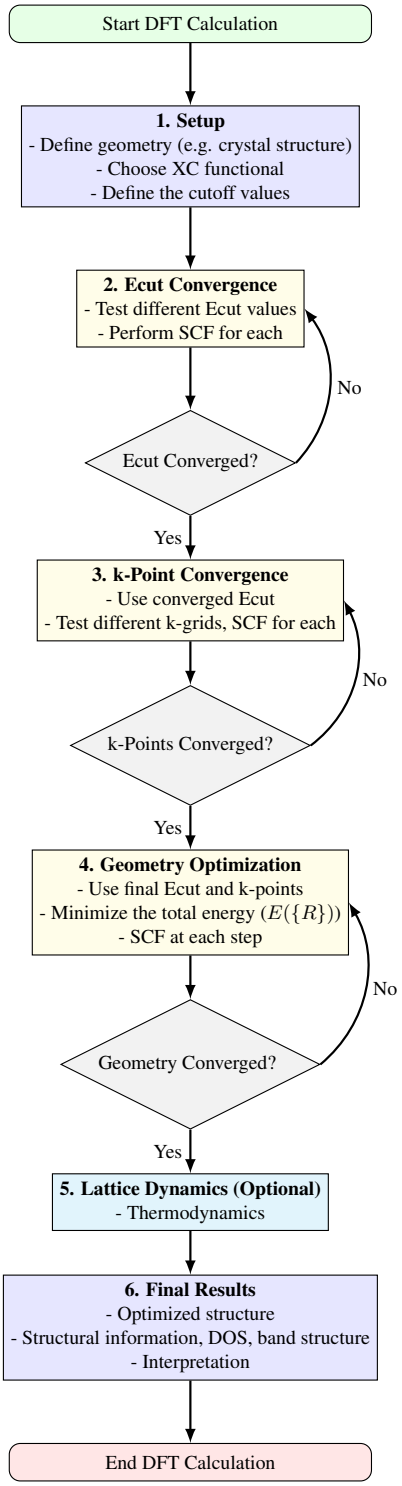

Figure 2.7: DFT (Density Functional Theory) workflow as described in this study. **XC**: exchange-correlation, **Ecut**: plane-wave energy cutoff, k**-grid**: k-point sampling of the Brillouin zone, **SCF**: self-consistent field, **DOS**: density of states. In **Step 1**, the geometry (atomic positions $\{R\}$) and computational parameters (XC functional, cutoff values) are chosen. **Step 2** tests different energy cutoffs to ensure convergence. **Step 3** finds the optimal k-point grid using the chosen Ecut. **Step 4** performs geometry optimization, where atomic positions $\{R\}$ are relaxed. For steps **2-4**, SCF cycles are performed where the Kohn–Sham equation (Equation 2.4) is solved iteratively to update the electron density ($\rho(r)$) until convergence is achieved. Finally, **Step 5** computes structural and electronic properties such as DOS and band structure.

2.5.3 CASTEP: Implementation Details

All DFT calculations in this thesis are performed with the CASTEP 20.11 Ab Initio Total Energy Program (Clark *et al.*, 2005), using the Perdew–Burke–Ernzerhof for solids (PBEsol) functional (Perdew *et al.*, 2008), which is particularly well suited for studying periodic systems. CASTEP provides a robust implementation of plane-wave DFT, supports a range of exchange–correlation functionals (including PBEsol), and offers efficient algorithms for structural optimization and property calculations. Moreover, CASTEP is freely available to UK academic institutions, making it a practical choice for large-scale mineral physics simulations such as our investigation of bridgmanite. The calculations were carried out on the Oxford Advanced Research Computing (ARC) facility at the University of Oxford (Richards, 2015), using a single compute node with 48 CPU cores in parallel and 2 GB of memory per core (96 GB total). In practice, single-point energy calculations required a few hours of wall-clock time, while structural relaxations and equation-of-state calculations typically ranged from 12 to 48 hours depending on system size and convergence settings. Parallel execution in CASTEP allowed efficient use of these resources, making it feasible to model multiple compositions and pressure–temperature conditions within the available computing time.

2.6 Equation of State (EOS)

An equation of state (EOS) connects thermodynamic variables such as pressure P, temperature T, and volume V. For crystalline solids under compression, EOS formulations are commonly derived from finite-strain theory, which expands the free energy of a solid as a function of Eulerian strain. The Birch–Murnaghan EOS is one such model, obtained by expressing the pressure as the derivative of the elastic free energy with respect to strain (Birch, 1947). In its third-order form (BM3-EOS), shown in Equation 2.10, the relationship between pressure and volume is parameterized by

the zero-pressure volume V_0, the bulk modulus K_0, and its first pressure derivative K_0'. Because it provides a physically motivated yet relatively simple expression for the P–V relation, the Birch–Murnaghan EOS is widely used to describe the behavior of bridgmanite and other lower-mantle phases at high pressure (Figure 1.4).

$$P(V) = \frac{3}{2}K_0\Big[\Big(\frac{V_0}{V}\Big)^{\frac{7}{3}} - \Big(\frac{V_0}{V}\Big)^{\frac{5}{3}}\Big] \times \Big\{1 + \frac{3}{4}\big(K_0' - 4\big)\Big[\Big(\frac{V_0}{V}\Big)^{\frac{2}{3}} - 1\Big]\Big\} \tag{2.10}$$

Assuming $K_0' = 4$ reduces Equation 2.10 to the second-order Birch–Murnaghan EOS (BM2-EOS). Holding the pressure derivative of the bulk modulus constant fixes the rate at which the material stiffens under compression (Birch, 1947; Anderson, 1995). This holds the curvature of the pressure–volume (P-V) or pressure–strain (P-f) relationship constant. While this simplification improves fit stability for sparse or low-pressure datasets, it limits the model's ability to reproduce nonlinear stiffening at higher compressions. BM2-EOS is therefore most appropriate for small volume reductions ($<$10%) or pressures below 50–70 GPa, beyond which deviations from experimental data can become significant (Dewaele *et al.*, 2004).

Although BM3-EOS better captures high-pressure behavior, fixing $K_0' = 4$ remains a common simplification in studies of mantle minerals (Knittle and Jeanloz, 1987). The isothermal bulk modulus K_T quantifies resistance to compression at constant temperature (Equation 2.11).

$$K_T = -V\left(\frac{\partial P}{\partial V}\right)_T \tag{2.11}$$

An alternative to the Birch–Murnaghan EOS is the Vinet EOS, also used in high-pressure mineral physics (Vinet *et al.*, 1987, 1989). Derived from an analytic interatomic potential (Hofmeister, 1993), it often provides better fits to experimental data at extreme compressions than BM3-EOS

(Etter and Dinnebier, 2014). Its P-V relation is given by Equation 2.12.

$$P(V) = 3K_0\left(\frac{V}{V_0}\right)^{-\frac{2}{3}}\left[1-\left(\frac{V}{V_0}\right)^{\frac{1}{3}}\right]\exp\left\{\tfrac{3}{2}(K_0'-1)\left[1-\left(\frac{V}{V_0}\right)^{\frac{1}{3}}\right]\right\} \tag{2.12}$$

While the Vinet EOS may better fit measurements at extreme pressures, differences from BM3-EOS are typically small below 100 GPa, making both usually viable for modeling mantle minerals (Etter and Dinnebier, 2014). EOS choice depends on data quality and pressure range: Birch–Murnaghan is well-suited for low to moderate pressures ($<$100 GPa), limited data, and modest compression (Dewaele *et al.*, 2006; Anderson, 1995; Angel, 2000). Its widespread use also facilitates comparison with prior work (Figure 1.4) (Yagi *et al.*, 1982). Vinet, by contrast, is derived directly from interatomic potential theory and often provides a better fit when volume reductions exceed 15–20%, when very high-pressure data are available, or when the detailed repulsive and attractive interactions between ions strongly influence the pressure–volume relationship (Vinet *et al.*, 1989; Hama and Suito, 1996).

Thermal effects can be incorporated into either EOS by adding a thermal pressure term. In the Mie–Grüneisen–Debye formulation, the total pressure is written as the sum of an isothermal EOS (e.g., Birch–Murnaghan or Vinet) and a thermal contribution, as described in Equation 2.13.

$$P(V,T) = P_{\text{iso}}(V) + P_{\text{thermal}}(V,T) = P_{\text{iso}}(V) + \gamma(V)\,\frac{E_{\text{th}}(V,T)}{V} \tag{2.13}$$

Here, $\gamma(V)$ is the volume-dependent Grüneisen parameter, which is often approximated by a power-law form such as

$$\gamma(V) = \gamma_0\left(\frac{V}{V_0}\right)^{q}, \tag{2.14}$$

where γ_0 is the reference value at V_0 and q describes how γ evolves with compression. The thermal energy $E_{\text{th}}(V,T)$ is typically modeled using the Mie–Grüneisen–Debye formulation,

$$E_{\text{th}}(V,T) = 9nRT\left(\frac{T}{\Theta_D(V)}\right)^3 \int_0^{\Theta_D(V)/T} \frac{x^3}{e^x - 1}\,dx, \tag{2.15}$$

where n is the number of atoms per formula unit, R is the gas constant, and $\Theta_D(V)$ is the volume-dependent Debye temperature. Equations 2.13–2.15 together show that the thermal contribution to pressure depends not only on V, T, and γ, but also on additional parameters such as the Debye temperature and atomic composition. An example P–V–T surface for a hypothetical material is shown in Figure 2.8.

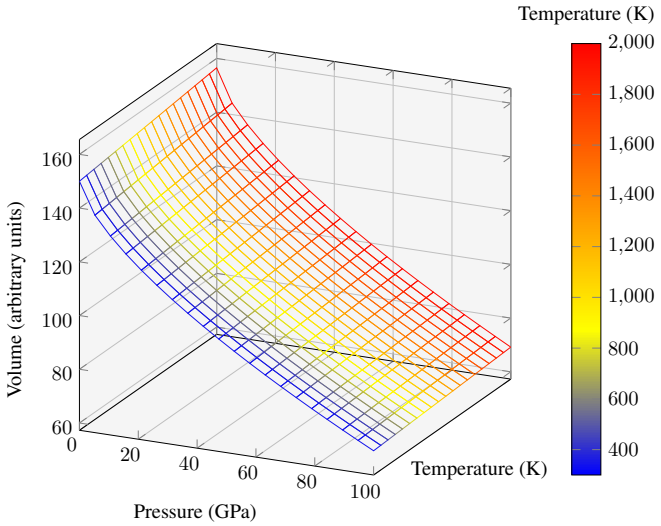

Figure 2.8: Example P–V–T grid, where pressure ranges from 0–100 GPa and temperature from 300–2000 K. Colors denote different temperatures; the reference volume at 300 K is set to 150 (arbitrary units). The surface is generated using a third-order Birch–Murnaghan EOS (K_0=240 GPa) combined with a Mie–Grüneisen–Debye thermal pressure contribution with $\gamma = 1.5$. The P–V curves at constant T are isotherms, and the V–T curves at constant P are isobars.

2.6.1 Euler Finite-Strain Analysis

The finite-strain formalism of the third-order Birch–Murnaghan equation of state (BM3-EOS) is employed to model the pressure–volume response and extract elastic parameters (Birch, 1947; Murnaghan, 1944; Poirier, 2000). In this approach, the Birch–Murnaghan EOS is expressed in terms of the Eulerian finite strain f (Equation 2.16) and the corresponding normalized stress F (Equation 2.17), rather than directly in terms of P and V. The resulting "f–F" representation (reduced stress vs. strain) serves as a diagnostic: linearity confirms that a third-order description suffices, while curvature indicates the need for higher-order terms (Angel, 2000).

$$f = \frac{1}{2}\left[\left(\frac{V_0}{V}\right)^{2/3} - 1\right] \tag{2.16}$$

$$F = \frac{P}{3f(1+2f)^{5/2}}. \tag{2.17}$$

Under BM3-EOS, F varies linearly with f (Equation 2.18), with intercept equal to the zero-pressure bulk modulus K_0 and slope proportional to $K_0(K_0' - 4)$, where K_0' is the first pressure derivative of the bulk modulus. An explicit form for pressure in terms of strain is given in Equation 2.19 (Jeanloz, 1981a; Anderson, 1995).

$$F(f) = K_0 + \frac{3}{2} K_0 \left(K_0' - 4\right) f \tag{2.18}$$

$$P = 3\, K_0\, f\, (1+2f)^{5/2} \left[1 + \frac{3}{2}(K_0' - 4)\, f\right] \tag{2.19}$$

Elastic parameters K_0 and K_0' are determined by nonlinear least-squares fitting of the measured $P(V)$ data to this strain-formulation of the BM3-EOS (Dewaele *et al.*, 2004; Angel, 2000).

The validity of the third-order approximation is confirmed when the experimental points fall on a straight line in the f–F plot. The intercept yields K_0, and the slope corresponds to $\frac{3}{2}K_0(K_0' - 4)$.

2.7 Perple_X Thermodynamic Modeling

Perple_X is a widely used thermodynamic modeling software designed for calculating phase equilibria in complex chemical systems (Connolly, 1990, 2005, 2009). It is particularly valuable in high-pressure mineral physics and petrology, where experimental constraints are often limited. By employing Gibbs free energy minimization, Perple_X determines stable phase assemblages, compositions, and physical properties of minerals and melts under specified pressure–temperature (P–T) conditions (Connolly, 2005; Hacker *et al.*, 2003).

The software operates using internally consistent thermodynamic datasets, which include equations of state (EOS) for solids and fluids, as well as activity models for multi-component solutions. Users define an input bulk composition and specify a range of P–T conditions over which equilibrium assemblages are computed. Perple_X then constructs phase diagrams, density profiles, and other relevant thermodynamic outputs, providing insights into the stability and properties of Earth and planetary materials (Connolly, 2005, 1990; Powell and Holland, 2008).

An advantage of Perple_X is its flexibility in incorporating various thermodynamic formalisms, making it suitable for modeling a wide range of geological processes. In high-pressure studies, it is particularly useful for interpreting experimental data, predicting mineral stability fields, and estimating key physical properties such as density, seismic velocities, and elastic moduli (Stixrude and Lithgow-Bertelloni, 2011; Hacker *et al.*, 2003).

Perple_X modeling provides a thermodynamic framework for interpreting experimental constraints on Fe-Al-bearing bridgmanite stability (Stixrude and Lithgow-Bertelloni, 2011; Nakajima

et al., 2012; Criniti *et al.*, 2021). By varying Fe and Al content within a starting pyrolitic bulk composition (Anderson, 1989), phase diagrams and modal abundance profiles help clarify how increasing substitution of these elements influences bridgmanite stability fields, elasticity, and density under lower mantle conditions (Connolly, 2005; Stixrude and Lithgow-Bertelloni, 2005).

Perple_X results provide a compositional and phase context that helps bridge discrepancies between these sample types, such as differences in density, seismic velocity, and inferred elastic moduli by showing how slight shifts in phase assemblage or mineral composition at fixed P—T conditions may contribute to apparent experimental differences (Murakami *et al.*, 2004; Ballaran *et al.*, 2012; Hirose, 2016).

Despite its strengths, Perple_X has limitations. The accuracy of its predictions depends on the quality of the thermodynamic dataset and solution models used. In this dissertation, `stx21ver` and `stx21_solution_model` from Stixrude and Lithgow-Bertelloni (2022) are used, as they offer the most comprehensive database for modeling mantle mineralogy and seismic velocities. Additionally, the software assumes equilibrium conditions, which may not always reflect the kinetic constraints present in natural systems (Powell and Holland, 2008; Hacker and Bebout, 1996). However, when used critically and in combination with experimental and computational methods, Perple_X serves as a powerful tool for understanding the thermodynamic behavior of minerals at extreme conditions (Connolly, 2005; Stixrude and Lithgow-Bertelloni, 2011; Holland and Powell, 2011).

Chapter 3

Elastic Behavior of Sintered Polycrystalline Fe-Al-bearing Bridgmanite at High-Pressures

3.1 Introduction

Bridgmanite, the most abundant mineral in the Earth's lower mantle, constitutes approximately 70% of its volume (Irifune *et al.*, 2010; Murakami *et al.*, 2012; Lin *et al.*, 2013). As the dominant phase, bridgmanite's elastic properties significantly influence seismic velocity profiles, anisotropy, and interpretations of mantle convection and compositional heterogeneities. Previous studies such as Ballaran *et al.* (2012) and Catalli *et al.* (2011) have extensively characterized the properties of single-crystal and powder bridgmanite samples (Table 3.1), however, natural mantle assemblages are inherently more complex, typically consisting of polycrystalline aggregates with extensive grain boundaries and compositional variations (e.g., Fe and Al substitution). These factors further impact the elastic and structural behavior of mantle minerals, necessitating investigations that reflect such mantle complexities.

The incorporation of iron (Fe) and aluminum (Al) into bridgmanite's $MgSiO_3$ lattice structure alters its physical properties. Iron, existing primarily as Fe^{2+} and Fe^{3+}, occupies distinct crystallographic sites with varying effects on bonding, compressibility, and electronic structure. Aluminum substitution can couple with Fe to maintain charge balance, influencing octahedral tilting and lattice distortions (Burns, 1993; Catalli *et al.*, 2009b). Understanding how these substitutions affect bridgmanite under lower mantle conditions is required for accurate geophysical modeling for regions such as large low-shear velocity provinces (LLSVPs) which exhibit seismic signatures

distinct from surrounding mantle material (Wang *et al.*, 2021).

Experimental studies typically use helium as a pressure-transmitting medium in diamond anvil cell (DAC) experiments due to its exceptional hydrostatic properties. However, some results presented in this study possibly indicate that helium may penetrate the grain boundaries of polycrystalline samples, potentially altering their compressibility.

To address these complexities and better replicate lower mantle conditions, this research utilizes pre-synthesized sintered polycrystalline bridgmanite samples with compositions representative of both the $MgSiO_3$ end-member and Fe-Al-bearing variants: $MgSiO_3$, $Mg_{0.83}Fe_{0.17}Si_{0.91}, Al_{0.09}O_3$, and $Mg_{0.68}, Fe_{0.32}Si_{0.70}, Al_{0.30}O_3$; M-brg, F1A1-brg, and F3A3-brg respectively. These samples are studied using *in situ* synchrotron X-ray diffraction across a broad pressure range (up to approximately 90 GPa) at ambient temperature (i.e., 300 K). These experiments on Fe-Al-bearing bridgmanite also systematically explored the impact of different noble-gas pressure media (helium, neon, and argon) and the use of a metallic glass gasket insert to prevent rhenium peaks in X-ray diffraction patterns (Dong *et al.*, 2022). This research aims to provide additions to the understanding of bridgmanite for interpreting seismic data and modeling the complex, heterogeneous nature of Earth's deep interior.

Table 3.1: X-ray diffraction experiments (this study and selected literature) on $MgSiO_3$, Fe-bearing, and Fe-Al-bearing bridgmanite (perovskite). The table is sorted by increasing iron content within each composition category. Symbols in the Reference column describe the sample type (e.g., single crystal, polycrystalline, powder).

Composition	P (GPa)	P Medium	Reference
Fe-Al-free			
$MgSiO_3$	0–43.5	He	This Study[†]
$MgSiO_3$	0–53.75	NaCl	Nishio-Hamane *et al.* (2008)[‖]
$MgSiO_3$	0–76.7	He	Ballaran *et al.* (2012)[*]
$MgSiO_3$	28.8–93.0	Ar	Lundin *et al.* (2008)[‖]
$MgSiO_3$	30–120	Ne	Mao *et al.* (2011)[‡]
Fe-bearing			
$(Mg_{0.96}, Fe_{0.04})SiO_3$	0–74.3	He	Ballaran *et al.* (2012)[*]
$(Mg_{0.91}, Fe_{0.09})SiO_3$	0–86.1	Ar, NaCl	Lundin *et al.* (2008)[‖]
$(Mg_{0.88}, Fe_{0.12})SiO_3$	20–127	-	Knittle and Jeanloz (1987)[‡]
$(Mg_{0.85}, Fe_{0.15})SiO_3$	0–107.9	Ar	Lundin *et al.* (2008)[‖]
$(Mg_{0.75}, Fe_{0.25})SiO_3$	60–135	Ne	Mao *et al.* (2011)[‡]
$(Mg_{0.46}, Fe^{3+}_{0.53})(Si_{0.49}, Fe^{3+}_{0.51})O_3$	24–85	Ne	Liu *et al.* (2018)[‡]
Fe-Al-bearing			
$Mg_{0.94}Fe^{2+}_{0.04}Fe^{3+}_{0.02}Al_{0.01}Si_{0.99}O_3$	0–85	He	Mao *et al.* (2017)[‡]
$Mg_{0.89}Fe^{2+}_{0.024}Fe^{3+}_{0.096}Al_{0.11}Si_{0.89}O_3$	0–110	He	Mao *et al.* (2017)[‡]
$(Mg_{0.88}, Fe_{0.13})(Si_{0.88}, Al_{0.11})O_3$	25–95	Ar	Catalli *et al.* (2011)[‖]
$(Mg_{0.85}, Fe_{0.15})(Si_{0.85}, Al_{0.15})O_3$	0–127.82	NaCl	Nishio-Hamane *et al.* (2008)[‖]
$Mg_{0.83}, Fe_{0.17}Si_{0.91}, Al_{0.09}O_3$	5.1–38.4	He	This Study[†]
$Mg_{0.83}, Fe_{0.17}Si_{0.91}, Al_{0.09}O_3$	22.0–33.5	He	This Study[†]
$Mg_{0.83}, Fe_{0.17}Si_{0.91}, Al_{0.09}O_3$	0.0; 70.7-86.8	He	This Study[†]
$Mg_{0.79}Fe_{0.08}Al_{0.22}Si_{0.91}O_3$	12.09–55.16	KCl	Okuda *et al.* (2019)[‡]
$Mg_{0.68}, Fe_{0.32}Si_{0.70}, Al_{0.30}O_3$	6.5–96.0	He	This Study[†]
$Mg_{0.68}, Fe_{0.32}Si_{0.70}, Al_{0.30}O_3$	3.74–35.38	He	This Study[†]
$Mg_{0.68}, Fe_{0.32}Si_{0.70}, Al_{0.30}O_3$	0.0; 2.1–63.5	Ne	This Study[†]
$Mg_{0.68}, Fe_{0.32}Si_{0.70}, Al_{0.30}O_3$	5.8–60.7	Ar	This Study[†]
$Mg_{0.662}Fe_{0.338}Si_{0.662}Al_{0.338}O_3$	0		Nakatsuka *et al.* (2021)[*]
$Mg_{0.60}Fe^{2+}_{0.03}Fe^{3+}_{0.38}Si_{0.62}Al_{0.36}O_3$	0–74.4	He	Ballaran *et al.* (2012)[*]
$Mg_{0.50}Fe_{0.50}Si_{0.50}Al_{0.50}O_3$	18–102	Ne	Zhu *et al.* (2020)[‡]

[†] Sintered Polycrystalline
[‡] Polycrystalline
[‖] Powder
[*] Single Crystal

3.2 Material and Methods

This section outlines the steps taken to synthesize, prepare, and analyze the sintered polycrystalline bridgmanite samples in this study, as well as the methods used to collect and interpret

experimental data under high-pressure conditions. The procedures for creating sintered polycrystalline bridgmanite are described, highlighting the purpose of pre-synthesizing the samples to control both structure and chemistry. The preparation of these samples for high-pressure experiments in the diamond anvil cell (DAC) is then detailed, including sample cutting (via FIB) and pressure medium selection. DAC setup is introduced, emphasizing the importance of quasi-hydrostatic conditions and accurate pressure monitoring. Finally, the data analysis approach is discussed, focusing on the collection of X-ray diffraction (XRD) patterns and subsequent data processing.

3.2.1 Synthesis of Sintered Polycrystalline Bridgmanite

This study investigates pre-synthesised, sintered, polycrystalline bridgmanite with three compositions: $MgSiO_3$, $(Mg_{0.83}Fe_{0.17}Si_{0.91}Al_{0.09})O_3$ (F1A1-brg), and $(Mg_{0.68}Fe_{0.32}Si_{0.70}Al_{0.30})O_3$ (F3A3-brg). Using pre-synthesized bridgmanite ensures that both the sample's composition and structure are characterized prior to experiments. While experimental conditions of DAC experiments may favor bridgmanite formation, kinetic barriers, such as high activation energies, can slow the transformation from precursor minerals (e.g., olivine, akimotoite, or majorite) to bridgmanite, limiting the reaction's progress within the time constraints of an experiment. Additionally, sintered polycrystalline samples are generally preferred in high-pressure experiments because they exhibit enhanced mechanical stability and more uniform stress distribution compared to single crystals, properties that better reproduce the expected bulk behavior of lower-mantle minerals. In this work, these advantages are assumed to apply to the synthesized bridgmanite samples, although the stress state and stability under load are not directly measured. This choice also reflects natural conditions, as deep-Earth minerals at high temperatures recrystallize into polycrystalline aggregates

with well-defined grain boundaries and orientations, representing the thermodynamically stable texture under mantle conditions (German, 1996; Rahaman, 2017; Ringwood, 1991; Karato *et al.*, 2013; Guo *et al.*, 2023).

$MgSiO_3$ (M-brg)

For synthesis of sintered polycrystalline $\mathrm{MgSiO_3}$, a glass is first produced to minimize impurities. This glass is created by thoroughly mixing MgO and $\mathrm{SiO_2}$ powders (both $< 1\,\mu$m in size, purity 99.9%), as detailed in Table 3.2, using an agate mortar and pestle to form the starting composition.

Initially, stoichiometrically correct amounts of MgO and $\mathrm{SiO_2}$ powders in grams were mixed and used for the glass synthesis. However, the retrieved glass is analyzed via SEM-EDS and showed approximately a 10% excess of $\mathrm{SiO_2}$ in SEM-EDS analysis; this data is unfortunately unable to be presented. Thus, an additional 10% MgO is added to the powder mixture to compensate for contamination of $\mathrm{SiO_2}$ from the typical mortar and pestle cleaning process (i.e., $\mathrm{SiO_2}$ powder and ethonal).

The $\mathrm{MgSiO_3}$ mixture is loaded into a Pt-capsule designed for piston-cylinder experiments at BGI (length: 10 mm, diameter: 5 mm, wall thickness: 0.25 mm), and the capsule is micro-welded to prevent sample loss during glass synthesis. The sealed capsule is placed inside an alumina crucible and heated in a Nabertherm furnace at 1650°C (1923 K) for 1 hour, followed by immediate quench in a water bath. The capsule is then carefully opened using a Well 4240 diamond wire saw, preventing crushing and Pt contamination. SEM-EDS analysis confirmed the glass has the desired stoichiometry with a 1:1:3 atomic ratio (Figure A.2, Table B.2).

After SEM-EDS analysis of the glass, it is then crushed and loaded into a Re-foil capsule for

Table 3.2: Calculated amounts of powders for MgO and SiO_2 for the synthesis of $MgSiO_3$ glass. Column one is the component. Column two is the amount in grams needed for the stoichiometrically correct ratio of MgO and SiO_2. Column three is the actual amount in grams used. Columns four and five give the corresponding values in moles.

Component	Amount (g)	Adjusted (g)	Moles	Adjusted Moles
MgO	1.00372	1.10409	0.0249	0.0274
SiO_2	1.49629	1.49629	0.0249	0.0249
Total	2.50001	2.60037	0.0498	0.0523

the synthesis of bridgmanite. The Re-capsule is placed into a standard BGI $7/3$ assembly. The 7/3 assembly refers to a high-pressure multianvil cell design developed at the Bayreuth Geoinstitut. It consists of a 7 mm edge-length Cr_2O_3-doped MgO octahedron as the pressure medium with a truncated 3 mm edge-length anvil geometry, hence the shorthand "7/3" (Criniti *et al.*, 2024). This configuration allows stable generation of pressures up to $\sim$27 GPa in a 1000-tonne Kawai-type multianvil press, with temperatures exceeding 2000 K when a $LaCrO_3$ furnace is used. The Re-foil capsule containing the sample is positioned at the octahedron center, surrounded by the furnace assembly and insulation layers, ensuring a quasi-hydrostatic pressure environment during heating. This assembly is widely employed in lower-mantle mineral physics studies because it balances sample volume (tens of micrograms) with the ability to reach relevant pressure–temperature conditions reproducibly. Synthesis is conducted at 25 GPa ($\pm$1 GPa) and 1650°C (1923 K; $\pm$100 K) for 5 minutes, followed by an immediate quench. Temperature for LVP synthesis is approximated using power, with reference to calibration curves and similar desired pressure–temperature conditions from previous runs that used the same assembly and LVP. After synthesis, the sample is cut, polished (10 μm thick), and the composition is verified via SEM-EDS.

Fe-Al-bearing Bridgmanite

Fe-Al-bearing bridgmanite samples F1A1-brg and F3A3-brg are synthesized using pre-synthesized glasses from Fei *et al.* (2024). The glass for each composition is ground into powder and loaded into Re-foil capsules that were approximately 1 mm in height and 0.5 mm in diameter for each synthesis.

For F1A1-brg, synthesis is performed using a 7/3 assembly in the 1200-ton Sumitomo press at BGI, with conditions of approximately 25 GPa ($\pm$1 GPa) and 1650°C (1923 K; $\pm$100 K) for 5 minutes. For F3A3-brg, synthesis is done using a 7/3 assembly in the 1000-ton Hymage press at BGI, at 27 GPa ($\pm$1 GPa) and 1650°C (1923 K; $\pm$100 K) for 5 minutes. Temperature is approximated using power, with reference to calibration curves and similar desired pressure-temperature conditions from previous runs that used the same assembly. Following synthesis, the samples were cut and polished (10 μm thick) for composition and phase verification by SEM-EDS (Figures A.4, A.5).

Charge Balancing

Bridgmanite can contain Mg, Fe, Si, Al, and O. Charge neutrality requires that the total positive charge from cations balance the total negative charge from oxygen (O^{2-}). Magnesium, silicon, and aluminum occur in fixed oxidation states (Mg^{2+}, Si^{4+}, Al^{3+}), whereas iron may exist as either Fe^{2+} or Fe^{3+}. Because SEM–EDS provides only the total Fe content, we treat x as the fraction of Fe present as Fe^{2+} and $(\mathrm{Fe}_{\mathrm{tot}} - x)$ as Fe^{3+}, and determine x by imposing charge neutrality.

For F1A1–brg $\left(\mathrm{Mg}_{0.83}\mathrm{Fe}_{0.17}\mathrm{Si}_{0.91}\mathrm{Al}_{0.09}\mathrm{O}_3\right)$, oxygen contributes $3 \times (-2) = -6$. The fixed-state cations contribute $0.83 \times 2 + 0.91 \times 4 + 0.09 \times 3 = 1.66 + 3.64 + 0.27 = +5.57$.

The Fe contribution is $2x + 3(0.17 - x) = 0.51 - x$. Imposing a total cation charge of +6 gives $5.57 + (0.51 - x) = 6$, yielding $x = 0.08$ and $0.17 - x = 0.09$. The charge-balanced formula is therefore $\mathrm{Mg_{0.83}Fe^{2+}_{0.08}Fe^{3+}_{0.09}Si_{0.91}Al_{0.09}O_3}$.

For F3A3–brg $\left(\mathrm{Mg_{0.68}Fe_{0.32}Si_{0.70}Al_{0.30}O_3}\right)$, the fixed-state cations contribute $0.68 \times 2 + 0.70 \times 4 + 0.30 \times 3 = 1.36 + 2.80 + 0.90 = +5.06$. The Fe contribution is $2x + 3(0.32 - x) = 0.96 - x$. Requiring a total cation charge of +6 leads to $5.06 + (0.96 - x) = 6$, which gives $x = 0.02$ and $0.32 - x = 0.30$. Thus, the charge-balanced formula is $\mathrm{Mg_{0.68}Fe^{2+}_{0.02}Fe^{3+}_{0.30}Si_{0.70}Al_{0.30}O_3}$.

Uncertainties (1σ) on cation proportions were determined from replicate SEM–EDS analyses and propagated to Fe valence using first–order error analysis. With $x \equiv \mathrm{Fe^{2+}} = (2\,\mathrm{Mg} + 4\,\mathrm{Si} + 3\,\mathrm{Al} + 3\,\mathrm{Fe_{tot}}) - 6$, $\mathrm{Fe^{3+}} = \mathrm{Fe_{tot}} - x$, and assuming independent errors, propagation gives $\sigma_x^2 = (2\sigma_{\mathrm{Mg}})^2 + (4\sigma_{\mathrm{Si}})^2 + (3\sigma_{\mathrm{Al}})^2 + (3\sigma_{\mathrm{Fe}})^2$, $\sigma^2_{\mathrm{Fe^{3+}}} = (2\sigma_{\mathrm{Mg}})^2 + (4\sigma_{\mathrm{Si}})^2 + (3\sigma_{\mathrm{Al}})^2 + (2\sigma_{\mathrm{Fe}})^2$. Reported compositions, expressed in atoms per formula unit (pfu, normalized to the three oxygen atoms for the $\mathrm{ABO_3}$ stoichiometry of bridgmanite, 1σ), are: F1A1–brg $\mathrm{Mg_{0.83\pm0.005}Fe_{0.17\pm0.005}Si_{0.91\pm0.005}Al_{0.09\pm0.005}O_3}$ with $\mathrm{Fe^{2+}} = 0.08 \pm 0.03$, $\mathrm{Fe^{3+}} = 0.09 \pm 0.03$; F3A3–brg $\mathrm{Mg_{0.68\pm0.005}Fe_{0.32\pm0.005}Si_{0.70\pm0.005}Al_{0.30\pm0.005}O_3}$ with $\mathrm{Fe^{2+}} = 0.02 \pm 0.03$, $\mathrm{Fe^{3+}} = 0.30 \pm 0.03$.

In these derivations, charge neutrality is satisfied solely by adjusting the $\mathrm{Fe^{2+}/Fe^{3+}}$ ratio under the assumption of full site occupancy. However, bridgmanite can also accommodate charge imbalance through the formation of cation vacancies, particularly on the A-site (Mg/Fe) (Fei *et al.*, 2021; Ismailova *et al.*, 2016). Because SEM–EDS analyses provide only total cation proportions, vacancies cannot be resolved directly here. The reported formulas should therefore be regarded as charge-balanced approximations, with the caveat that minor vacancy contributions may also play a role in charge compensation.

3.2.2 Diamond Anvil Cell (DAC)

This study employs diamond anvil cells (DAC) to conduct experiments under extreme conditions comparable to those in Earth's lower mantle. DAC preparation includes synthesis of starting materials (Chapter 3.2.1), gasket indentation, loading of samples and pressure standards, and introduction of a gas pressure medium.

At the Department of Materials, University of Oxford, a focused ion beam (FIB) is used to prepare bridgmanite sample disks (M-brg, F1A1-brg, and F3A3-brg; see Chapter 3.2.1). The FIB locates individual grains and sections them with the ion beam, then mills them into circular disks approximately 30 μm in diameter and 10 μm thick. A final low-energy ion beam polish minimizes surface damage and ensures parallel faces suitable for DAC loading. FIB preparation is chosen because it allows precise targeting of small grains and avoids mechanical damage that can occur during conventional polishing. Each disk is loaded into a DAC containing a pre-indented rhenium gasket with a precisely cut hole forming the sample chamber. Rhenium is selected as the gasket material due to its exceptional strength and resistance to deformation under high pressures. When available, sample loading is performed with a micro-manipulator (Microsupport Axis Pro SS) at Beamline I15–Extreme Conditions, Diamond Light Source (Diamond). The system includes a high-resolution microscope, two motorized micromanipulators equipped with needles, and a motorized sample stage with memory that allows switching between two sample locations.

Gas loading the DAC is conducted by beamline scientist Egor Komets using a specialized high-pressure gas-loading system. Helium (He), neon (Ne), or argon (Ar) served as the pressure-transmitting medium. Pressure is applied using a gas-driven membrane and jacket system connected to an external gas regulator. He is typically preferred as pressure media due to its low X-ray

scattering cross-sections, reducing background noise in diffraction patterns, and quasi-hydrostaticity. However, argon is also employed as an alternative pressure medium to investigate anomalous trends observed in datasets collected with helium. Neon was not intended to be loaded but was accidentally loaded. However, the addition of the Ne data is found to be extremely useful for comparing pressure media in this research. In some experiments, metallic glass gasket inserts (Dong *et al.*, 2022) are used to minimize diffraction from the rhenium gasket, which otherwise interfered due to the X-ray beam size at Diamond at the time of these experiments. Each DAC is mounted on a dedicated holder optimized for the specific experimental setup and beamline configuration.

At Diamond, *in situ* pressure measurements employed ruby fluorescence, gold diffraction, or both to accurately monitor applied pressure throughout each experimental run. However, for the experimental run using Ar neither gold nor ruby is able to be detected within the sample chamber either due to weak signal or are lost under the gasket, thus, Ar gas is used for the pressure scale for certain cases. Synchrotron X-ray diffraction (XRD) measurements used a focused beam diameter of $\leq$20 μm at Diamond. High-resolution optical microscopes and precision translation stages ensures accurate alignment of samples relative to the incident beam.

3.2.3 Data Analysis

X-ray diffraction (XRD) is one of the most widely used techniques for phase identification, crystallographic analysis, and determination of structural parameters. During data collection, diffraction images are recorded using 2-D detectors, and integration is performed using Dioptas (Prescher and Prakapenka, 2015) to convert the 2-D images into 1-D diffraction patterns.

As mentioned in Sections 2.4.1 and 3.2, ideally XRD data is analyzed using full-profile methods such as Rietveld refinement (Rietveld, 1969), which fits the entire diffraction pattern

using a structural model to refine lattice parameters, atomic positions, occupancies, and thermal parameters. Under high-pressure DAC conditions, however, the limited number of reflections often makes such full Rietveld analysis impractical. A common compromise is Le Bail or Pawley refinement, in which the whole pattern is fitted with profile functions but without refining the atomic structure, allowing reliable extraction of unit-cell parameters and peak intensities (Le Bail *et al.*, 1988; Pawley, 1981). These whole-pattern approaches require good signal-to-noise ratio across the 2θ range, minimal peak overlap or well-characterized peak broadening, adequate background subtraction, and at least for Rietveld, a reliable initial structural model. Despite polycrystalline, texturally equilibrated starting material in a nominally hydrostatic medium, our high-pressure data exhibit spotty or incomplete Debye–Scherrer rings and anisotropic broadening, conditions that degrade whole-pattern refinements. These issues are especially severe in Fe-bearing bridgmanite, where stress and defect accumulation further intensify line broadening (Prakapenka *et al.*, 2005; Zhang *et al.*, 2019; Klotz *et al.*, 2009; Singh, 1993; Konôpková *et al.*, 2015). Therefore, instead of relying on Le Bail or Rietveld analysis at high pressure, peak-based methods were used with PeakPo (Shim, 2017), while Rietveld refinement with *Match!* 4.1 Build 311 (Putz and Brandenburg, 2025) is restricted to ambient-condition XRD data.

3.3 Results

This section presents the *in situ* X-ray diffraction (XRD) experiments conducted at high pressures (300 K) on three pre-synthesized sintered polycrystalline bridgmanite samples: $\mathrm{MgSiO_3}$ (M-brg), $\mathrm{Mg_{0.83}, Fe_{0.17}Si_{0.91}, Al_{0.09}O_3}$ (F1A1-brg), and $\mathrm{Mg_{0.68}, Fe_{0.32}Si_{0.70}, Al_{0.30}O_3}$ (F3A3-brg). Table 3.3 yielded pressure-volume (P–V) data refined as described in Section 2.4.1.

Initial lattice parameters are taken from Yagi *et al.* (1978) and starting EOS parameters ($K_0 = 259.6(28)$ GPa, $K_0' = 3.5(1)$) from Mao *et al.* (2011). This approach ensures that, provided the starting parameters represents the correct phase and is sufficiently close to the experimental data, the fitting process converges to a consistent solution independent of these initial parameters. The compression behavior of the unit-cell volume with increasing pressure allows determination of the isothermal bulk modulus (K_0) and its pressure derivative (K_0').

From ambient to high pressure, all three compositions compress nonlinearly, with Fe-Al substitution systematically increasing the zero-pressure volume V_0 and decreasing the bulk modulus K_0. Residuals of the third-order Birch-Murnaghan fits (Eq. 3.1) reveal minor medium-dependent deviations. Below, the ambient characterization is discussed (Section 3.3.1), the trend in lattice parameters with pressure (Section 3.3.2), and then the P–V trends are quantified and the fitted EOS parameters are presented (Section 3.3.3).

3.3.1 Ambient Pressure Characterization and Phase Identification

Table B.6 lists all pressure points at which XRD patterns were collected for all compositions, along with the refined lattice parameters and unit-cell volumes. Figures 3.1, 3.2, and 3.3 show the ambient-pressure XRD patterns used to verify phase purity and indexing for M-brg, F1A1-brg, and F3A3-brg, respectively.

For M-brg, the refined ambient-pressure lattice parameters using PeakPo were determined to be $a = 4.7779(20)$ Å, $b = 4.9345(21)$ Å, and $c = 6.8970(30)$ Å. Rietveld refinement is also done using *Match!* (Putz and Brandenburg, 2025), and the refined ambient-pressure lattice parameters were determined to be $a = 4.7778(3)$ Å, $b = 4.9328(4)$ Å, and $c = 6.8917(7)$ Å(see Table B.6).

For F1A1-brg, the refined ambient-pressure lattice parameters using PeakPo were determined

Table 3.3: Summary of X-ray diffraction experiments on bridgmanite samples. Run numbers (column one) are arbitrarily assigned. $\mathbf{P}_m$ is pressure medium and $\mathbf{P}_s$ is pressure scale. Asterisk (*) indicates runs using metallic glass gasket inserts (Dong *et al.*, 2022). Exclamation mark (!) denotes datasets with anomalous data discussed in later text. Table B.6 list the elastic parameters with uncertainties for all these experimental runs for M-brg, F1A1-brg, and F3A3-brg, respectively.

Composition	Run	P (GPa)	$\mathbf{P}_m$	$\mathbf{P}_s$	X-ray energy (keV)
M-brg $\left[\mathrm{MgSiO_3}\right]$					
	1	0.00	–	–	29.201
	2	5.55 – 19.12	He	Au	39.995
	3!	14.5 – 43.5	He	ruby	29.201
F1A1-brg $\left[\mathrm{Mg_{0.83}Fe_{0.17}Si_{0.91}Al_{0.09}O_3}\right]$					
	1!	0.00	–	–	29.201
	2	21.3 – 33.2	He	ruby	29.201
	3*	4.77 – 36.77	He	Au	29.201
	4*	69.89 – 89.07	He	Au	29.201
F3A3-brg $\left[\mathrm{Mg_{0.68}, Fe_{0.32}Si_{0.70}, Al_{0.30}O_3}\right]$					
	1	0.00	–	–	29.201
	2!	6.5 – 96.0	He	Au	29.201
	3	3.74 – 35.38	He	Au	39.995
	4*	2.1 – 63.5	Ne	Au	29.201
	5*	5.8 – 60.7	Ar	Ar	29.201

to be $a = 4.7848(20)$ Å, $b = 4.9462(23)$ Å, and $c = 6.9250(34)$ Å. Rietveld refinement is also done using *Match!* , and the refined ambient-pressure lattice parameters were determined to be $a = 4.7826(5)$ Å, $b = 4.9480(4)$ Å, and $c = 6.9233(8)$ Å(see Table B.6).

Although the synthesis target is bridgmanite for F1A1-brg (Section 3.2.1), several peaks with d-spacings of 3.5114, 2.6081, 2.3742, 1.7557, 1.4116, and 1.3707 Å were detected that could not be indexed to the bridgmanite phase. For reflections attributed to akimotoite (ilmenite), the fitting procedures used published EOS values strictly as starting parameters rather than constraints.

PeakPo fitting for akimotoite is done using the lattice parameters and EOS from Wang *et al.* (2004) as the initial starting values for refinement, yielding lattice parameters for akimotoite of $a = 4.7438(52)$ Å and $c = 13.513(28)$ Å . Similarly, *Match!* refinement is done using the

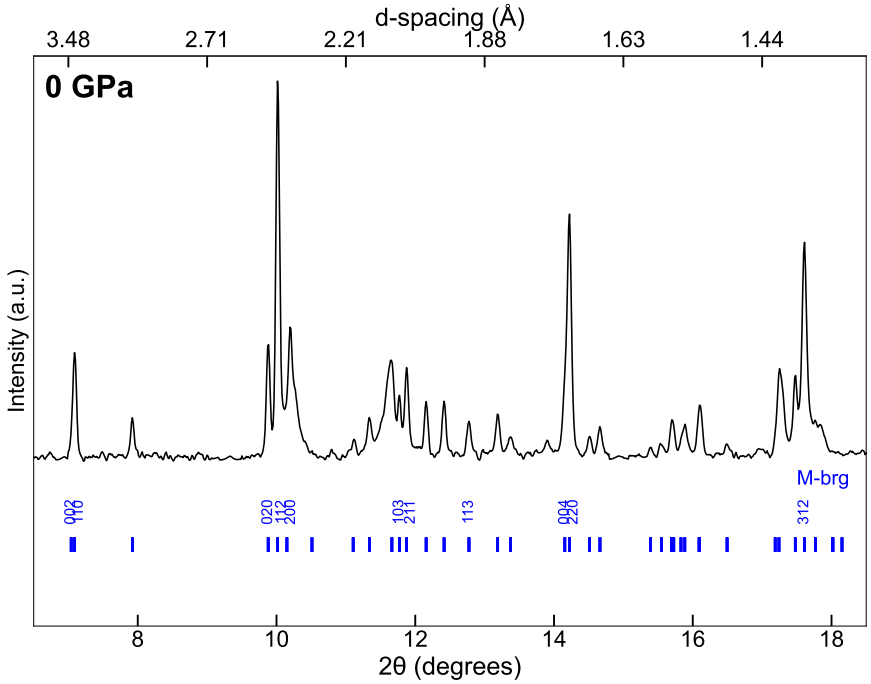

Figure 3.1: X-ray diffraction (XRD) pattern of M-brg at 0 GPa (Run 1 for M-brg in Table B.6). The pattern shows the measured intensity as a function of 2θ (degrees), with corresponding d-spacings (Å) labeled along the top axis. Tick marks and Miller indices indicate the Bragg peak positions for orthorhombic bridgmanite. Prominent reflections with over 10% intensity (arbitrary unit), are labeled. The pattern is collected at ambient pressure to verify phase purity and indexing prior to compression experiments. The unit-cell parameters are listed in Table B.6.

lattice parameters and EOS from Horiuchi *et al.* (1982) as the initial starting values for refinement, resulting in lattice parameters for akimotoite of $a = 4.7451$ Å and $c = 13.521$ Å . Both fits converge to consistent results independent of the starting values.

For F3A3-brg, the refined ambient-pressure lattice parameters using PeakPo are determined to be $a = 4.8076(32)$ Å, $b = 4.9954(35)$ Å, and $c = 6.9845(43)$ Å(see Table B.6). Rietveld refinement is also done using *Match!* (Putz and Brandenburg, 2025), and the refined ambient-pressure lattice parameters are determined to be $a = 4.8054(7)$ Å, $b = 4.9934(6)$ Å, and $c = 6.9764(8)$ Å.

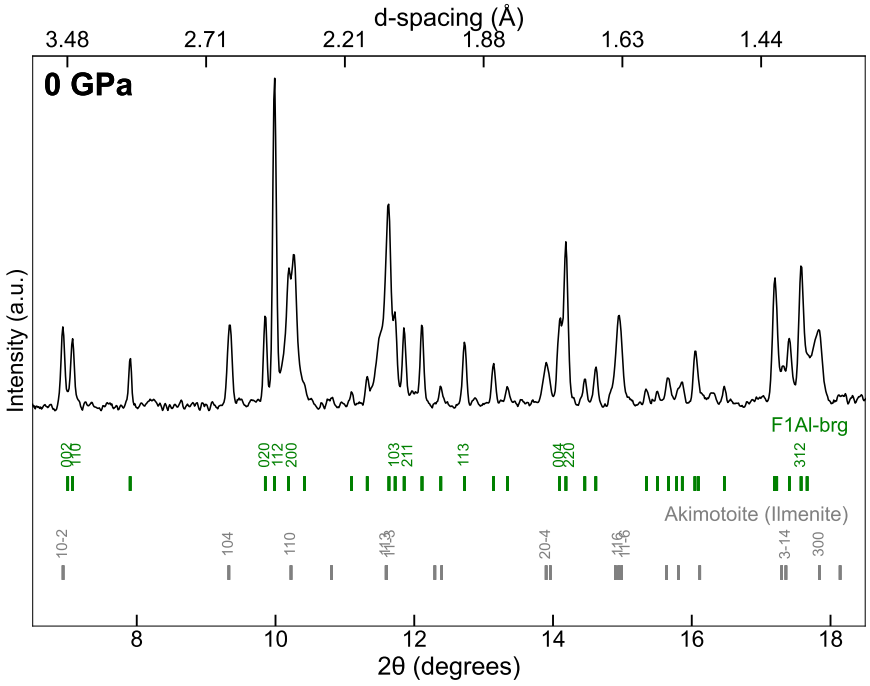

Figure 3.2: X-ray diffraction (XRD) pattern of F1A1-brg at 0 GPa (Run 1 for F1A1-brg in Table B.6). The pattern shows the measured intensity as a function of 2θ (degrees), with corresponding d-spacings (Å) labeled along the top axis. Tick marks and Miller indices indicate the Bragg peak positions for orthorhombic bridgmanite. Prominent reflections with over 10% intensity (arbitrary unit) are labeled. The pattern is collected at ambient pressure to determine V_0. Akimotoite (ilmenite) (gray) is also detected at 0 GPa.

In this XRD pattern, all but three peaks could be indexed to the orthorhombic bridgmanite phase. These peaks at d-spacing of 2.5547, 1.740258, and 1.407949 Å (2-θ = 9.5338, 14.0143, and 17.3450) are assigned to Al_2O_3 corundum; this phase is identified as minor due to the spotty diffraction rings. The refined ambient-pressure lattice parameters using PeakPo are determined to be $a = 4.7693(101)$ Åand $c = 12.9901(619)$ Å.

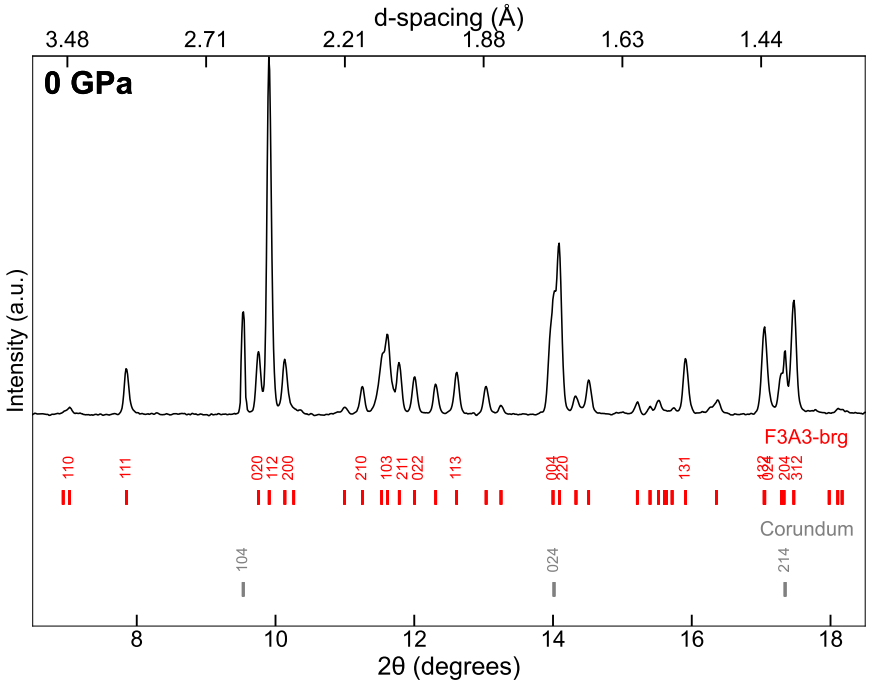

Figure 3.3: X-ray diffraction (XRD) pattern of F3A3-brg at 0 GPa (Run 1 for F3A3-brg in Table B.6). The pattern shows the measured intensity as a function of 2θ (degrees), with corresponding d-spacings (Å) labeled along the top axis. Tick marks and Miller indices indicate the Bragg peak positions for orthorhombic bridgmanite. Prominent reflections with over 10% intensity (arbitrary unit) used for fitting, are labeled. The pattern is collected at ambient pressure to verify phase purity and indexing prior to compression experiments. The unit-cell parameters are listed in Table B.6. Corundum (Al_2O_3) has been assigned to the peaks at d-spacing = 2.5547, 1.740258, and 1.407949 Å (2-θ = 9.5338, 14.0143, and 17.3450).

3.3.2 Pressure-Dependent Lattice Parameters

Lattice parameters a, b, and c were refined from the XRD patterns over the experimental pressure range for all compositions (Table B.6).

Figures 3.4, 3.5, and 3.6 show the pressure dependence of the lattice parameters for M-brg, F1A1-brg, and F3A3-brg, respectively. These figures illustrate how each axis compresses non-linearly with increasing pressure, reflecting the material's bulk modulus (K_0) and its pressure derivative (K_0') from BM3-EOS. Although all three axes decrease in a generally similar fash-

ion, subtle differences can appear at higher pressures. The finite strain curves capture the main compression trend for bridgmanite at lower mantle pressures.

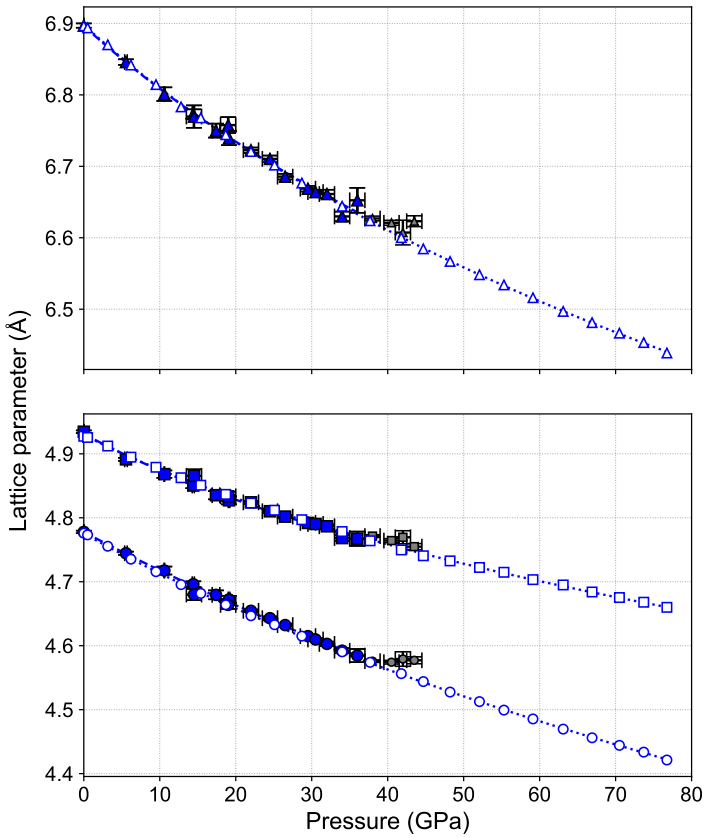

Figure 3.4: Lattice parameters a (circles), b (squares), and c (triangles) for M-brg (blue and gray) with the blue data points being the fitted data and gray being non-fitted data which is discussed in Section 3.4. $MgSiO_3$ from Ballaran *et al.* (2012) (white) as a function of pressure, measured from X-ray diffraction. Finite strain (Birch-Murnaghan) fits are shown for each dataset.

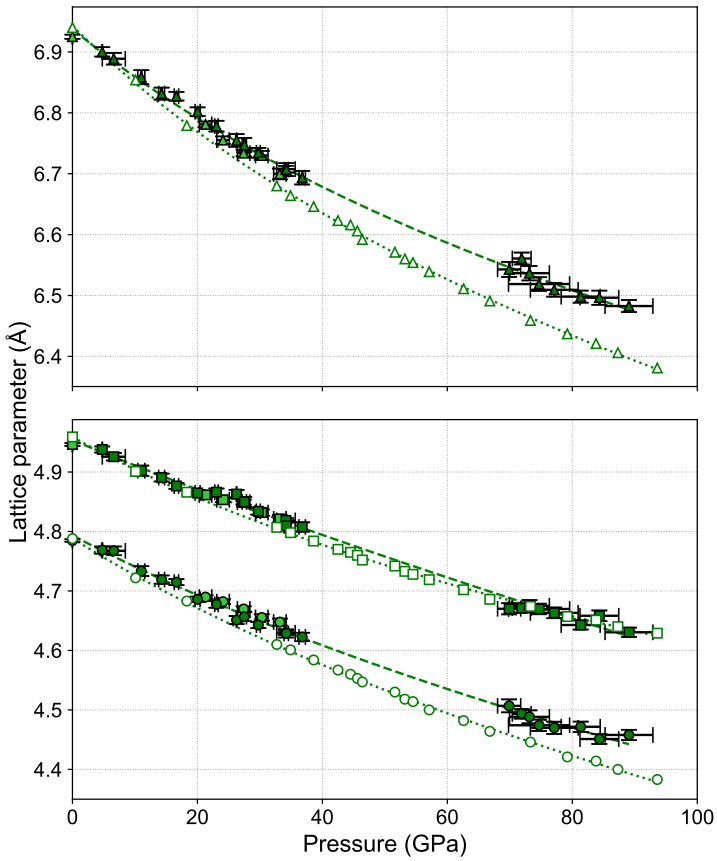

Figure 3.5: Lattice parameters a, b, and c of F1A1-brg as a function of pressure, measured from X-ray diffraction. Data points correspond to individual experimental measurements with associated uncertainties. Dark green indicates data collected from experiments using metallic glass gasket insert and light green indicated data from experiments without metallic glass gasket insert. $Mg_{0.88}Fe_{0.13}Si_{0.88}Al_{0.11}O_3$ from Catalli *et al.* (2011) (white) as a function of pressure, measured from X-ray diffraction. Finite strain (Birch-Murnaghan) fits are shown for each dataset.

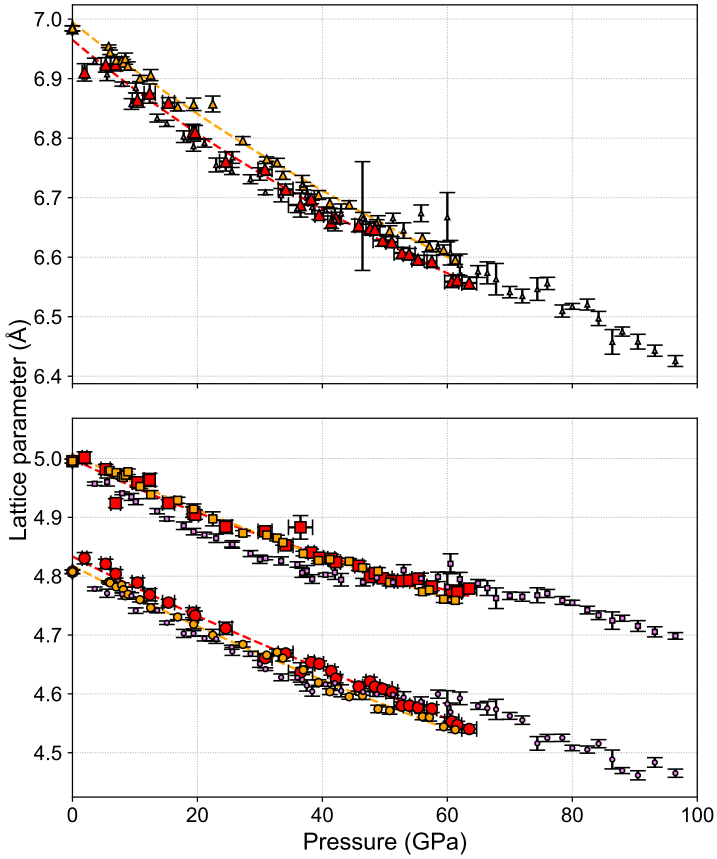

Figure 3.6: Lattice parameters a (circles), b (squares), and c (triangles) of F3A3-brg as a function of pressure, measured from X-ray diffraction. All three pressure media are shown: Ne (red), Ar (orange), and He (pink). Data points correspond to individual experimental measurements with associated uncertainties. Curves represent finite strain (Birch-Murnaghan) fits to each axis in Ne and Ar.

3.3.3 Pressure-Volume Trends and Equation of State (EOS) Parameters

Pressure-volume (P–V) data for M-brg, F1A1-brg and F3A3-brg are plotted in Figures 3.7, 3.8, and 3.9, respectively. These plots show the characteristic nonlinear decrease in unit-cell volume with pressure. The full P–V information is listed in Table B.6.

Equation of state (EOS) fits capture the curvature of these P–V trends. Tables 3.4, 3.5, and 3.10 list the fitted EOS parameters using third-order Birch-Murnaghan (BM3), second-order Birch-Murnaghan (BM2), and Vinet. However, data above 36 GPa for M-brg is excluded from EOS fits due to unexpected P–V behavior which is also seen in the F3A3-brg in He dataset.

Table 3.4: Fitted EOS parameters for M-brg and $MgSiO_3$ bridgmanite from Ballaran *et al.* (2012). For M-brg the V_0 refined from XRD collected at ambient conditions is 162.53(31) $Å^3$, and the reported V_0 from Ballaran *et al.* (2012) is 162.30(8) $Å^3$.

Composition	**EOS**	V_0 ($Å^3$)	K_0 (GPa)	K_0'	**Study**
M-brg	BM3	162.30(40)	254(20)	4.49(99)	This Study
	BM2	162.11(16)	263(4)	4.00(fixed)	–
	Vinet	162.29(40)	252(20)	6.01(101)	–
$MgSiO_3$	BM3	162.36(5)	251(1)	4.12(10)	Ballaran *et al.* (2012)

Table 3.5: Fitted EOS parameters for F1A1-brg. The V_0 is measured directly from XRD collected at ambient conditions for F1A1-brg is 163.89(13) $Å^3$. Reported V_0 from (Catalli *et al.*, 2011) is 164.81(4) $Å^3$. however, EOS reported below has also been fitted using the same python script as data in this study.

Composition	**EOS**	V_0 ($Å^3$)	K_0 (GPa)	K_0'	**Study**
F1A1-brg	BM3	164.84(37)	304(14)	3.05(30)	This Study
	BM2	165.85(25)	263(3)	4.00(fixed)	-
	Vinet	165.31(49)	288(17)	4.77(50)	-
$Mg_{0.88}Fe_{0.13}Si_{0.88}Al_{0.11}O_3$	BM3	165.04(39)	243(8)	3.72(20)	Catalli *et al.* (2011)

Across all three sintered bridgmanite compositions, the unit-cell volume decreases nonlinearly with pressure, as expected for mantle silicates. Substitution of Fe and Al systematically increases the zero-pressure volume V_0 and softens the bulk modulus K_0, reflecting the larger ionic radii and

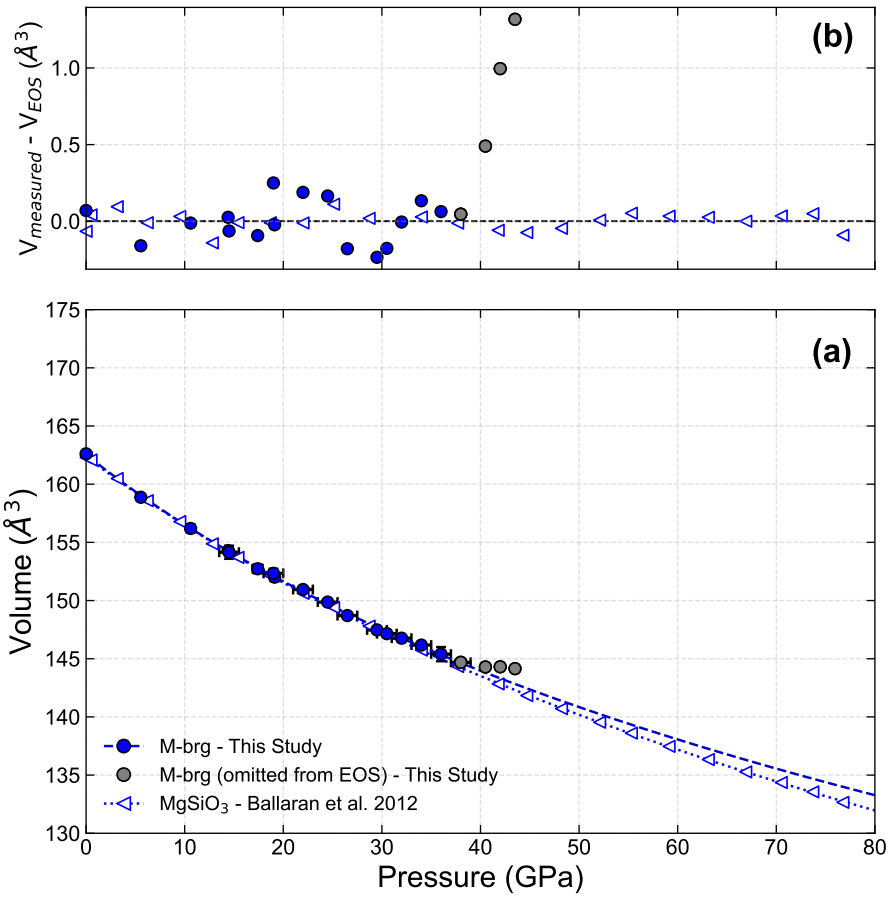

Figure 3.7: (a) Pressure-volume data for M-brg (blue circles) (Table B.6) is fit with BM3-EOS (blue dashed curve) and single-crystal $MgSiO_3$ data from Ballaran *et al.* (2012) (triangles) is fit with BM3-EOS (blue dotted curve). The BM3-EOS fit for M-brg excludes the last four data points (gray circles) due to anomalous incompressibility (see Section 3.4). EOS parameters for fits BM3, BM2, and Vinet are listed in Table 3.4. **(b)** Plotted difference between volume measured from XRD analysis and volume from BM3-EOS fit for both M-brg (blue and gray circles) and single-crystal $MgSiO_3$ data from Ballaran *et al.* (2012) (triangles).

altered bonding environments.

The quality of each EOS fit (BM3, BM2, and Vinet) is assessed by reduced chi-squared statistic, χ^2_ν, where n is the number of data points, p is the number of fitted parameters, and σ_i is

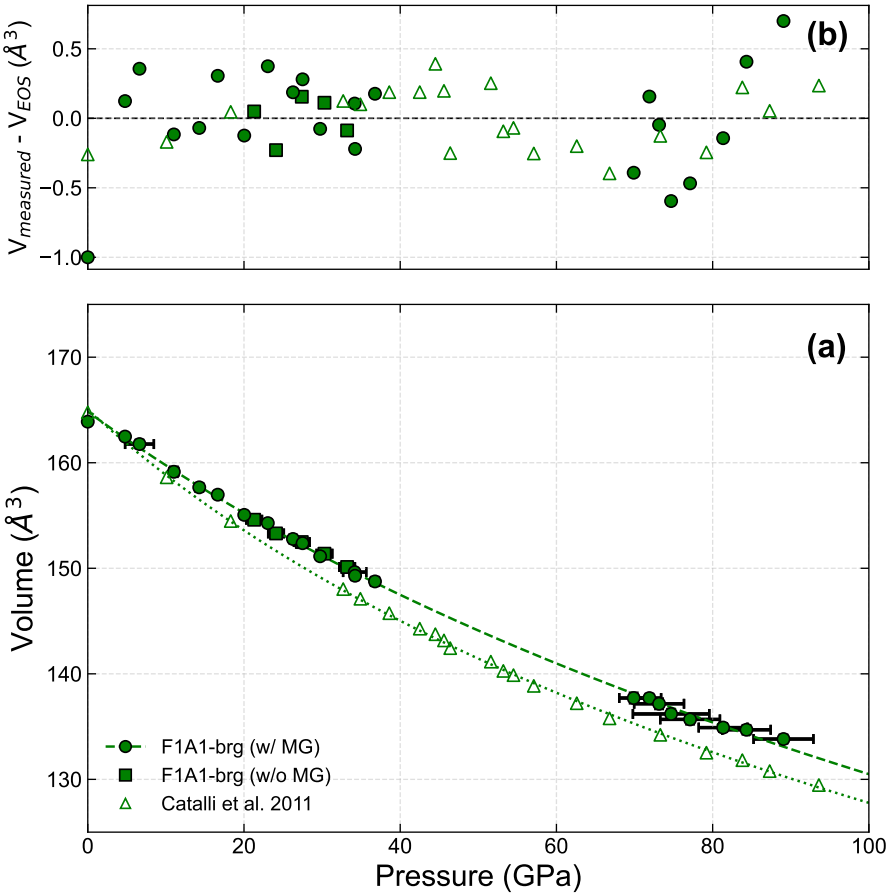

Figure 3.8: (a) P–V data for F1A1-brg using the metallic glass gasket insert (w/ MG, green circles) and without the metallic glass gasket insert (w/o MG, green squares) (Table B.6). Both were fitted together with BM3-EOS (dashed green curve) and Fe-Al-bridgmanite ($Fe_{0.13}$, $Al_{0.11}$) from Catalli *et al.* (2011) is plotted (green triangles) with BM3-EOS (green dotted curve). Parameters for BM3-EOS, BM2-EOS, and Vinet are listed in Table 3.5. (b) Plotted difference between volume measured from XRD analysis and volume from BM3-EOS fit for both F1A1-brg (w/ MG, green circles and w/o MG, green squares) and Fe-Al-bridgmanite ($Fe_{0.13}$, $Al_{0.11}$) data from Catalli *et al.* (2011) (green triangles).

the uncertainty of each observation (Equation 3.1).

$$\chi^2_\nu = \frac{1}{n-p}\sum_{i=1}^{n}\left(\frac{P_i^{\text{obs}} - P_i^{\text{fit}}}{\sigma_i}\right)^2 \tag{3.1}$$

A value of $\chi^2_\nu \approx 1$ indicates that the model is statistically appropriate given the uncertainties, while

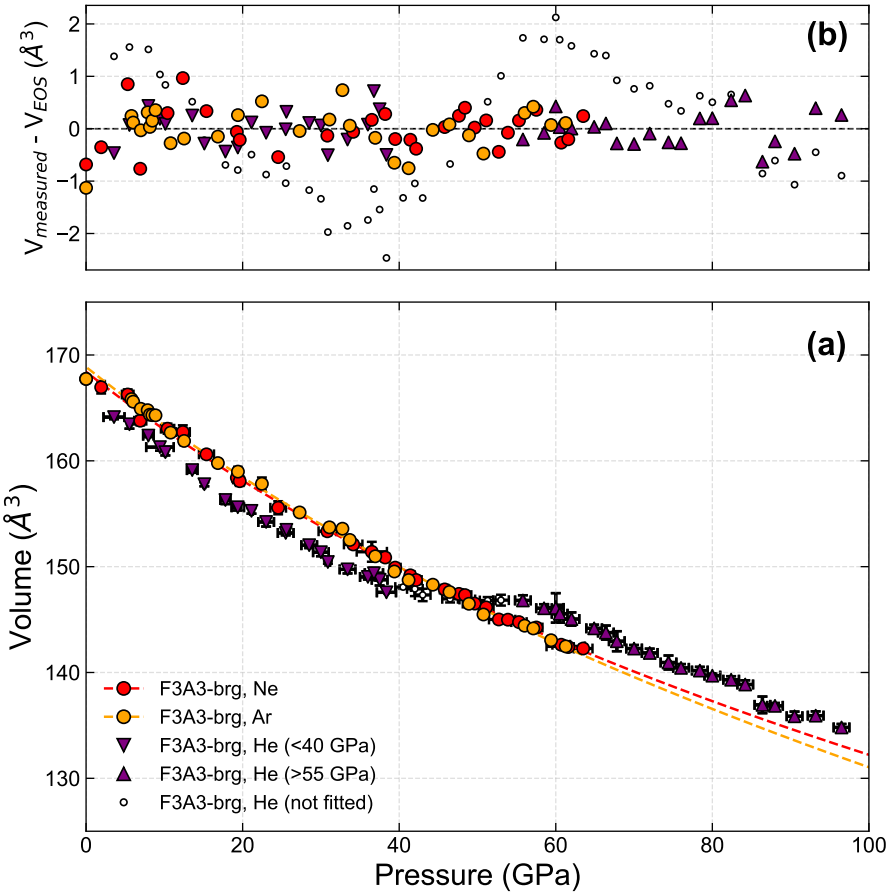

Figure 3.9: (a) Pressure-volume data for F3A3-brg Ar (orange circles), Ne (red circles), and He (white circles (full dataset) and purple triangles (down pointed, <40 GPa; up pointed, >55 GPa) (Table B.6). BM3-EOS is plotted for Ar (orange dashed curves) and Ne (red dashed curves). EOS parameters for BM3-EOS, BM2-EOS, and Vinet are listed in Table 3.10. (b) Plotted difference between volume measured from XRD analysis and volume from BM3-EOS fit for F3A3-brg datasets Ar (orange circles), Ne (red circles), and He (white circles are the full, unfitted He dataset; purple triangles: <40 GPa, down pointed and >55 GPa, up pointed).

significant deviations suggest potential model inadequacies or poor estimation of experimental errors.

For M-brg, BM3-EOS has $\chi^2_\nu = 1.43$ and Vinet has $\chi^2_\nu = 1.45$, in contrast to $\chi^2_\nu = 16.02$ for BM2-EOS (Figure 3.11). The EOS parameters are compared with single-crystal $MgSiO_3$ data from Ballaran *et al.* (2012).

Figure 3.10: Fitted BM3, BM2, and Vinet EOS parameters for F3A3-brg. V_0 measured directly from XRD collected at ambient conditions for F3A3-brg is $163.89(13)$.

P media	**EOS**	V_0 (Å^3)	K_0 (GPa)	K_0'
Ne (*)	BM3	168.42(30)	287(12)	3.13(40)
	BM2	168.91(24)	262(4)	4.00(fixed)
	Vinet	168.42(30)	288(14)	4.47(50)
Ar (*)	BM3	168.87(28)	288(13)	2.72(40)
	BM2	169.58(24)	251(3)	4.00(fixed)
	Vinet	168.82(29)	292(15)	3.85(50)
He $<$ 40 GPa (!)	BM3	167.33(42)	228(19)	5.27(120)
	BM2	166.99(25)	250(5)	4.00(fixed)
	Vinet	167.31(42)	227(19)	6.79(110)
He $>$ 55 GPa (!)	BM3	167.73(49)	386(14)	1.72(30)
	BM2	172.37(144)	247(14)	4.00(fixed)
	Vinet	167.72(47)	404(17)	2.13(30)

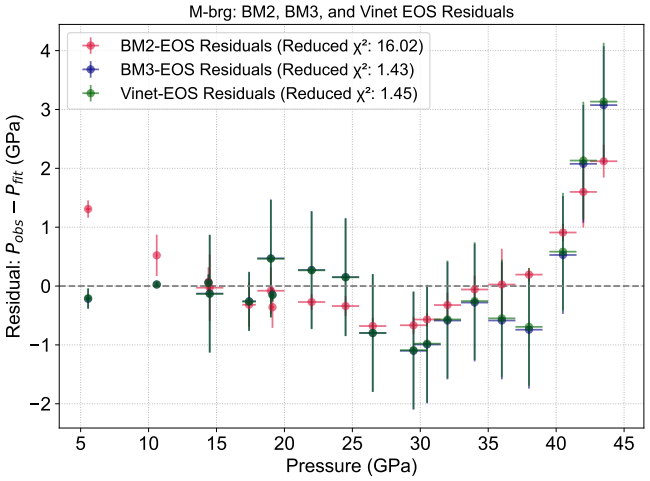

Figure 3.11: Residuals between observed and fitted pressures for BM3-EOS (blue), Vinet (green), and BM2-EOS (red) applied to the M-brg dataset. Residuals are plotted as $P_{\text{obs}} - P_{\text{fit}}$ versus pressure, with error bars corresponding to experimental uncertainties. The BM3-EOS model (blue) exhibits significantly reduced scatter and lower systematic deviation compared to the BM2-EOS model (red). Reduced chi-squared values are indicated in the legend: $\chi^2_\nu = 1.43$ for BM3-EOS, $\chi^2_\nu = 1.45$ for Vinet, and $\chi^2_\nu = 16.02$ for BM2-EOS.

For F1A1-brg, residual analysis (Figure 3.12) shows that BM3-EOS $\chi^2_\nu = 1.15$ and Vinet $\chi^2_\nu = 1.14$ have a significantly better fit compared to BM2-EOS $\chi^2_\nu = 13.29$. The EOS parameters are compared with powder $Mg_{0.88}Fe_{0.13}Si_{0.88}Al_{0.11}O_3$ data from Catalli *et al.* (2011).

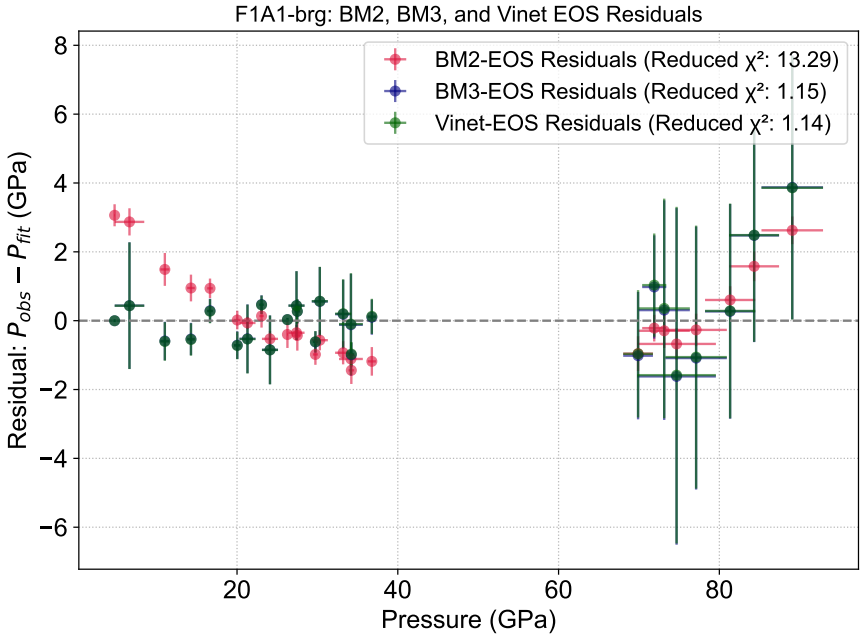

Figure 3.12: Residuals between observed and fitted pressures for BM3-EOS (blue), Vinet (green), and BM2-EOS (red) applied to the F1A1-brg datasets. Residuals are plotted as $P_{\text{obs}} - P_{\text{fit}}$ versus pressure, with error bars representing experimental uncertainties. The BM3-EOS model (blue) and Vinet (green) show significantly reduced scatter and lower systematic deviation compared to the BM2-EOS model (red). Reduced chi-squared values are $\chi^2_\nu = 1.15$ for BM3-EOS, $\chi^2_\nu = 1.14$ for Vinet, and $\chi^2_\nu = 13.29$ for BM2-EOS.

For F3A3-brg, residual analysis for all EOS (Figure 3.13) further shows the differing model fits across media, with notably lower χ^2_ν values for BM3-EOS in most cases, except in Ar due to the small uncertainties.

All refined volumes carry a typical uncertainty as determined from peak-fitting residuals. The BM3-EOS fits yield reduced chi-squared values χ^2_ν between 1.1 and 1.5 for all three compositions, demonstrating that the error estimates are consistent with the observed scatter in P–V data and that

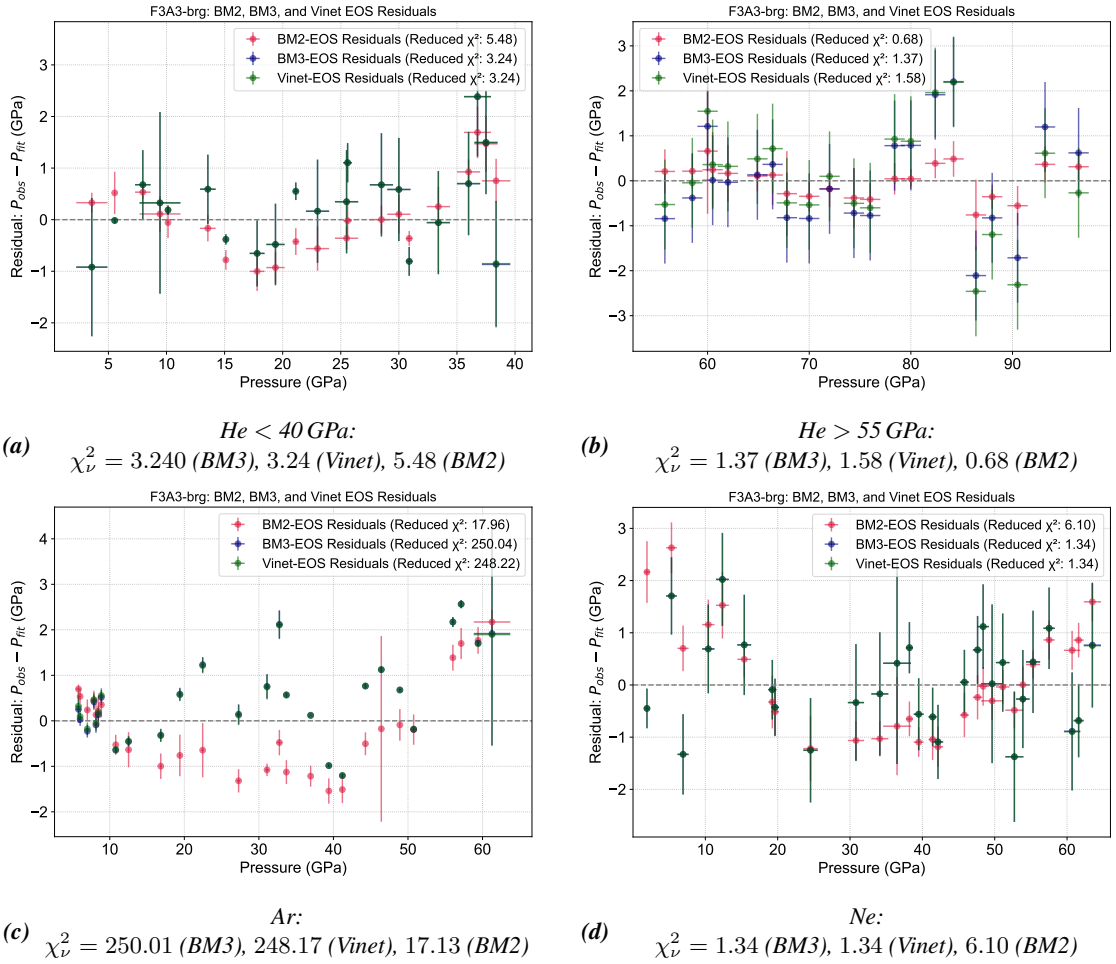

(a) *He < 40 GPa:* $\chi^2_\nu = 3.240$ *(BM3),* 3.24 *(Vinet),* 5.48 *(BM2)*

(b) *He > 55 GPa:* $\chi^2_\nu = 1.37$ *(BM3),* 1.58 *(Vinet),* 0.68 *(BM2)*

(c) *Ar:* $\chi^2_\nu = 250.01$ *(BM3),* 248.17 *(Vinet),* 17.13 *(BM2)*

(d) *Ne:* $\chi^2_\nu = 1.34$ *(BM3),* 1.34 *(Vinet),* 6.10 *(BM2)*

Figure 3.13: Residuals between observed and fitted pressures for BM3-EOS (blue), Vinet (green), and BM2-EOS (red) applied to F3A3-bridgmanite datasets. Residuals are plotted as $P_{\text{obs}} - P_{\text{fit}}$ versus pressure, with error bars showing experimental uncertainties. Each plot compares residuals for a different pressure medium: (a) He < 40 GPa; (b) He > 55 GPa; (c) Ar; (d) Ne. Lower χ^2_ν values indicate better model fits.

the BM3 model is statistically valid given these uncertainties. Although Rietveld refinement is not feasible for high-pressure diffraction analysis due to limited diffraction quality, the consistency of $\chi^2_\nu \approx 1$ confirms that the BM3 model remains statistically valid under the experimental conditions.

The M-brg BM3-EOS result, $K_0 = 254(20)$ GPa and $K_0' = 4.49(99)$, agrees within uncertainty with earlier DAC study from Ballaran *et al.* (2012) reporting $K_0 = 251(1)$ GPa, $K_0' = 4.12(10)$.

The F1A1-brg and F3A3-brg moduli do not follow the trend of decreasing K_0. With increasing Fe-Al content, the bulk moduli has a non-monotonic trend with $K_0 = 304(14)$ GPa and $K_0' = 3.05(30)$ for F1A1-brg, and $K_0 = 287(12)$ GPa and $K_0' = 3.13(40)$ for F3A3-brg in Ne. This inconsistency highlights that sintered polycrystalline samples, particularly those with Fe/Al substitutions such as F1A1-brg and F3A3-brr studied here, may introduce unexpected stiffening or softening depending on their chemistry.

3.4 Discussion

This study examines the high-pressure behavior at 300 K of three bridgmanite compositions using *in situ* XRD: $MgSiO_3$ (M-brg), $(Mg_{0.83}, Fe_{0.17}Si_{0.91}, Al_{0.09})O_3$ (F1A1-brg), and $(Mg_{0.68}, Fe_{0.32}Si_{0.70}, Al_{0.30})O_3$ (F3A3-brg), to understand how iron and aluminum substitutions affect compressibility. The performance and potential artifacts of different pressure-transmitting media under these experimental conditions are evaluated first. Trends in bulk and shear moduli, as well as derived equations of state, are then examined in light of Fe-Al substitution. A detailed assessment of cation site-occupancy effects on unit-cell volume, density, and lattice parameters follows. The final section synthesizes these insights to understand the Earth's lower mantle. Collectively, these findings work towards accurate EOS determination in bridgmanite and enhance geophysical models of lower-mantle structure and dynamics.

3.4.1 Evaluating Pressure Medium

Anomalous incompressibility is observed in M-brg above 36 GPa and in F3A3-brg between 40 GPa and 55 GPa when He is used as the pressure medium (Figure 3.9). In these regimes, unit-cell volumes deviate up to 5% above BM3-EOS predictions, then for F3A3-brg rebound to

near-expected volumes at 55–89 GPa. In contrast, Ne- and Ar-loaded F3A3-brg runs, which solidify at 4.8 GPa and 10 GPa respectively, follow smooth P–V trends to 60 GPa, pinpointing a He-specific effect (Finger *et al.*, 1981; Klotz *et al.*, 2009).

Sintered polycrystalline bridgmanite preserves an interconnected network of defect-rich grain boundaries that can serve as fast diffusion pathways for small atoms (Farver *et al.*, 1994; Farver and Yund, 2000; Milke *et al.*, 2001, 2007; Hayden and Watson, 2008; Dohmen and Milke, 2010; Demouchy, 2010; Marquardt *et al.*, 2011a,b; Gardés *et al.*, 2012; Marquardt and Faul, 2018). Helium, with its small atomic radius and high mobility, can infiltrate these channels under pressure, reducing the apparent compressibility. In contrast, powders even though porous can collapse under load, limiting He access. At lower-mantle conditions, fine-grained bridgmanite ($<1\mu$m) retains an interconnected network of defect-rich grain boundaries. In Fe-Al-bearing bridgmanite, iron increases boundary disorder and widens diffusion pathways (Marquardt and Faul, 2018). Helium diffusing along these pathways may go undetected in XRD, potentially explaining the scarcity of similar reports in the literature.

In Ne- and Ar-loaded F3A3-brg runs, BM3-EOS parameters are $K_0 = 287(12)$,GPa, $K_0' = 3.13(40)$ (Ne) and $K_0 = 288(13)$,GPa, $K_0' = 2.72(40)$ (Ar), both with $\chi^2_\nu \approx 1.3$. No anomalous stiffening occurs, confirming expected lattice response when permeation is inhibited.

An F1A1-brg experiment in He to 89 GPa using a metallic-glass gasket insert (Dong *et al.*, 2022) did not exhibit the anomalous incompressibility. Although it remains unclear if the gasket insert prevented He infiltration, Dong *et al.* (2022) tested similar inserts against permeable gases (H_2, Ne) and recommended further evaluation for He. Similar approaches in hydrogen-loaded DACs apply Au coatings to block gas ingress, highlighting gasket design's critical role when using permeable media (Takemura, 2007).

Helium remains favored among DAC users for its quasi-hydrostaticity and solidifying above 12.1 GPa, but theory suggests it is ideal only below 15 GPa, with Ne preferable at higher pressures (Liang *et al.*, 2024). Moreover, solid He at low temperature develops high shear strength and may deform anisotropically during pressurization, causing non-reproducible lattice parameters, loss of hydrostaticity akin to other solidified media, and deformation artifacts that obscure true compressibility (Takemura, 2001, 2007). Indeed, uniaxial stress in Au within He is observed above 30 GPa, compromising EOS accuracy. While ruby-fluorescence line-widths and splitting have been employed to diagnose non-hydrostaticity (Takemura, 2007), ruby peaks can remain deceptively sharp under stress, limiting their reliability (Chai and Michael Brown, 1996).

Noble-gas solubility models and DFT computations indicate that He can occupy vacancies in perovskite-structure minerals, substantially increasing bulk modulus and suppressing octahedral rotations (Shcheka and Keppler, 2012; Racioppi *et al.*, 2023). DFT simulations of He in A-sites of AlF_3 perovskite (to 10 GPa) predict an increase in K_0 from 50 to 160 GPa, analogous to the anomaly (Racioppi *et al.*, 2023). Historical XRD studies on forsterite under He also report persistent peak broadening upon decompression, attributed to He retention in the lattice (Downs *et al.*, 1996).

As detailed in Section 3.3, BM3-EOS fits to F3A3-brg data below and above 55 GPa yield $K_0 = 245(25)$ GPa and $402(90)$ GPa, respectively (Table 3.7), showing a striking shift in compressibility. This suggests He may enter into bridgmanite between 40–55 GPa, consistent with intercalation models (Racioppi *et al.*, 2023) and solubility predictions (Shcheka and Keppler, 2012).

Several studies propose that bridgmanite-rich regions may sequester mantle He, influencing deep-Earth geodynamics (Ballmer *et al.*, 2017; Bouhifd *et al.*, 2013; Jephcoat, 1998; Porcelli and Halliday, 2001). If confirmed, He incorporation would significantly impact bridgmanite's elastic and transport properties.

While the presented data align with DFT and solubility-model predictions, direct confirmation of He in Fe-Al-bearing bridgmanite requires complementary *in situ* spectroscopy, high-resolution microscopy, and advanced modeling. Future efforts should prioritize these techniques to ascertain He's structural and elastic effects under extreme $P - T$ conditions.

To avoid overestimating K_0 or misinterpreting K_0' in Earth-relevant materials, the use of Ne or Ar for high-pressure XRD is recommended. When He is unavoidable, employ diffusion barriers and multiple hydrostaticity diagnostics to mitigate medium-induced artifacts.

3.4.2 Fe-Al Substitution, Elastic Trends, and EOS

The P–V data reveal two principal compositional effects. First, the zero-pressure volume V_0 increases monotonically with Fe-Al content, from 162.30(40) Å^3 in M-brg to 164.84(37) Å^3 in F1A1-brg and 168.42(30) Å^3 in F3A3-brg. This trend reflects the substitution of larger Fe^{2+} (0.78 Å) and Al^{3+} (0.535 Å) for smaller Mg^{2+} (0.72 Å) and Si^{4+} (0.40 Å) in the perovskite lattice (Yagi *et al.*, 1978; Catalli *et al.*, 2011).

Second, the isothermal bulk modulus K_0 exhibits a non-monotonic dependence on Fe-Al (Table 3.6). For the results, small Fe/Al addition stiffened the lattice, raising K_0 from 254(20) GPa (M-brg) to 304(14) GPa (F1A1-brg). Further substitution for F3A3-brg softens the structure with K_0=287(12) GPa (F3A3-brg, Ne). The initial stiffening may arise from improved grain-boundary cohesion, subtle cation ordering, or a higher Fe^{2+}/Fe^{3+} ratio that increases local rigidity. At higher Fe-Al, the average M–O bond length grows, causing the observed softening.

At the same time, the pressure derivative K_0' declines from 4.49(99) in M-brg to 3.05(30) in F1A1-brg and 3.13(40) in F3A3-brg, indicating progressively flatter P–V curvature with increasing Fe-Al. This behavior aligns with *ab initio* and molecular dynamics results (Tsuchiya and Tsuchiya,

Table 3.6: Fitted BM3, BM2, and Vinet equation of state (EOS) parameters for M-brg, F1A1-brg, and F3A3-brg compositions. V_0 is the fitted zero-pressure volume from EOS. χ^2_ν is the reduced chi-squared. Asterisks (*) indicate experiments with the metallic glass gasket insert.

Composition	**EOS**	V_0 (Å^3)	K_0 (GPa)	K_0'	χ^2_ν
M-brg	BM3	162.30(40)	254(20)	4.49(99)	1.43
	BM2	162.11(16)	263(4)	4.00(fixed)	16.02
	Vinet	162.29(40)	252(20)	6.01(101)	1.45
F1A1-brg	BM3	164.84(37)	304(14)	3.05(30)	1.15
	BM2	165.85(25)	263(3)	4.00(fixed)	13.29
	Vinet	165.31(49)	288(17)	4.77(50)	1.14
F3A3-brg, Ne (*)	BM3	168.42(30)	287(12)	3.13(40)	1.34
	BM2	168.91(24)	262(4)	4.00(fixed)	6.10
	Vinet	168.42(30)	288(14)	4.47(50)	1.34
F3A3-brg, Ar (*)	BM3	168.87(28)	288(13)	2.72(40)	250.04
	BM2	169.58(24)	251(3)	4.00(fixed)	17.96
	Vinet	168.82(29)	292(15)	3.85(50)	248.22
F3A3-brg, He $<$ 40 GPa	BM3	167.33(42)	228(19)	5.27(120)	3.24
	BM2	166.99(25)	250(5)	4.00(fixed)	5.48
	Vinet	167.31(42)	227(19)	6.79(110)	3.24
F3A3-brg, He $>$ 55 GPa	BM3	167.73(49)	386(14)	1.72(30)	1.37
	BM2	172.37(144)	247(14)	4.00(fixed)	0.68
	Vinet	167.72(47)	404(17)	2.13(30)	1.58

2006; Shukla *et al.*, 2015; Zhang *et al.*, 2016).

Figure 3.14 displays confidence ellipses (68%, 95%, 99%) in K_0-K_0' space for BM3 (blue), BM2 (red), and Vinet (green). The BM2 fit (fixed $K_0' = 4$) forms a narrow vertical band that neither overlaps the BM3 solution nor the literature spread, highlighting its over-constraint. Vinet yields higher K_0' with larger uncertainties, while BM3 strikes the best balance ($\chi^2_\nu \approx 1.1$-1.5), capturing both compositional trends and the non-monotonic K_0 variation.

Comparisons with prior studies (Table 3.7) show that the BM3 parameters for M-brg ($V_0 = 162.30\,\text{Å}^3$, $K_0 = 254\,\text{GPa}$, $K_0' = 4.49$) agree well with earlier determinations (Ballaran *et al.*, 2012; Tange *et al.*, 2012; Fiquet *et al.*, 2000). For F1A1-brg, the stiff $K_0 = 304(14)$ GPa contrasts

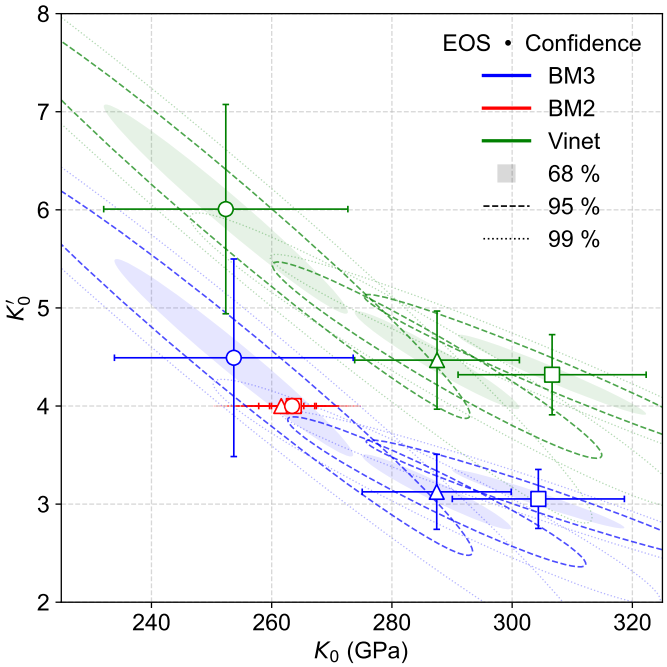

Figure 3.14: Confidence ellipses (68%, 95%, 99%) for K_0 vs. K_0' from BM3 (blue), BM2 (red), and Vinet (green) fits. Symbol shapes: circle=M-brg, square=F1A1-brg, triangle=F3A3-brg.

with the 243(8) GPa of Catalli *et al.* (2011) and 252(7) GPa of Okuda *et al.* (2017), likely reflecting differences in synthesis method, pressure medium, and gasket design. F3A3-brg exhibits medium-dependent K_0; under He, $K_0 = 228(19)$ GPa below 40 GPa and stiffens to $K_0 = 386(14)$ GPa above 55 GPa, whereas Ne/Ar consistently yield ∼287-288 GPa, anomalies attributable to non-hydrostatic stress or He uptake (Racioppi *et al.*, 2023; Downs *et al.*, 1996).

Finally, finite-strain (F vs. f_E) plots (Figure 3.15) confirm consistency. M-brg display linear trends while F1A1-brg displays a negative trend. F3A3-brg in He splits into two regimes with low-pressure softening and high-pressure stiffening, while Ne/Ar each define single linear trends with slopes corresponding to their BM3 moduli.

Figure 3.16 shows the axial Eulerian strain for each lattice parameter. In all compositions the b-axis is stiffest, while the c-axis is most compliant, reflecting the compressional behavior of the

Table 3.7: BM3-EOS parameters for bridgmanite compositions studied in this work and literature (Ballaran *et al.*, 2012; Catalli *et al.*, 2011; Tange *et al.*, 2012; Fiquet *et al.*, 2000; Knittle and Jeanloz, 1987; Okuda *et al.*, 2017).

Composition		V_0 (Å^3)	K_0 (GPa)	K_0'	**Reference**
M-brg (He)		162.30(40)	254(20)	4.49(99)	This Study
$MgSiO_3$		162.36(4)	251(2)	4.11(7)	Ballaran *et al.* (2012)
$MgSiO_3$	<40 GPa	162.36(5)	252(3)	4.1(2)	Ballaran *et al.* (2012)
$MgSiO_3$		162.373	256.7(15)	4.09(6)	Tange *et al.* (2012)
$MgSiO_3$		162.27(1)	253(9)	3.9(2)	Fiquet *et al.* (2000)
$(Mg_{0.96},Fe_{0.04})SiO_3$		163.09(6)	253(2)	3.99(7)	Ballaran *et al.* (2012)
$(Mg_{0.96},Fe_{0.04})SiO_3$	<40 GPa	163.16(6)	245(4)	4.4(3)	Ballaran *et al.* (2012)
$(Mg_{0.88},Fe_{0.12})SiO_3$			266(6)	3.9(4)	Knittle and Jeanloz (1987)
F1A1-brg (He; glass gasket insert)		164.84(37)	304(14)	3.05(30)	This Study
$(Mg_{0.88}Fe_{0.13}Si_{0.88}Al_{0.11})O_3$		165.04(39)	243(8)	3.72(20)	Catalli *et al.* (2011)
$Mg_{0.832}Fe_{0.209}Al_{0.060}Si_{0.916}O_3$		164.68	252(7)	3.78(22)	Okuda *et al.* (2017)
F3A3-brg (He)	<40 GPa	167.33(42)	228(19)	5.27(130)	This Study
F3A3-brg (He)	>55 GPa	167.73(49)	386(14)	1.72(30)	This Study
F3A3-brg (Ne; glass gasket insert)		168.42(30)	287(9)	3.13(40)	This Study
F3A3-brg (Ar; glass gasket insert)		168.87(28)	288(13)	2.72(40)	This Study
$Mg_{0.6},Fe^{2+}_{0.03}Fe^{3+}_{0.38}Si_{0.62}Al_{0.36}O_3$		168.93(5)	240(2)	4.12(8)	Ballaran *et al.* (2012)
$Mg_{0.6},Fe^{2+}_{0.03}Fe^{3+}_{0.38}Si_{0.62}Al_{0.36}O_3$	<40 GPa	168.99(4)	234(2)	4.6(1)	Ballaran *et al.* (2012)

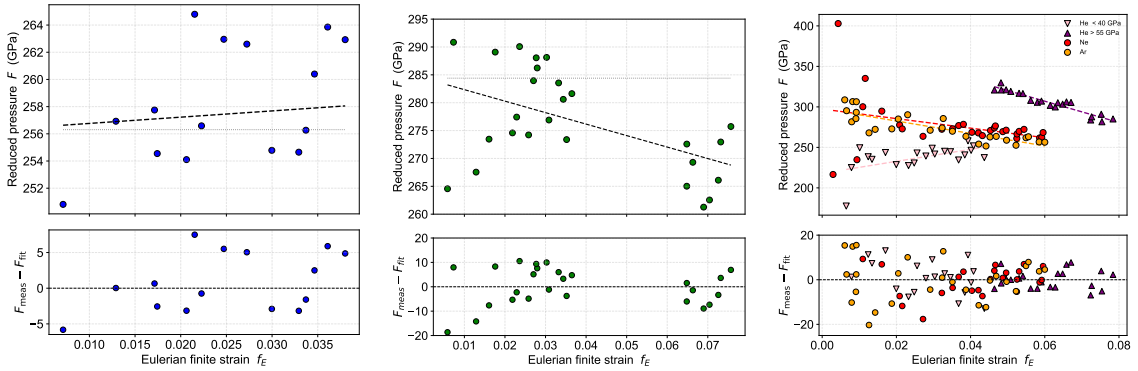

Figure 3.15: Reduced pressure F versus Eulerian strain f_E for M-brg, F1A1-brg, and F3A3-brg.

sintered polycrystalline bridgmanite samples.

In summary, Fe-Al substitution may initially stiffens bridgmanite, however, higher levels of Fe-Al may lengthen M–O bonds and soften it, with K_0' steadily decreasing. BM3-EOS provides the most balanced description across all datasets and compositions.

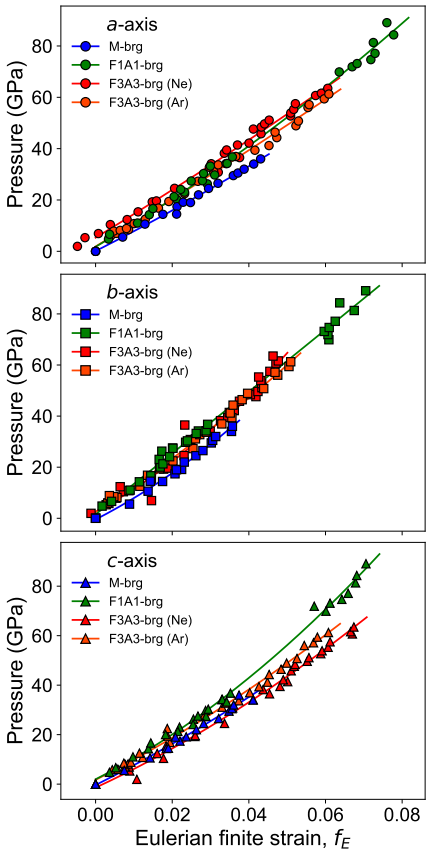

Figure 3.16: Eulerian strain versus pressure for the lattice parameters of M-brg, F1A1-brg, and F3A3-brg.

3.4.3 Effects of Fe-Al Substitution and Site Occupancy on Bridgmanite Density, Elasticity, and Lattice Parameters

The density of bridgmanite increases systematically with Fe and Al content due to the coupled substitution $Fe^{3+}_A + Al^{3+}_B \leftrightarrow Mg^{2+}_A + Si^{4+}_B$, which adds mass and slightly expands the lattice. Despite Al^{3+} being lighter than Si^{4+}, the net effect is an upward trend in density (Figure 3.17) (Huang *et al.*, 2021b; Saikia *et al.*, 2009). The F1A1-brg sample plots above this trend which may be due to the akimotoite biasing its mass–volume balance (Figure 3.2) (Kulka *et al.*, 2020; Zhao *et al.*, 2022). Fe–Al enrichment stabilizes akimotoite by lowering its Gibbs free energy and shifting the Ak–Brg transition to higher pressures (Panero *et al.*, 2006; Huang *et al.*, 2021b).

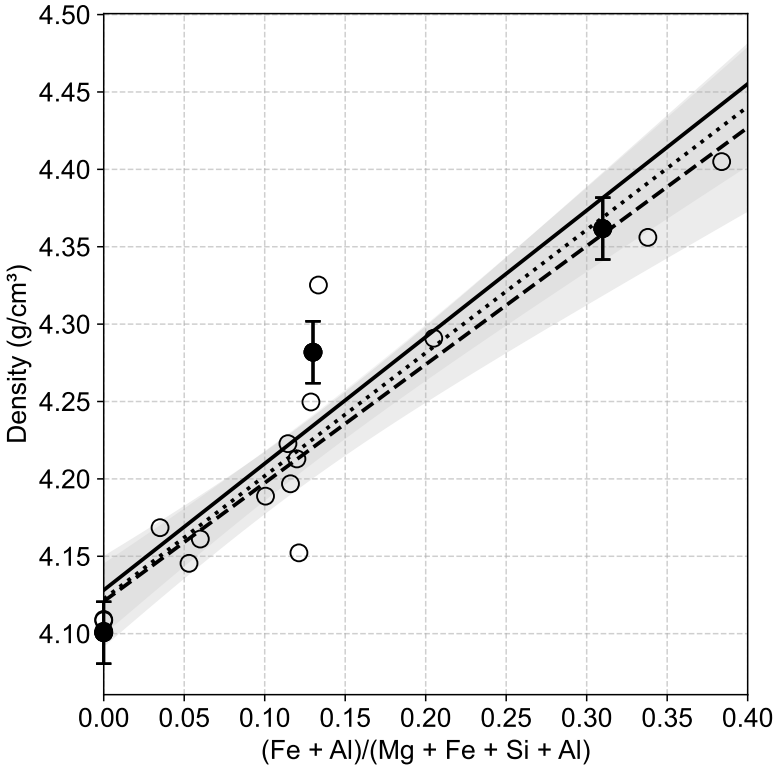

Figure 3.17: Density vs. cation ratio $(\mathrm{Fe} + \mathrm{Al})/(\mathrm{Mg} + \mathrm{Fe} + \mathrm{Si} + \mathrm{Al})$. Solid circles: this study; literature: triangles. Solid, dashed and dotted lines are fits to experimental, literature, and combined datasets, with 95% confidence intervals shaded.

Under a fixed K_0' Birch–Murnaghan EOS (BM2), all compositions collapse onto K_0 ≈262–263 GPa, masking compositional effects. Allowing K_0' to vary reveals that increased (Fe-Al) raises K_0'. BM3 fits give $K_0 = 254(20)$, 304(14), and 287(12) GPa for M-, F1A1-, and F3A3-brg and Vinet fits yield 252(20), 288(17), and 288(12) GPa (Table 3.6, Figure 3.18). At 300 K, the stiffness of bridgmanite arises largely from the Si–O octahedral framework. The incorporation of Fe^{2+} (high-spin d^6), Fe^{3+} (high-spin d^5), or Al^{3+} (d^0) contributes little additional electronic stabilization, because these cations have negligible (or zero) crystal field stabilization energy (CFSE). As a result, the elastic behavior is dominated by the Si–O network rather than by the electronic configurations of Fe or Al (Wehinger *et al.*, 2015; Burns, 1993). Thus cation swaps perturb bond compressibility

and octahedral tilts under pressure, reflected in higher K_0' (Catalli *et al.*, 2011; Ballaran *et al.*, 2012).

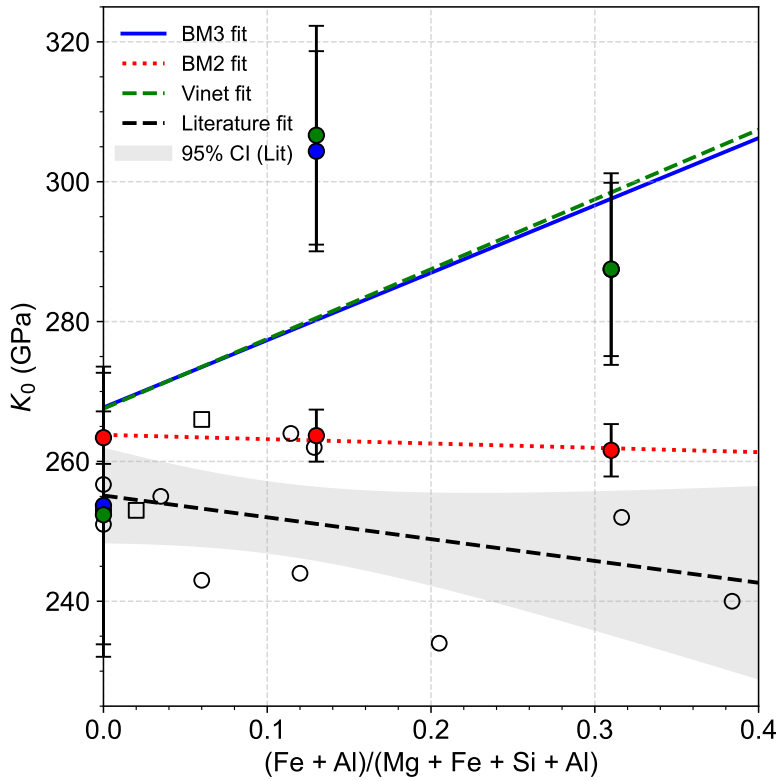

Figure 3.18: Zero-pressure bulk modulus K_0 vs. cation ratio for BM3 (blue), BM2 (red), and Vinet (green) fits to our data, compared to literature (open shapes, black dashed) (squares are Al-free, circles are Fe-Al-bearing) and its 95% confidence interval.

Lattice-parameter trends mirror these findings. "In–plane" axes (a, b) grow modestly with (Fe-Al), while the "out-of-plane" c-axis shows weak, scattered variation (Figure 3.20). Unit-cell volume stays near expectations, indicating any c-axis contraction is offset by a–b expansion (Figure 3.19).

Differences in site occupancy and oxidation state further modulate P–V. Powder XRD studies (Catalli *et al.*, 2011; Hummer and Fei, 2012) suggest Al and Fe^{3+} mix evenly on A and B sites, whereas single-crystal data (Vanpeteghem *et al.*, 2006b) show a stronger Fe^{3+} preference for B-sites. Al incorporation promotes Fe^{3+} over Fe^{2+}, enhancing charge-coupled substitution and altering

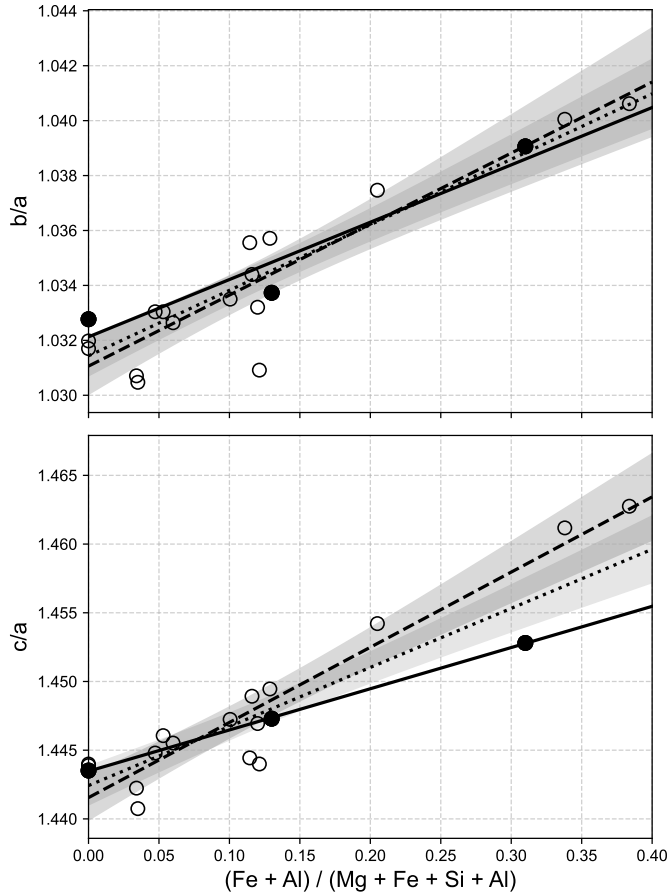

Figure 3.19: Variation in the lattice ratios b/a and c/a as functions of the cation ratio $(\mathrm{Fe} + \mathrm{Al})/(\mathrm{Mg} + \mathrm{Fe} + \mathrm{Si} + \mathrm{Al})$. Left: b/a; right: c/a. Solid, dashed, and dotted lines: experimental, literature, and combined fits; shaded regions: 95% confidence intervals.

average bond lengths. Under high pressure, Fe^{2+} and Fe^{3+} undergo partial high-spin to low-spin transitions, introducing curvature or kinks in P–V curves above 40 GPa (Ballaran *et al.*, 2012). A 4–5 mol% increase in Fe^{2+} produces a more pronounced density effect than equivalent Fe^{3+} enrichment, underlining the influence of oxidation state and site preference (Ballaran *et al.*, 2012). Moreover, bridgmanite in the lower mantle is thought to be richer in Fe^{3+} than Fe^{2+} (Kurnosov *et al.*, 2017). Even F1A1-brg ($Fe_{0.17}$, $Al_{0.09}$) vs. MORB-like ($Fe_{0.13}$, $Al_{0.11}$) comparison can shift V_0, K_0, and spin-transition pressures.

Experimental protocols also introduce offsets. Pressure medium (He vs. Ne/Ar) and calibration

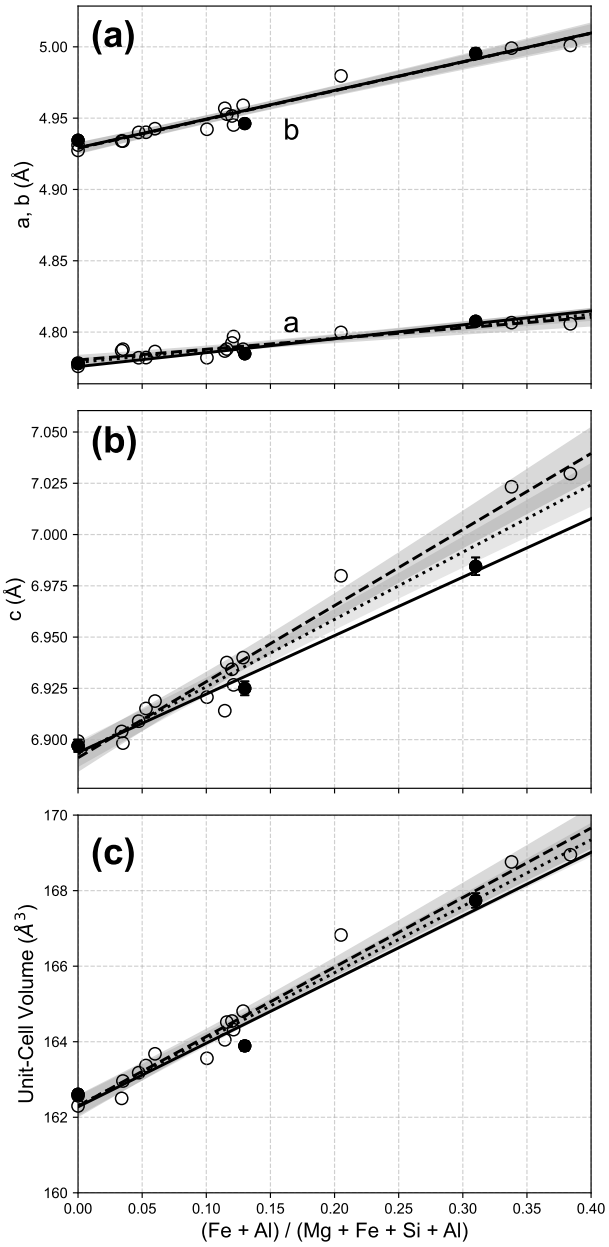

Figure 3.20: Lattice constants and unit-cell volume vs. cation ratio: (a) a, b; (b) c; (c) volume. Line styles and confidence intervals as in Figure 3.19.

standards (ruby, Au) affect measured volumes. Microstructure, including grain size, texture, secondary phases, further modifies stress accommodation. In sintered samples, grain-boundary networks both facilitate He diffusion and introduce lattice strain, effects absent in single-crystal

work (Section 3.4.1) (Sato *et al.*, 2011; Wang *et al.*, 2023; Shen *et al.*, 2011).

Finally, the perovskite structure makes substitutions most impactful along c. Fe or Al at B-sites disrupts octahedral stacking, increasing c-axis flexibility or distortion under pressure (Figure 3.20c) (Tsuchiya and Tsuchiya, 2006; Irifune *et al.*, 2010). This behavior yields the largest deviations in lattice parameters, volume, and stiffness under lower-mantle conditions.

3.4.4 Implications for Earth's Lower Mantle Structure and Dynamics

The presented measurements of zero-pressure volume and bulk modulus for sintered polycrystalline bridgmanite (Table 3.6) reveal systematic compositional effects that have direct implications for how the lower mantle is modeled. First, the density increases by roughly 1.9–6.4% and the isothermal bulk modulus K_0 by up to 20% as Fe and Al content rises from the end member M-brg through F1A1-brg to F3A3-brg. Such compositional stiffening means that Fe-Al-enriched bridgmanite domains could be both denser and less compressible than pure $MgSiO_3$, potentially generating lateral contrasts in seismic-wave speed and density on the order of a few percent (Fu *et al.*, 2023; Shukla *et al.*, 2015; Ballaran *et al.*, 2012; Huang *et al.*, 2021b; Wolf *et al.*, 2015).

Second, because seismic velocities depend on both bulk and shear response, it is important to note that we have not yet measured the shear modulus G. Conversion of both K and ρ into both V_p and V_s therefore requires adopting a representative G or assuming a Poisson's ratio. Future work on the compositional and temperature dependence of G is required to translate the presented bulk modulus contrasts into full seismic-wave predictions.

Third, the anomalous stiffening for F3A3-brg in He-loaded experiments that is absent when using Ne or Ar highlights that grain-boundary pathways in polycrystalline bridgmanite may even allow noble-gas infiltration under lower-mantle pressures (Section 3.4.1). In natural lower-mantle

aggregates, similarly interconnected grain boundaries could transiently host light volatiles, subtly altering compressibility and thus seismic velocities *in situ* (Sans *et al.*, 2015; Criniti *et al.*, 2024).

Finally, all of the data here are at 300 K, whereas the lower-mantle spans 1,800–3,000 K. Thermal softening typically lowers both K and density and may change the magnitude of Fe-Al effects (e.g. Shukla *et al.* (2015)). Extending these measurements to simultaneous high-P, high-T conditions will therefore be essential to fully quantify how Fe-Al composition modulates seismic properties in Earth's deep interior.

Taken together, these results suggest that realistic seismic models of the lower mantle should account not only for temperature and pressure but also for variations in bridgmanite composition (e.g. Fe-Al content), microstructural state (e.g. grain-boundary connectivity), and the full elastic tensor (including G). In particular, regions enriched in Fe and Al such as those invoked for large low-shear-velocity provinces (Wang *et al.*, 2021) may exhibit elevated densities and bulk moduli that help explain their distinct seismic signatures without invoking extreme temperature anomalies alone (Fukui *et al.*, 2016; Wentzcovitch *et al.*, 2023).

3.5 Conclusion

This study utilized three pre-synthesized sintered polycrystalline bridgmanite samples: $\mathrm{MgSiO_3}$ (M-brg) and Fe,Al-bearing variants, $(\mathrm{Mg_{0.83}, Fe_{0.17}})(\mathrm{Si_{0.91}, Al_{0.09}})\mathrm{O_3}$ (F1A1-brg) and $(\mathrm{Mg_{0.68}, Fe_{0.32}})(\mathrm{Si_{0.70}, Al_{0.30}})\mathrm{O_3}$ (F3A3-brg), to study *in situ* high-pressure X-ray diffraction (XRD) using diamond anvil cells (DACs) in order to understand the elastic behavior of Fe-Al-bearing bridgmanite. XRD analysis revealed pressure-induced contraction of the lattice parameters consistent with an orthorhombic perovskite structure. Fitting the pressure-volume data with a third-order Birch-Murnaghan equation of state produced EOS parameters for all three compositions,

with M-brg showing parameters in close agreement with literature values from Ballaran *et al.* (2012). The F1A1-brg sample, with minor secondary phases detected at ambient conditions, exhibited a stiffer compressional behavior (K_0 = 304 GPa) compared to M-brg. The expected trend is that K_0 decreases with increasing Fe content, however, the influence of Al appears to dominate, and helium incorporation at pressures >69 GPa may also contribute to the increased K_0 observed in F1A1-brg.

For the F3A3-brg composition, the pressure medium became a point of interest. Data collected in helium displayed anomalous incompressibility between 40-55 GPa, possibly due to helium diffusing along the extensive grain boundaries of sintered samples. In contrast, experiments using neon and argon produced consistent compressional trends. These latter experiments also incorporated a metallic glass gasket insert (Dong *et al.*, 2022) that likely helped maintain similar pressure conditions. Such discrepancies show the importance of choosing an appropriate pressure medium and gasket configuration when investigating material properties at extreme conditions.

Subtle compositional variations (i.e., Fe and Al content) together with experimental conditions significantly influence the structural and elastic properties of bridgmanite-a dominant lower mantle phase. For example, the increased bulk moduli observed in the Fe-Al-bearing F1A1-brg and F3A3-brg indicate that these minerals are stiffer in compression, thus, denser. However, if this increase in bulk stiffness is not matched by a proportional increase in shear resistance (i.e., the shear modulus does not increase in tandem), the shear wave velocity (V_s) can remain low. This is consistent with the seismic signature of large low-shear velocity provinces (LLSVPs). Such variations in elastic properties, where enhancements in volumetric rigidity are not mirrored by changes in shear rigidity, can significantly affect seismic wave velocities (V_p and V_s) and anisotropy in the deep mantle, thereby influencing seismic imaging and geodynamic models. Additionally, the observed differences in compressional behavior between experiments on F3A3-brg in different

pressure media, hint at potential modifications in grain-boundary diffusion processes that, under lower mantle conditions, may influence both dynamic properties and the redistribution of volatile elements.

Furthermore, the divergent compressional behavior of F3A3-brg in He versus Ne/Ar media shows not a flaw in the methodology in this study but the inherent complexity of real-world experiments. Earlier work showing that non-hydrostatic stresses and pressure-medium choice can measurably influence EOS parameters highlights the influence He may have played in this work (Downs *et al.*, 1996). Far from undermining these findings, this sensitivity highlights the value of experimental studies which capture nuanced, multivariate effects such as grain-boundary diffusion and stress anisotropy, that idealized computational models may not fully reproduce.

Chapter 4

Elastic Properties of Metastable Fe-Al Majoritic Garnet up to 83 GPa at 300 K

4.1 Introduction

Silicate garnets, $X_3Y_2(SiO_4)_3$, represent an important phase in Earth's upper mantle and transition zone (Frost, 2008; Ringwood, 1991). In the ideal garnet structure, an eight-fold dodecahedral X-site is occupied by large divalent cations (Mg^{2+}, Fe^{2+}), while a six-fold octahedral Y-site hosts trivalent ions (Al^{3+}, Fe^{3+}) (Juhin *et al.*, 2010). Under ambient pressures, Si^{4+} resides exclusively in four-fold tetrahedral coordination, but with increasing depth a fraction of Si^{4+} migrates into the Y-site and assumes six-fold coordination (Ito and Takahashi, 1989; Ringwood, 1975; Kiseeva *et al.*, 2018).

Two crystallographic descriptions are used in this study to model garnet and majorite diffraction patterns. The conventional cubic setting, space group *Ia-3d*, contains eight formula units per unit cell and assumes complete equivalence of the three lattice axes ($a = b = c$). When cation ordering or compression breaks that equivalence, refinements usually improve in the tetragonal setting, space group $I4_1/acd$, where the c axis is allowed to differ from a and b ($a = b \neq c$). Small departures of the c/a ratio from unity, typically one to three percent, track the distortion with high sensitivity (Nakatsuka *et al.*, 1999; Cesare *et al.*, 2019). Both symmetries are therefore applied in the discussion that follows because the cubic cell provides a convenient baseline whereas the tetragonal cell captures the anisotropy and subtle high-pressure behavior of Fe-Al-rich majorite.

Majorite garnet, stable throughout much of the transition zone (410-660 km) (Kulka *et al.*, 2020), is widely recognized as the second most abundant mantle phase after bridgmanite (Irifune

and Ringwood, 1993; Irifune *et al.*, 1994; Frost, 2008). Its ability to incorporate substantial Fe and Al, together with pressure-driven changes in Si coordination, directly modulates density, elastic moduli, and seismic wave speeds (Nakatsuka *et al.*, 1999; Irifune, 1987). Consequently, majorite's thermoelastic properties are critical for interpreting mantle heterogeneity, subduction dynamics, and the character of seismic discontinuities near 520 km depth and deeper.

Nevertheless, garnet-majorite metastability along lower-mantle P–T paths remains actively debated. In cold subducting slabs, sluggish kinetics may retard the transformation to denser perovskite, giving rise to deep-focus seismicity and anomalous slab buoyancy (van Mierlo *et al.*, 2013; Yoshioka *et al.*, 1997; Kubo *et al.*, 2002). Such metastable persistence can produce localized velocity anomalies and influence slab stagnation near the base of the transition zone (King *et al.*, 2015; Gasc *et al.*, 2022), emphasizing the need for precise measurements of majorite compressibility and elastic anisotropy at pressures approaching those of the lower mantle.

Initial attempts to synthesize Fe-Al-bearing bridgmanite in a multi-anvil large-volume press (LVP) appeared successful when examined by *ex situ* X-ray diffraction prior to the *in situ* synchrotron experiments presented in this chapter. Methods and materials used for this sample synthesis are discussed in Section 4.2. However, *in situ* synchrotron X-ray diffraction revealed that the sample within the sample chamber of the diamond anvil cell was instead garnet, not bridgmanite (see Chapters 2.1 and 3). Such surprises are not uncommon in high-pressure experiments, where complex phase equilibria and sluggish kinetics can yield mixed or metastable assemblages (Gasparik, 2000; Sinmyo *et al.*, 2019). Recognizing the importance of this unforeseen result, the present chapter focuses on the structural characterization and compressibility of Fe-Al majoritic garnet up to 83 GPa at 300 K.

By fitting pressure-volume data collected in a diamond-anvil cell, we constrain the equation

of state and elastic parameters of Fe-Al majorite beyond its thermodynamic stability field. These results illuminate the potential persistence of garnet phases under lower-mantle conditions and provide essential benchmarks for modeling seismic anisotropy and slab dynamics in cold subduction zones (Bina and Helffrich, 1994; Kirby *et al.*, 1996; Dennis and Walker, 1965).

4.2 Material and Methods

Polycrystalline Fe-Al-bearing bridgmanite was synthesized in a 7/3 multi-anvil assembly using the 1,200-ton Sumitomo press at the Bayreuth Geoinstitute (BGI), Germany. Starting materials are finely ground Fe–Al-bearing Mg-silicate glasses: $(\mathrm{Mg}_{0.83}\mathrm{Fe}_{0.17})(\mathrm{Si}_{0.91}\mathrm{Al}_{0.09})\mathrm{O}_3$ (F1A1-brg-maj), the same composition with an additional 10 wt% Pt (F1A1-Pt-brg-maj), $(\mathrm{Mg}_{0.68}\mathrm{Fe}_{0.32})(\mathrm{Si}_{0.70}\mathrm{Al}_{0.30})\mathrm{O}_3$ (F3A3-brg-maj), the same with 10 wt% Pt (F3A3-Pt-brg-maj), and $(\mathrm{Mg}_{0.60}\mathrm{Fe}_{0.40})(\mathrm{Si}_{0.60}\mathrm{Al}_{0.40})\mathrm{O}_3$ (F4A4-brg-maj), again with 10 wt% Pt (F4A4-Pt-brg-maj) (Figure 4.1). These are prepared following the protocols of Sections 2.1 and 3.2.1, with modifications to capsule loading to accommodate layered samples. A Pt capsule was sequentially loaded with six alternating layers of glass, each separated by 10 μm Pt discs to prevent element diffusion during high-pressure treatment. Three layers contained 10 wt% Pt powder to facilitate laser absorption and *in situ* pressure calibration in later DAC experiments (Fei *et al.*, 2024).

Figure 4.1 presents the six compositions post LVP synthesis. The capsule assembly was compressed to 25 GPa and heated to 1800 K (based on the press calibration curve, as no thermocouple was used), held for 10 minutes, then quenched by rapid power cut. After recovery, the capsule was cut and polished at BGI to expose the six synthesized layers for preliminary phase identification by scanning electron micro-probe with energy dispersive X-ray spectroscopy.

For DAC experiments, the F3A3-brg-maj layer is extracted as 30 μm-diameter, 10 μm-thick

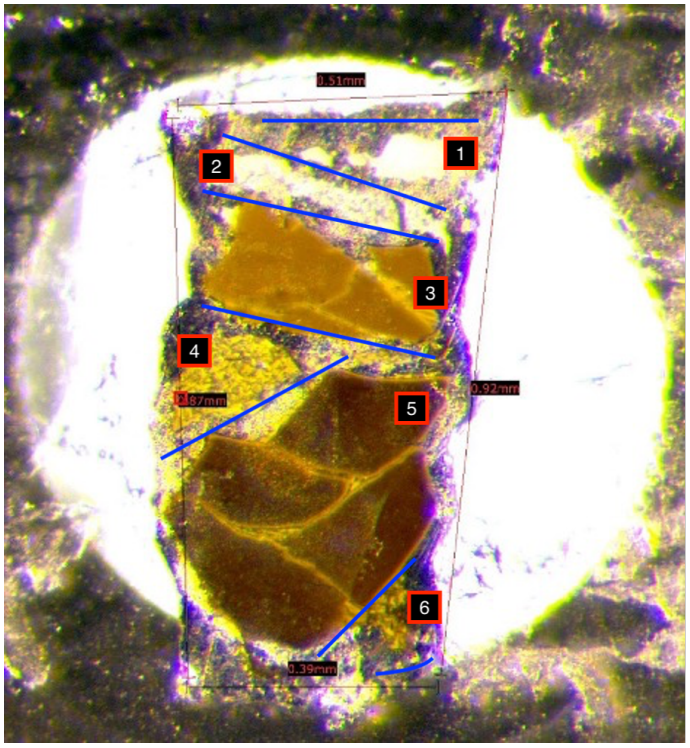

Figure 4.1: Laterally cut and polished Pt capsule (0.9 mm in height and 0.5 mm in width) of synthesized LVP samples. The compositional layers are each separated by Pt disks which are indicated by the blue lines. Compositions are noted as: [1] $Mg_{0.83}, Fe_{0.17}Si_{0.91}, Al_{0.09}O_3$ (F1A1-brg-maj), [2] $Mg_{0.83}, Fe_{0.17}Si_{0.91}, Al_{0.09}O_3$ with 10 wt% Pt (F1A1-Pt-brg-maj), [3] $Mg_{0.68}, Fe_{0.32}Si_{0.70}, Al_{0.30}O_3$ (F3A3-brg-maj), [4] $Mg_{0.68}, Fe_{0.32}Si_{0.70}, Al_{0.30}O_3$ with 10 wt% Pt (F3A3-Pt-brg-maj), [5] $(Mg_{0.60}, Fe_{0.40})(Si_{0.60}, Al_{0.40})O_3$ (F4A4-brg-maj), and [6] $(Mg_{0.60}, Fe_{0.40})(Si_{0.60}, Al_{0.40})O_3$ with 10 wt% Pt (F4A4-Pt-brg-maj).

disks via focused-ion-beam (FIB) at the University of Oxford. Individual disks, Pt pressure-marker grains, and ruby spheres are loaded into a pre-indented Re gasket (thickness $\sim$40 μm) with a 120 μm sample chamber. Argon is loaded as the pressure medium at DESY to ensure quasi-hydrostatic conditions.

In situ X-ray diffraction is conducted at the P02.2 Extreme Conditions beamline, PETRA III (DESY, Hamburg). A monochromatic 42.7 keV (0.2905Å) X-ray beam (3×8 μm^2) is focused on the sample, and diffraction images are recorded on a PerkinElmer detector. Pressure is increased in steps from 19.56(31) to 83.43(39) GPa, measured via the ruby fluorescence scale and Pt EOS

(Holmes *et al.*, 1989). Two-dimensional images are integrated and converted to 1-D patterns using the Dioptas software package (Prescher and Prakapenka, 2015).

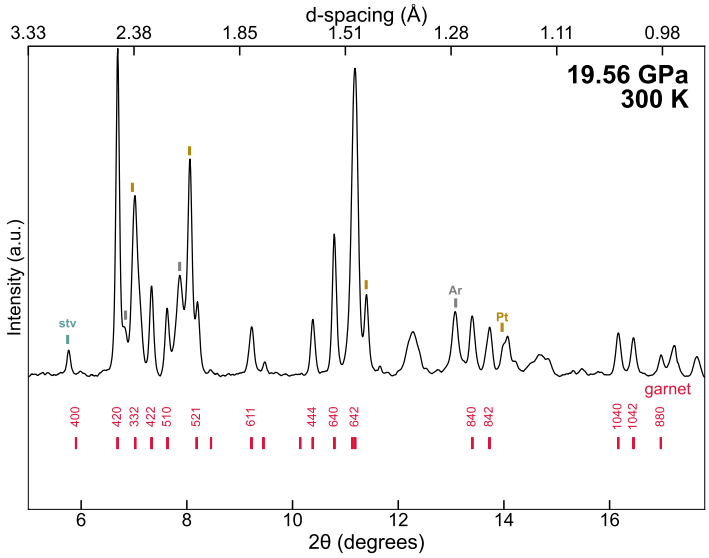

Figure 4.2: X-ray diffraction (XRD) pattern of F3A3-brg-maj at 19.56 GPa. The pattern shows the measured intensity as a function of 2θ (degrees), with corresponding d-spacings (Å) labeled along the top axis. Tick marks and Miller indices indicate the Bragg peak positions for cubic garnet. Prominent reflections with over 10% intensity (arbitrary unit), are labeled. Only one peak at d-spacing = 2.8877 is assigned to stishovite. Phases are fit using PeakPo.

Figure 4.2 shows XRD pattern collected at 19.56(31) GPa. Bragg peaks are indexed to cubic and tetragonal garnet symmetry using PeakPo analysis software (Shim, 2017). Tetragonal distortion consistent with majorite is investigated but remained below refinement limits. Unit-cell parameters are refined at each pressure step, and contributions from Pt and Ar peaks are accounted for using published unit-cell data (Ye *et al.*, 2017; Errandonea *et al.*, 2006). A weak feature at 2.8877 Å is assigned to stishovite, though its singular occurrence precludes definitive phase identification.

Following the *in situ* XRD synchrotron experiment, *ex situ* XRD mapping of the recovered LVP samples is performed at ambient conditions at Diamond Light Source, UK. Mapping confirmed the presence of orthorhombic bridgmanite in regions near where the sample for the *in situ* XRD is

collected. This means that something had to have happened between sample cutting and sample loading for the *in situ* synchrotron XRD. Unindexed reflections marked in Figure 4.3, likely correspond to minor secondary phases.

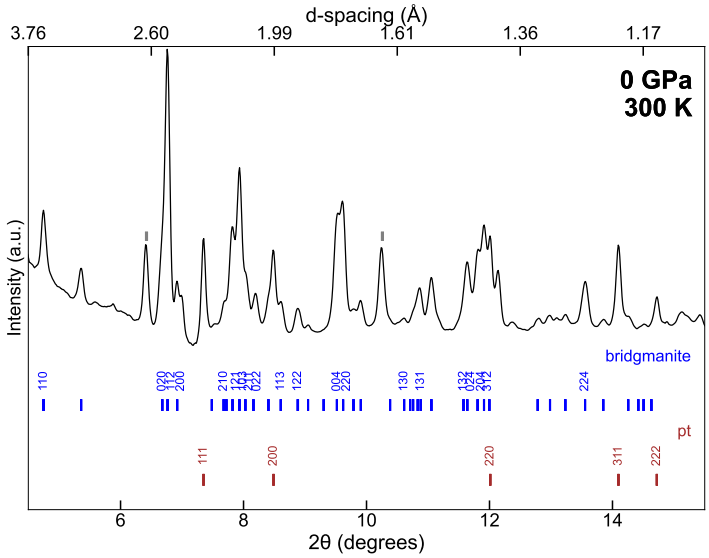

Figure 4.3: Representative X-ray diffraction (XRD) pattern of F3A3-brg-maj at 0 GPa from non-DAC loaded XRD mapping of the LVP capsule. Pt peaks are identified despite Pt not being incorporated into the sample, however, the LVP capsule used was Pt and may have diffused into the sample. The pattern shows the measured intensity as a function of 2θ (degrees), with corresponding d-spacings (Å) labeled along the top axis. Tick marks and Miller indices indicate the Bragg peak positions for orthorhombic bridgmanite. Prominent reflections with over 10% intensity (arbitrary unit), are labeled. The pattern was collected at ambient pressure to verify phase purity. Unidentified peaks at d-spacing = 2.591, 1.623 Å (2θ = 6.4219, 10.2592) are indicated with gray tick marks above each of the peaks. Phases were fit using PeakPo.

4.3 Results

Table B.7 lists the refined unit-cell parameters for F3A3-brg-maj over the 19.56(31)-83.43(39) GPa range, obtained via both cubic and tetragonal fits. Figure 4.2 shows the representative 1-D XRD pattern at 19.56(31) GPa and 300 K. All patterns were indexed and fitted in PeakPo (Shim, 2017), with no additional reflections appearing over compression, indicating that the garnet (and

stishovite) remain intact to the highest pressures explored. Systematic shifts of Bragg peaks to larger 2θ confirm uniform lattice contraction.

4.3.1 Pressure–Volume Equation of State Fits

Pressure–volume (P–V) data for both the cubic and tetragonal structural models were fitted using a third-order Birch–Murnaghan (BM3) equation of state (EOS). Figure 4.4 shows the experimental P–V measurements alongside the BM3 fits, with residuals plotted in panel (b).

Constraining the pressure derivative to $K_0' = 4.0$ (BM2) yields a zero-pressure volume V_0 of $1479.72 \pm 4.9\,\text{Å}^3$ and a bulk modulus $K_0 = 227 \pm 6\,\text{GPa}$ for the cubic garnet. For the tetragonal phase, the BM2 parameters are $V_0 = 1470.73 \pm 4\,\text{Å}^3$ and $K_0 = 241.2 \pm 5\,\text{GPa}$. These values agree closely with previous reports for Fe–Al–bearing majorite (Jeanloz (1981b), Faust and Knittle (1996)), confirming comparable bulk compressibility.

Allowing K_0' to vary, the BM3 fits for the cubic garnet give $V_0 = 1513.43 \pm 27\,\text{Å}^3$, $K_0 = 157 \pm 43\,\text{GPa}$, and $K_0' = 6.07 \pm 1.5$. For the tetragonal structure, $V_0 = 1513.45 \pm 23\,\text{Å}^3$, $K_0 = 148 \pm 36\,\text{GPa}$, and $K_0' = 6.82 \pm 1.5$. These BM3 V_0 values agree with those reported by Yagi *et al.* (1992) for $MgSiO_3$ end-member garnet ($1513.1\,\text{Å}^3$) and by Faust and Knittle (1996) for a theoleiitic basalt–composition garnet ($1513.31\,\text{Å}^3$).

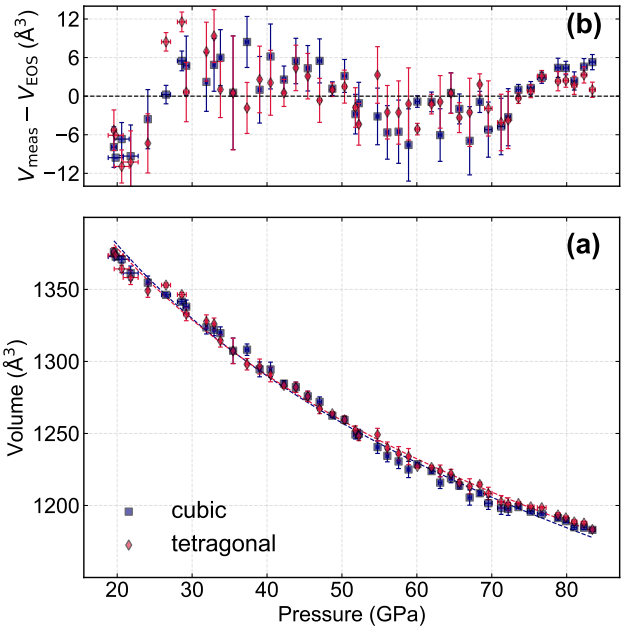

Figure 4.4: (a) Pressure-volume data with BM3-EOS fits for cubic garnet (blue squares and dashed curves) and tetragonal garnet (red rhombuses and dashed curves). (b) Plotted difference between volume measured and from fit.

4.4 Discussion

The elastic behavior of Fe-Al majoritic garnet up to 83 GPa at 300 K is characterized by calculated zero-pressure volumes and bulk moduli whether a cubic or tetragonal BM3 equation of state is applied, confirming that the tetragonal distortion has minor impact on overall compressibility. Eulerian strain–stress (f–F) analysis reveals three distinct regimes with rapid stiffening below 30 GPa, a plateau from 30–60 GPa, and hardening above 60 GPa, suggesting metastable accommodation mechanisms and incipient polyhedral collapse under extreme compression. While these transitions can reflect intrinsic structural adjustments, potential contributions from experimental factors such as non-hydrostatic stress due to the pressure medium or minor stishovite formation not explicitly modeled in the fits cannot be fully excluded. Normalized lattice parameters contract monotonically and nearly uniformly, with deviations under 2% between cubic and tetragonal fits, validating both

the diffraction refinements and EOS inversions. These results establish benchmarks for Fe-Al majorite elasticity under lower-mantle conditions and set the stage for deeper examination of experimental uncertainties, EOS comparison, compositional effects, and geophysical implications.

4.4.1 Experimental Considerations and Limitations

Accurate determination of garnet elasticity at extreme pressures hinges on the control of pressure, sample environment, and diffraction refinement. In the present study, pressure was measured via Pt, yielding uncertainties of $\pm$0.11–1 GPa that propagate into both unit-cell volumes and derived EOS parameters. Although argon loading ensured a quasi-hydrostatic medium to $\approx$60 GPa, some nonhydrostatic stress likely developed beyond that point, potentially broadening Bragg peaks and slightly biasing refined lattice constants.

Refinements enforcing cubic versus tetragonal symmetry both returned statistically indistinguishable volumes, yet the inherent limitation of the diffraction geometry prevented direct refinement of a tetragonal distortion. As a result, the cubic and tetragonal BM3 fits should be viewed as two end-member models bracketing the true structure rather than mutually exclusive descriptions. Error bars on K_0 and K_0' from the free-parameter BM3 fits reflect both counting statistics and covariance between parameters. Fixing K_0' to 4 in the BM2 fits reduced this uncertainty but at the cost of masking any real high-pressure stiffening beyond the second-order behavior.

4.4.2 Pressure-Volume EOS Fits

The third-order Birch–Murnaghan (BM3) fits to the pressure–volume data yield virtually identical zero-pressure volumes for both the cubic and tetragonal models and bulk moduli that overlap within experimental uncertainty (Table 4.1). Constraining the pressure derivative to K_0'=4

(BM2) produces a stiffer response (cubic K_0=227 GPa; tetragonal K_0=241 GPa) than the fully free BM3 fits (cubic K_0=157±43 GPa, K_0'=6.07±1.5; tetragonal K_0=148±36 GPa, K_0'=6.82±1.5). These values bracket literature results for Fe–Al majorite (e.g. Jeanloz (1981b) 221 GPa; Faust and Knittle (1996) 180 GPa) and align closely with theoretical predictions. The slight elevation of K_0 in the BM2 tetragonal fit hints at real high-pressure stiffening that is masked when K_0' is fixed.

Table 4.1: Fitted EOS parameters for cubic and tetragonal garnet structures (this study) and select literature values. Uncertainties in parentheses; fixed and constrained parameters noted.

Composition	**EOS**	V_0 (Å^3)	K_0 (GPa)	K_0'	**Reference**
					This study
F3A3-brg-maj (cubic)	BM3	1513.43(27)	157(43)	6.01(1.5)	
	BM2	1479.72(4.9)	227(6)	4†	
	Vinet	1513.43(25)	155(38)	6.24(1.2)	
F3A3-brg-maj (tetragonal)	BM3	1513.45(23)	148(36)	6.82(1.5)	
	BM2	1470.73(4)	241(5)	4†	
	Vinet	1513.45(20)	148(30)	6.88(1)	
					Literature
Fe-majorite	BM3	1527.4	221(15)	4.4(4.8)	Jeanloz (1981b)
majorite[1]	BM3	1517.31	180*	7(1)	Faust and Knittle (1996)
majorite[2]	BM3	1516	163.6	4.44	Lou *et al.* (2020)
majorite[3]	BM2	1513.1	161.2	4†	Yagi *et al.* (1992)
majorite[3]	BM2	1524.6(5)	169.3(34)	4†	Hazen *et al.* (1994)
majorite[1]	BM2	1517.31	226.2(9.3)	4†	Faust and Knittle (1996)
Ca-majorite	BM2	1547.0(3)	164.8(23)	4†	Hazen *et al.* (1994)
Na-majorite	BM2	1485.5(3)	191.5(25)	4†	Hazen *et al.* (1994)

[1] Theoleiitic basalt composition ($Mg_{0.31}Fe_{1.4}Ca_{0.82}K_{0.06}Al_{0.67}Si_{3.9}O_{12}$).
[2] Theory.
[3] $MgSiO_3$ end-member.
† Fixed K_0'.

4.4.3 Euler Strain Analysis

To further examine the behavior of garnet at high-pressure, the reduced Eulerian stress F is plotted against Eulerian finite strain f (f–F plot) of the Birch–Murnaghan EOS (Figure 4.5). Eulerian finite-strain analysis provides an alternative visualization of the EOS fits through the

reduced stress F versus finite strain f. The finite strain is defined by Equation 2.16 and the reduced stress is defined by Equation 2.17 (see Section 2.6.1).

The f–F plot (Figure 4.5) exhibits three distinct compressibility regimes. In the low–pressure window (0–30 GPa, shaded gray), both cubic (blue) and tetragonal (red) data rise steeply with increasing strain, indicating rapid initial stiffening. Between 30 and 60 GPa (shaded blue), F remains nearly constant over $0.045 \leq f \leq 0.07$, revealing a plateau in effective bulk modulus as the structure accommodates further volume reduction with minimal additional resistance. Above 60 GPa (shaded green), F increases again for $f > 0.07$, marking renewed hardening under extreme compression. Solid lines in each region are linear regressions of $F(f)$.

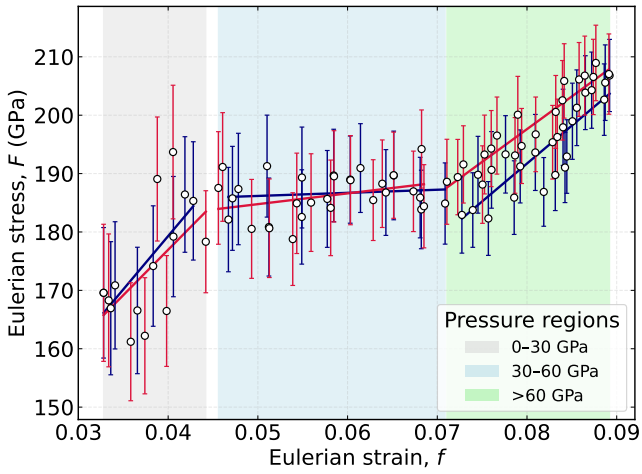

Figure 4.5: Euler stress-strain (f-F) plot for F3A3-brg-maj fitted with cubic (blue) and tetragonal (red) structures.

4.4.4 Normalized Lattice-Parameter Trends

The compressional behavior of garnet is illustrated by the pressure dependence of normalized lattice parameters in Figure 4.6 Zero-pressure lattice parameters a_0^{cubic} (cubic), a_0^{tet} (tetragonal) and c_0^{tet} (tetragonal) were determined from orthogonal distance regression (ODR) fits of the third-order

Birch–Murnaghan equation of state (Boggs and Rogers, 1989), which accounts for uncertainties in both pressure and lattice measurements. The fitted functions were numerically inverted to give $x(P)$, plotted as solid curves with bootstrap-derived 95% confidence intervals.

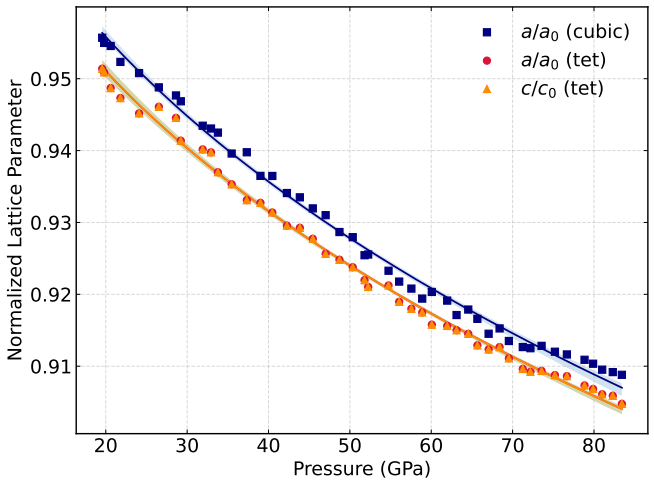

Figure 4.6: Normalized lattice parameters of F3A3-brg-maj as a function of pressure. The fitting of the cubic lattice parameter (a_{cubic}) is shown as blue squares, while the tetragonal lattice parameters a_{tet} and c_{tet} are shown as red circles and orange triangles with 95% confidence intervals, respectively.

All trends show monotonic compression, but the tetragonal refinements reveal a small yet systematic anisotropy: c/c_0 decreases more rapidly than a/a_0, particularly above 45 GPa. The cubic a/a_0 curve lies slightly above both tetragonal trends, indicating that enforcing cubic symmetry modestly overestimates stiffness. These results imply subtle symmetry lowering distortions and increased anisotropy in garnet at lower-mantle pressures.

4.4.5 Effects of Fe-Al Substitution

In majoritic garnet, Fe and Al occupy both the dodecahedral (X) and octahedral (Y) sites in ways that directly control compressibility and elastic anisotropy (Irifune, 1987; McCammon

et al., 2004; Bolfan-Casanova *et al.*, 2003). In F3A3-brg-maj, Fe^{2+} substitutes into the eight-fold X-site alongside Mg^{2+}, while Al^{3+} occupies the six-fold Y-site. Because Fe^{2+} has a larger ionic radius (0.78 $\mathring{A}^3$) than Mg^{2+} (0.72 $\mathring{A}^3$), X-site enrichment in Fe^{2+} tends to expand the zero-pressure volume and, in many garnet solid solutions, lower the bulk modulus relative to a Mg-endmember (Yagi *et al.*, 1992; Hazen *et al.*, 1994). However, in practice the simultaneous presence of Al^{3+}/Fe^{2+} in the Y-site and the pressure-induced migration of Si^{4+} into octahedral coordination complicates that simple trend (Ito and Takahashi, 1989; Bolfan-Casanova *et al.*, 2003).

The BM3 zero-pressure volume (V_0 ≈1513.4 Å^3) closely matches that of pure Mg-majorite (1513.1 Å^3; Yagi *et al.* (1992)), indicating a near balance between Fe-driven expansion and Al-driven contraction.

Bulk modulus trends reflect a similar interplay. When K_0' is fixed at 4 (BM2), the apparent stiffness (K_0=227 GPa cubic; 241 GPa tetragonal) significantly exceeds Mg-majorite values (161; Yagi *et al.* (1992)) and aligns with Fe-rich majorite measurements (221 GPa; Jeanloz (1981b)). Allowing K_0' to refine (BM3) lowers the best-fit K_0 (157±43 GPa cubic; 148±43 36 GPa tetragonal) but yields K_0' ≈6–7, which is higher than typical Mg-endmember values (4–5) and consistent with pressure-induced Si to six-fold migration enhancing octahedral flexibility at high strain (Ito and Takahashi, 1989).

Overall, the combined effects of Fe^{2+} X-site enlargement and Al^{3+}/Si^{4+} Y-site contraction produce compressibility intermediate between Mg-endmember and Fe-rich garnets. The virtually identical volumes and bulk moduli from both cubic and tetragonal fits confirm that any tetragonal distortion lies below the resolution of the present diffraction data.

4.4.6 Geophysical Implications

The presented XRD measurements demonstrate that Fe–Al majoritic garnet can remain mechanically robust to at least 83 GPa and 300 K, with no abrupt volume collapse or loss of framework integrity. Metastable persistence of garnet into the lower-mantle could stiffen cold subducted lithosphere beyond the nominal 660 km discontinuity, increasing slab buoyancy and promoting stagnation at the base of the transition zone. In particular, the plateau in effective bulk modulus between 30 and 60 GPa suggests that garnet-rich domains would resist further compression with minimal change in seismic impedance, potentially obscuring the signature of coexisting bridgmanite or post-perovskite phases.

The smooth contraction of both a/a_0 and c/c_0 implies that intrinsic garnet-driven seismic anisotropy may be weak unless amplified by lattice-preferred orientation. Regions of high garnet abundance in cold slabs are therefore unlikely to generate strong shear-wave splitting signals, though they could contribute to subtle azimuthal-anisotropy anomalies detected in transition-zone tomography. Renewed stiffening above 60 GPa may produce a positive velocity gradient, shifted to greater depths in unusually cold or garnet-enriched regions.

Finally, the elevated pressure derivative $K_0' \approx 6$ indicates that garnet compressibility increases sharply at high strain, thereby amplifying density contrasts between slab and ambient mantle with depth. Such contrasts could help explain delayed slab penetration into the lower mantle beneath old, thick lithosphere and may focus deep-focus seismicity by concentrating stress within metastable garnet domains.

4.4.7 Future Directions

Extending these 300 K measurements to dynamic properties will be required. *In situ* determination of compressional and shear wave velocities (V_P, V_S) in Fe-Al majorite at high pressure and ideally at simultaneous high temperature, would directly link the bulk and shear moduli derived here to seismic observables, reducing uncertainties in mantle velocity models. Complementary thermal-EOS experiments, conducted over 1,200–2,000 K, would establish the full thermoelastic behavior of Fe–Al majorite and reveal any thermal softening or phase-boundary shifts that occur under realistic mantle conditions.

Spectroscopic investigations under pressure offer another prospect for further work. The pressure derivative of the smoothed P–V curve (Fig. A.7) shows three broad features a peak near 24 GPa, a softening around 50–55 GPa, and renewed stiffening above 70 GPa. While these could reflect subtle rearrangements of octahedral site relaxation or incipient spin-crossover, the current diffraction data and stress conditions cannot unambiguously distinguish among these mechanisms. Targeted spectroscopic experiments (e.g. Mössbauer, XES) and better controlled hydrostatic loading will be needed to test whether these K_{inst} anomalies arise from genuine electronic or structural transitions, or from modeling biases in finite-difference differentiation under non-ideal stress.

Finally, exploring the kinetic limits of the garnet→perovskite transformation in Fe-Al compositions remains essential for understanding slab metastability. Time-resolved experiments at elevated temperatures and pressures can map out the metastable persistence field and quantify the rates of nucleation and growth of perovskite, clarifying how cold slab interiors might retain garnet to depths well beyond its equilibrium stability. Pursuing these complementary approaches will yield a comprehensive framework for Fe-Al majoritic garnet, closing the gap between laboratory

data and dynamic mantle processes.

4.5 Conclusion

High-pressure synchrotron X-ray diffraction on Fe-Al majoritic garnet to 83 GPa at 300 K confirms a continuous, compression with no abrupt volume collapse or symmetry change. Third-order Birch–Murnaghan fits yield zero-pressure volumes of ≈1513.4 $Å^3$ and bulk moduli bracketing 148–157 GPa (BM3) or 227–241 GPa (BM2), values that align with both Mg-endmember and Fe-rich literature end-members when compositional effects are accounted for.

Eulerian f–F analysis identifies three elastic regimes with rapid stiffening below 30 GPa, a plateau from 30–60 GPa, and renewed hardening above 60 GPa revealing metastable accommodation mechanisms that may persist into lower-mantle conditions.

Compositional balance between X-site Fe^{2+} enlargement and Y-site Al^{3+} contraction produces a net volume and stiffness intermediate between end-members, while the elevated pressure derivative ($K_0' \approx 6 - -7$) underscores enhanced high-strain compressibility.

Geophysical implications include potential garnet metastability in cold slabsand amplified density contrasts that could influence slab stagnation and deep-focus seismicity. Future dynamic, thermal, and spectroscopic investigations coupled with kinetic studies of the garnet-to-perovskite transformation will be essential to integrate these static benchmarks into comprehensive models of transition-zone and lower-mantle processes.

Chapter 5

Ab Initio Density Functional Theory Calculations on Fe-Al-Bridgmanite from 0 to 140 GPa at 0 K

5.1 Introduction

Direct laboratory experiments under lower-mantle conditions face two major challenges: atomic-scale characterization of materials and the need to achieve and sustain extreme pressures and temperatures. Additionally, access to *in situ* X-ray diffraction (XRD) facilities is limited by competitive proposal cycles. Density functional theory (DFT) provides a quantum-mechanical framework for predicting mineral behavior without sole reliance on experiments. Using DFT, researchers can determine phase stability, elastic moduli, and pressure-volume-temperature relationships from first principles.

Previous DFT studies have explored the influence of iron and aluminum in bridgmanite, focusing on their impact on elasticity, spin transitions, and thermodynamic properties (Shukla and Wentzcovitch, 2016; Shukla *et al.*, 2015; Mohn and Trønnes, 2016; Li *et al.*, 2005). Li *et al.* (2005) examined the elastic properties of $\mathrm{MgSiO_3}$ and $(\mathrm{Mg_{1-x}, Fe_x})(\mathrm{Si_{1-x}, Al_x})\mathrm{O_3}$ with x = 0.0625, but did not include temperature effects, limiting the direct comparison with high-temperature experimental data. Shukla and Wentzcovitch (2016) used LDA + U calculations to investigate the thermoelastic properties of Fe^{3+}- and Al-bearing bridgmanite, with a focus on the effects of the iron spin crossover under lower mantle condition by looking at $(\mathrm{Mg_{1-x}, Al_x})(\mathrm{Si_{1-x}, Al_x})\mathrm{O_3}$, $(\mathrm{Mg_{1-x}, Fe_x})(\mathrm{Si_{1-x}, Fe_x})\mathrm{O_3}$, and $(\mathrm{Mg_{1-x}, Fe_x})(\mathrm{Si_{1-x}, Al_x})\mathrm{O_3}$ with x = 0.125. Their work tested whether $\mathrm{Fe^{3+}}$ would stay high-spin or switch to low-spin under mantle pressures, depending on

which crystal site (A or B) it occupied and whether Al^{3+} was also in the mix. They stated that Fe^{3+} needs to be on the B-site which has octahedral coordination (replacing Si) for the spin transition to occur. This is in agreement with Burns (1993), who explain this phenomenon as being due to crystal field splitting in octahedral coordination. However, their work expanded this concluding that aluminum suppresses the elastic anomalies associated with the spin crossover of Fe^{3+} in bridgmanite since Al only occupies the B-site which means that even though Fe^{3+} prefers the B-site, it must then occupy the A-site.

Building on these previous studies, this chapter presents DFT calculations at 0 K from 0 to 140 GPa to examine the effects of Fe and Al substitution in bridgmanite. Three compositions are investigated: pure $MgSiO_3$ as a reference, $(Mg_{0.75}, Fe_{0.25})(Si_{0.75}, Al_{0.25})O_3$ (FeAl25), and $(Mg_{0.50}, Fe_{0.50})(Si_{0.50}, Al_{0.50})O_3$ (FeAl50). All iron was placed in the A-site to avoid spin crossover effects. Additionally, when Fe^{3+} is in the presence of Al, the Fe^{3+} is predominately on the A-site due to charge-coupled substitution mechanisms. This coupled substitution (Fe^{3+} + Al^{3+} $\leftrightarrow$ Mg^{2+} + Si^{4+}) stabilizes Fe^{3+} in the larger 12-fold coordinated A-site, while Al preferentially occupies the octahedral B-site. Such behavior has been observed in both experimental studies and theoretical predictions of Fe-Al-bearing bridgmanite compositions under lower mantle conditions (McCammon, 1997; Xu *et al.*, 2015; Catalli *et al.*, 2011; Nishio-Hamane *et al.*, 2005; Zhang *et al.*, 2014). This site preference is critical for understanding the valence state, spin state, and partitioning behavior of iron in the deep Earth. These 0 K data provide a baseline for subsequent high-temperature DFT calculations and offer insights into how Fe and Al substitution in the A- and B- sites respectively, elastically behave and how they may influence geophysical behavior of the deep mantle.

5.2 Methods

All calculations are performed using the CASTEP 20.11 Ab Initio Total Energy Program (Clark *et al.*, 2005) with the Perdew–Burke–Ernzerhof for solids (PBEsol) (Perdew *et al.*, 2008) exchange-correlation functional under the generalized gradient approximation (GGA). Convergence tests for cutoff energies and k-point grids are systematically carried out to identify suitable computational parameters (CASTEP Developers Group, 2024). Orthorhombic bridgmanite (i.e., perovskite) structures are constructed for $\mathrm{MgSiO_3}$, FeAl25, and FeAl50.

The calculations began with$\mathrm{MgSiO_3}$ with 20 atoms to establish reference parameters validated against experimental and theoretical benchmarks. Fe and Al are then substituted into the structure, requiring additional tests to find the most stable atomic arrangements. Geometry optimizations are performed at pressures from 0 to 140 GPa in 5 GPa increments, allowing cell volume, cell parameters, and atomic positions to relax at each pressure step. These relaxed structures are used to compute pressure–volume (P–V) relationships, lattice parameter evolution, and elastic properties.

5.2.1 Convergence tests

$MgSiO_3$

Cutoff energies from 400 to 900 eV (in steps of 100 eV) are tested for $\mathrm{MgSiO_3}$. Convergence analyses indicated that beyond 800 eV the change in total force fell below $2 \times 10^{-3}\,\mathrm{eV/Å}$ (Figures A.8–A.9). Next, k-point meshes ranging from $3 \times 3 \times 2$ up to $8 \times 8 \times 6$ are compared. A $4 \times 4 \times 3$ mesh at 800 eV met our convergence threshold (forces $< 2 \times 10^{-5}\,\mathrm{eV/Å}$) without excessive computational cost (Figures A.10–A.11). These optimized parameters (800 eV cutoff, $4 \times 4 \times 3$ k-mesh) are then used for all subsequent geometry optimizations of $\mathrm{MgSiO_3}$ at pressures between 0 and 140 GPa.

Fe and Al Configuration within the Structure

Fe and Al can occupy different A- and B-sites in $\mathrm{ABO_3}$ perovskites. Table 5.1 lists the fractional atomic coordinates for the perovskite structure (from CrystalMaker X 10.8.1 (CrystalMaker, 2023)). For FeAl25, one Fe and one Al atom are introduced, testing multiple site choices (Table B.8, Figure A.12). Referring to Table B.8, "Position 1" provided the most stable configuration. Similarly, FeAl50 involved two Fe and two Al atoms (Table B.9, Figure A.16), and referring to Table B.9, "Position 2" minimized the total energy. Once the optimal placements are established, cutoff energies from 400 eV up to 1100 eV and k-point grids from $3 \times 3 \times 2$ up to $6 \times 6 \times 4$ are tested. Ultimately, 900 eV and a $5 \times 5 \times 5$ mesh are chosen for both FeAl25 and FeAl50, balancing convergence (forces $< 2 \times 10^{-5}\,\mathrm{eV/Å}$) with computational efficiency (Figures A.13–A.15 and A.17–A.19) (CASTEP Developers Group, 2024). These parameters are then used for all geometry optimizations of FeAl25 and FeAl50 at pressures between 0 and 140 GPa. Table B.10 summarizes the final cutoff energies and k-meshes for each composition.

Table 5.1: Fractional atomic positions for cations (A and B) and anion (O) in the orthorhombic perovskite structure. **A** positions are substituted with Mg and Fe, while B positions are substituted with Si and Al. The fractional coordinates for this study are obtained using CrystalMaker X (10.8.1) (CrystalMaker, 2023).

Atomic Position	x	y	z
A_1	0.5141	0.5560	0.2500
A_2	0.0141	0.9440	0.7500
A_3	0.4859	0.4440	0.7500
A_4	0.9859	0.0560	0.2500
O	0.1028	0.4660	0.2500
O	0.6028	0.0340	0.7500
O	0.8972	0.5340	0.7500
O	0.3972	0.9660	0.2500
O	0.1961	0.2014	0.5531
O	0.6961	0.2986	0.4469
O	0.8039	0.7986	0.0531
O	0.3039	0.7014	0.9469
O	0.8039	0.7986	0.4469
O	0.3039	0.7014	0.5531
O	0.1961	0.2014	0.9469
O	0.6961	0.2986	0.0531
B_1	0.5000	0.0000	0.5000
B_2	0.0000	0.5000	0.5000
B_3	0.5000	0.0000	0.0000
B_4	0.0000	0.5000	0.0000

5.3 Results

This study presents the structural evolution of $MgSiO_3$, FeAl25, and FeAl50 as functions of pressure at 0 K from 0 to 140 GPa. The obtained pressure-volume (P–V) data, fitted with a third-order Birch-Murnaghan Equation of State (BM3-EOS), is shown in Figure 5.1 and tabulated in Table B.11. The incorporation of Fe and Al increases the zero-pressure volume (V_0) and reduces the bulk modulus (K_0), reflecting the influence of larger cationic radii and altered bonding on compressibility.

As pressure increases from 0 to 140 GPa, the volumes of all compositions decrease non-

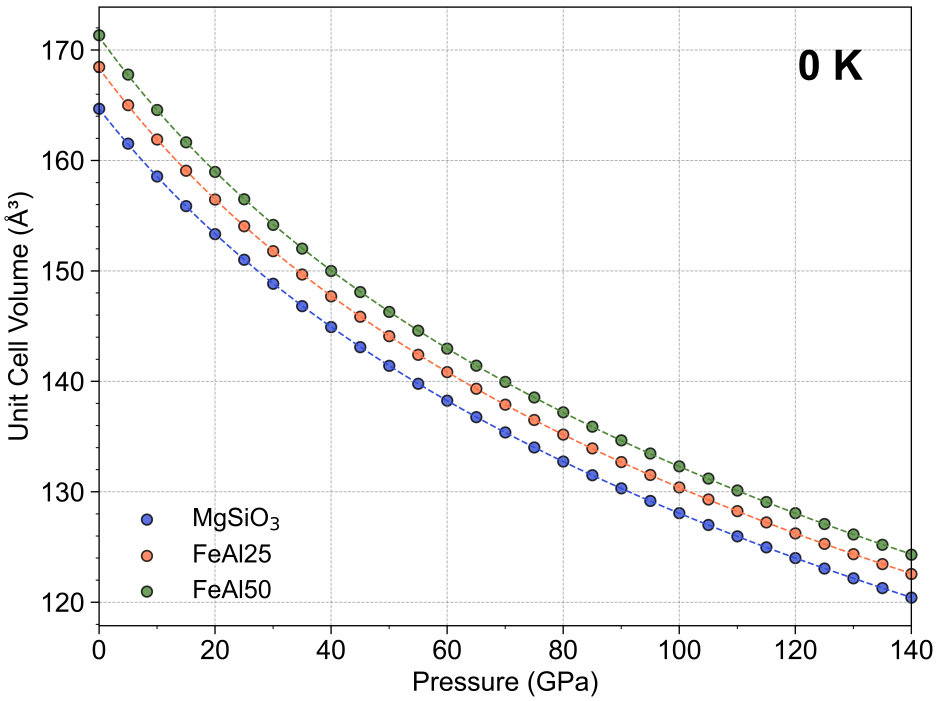

Figure 5.1: Unit cell volumes (Å^3) plotted as a function of pressure (GPa) for $MgSiO_3$ (blue), FeAl25 (orange), and FeAl50 (green). The curves are of BM3-EOS fits showing the expected compression behavior, with volume decreasing non-linearly as pressure increases. Table B.11 lists the P–V information. Table 5.2 lists the calculated BM3-EOS parameters. These datasets were obtained through geometry optimization under varying pressure.

Table 5.2: Calculated 3rd-order Birch-Murnaghan Equation of State (BM3-EOS) parameters for DFT calculations at 0 K. The leftmost column lists the compositions. The columns to the right of the compositions list the calculated values for each composition: V_0 (Å^3), volume at 0 GPa; K_0 (GPa), bulk modulus; K_0', bulk modulus derivative; ρ (g/cm^3), density.

Composition	V_0 (Å^3)	K_0 (GPa)	K_0'	ρ (g/cm^3)
$MgSiO_3$	164.71(1)	243.4(3)	3.90(1)	4.05(1)
FeAl25	168.35(3)	237.2(5)	3.92(1)	4.26(1)
FeAl50	171.20(4)	234.1(6)	3.92(1)	4.49(1)

linearly, consistent with typical compression behavior observed in mantle minerals. The unit cell parameters and volumes for $MgSiO_3$, FeAl25, and FeAl50 are listed in Table B.11.

The BM3-EOS values presented in Table 5.2 describe the relationship between pressure,

volume, and compressibility for each composition. These BM3-EOS fittings were performed using the P–V data presented in Figure 5.1, to give V_0 (volume at zero pressure), K_0 (bulk modulus, a measure of incompressibility), and K_0' (pressure derivative of the bulk modulus, which reflects how compressibility changes under increasing pressure), and density (ρ, g/cm^3) is also listed.

The results show an increase in V_0 with the substitution of Fe and Al into the orthorhombic perovskite lattice. $MgSiO_3$ has the smallest volume, V_0 = 164.71(1) Å^3, while FeAl25 and FeAl50 exhibit systematically larger volumes, V_0 = 168.35(3) Å^3 and 171.20(4) Å^3, respectively. This reflects the incorporation of larger cations (Fe and Al) into the lattice, which leads to lattice expansion. The bulk modulus (K_0) values similarly show a compositional dependency, decreasing with increased Fe and Al content. $MgSiO_3$ exhibits the highest K_0, 243.4(3) GPa, consistent with its relatively higher incompressibility. FeAl25 and FeAl50, with K_0 values of 237.2(5) GPa and 234.1(6) GPa, respectively, demonstrate increased compressibility due to the weaker bonding environment associated with Fe and Al substitutions. The pressure derivative of the bulk modulus, K_0', remains relatively stable across the compositions, with values ranging from 3.90(1) to 3.92(1).

In addition to volume, the lattice cell parameters were also calculated. Figure 5.2 presents the lattice parameters (a, b, and c) for all three compositions with increasing pressure. All lattice parameters decrease with increasing pressure. The rate of compression for each lattice parameter shown as the fitted lines in Figure 5.2. For the a-axis, the compression curves and the lattice parameter are similar for all compositions, indicating that the substitution does not significantly affect the a-axis nor its compressional behavior. The slope of the b-axis compression is slightly less steep compared to the a-axis, suggesting slightly less compressibility along this direction. The compression rate of the c-axis is somewhat steeper than both the a- and b-axes, showing greater compressibility along this direction.

Figure 5.2: Lattice parameters a (circles), b (squares), and c (triangles) shown as a function of pressure for $MgSiO_3$ (blue), FeAl25 (orange), and FeAl50 (green) compositions at 0 K. Fit are of 3rd-order fits for compressibility in colors for their corresponding compositions. The compressibilty calculations are presented in Table B.12.

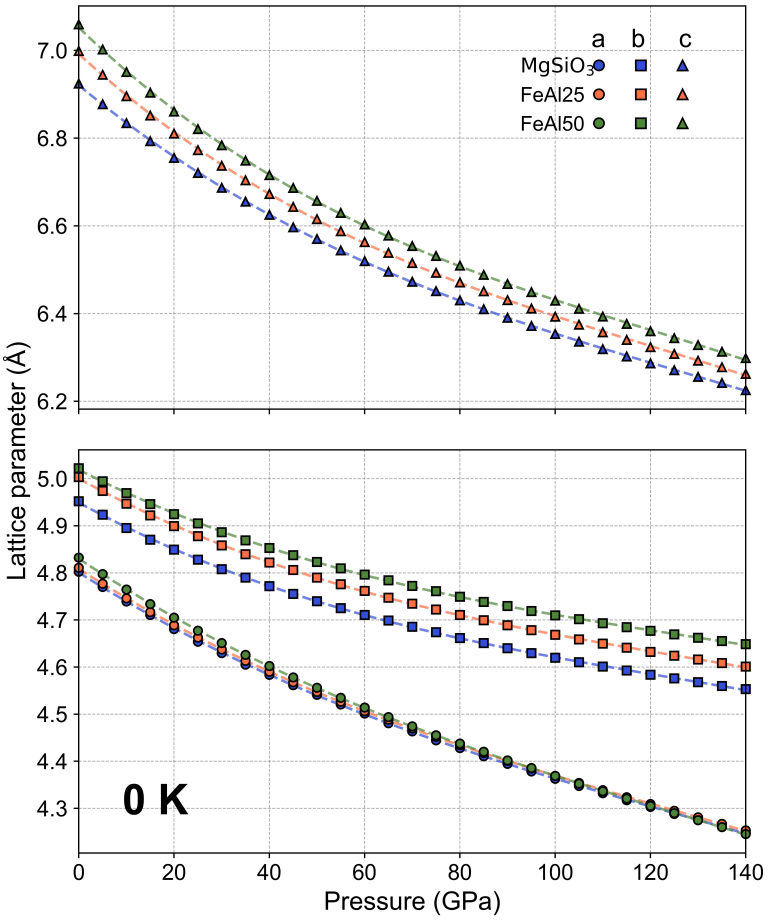

Figure 5.3 illustrates the normalized lattice parameters as a function of increasing pressure, highlighting the differences in lattice parameter compressibility. For parameter a, the compressibility of MgSiO3 and FeAl25 is comparable, whereas FeAl50 consistently exhibits a higher compressibility. Similarly, for parameter b, MgSiO3 and FeAl25 display comparable compressibility, but FeAl50 shows a consistently lower compressibility. In contrast, for parameter c, MgSiO3 demonstrates the lowest compressibility, while FeAl50 exhibits the highest. Overall for each com-

position, parameter a exhibits the highest compressibility, while b shows the lowest compressibility. However, for FeAl25 and FeAl50, parameter c exhibits higher compressibility at lower pressures (0–20 GPa), a behavior not observed in $MgSiO3$ (Table B.12).

Figure 5.3: Normalized lattice parameters (l/l_0) for a (circles), b (squares), and c (triangles) shown as a function of pressure for $MgSiO_3$ (blue), FeAl25 (orange), and FeAl50 (green) compositions at 0 K. Fit are of 3rd-order fits for isothermal compressibility derived from Equation 2.10 in colors for their corresponding compositions. The compressibilty calculations are presented in Table B.12.

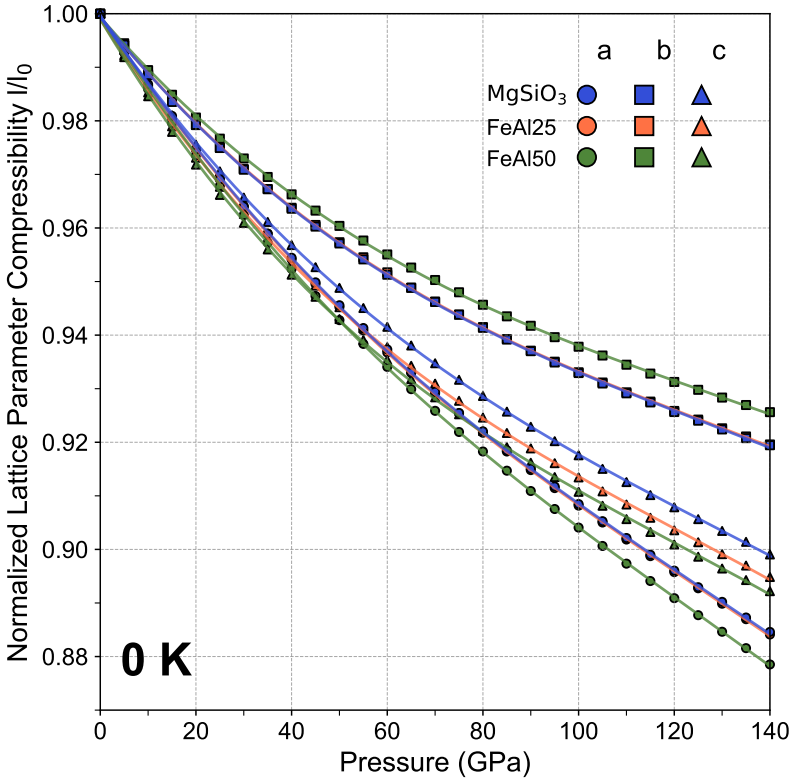

The lattice ratios as functions of pressure (0-140 GPa) provide additional indicators of structural change under compression, illustrating compositional effects. Figure 5.4 and Figure 5.5 present the b/a and c/a lattice ratios, respectively.

The b/a axial ratio as a function of pressure for $MgSiO_3$, FeAl25, and FeAl50 bridgmanite compositions is presented in Figure 5.4. Across all compositions, the b/a ratio increases linearly with pressure, signifying systematic anisotropic deformation of the crystal lattice under compression.

For $MgSiO_3$, the b/a ratio at 0 GPa is 1.030161 and increases to 1.058625 at 140 GPa. The substitution of Fe and Al into the lattice leads to elevated b/a ratios at all pressures. At 0 GPa for FeAl25 the b/a ratio is 1.039291, while for FeAl50 it is 1.039048. However, the b/a at 140 GPa FeAl25 is 1.068073 and for FeAl50 is 1.078133.

Figure 5.4: Pressure dependence of the b/a lattice parameter ratio with pressure (0–140 GPa) for $MgSiO_3$ (blue), FeAl25 (orange) and FeAl50 (green). Across all compositions, the b/a ratio increases linearly with pressure, reflecting differential compression along the a- and b-axes. The higher b/a ratios observed in FeAl50 compared to FeAl25 and $MgSiO_3$ indicate greater structural anisotropy induced by Fe and Al substitutions. This behavior likely arises from the larger ionic radii of Fe and Al relative to Mg and Si, coupled with changes in bonding characteristics within the orthorhombic perovskite structure.

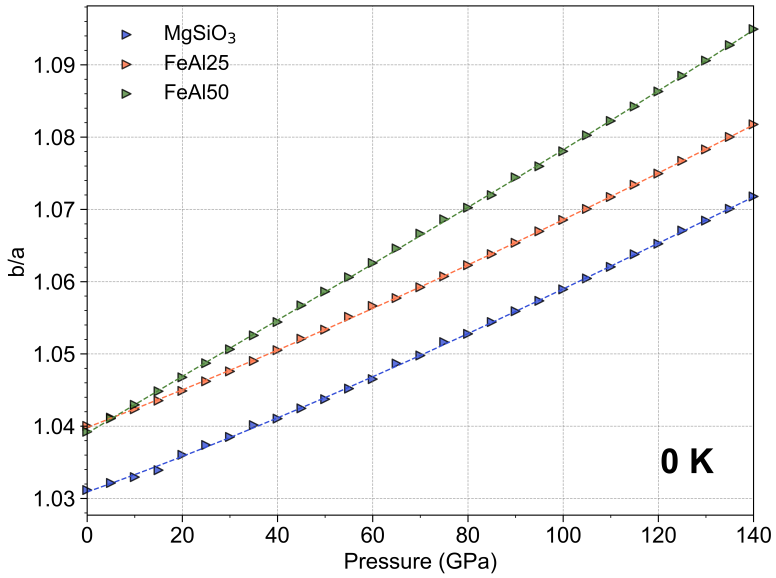

The c/a axial ratio as a function of pressure for $MgSiO_3$, FeAl25, and FeAl50 bridgmanite compositions is presented in Figure 5.5. The overall trend for c/a is similar to b/a and shows an increasing trend with pressure which is seen in the linear fits. This is consistent with the unit cell becoming more anisotropic with increasing pressure, likely due to the differential compressibilities of the lattice parameters c and a. However, unlike the b/a ratios, the c/a ratios show a slight curvature in the data points which becomes more pronounced with higher Fe and Al incorporation.

Figure 5.5: Pressure dependence of the c/a lattice parameter ratio with pressure (0–140 GPa) for $MgSiO_3$, FeAl25, and FeAl50.

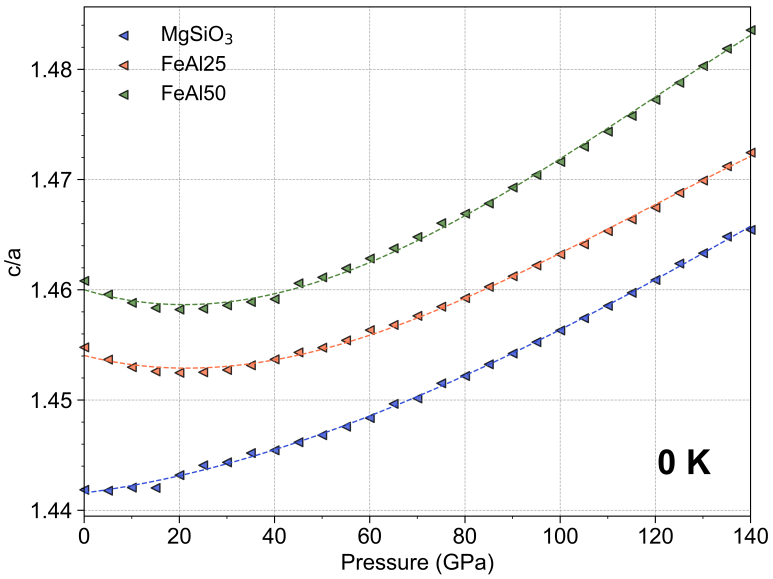

Density calculations (Figure 5.6) indicate that the densities of all compositions increase with pressure, reflecting the reduction in unit cell volumes. $MgSiO_3$ consistently exhibits the lowest density across the pressure range. FeAl25 and FeAl50 show progressively higher densities due to the incorporation of heavier Fe and Al atoms. The observed density trends highlight how compositional variations influence mineral density.

Figure 5.6: Density (g/cm^3) as a function of pressure (0-140 GPa) for $MgSiO_3$ (blue), FeAl25 (orange), and FeAl50 (green) at 0 K. The density increases with pressure for all compositions, following a non-linear trend consistent with typical mantle mineral compression behavior. Dashed lines represent fits to the data points.

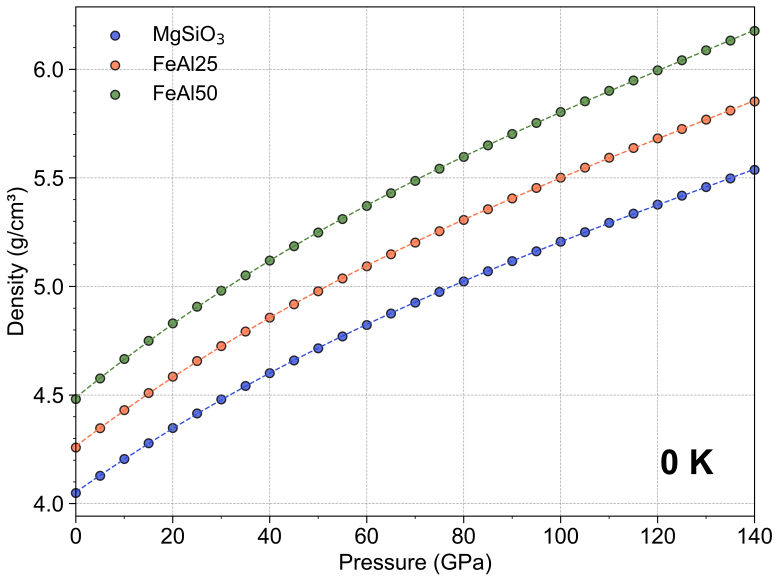

5.4 Discussion

The presented *ab initio* DFT results for $MgSiO_3$, FeAl25 and FeAl50 demonstrate how iron and aluminum substitutions influence the structural and elastic properties of bridgmanite under compression. Results show that substitution of Fe and Al lead to an increase in the initial zero-pressure volume (V_0), decreases in the bulk modulus (K_0), and slight changes in the pressure derivative of the bulk modulus (K_0').

Density calculations reveal that compositional variations significantly influence mineral density under pressure. $MgSiO_3$ has the lowest density (ρ) due to its lower atomic mass. In contrast, FeAl25 and FeAl50, enriched with heavier Fe and Al, exhibit progressively higher densities (Figure 5.7). This systematic increase in density with Fe and Al substitution has implications for interpreting seismic data and modeling lower mantle heterogeneities, suggesting that Fe-Al-enriched regions would have higher densities, and thus, distinct seismic signatures (Vanpeteghem

et al., 2006b; Ballaran *et al.*, 2012; Muir and Brodholt, 2016).

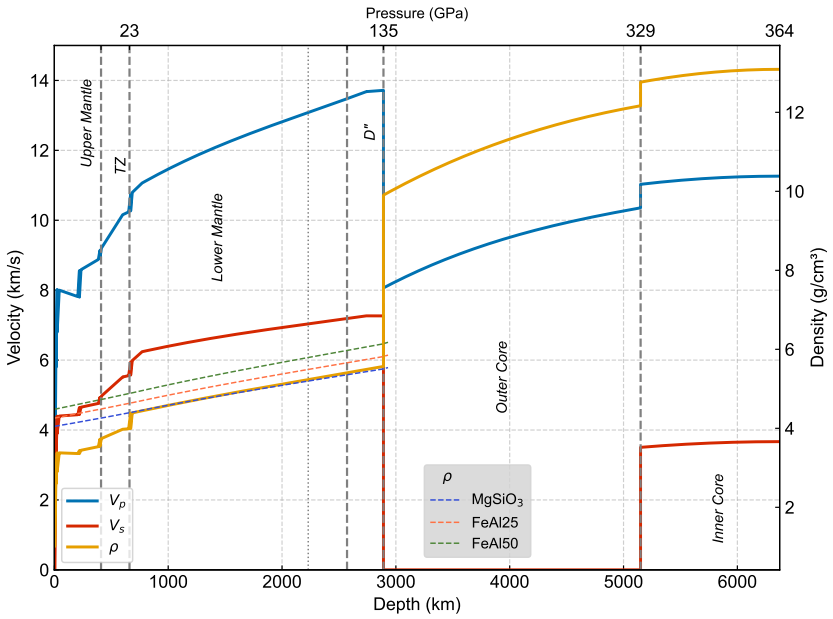

Figure 5.7: PREM-based seismic velocity profile (solid lines) (Dziewonski and Anderson, 1981), illustrating how velocity and density vary with depth. The figure highlights transitions from the upper mantle, through the transition zone (TZ), into the lower mantle, and ultimately into the liquid outer core and solid inner core. Density (ρ) for each composition at 0 K are included as dashed lines.

The lattice parameters exhibit anisotropic compressional behavior, with the a-axis generally being the most compressible and the b-axis the least, while the c-axis shows intermediate behavior that varies with Fe-Al content (Figure 5.2 and Figure 5.3). This behavior becomes more pronounced with increasing Fe-Al substitution, particularly at pressures < 20 GPa, where FeAl50 shows enhanced compressibility along the c-axis compared to $MgSiO_3$.

The orthorhombic perovskite structure, characterized by differential tilting of SiO_6 octahedra along each axis, contributes to this directional stiffness. Fe and Al incorporation modifies octahedral tilting and polyhedral distortions, likely due to differences in Fe-O and Al-O bond lengths and site-specific substitutions (Table B.8, Table B.9) (Pauling, 1928; Yagi *et al.*, 1978; Anderson, 1983;

Andrault *et al.*, 2001; Criniti *et al.*, 2021). In FeAl25, the shortest Fe-Al nearest-neighbor distance is 2.79 Å, whereas FeAl50 exhibits two distinct Fe-Al separations of 3.03 Å and 3.14 Å. The shorter Fe-Al separation in FeAl25 promote lattice stiffening, while the larger distance in FeAl50 give rise to relative lattice softening which is reflected in their respective thermal-EOS parameters presented in Chapter 6.

The pressure-volume behavior of individual coordination polyhedra in bridgmanite (Figure 5.8) reveals how Fe-Al substitution changes compressibility in the lower mantle. All four polyhedral volumes (Si, Mg, Al, and Fe) contract smoothly from 0 to 140 GPa, demonstrating that the corner-sharing framework remains intact under extreme pressures. At ambient conditions, Si-polyhedra volumes are nearly identical across compositions (7.76 $Å^3$ in $MgSiO_3$, 7.80 $Å^3$ in FeAl25, and 7.82 $Å^3$ in FeAl50), whereas the Mg-polyhedra shows a modest decrease from 12.17 $Å^3$ ($MgSiO_3$) to 12.05 $Å^3$ (FeAl50) but an lower 9.67 $Å^3$ in FeAl25, indicating non-linear site distortions upon partial substitution.

The Al- and Fe-polyhedra in the Fe-Al-bearing compositions exhibit slightly less relative volume reduction at high pressure than their Si and Mg counterparts, implying enhanced stiffness in these substituted sites. Overall, Fe-Al incorporation not only alters ambient polyhedral volumes in a non-systematic way but also dampens the rate of compression in specific sites, an effect that may influence bridgmanite's aggregate elastic properties and the seismic signature of Fe/Al-enriched regions in the lower mantle.

Further illustrating this behavior, Figure 5.4 and Figure 5.5 show how the b/a and c/a lattice ratios evolve with increasing pressure. Both ratios increase across all compositions, reflecting faster compression along the a-axis relative to b and c. The linear trend in b/a and the more nonlinear increase in c/a indicate that the crystal structure becomes progressively more anisotropic

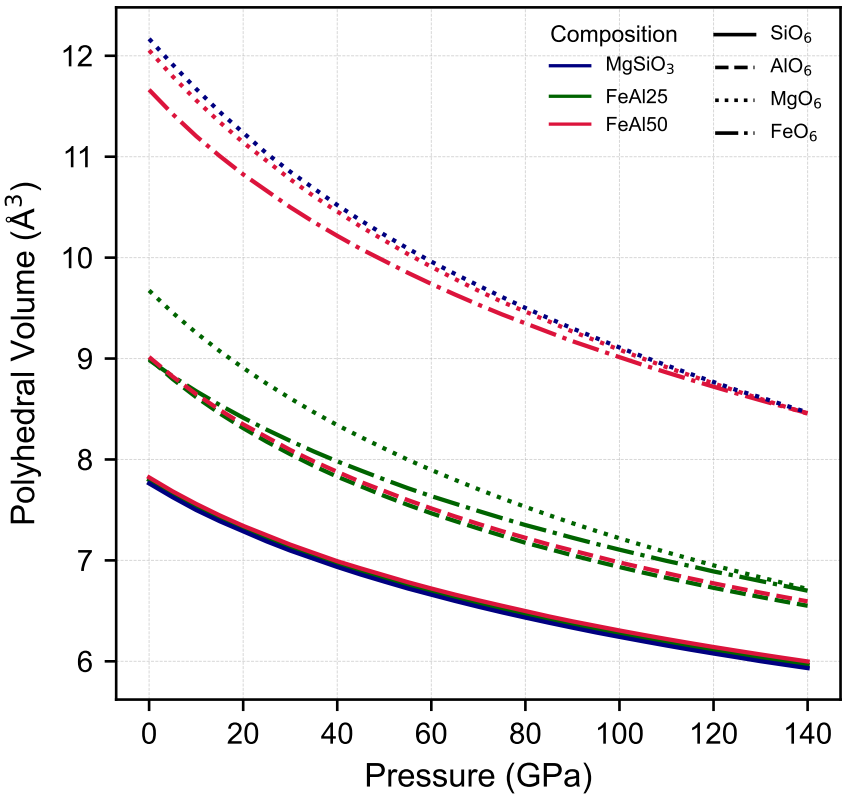

Figure 5.8: Polyhedral volumes ($Å^3$) for SiO_6 (solid lines), AlO_6 (dashed), MgO_6 (dotted) and FeO_6 (dash-dot) are plotted as a function of pressure (0–140 GPa) for $MgSiO_3$ bridgmanite (blue), FeAl25 (green) and FeAl50 (red).

under compression, a characteristic response of orthorhombic perovskites where axis-specific shortening is driven by weaker bonding or enhanced polyhedral tilting along certain directions (Huang *et al.*, 2021b). Notably, at 0 GPa, FeAl25 exhibits a slightly higher b/a ratio than FeAl50, but above 10 GPa, FeAl50 surpasses FeAl25. This crossover likely reflects composition-dependent differences in how fixed Fe and Al substitutions influence octahedral tilting and lattice distortions under compression. Although Fe and Al remain on the A- and B- sites, respectively, variations in cation concentration can modify local bonding environments and polyhedral distortions, which in turn affect axial tilting. This could explain why FeAl25 initially displays greater tilt along the b-axis, while FeAl50 develops more pronounced tilting as pressure increases.

Consistent with these structural changes, the unit-cell volume (V_0) increases systematically from pure $MgSiO_3$ to FeAl25 and FeAl50 (Table 5.2), reflecting the coupled substitution of larger Fe^{3+} and Al^{3+} cations into the Mg^{2+} and Si^{4+} sites, respectively (Figure 1.3) (Pauling, 1928; Karki *et al.*, 1997; Criniti *et al.*, 2021). This lattice expansion is accompanied by a decrease in bulk modulus (K_0) with increasing Fe content, indicating enhanced compressibility. However, Al alone has been shown to increase K_0 (Andrault *et al.*, 2001), highlighting the complex interplay between Fe and Al effects on bridgmanite elasticity.

Previous *ab initio* and experimental studies similarly report greater compressibility and lower sound velocities for Fe-bearing bridgmanite at ambient pressure, while at lower mantle pressures, pressure-induced stiffening can result in higher shear velocities compared to the Mg end-member (Warren and Ackland, 1996; Warren *et al.*, 1998; Andrault *et al.*, 2001; Kurnosov *et al.*, 2017; Garnero and McNamara, 2008; Hummer and Fei, 2012). For example, Kurnosov *et al.* (2017) demonstrated via high-pressure Brillouin spectroscopy and X-ray diffraction that coupled Fe-Al substitution reduces both bulk and shear moduli, similar to the effect observed with Al substitution alone.

Despite reductions in K_0, the pressure derivative K_0' remains relatively constant (3.90-3.99) across all compositions studied, suggesting that while Fe-Al substitutions lower incompressibility at pressures below 20 GPa, the rate of stiffening with increasing pressure is largely unaffected. A slight increase in K_0' for FeAl25 and FeAl50 at higher pressures (>20 GPa) indicates modest structural stiffening under compression due to these substitutions.

5.5 Conclusion

In this chapter, *ab initio* DFT calculations at 0 K and pressures from 0 to 140 GPa for three bridgmanite compositions, $MgSiO_3$, FeAl25 and FeAl50 were presented to assess how iron and aluminum substitutions influence structural and elastic behavior. The results showed that introducing Fe and Al cause a systematic increase in the initial volume (V_0) and a decrease in bulk modulus (K_0). This indicates that Fe-Al-bearing bridgmanite is more compressible than the Mg end-member without lattice dynamics. All compositions show anisotropic compression, with the a-axis generally most compressible and the b-axis the least compressible. FeAl50, in particular, increases this anisotropy, as seen in the rising b/a and c/a axial ratios. Although Fe-Al-bearing compositions are softer at lower pressures, the pressure derivative (K_0') remains nearly constant for all compositions, suggesting only minor changes in how compressibility evolves with increasing pressure at 0 K. Overall, these results demonstrate that even moderate amounts of Fe and Al can significantly affect bridgmanite's density, stiffness, and anisotropy at mantle pressures. The DFT calculations presented here provide an essential foundation for incorporating temperature effects. To extend this work, thermodynamic modeling was performed, as detailed in Chapter 6.

Chapter 6

Ab Initio Density Functional Theory Calculations on Fe-Al-Bridgmanite from 0 to 140 GPa at High-Temperatures

6.1 Introduction

Despite its importance, direct experimental constraints on bridgmanite's high-temperature behavior remain limited at true lower-mantle conditions (Zhang *et al.*, 2016). These thermal effects introduce anharmonicity, thermal expansion, and temperature-dependent elastic softening that cannot be captured by static, 0 K first-principles calculations alone (see Chapter 5).

Prior work has shown that anharmonic contributions and thermoelastic parameters are essential for realistic models of lower-mantle minerals (Anderson, 1967; Anderson and Sumino, 1980; Stacey and Isaak, 2003; Shukla *et al.*, 2016; Zhang *et al.*, 2016). Anharmonic contributions refer to deviations from the ideal harmonic approximation, in which atomic vibrations are assumed to be perfectly periodic and independent of vibration amplitude. In real materials, atomic interactions become increasingly non-linear at elevated temperatures, leading to phonon–phonon interactions that modify vibrational frequencies, thermal expansion, heat capacity, and elastic properties. These anharmonic effects become especially significant in lower-mantle minerals at high pressure and temperature, where they influence the thermal equation of state and seismic velocities. Additionally, iron-bearing bridgmanite can exhibit spin transitions that are temperature-sensitive, further modifying its physical behavior (Lin *et al.*, 2013, 2007; Badro *et al.*, 2004; Catalli *et al.*, 2009a, 2011). Extending density functional theory (DFT) to finite temperature-dependent properties obtained from lattice-dynamics calculations carried out within the quasi-harmonic approximation (QHA)

allows for the prediction of how bridgmanite's bulk modulus, shear modulus, and thermal expansion evolve under combined high-P–T conditions (Wan *et al.*, 2024; Baroni *et al.*, 2001).

Experimental studies provide essential constraints on high-temperature mineral properties but face inherent limitations as discussed in Chapters 3 and 4. Experiments utilizing *in situ* X-ray diffraction and Brillouin spectroscopy techniques have improved our understanding of bridgmanite's thermal equation of state and elastic properties, yet high-pressure, high-temperature data remain scarce, particularly for compositions containing iron and aluminum (Sinogeikin *et al.*, 2004) (see Chapter 3). Computational methods, particularly density functional theory combined with the quasi-harmonic approximation (QHA), offer a powerful approach to bridging this gap by systematically predicting how temperature affects bridgmanite's stability, elasticity, and thermodynamic properties (Baroni *et al.*, 2001).

This chapter builds on the 0 K calculations presented in Chapter 5 by incorporating temperature effects through thermodynamic calculations using CASTEP 20.11 (Clark *et al.*, 2005). The same compositions of pure $MgSiO_3$, $(Mg_{0.75}, Fe_{0.25})(Si_{0.75}, Al_{0.25})O_3$ (FeAl25), and $(Mg_{0.50}, Fe_{0.50})(Si_{0.50}, Al_{0.50})O_3$ (FeAl50), are investigated from 0 to 140 GPa and from 300 to 3600 K, allowing for direct comparison between static and temperature-dependent behaviors. These calculations provide information into how bridgmanite's bulk modulus, shear modulus, and thermal expansion evolve at temperatures relevant to the lower mantle.

6.2 Methods

All ground-state (0 K) total-energy and geometry-optimization calculations for $MgSiO_3$, FeAl25, and FeAl50 (see Chapter 5) are carried out using CASTEP 20.11 (Clark *et al.*, 2005) with the PBEsol exchange-correlation functional (Perdew *et al.*, 2008). The plane-wave cut-off energy

and Monkhorst-Pack k-point grid are increased stepwise until the change in any Hellmann-Feynman force fell below the convergence threshold listed in Table B.10 (Monkhorst and Pack, 1976). For each composition, a series of calculations is performed in which the unit-cell volume is fixed to specific values corresponding to pressures from 0 to 140 GPa, and the internal atomic positions are relaxed at each volume. This yields the relationship between total energy and volume, $E_{\mathrm{static}}(V)$, known as the "cold curve," which describes the material's static (0 K) equation of state. The most stable Fe/Al arrangement is determined by testing all symmetry-distinct configurations in the orthorhombic perovskite cell and selecting the structure with lowest enthalpy and residual forces (Tables B.8, B.9).

Within the quasi-harmonic approximation (QHA) implemented in CASTEP (Dove, 1993; Poirier, 2000; Clark *et al.*, 2005), the Helmholtz free energy $F(V,T)$ is expressed as the sum of the static 0 K energy $E_{\mathrm{static}}(V)$ and a vibrational term $F_{\mathrm{vib}}(V,T)$ that depends on volume and temperature (Equation 6.1) (Wallace and Callen, 1972):

$$F(V,T) = E_{\mathrm{static}}(V) + F_{\mathrm{vib}}(V,T). \tag{6.1}$$

In this framework, the crystal lattice is treated as a collection of quantized vibrations (phonons), whose frequencies change systematically with compression or expansion of the crystal. Unlike molecular dynamics (MD), which simulates atomic motion directly in time and naturally includes anharmonic effects, the QHA is a lattice-dynamics approach based on small atomic displacements around equilibrium positions. It captures the temperature dependence of thermodynamic and elastic properties by allowing phonon frequencies to vary with volume, while still neglecting explicit phonon–phonon interactions. Thus, QHA provides a computationally efficient way to approximate

finite-temperature behavior without requiring long MD trajectories or empirical potentials.

For a harmonic crystal, the vibrational contribution is given by Equation 6.2, where each phonon mode contributes a zero-point energy $\frac{1}{2}\hbar\omega$ plus a temperature-dependent term.

$$F_{\mathrm{vib}}(V,T) = k_{\mathrm{B}}T \sum_{\mathbf{q},j} w_{\mathbf{q}} \, \ln\!\left[2\sinh\!\left(\tfrac{\hbar\omega_j(\mathbf{q},V)}{2k_{\mathrm{B}}T}\right)\right]. \tag{6.2}$$

Phonon frequencies $\omega_j(\mathbf{q}, V)$ are obtained from the force-constant matrix $\Phi_{\alpha\beta}(l\kappa, l'\kappa') = \partial F_\alpha(l\kappa)/\partial u_\beta(l'\kappa')$, which represents the derivative of the Hellmann–Feynman force with respect to an atomic displacement (i.e., the second derivative of the total energy). Since CASTEP provides analytic Hellmann–Feynman forces but not their derivatives, Φ is constructed by finite-difference differentiation. Each symmetry-unique atom in the 20-atom $Pnma$ cell is displaced by ± 0.0053 Å, forces are recorded, and central differences are formed. The displacement magnitude (0.0053 Å) corresponds to the default value used in CASTEP and falls within the standard range (0.005–0.02 Å) adopted in finite-difference phonon calculations. This amplitude is small enough to remain within the harmonic regime where forces vary linearly with displacement, yet large enough to exceed numerical noise in the computed Hellmann–Feynman forces. Fourier transformation of Φ yielded $\omega_j(\mathbf{q}, V)$ at 16 symmetry-reduced points of a $4 \times 4 \times 4$ Monkhorst–Pack q-mesh (Parlinski *et al.*, 1997; Refson *et al.*, 2021).

Equations 6.1 and 6.2 are evaluated for temperatures from 300 K to 3600 K in 300 K increments. At each temperature, the calculated $F(V,T)$ values are fitted with a third-order Birch-Murnaghan equation of state (Birch, 1947). The minimum of this fit yields the equilibrium volume $V_0(T)$, and its curvature yields the isothermal bulk modulus $K_0(T)$ and its pressure derivative $K_0'(T)$. Repeating this process over the full (V,T) grid produces a smooth P-V-T surface, from

which density, thermal expansion $\alpha(T)$, Grüneisen parameter $\gamma(T)$, heat capacity $C_P(T)$ and thermal pressure $P_{\mathrm{th}}(T)$ are derived following the standard QHA formalism (Wallace and Callen, 1972; Poirier, 2000).

Chapter 5 shows that static calculations converge at cut-off energies of 800-900 eV with k-meshes of $4 \times 4 \times 3$ or finer, resulting in energy and force changes well below default CASTEP thresholds. Phonon calculations utilized the $4 \times 4 \times 4$ q-mesh (63 irreducible points), producing smooth phonon densities of states and well-resolved frequencies. These calculations from Chapter 5 are used as the basis for the lattice-dynamics calculations using QHA in this chapter.

6.3 Results

Bridgmanite compositions of pure $\mathrm{MgSiO_3}$, FeAl25, and FeAl50 are modeled using the QHA to determine their complete thermal equations of state (Poirier, 2000). For each composition, static 0 K DFT energies (i.e., $E_{\mathrm{static}}(V) = E_0$ at 0 K) from Chapter 5 are combined with volume-dependent phonon spectra to construct the Helmholtz free energy surface $F(V, T)$ on a dense grid relevant to lower-mantle conditions.

All compositions are presented using a second-order Birch–Murnaghan (BM2) equation of state (EOS) with $K_0' = 4$. In principle, a third-order Birch–Murnaghan (BM3) fit in terms of Helmholtz free energy is given by Equation 6.3 where F_0 is the Helmholtz free energy at the reference volume V_0, K_0 is the isothermal bulk modulus at V_0, K_0' is its pressure derivative, and V_0 is the equilibrium volume.

$$F(V) \;=\; F_0 \;+\; \frac{9\,V_0\,K_0}{16}\left\{\left[\left(\frac{V_0}{V}\right)^{2/3} - 1\right]^3 K_0' \;+\; \left[\left(\frac{V_0}{V}\right)^{2/3} - 1\right]^2\left[6 \;-\; 4\left(\frac{V_0}{V}\right)^{2/3}\right]\right\}, \quad (6.3)$$

Equation 6.3 includes F_0 as an extra fitting parameter compared to the usual pressure–volume (P–V) form of BM3, which only fits V_0, K_0, and K_0'. In preliminary third-order Birch–Murnaghan (BM3) fits, K_0 and K_0' were strongly correlated and K_0' was poorly identified, leading to unstable solutions and occasional non-physical optima. This behavior arises because our DFT datasets sample a relatively narrow strain range around V_0, so the curvature (K_0) and its pressure derivative (K_0') are not independently constrained. In such cases, the objective function develops a shallow valley in the (K_0, K_0') plane, and small numerical noise can steer the optimizer toward false minima.

To avoid over-parameterization and ensure consistent, physically sensible results across compositions, we therefore adopt the second-order Birch–Murnaghan form (BM2) with K_0' fixed to 4. Fixing $K_0' = 4$ is standard practice when the data do not constrain K_0' and is justified by finite-strain theory near ambient strain. It stabilizes the fit, yields K_0 values that are robust to modest changes in the assumed K_0', and provides residuals that are statistically indistinguishable from the unstable BM3 fits on these datasets.

$MgSiO_3$

To extract thermodynamic parameters, the $F(V, T)$ surface for $MgSiO_3$ is fit at each temperature using BM2-EOS with $K_0' = 4$ held fixed. Figure A.20 using BM3-EOS is also included for reference.

Figure 6.1 and Table 6.1 summarize the temperature dependence of fitted properties derived from the BM2-EOS. The equilibrium volume V_0 (Figure 6.1a) increases from 166.67 $Å^3$ at 0 K to 189.56 $Å^3$ at 3600 K, consistent with thermal expansion. While E_0 appears to decrease with increasing temperature, this trend does not represent the actual thermodynamic internal energy (which increases with thermal excitation). Instead, the decrease in $E_0(T)$ reflects a shift in the

equilibrium volume $V_0(T)$ to larger values due to thermal expansion. This trend reflects the effect of thermal expansion on the free energy surface: although the actual thermodynamic internal energy increases with temperature, the energy minimum of $F(V,T)$ shifts to larger volumes, resulting in a fitted $E_0(T)$ that decreases in magnitude. Because the BM2-EOS fits trace the minimum of the free energy surface at each T, the fitted $E_0(T)$ effectively tracks the energy of the relaxed structure under zero pressure by incorporating thermal pressure and volume effects rather than the accumulated thermal energy itself.

The isothermal bulk modulus $K_0(T)$ (Figure 6.1c) decreases steadily with increasing temperature, from 232.58 GPa at 0 K to 149.46 GPa at 3600 K. This softening of the material with temperature reflects thermal expansion and anharmonic vibrational effects that reduce the resistance of the lattice to compression.

Table 6.1: BM2-EOS polynomial fits to the temperature-dependent properties of $MgSiO_3$: Reference volume $V_0(T)$; Internal energy $E_0(T)$; Isothermal bulk modulus $K_0(T)$; Pressure derivative of bulk modulus $K_0'(T)$.

Property	**Polynomial Expression**
$V_0(T)$	$-6.94\times10^{-17}T^5+7.38\times10^{-13}T^4+-2.91\times10^{-9}T^3+5.78\times10^{-6}T^2+5.23\times10^{-4}T^1+1.67\times10^{2}$
$E_0(T)$	$3.38\times10^{-17}T^5+-4.20\times10^{-13}T^4+2.17\times10^{-9}T^3+-7.04\times10^{-6}T^2+9.58\times10^{-4}T^1+-1.27\times10^{4}$
$K_0(T)$	$3.65\times10^{-16}T^5+-3.80\times10^{-12}T^4+1.48\times10^{-8}T^3+-2.57\times10^{-5}T^2+-5.87\times10^{-3}T^1+2.33\times10^{2}$
$K_0'(T)$	4.0 (fixed)

Figure 6.2 presents the Helmholtz free energy $F(V,T)$ as a function of volume (top) and pressure-volume isotherms (bottom) for $MgSiO_3$ bridgmanite across the 0–3600 K range. The $F(V,T)$ curves exhibit well-defined minima that systematically shift to larger volumes with increasing temperature. The pressure-volume isotherms display a corresponding increase in equilibrium volume at zero pressure. The isotherms also become progressively shallower with temperature. At fixed volume, the pressure increases with temperature, and the spacing between

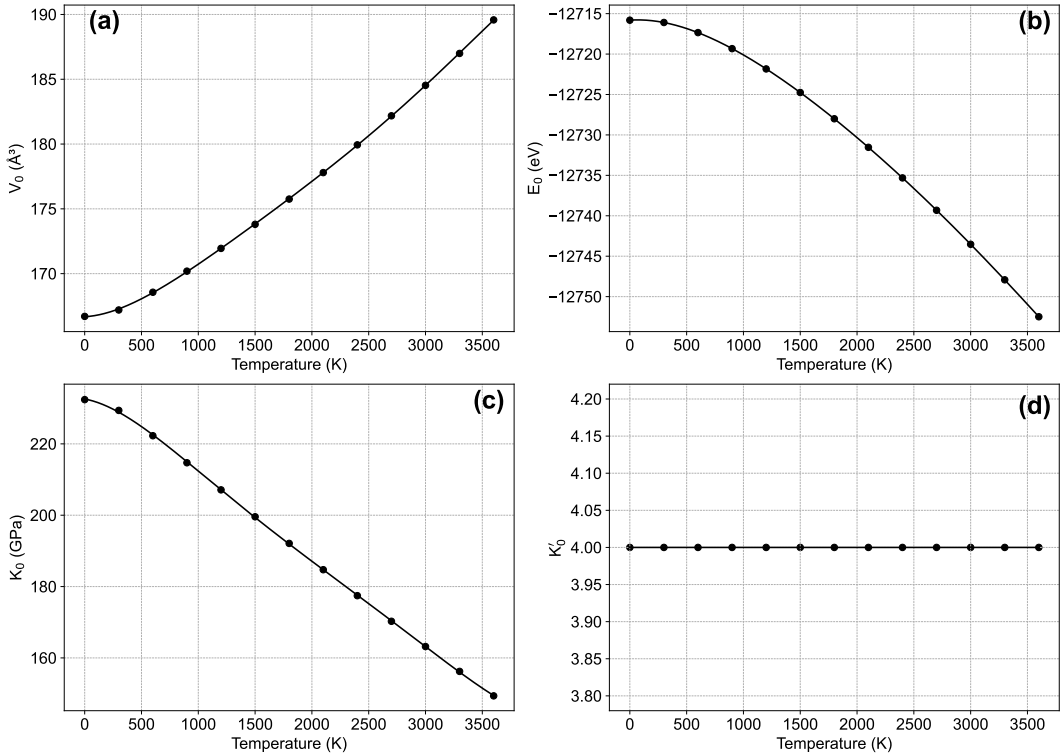

Figure 6.1: Temperature dependence of thermodynamic and elastic parameters for $\mathrm{MgSiO_3}$ bridgmanite at 0 GPa based on *ab initio* DFT calculations. (a) The unit cell volume (V_0) shows nonlinear thermal expansion with increasing temperature. (b) The static internal energy (E_0) becomes less negative with temperature, reflecting the contribution of thermal energy. (c) The isothermal bulk modulus (K_0) decreases linearly as temperature increases, consistent with the thermal softening of bridgmanite. (d) The first pressure derivative of the bulk modulus (K_0) set constant to 4 for the studied temperature range.

isotherms grows with temperature.

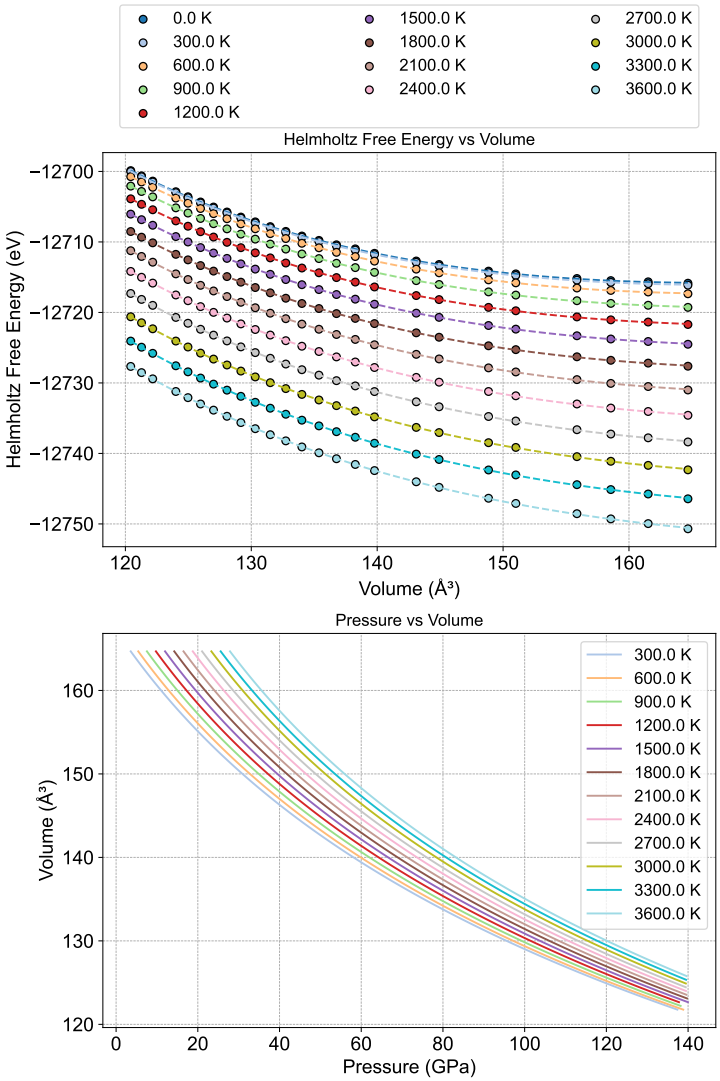

Figure 6.2: Helmholtz free energy and pressure-volume behavior of $MgSiO_3$ bridgmanite from 0–3600 K. (Top) Helmholtz free energy $F(V,T)$ (eV) as a function of volume, showing the temperature-dependent shift in the energy minimum to larger volumes due to thermal expansion. (Bottom) Pressure-volume isotherms derived from second-order Birch-Murnaghan fits to $F(V,T)$ surfaces.

FeAl25

The thermodynamic properties of Fe-Al-bearing bridgmanite with $Fe_{0.25}$ and $Al_{0.25}$ substitution (FeAl25) are extracted by fitting the Helmholtz free energy surface $F(V,T)$ at each temperature

using a BM2-EOS ($K_0' = 4$). Figure 6.3 and Table 6.2 summarize the temperature-dependent behavior of fitted BM2-EOS parameters.

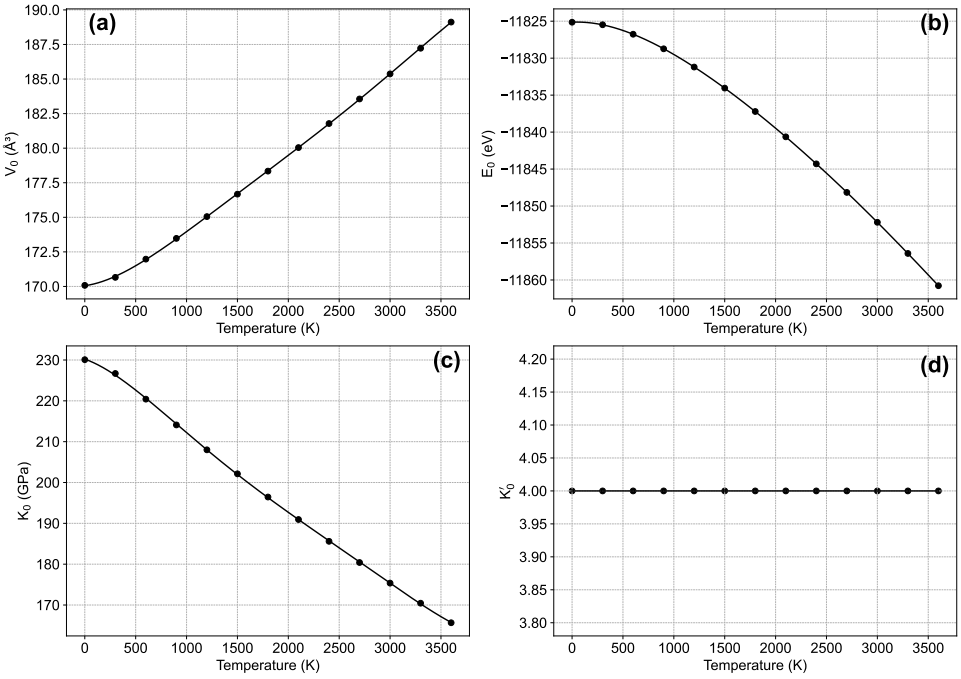

Figure 6.3: Temperature dependence of thermodynamic and elastic parameters for FeAl25 bridgmanite based on *ab initio* DFT calculations. (a) The unit cell volume (V_0) shows nonlinear thermal expansion with increasing temperature. (b) The static internal energy (E_0) becomes less negative with temperature, reflecting the contribution of thermal energy. (c) The isothermal bulk modulus (K_0) decreases linearly as temperature increases, consistent with the thermal softening of bridgmanite. (d) The first pressure derivative of the bulk modulus (K_0) set constant to 4 for the studied temperature range.

Table 6.2: BM2-EOS polynomial fits to the temperature-dependent properties of FeAl25 bridgmanite: $V_0(T)$, $E_0(T)$, $K_0(T)$, and fixed K_0'.

Property	**Polynomial Expression**
$V_0(T)$	$-6.15 \times 10^{-17}T^5 + 6.49 \times 10^{-13}T^4 - 2.56 \times 10^{-9}T^3 + 4.88 \times 10^{-6}T^2 + 1.01 \times 10^{-3}T + 1.70 \times 10^{2}$
$E_0(T)$	$3.38 \times 10^{-17}T^5 - 4.16 \times 10^{-13}T^4 + 2.13 \times 10^{-9}T^3 - 6.78 \times 10^{-6}T^2 + 6.77 \times 10^{-4}T - 1.18 \times 10^{4}$
$K_0(T)$	$2.84 \times 10^{-16}T^5 - 2.92 \times 10^{-12}T^4 + 1.10 \times 10^{-8}T^3 - 1.76 \times 10^{-5}T^2 - 8.77 \times 10^{-3}T + 2.30 \times 10^{2}$
$K_0'(T)$	4.0 (fixed)

The equilibrium volume $V_0(T)$ increases from 170.05 Å^3 at 0 K to 189.10 Å^3 at 3600 K,

consistent with positive thermal expansion (Figure 6.3a). The static internal energy $E_0(T)$ becomes progressively less negative with increasing temperature (Figure 6.3b). The isothermal bulk modulus $K_0(T)$ shows a marked decrease from ∼230.22 GPa at 0 K to ∼165.74 GPa at 3600 K (Figure 6.3c), reflecting thermal softening of the FeAl25 structure. The fixed pressure derivative $K_0' = 4$ (Figure 6.3d) is retained across the full temperature range.

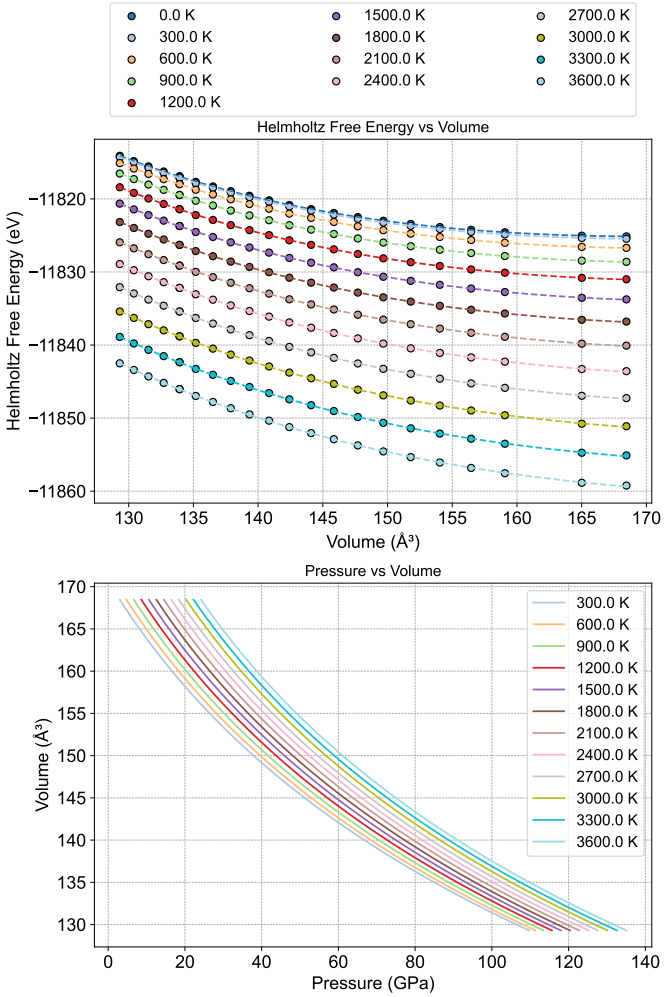

Figure 6.4: Helmholtz free energy and pressure-volume behavior of FeAl25 bridgmanite from 0–3600 K. (Top) $F(V, T)$ curves showing shift in equilibrium volume with temperature. (Bottom) Pressure-volume isotherms derived from BM2 fits to the free energy surface.

Figure 6.4 presents the Helmholtz free energy curves $F(V, T)$ and derived pressure-volume

isotherms from 0 to 3600 K. The minimum of $F(V,T)$ shifts to larger volumes with increasing temperature, capturing the effect of thermal expansion. The corresponding pressure-volume curves reveal lower stiffness (shallower slopes) at higher temperatures and a clear increase in equilibrium volume with temperature.

FeAl50

The thermodynamic properties of FeAl50 bridgmanite ($Fe_{0.5}Al_{0.5}$) are determined by fitting the Helmholtz free energy surface $F(V,T)$ at each temperature using a second-order Birch-Murnaghan equation of state (BM2) with the pressure derivative $K_0' = 4$ held fixed. Figure 6.5 and Table 6.3 present the fitted temperature-dependent parameters derived from these EOS fits.

The equilibrium volume $V_0(T)$ increases from 172.70 Å^3 at 0 K to 195.11 Å^3 at 3600 K (Figure 6.5a). The static internal energy $E_0(T)$ decreases monotonically with increasing temperature (Figure 6.5b). The isothermal bulk modulus $K_0(T)$ decreases from 227.33 GPa at 0 K to 157.84 GPa at 3600 K (Figure 6.5c). The pressure derivative $K_0'(T)$ is held fixed at 4.0 across all temperatures (Figure 6.5d).

Table 6.3: BM2-EOS polynomial fits to the temperature-dependent properties of FeAl50 bridgmanite: $V_0(T)$, $E_0(T)$, $K_0(T)$, and fixed K_0'.

Property	**Polynomial Expression**
$V_0(T)$	$-6.71\times10^{-17}T^5+7.09\times10^{-13}T^4+-2.78\times10^{-9}T^3+5.42\times10^{-6}T^2+1.07\times10^{-3}T^1+1.73\times10^{2}$
$E_0(T)$	$3.89\times10^{-17}T^5+-4.72\times10^{-13}T^4+2.37\times10^{-9}T^3+-7.39\times10^{-6}T^2+7.47\times10^{-4}T^1+-1.09\times10^{4}$
$K_0(T)$	$3.17\times10^{-16}T^5+-3.27\times10^{-12}T^4+1.25\times10^{-8}T^3+-2.08\times10^{-5}T^2+-9.22\times10^{-3}T^1+2.27\times10^{2}$
$K_0'(T)$	4.0 (fixed)

Figure 6.6 shows the Helmholtz free energy curves $F(V,T)$ and the corresponding pressure-volume isotherms from 0 to 3600 K. The free energy curves exhibit volume shifts with increasing

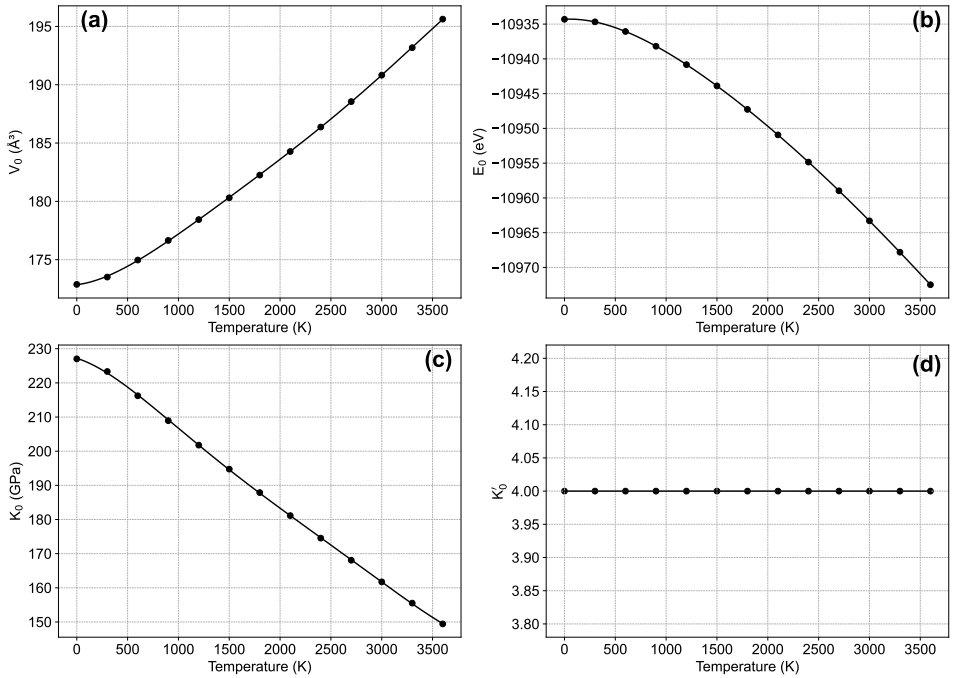

Figure 6.5: Temperature dependence of thermodynamic and elastic parameters for FeAl50 bridgmanite based on *ab initio* DFT calculations. (a) The unit cell volume (V_0) shows nonlinear thermal expansion with increasing temperature. (b) The static internal energy (E_0) becomes less negative with temperature, reflecting the contribution of thermal energy. (c) The isothermal bulk modulus (K_0) decreases linearly as temperature increases, consistent with the thermal softening of bridgmanite. (d) The first pressure derivative of the bulk modulus (K_0) set constant to 4 for the studied temperature range.

temperature, and the associated isotherms show changes in compressibility as a function of T.

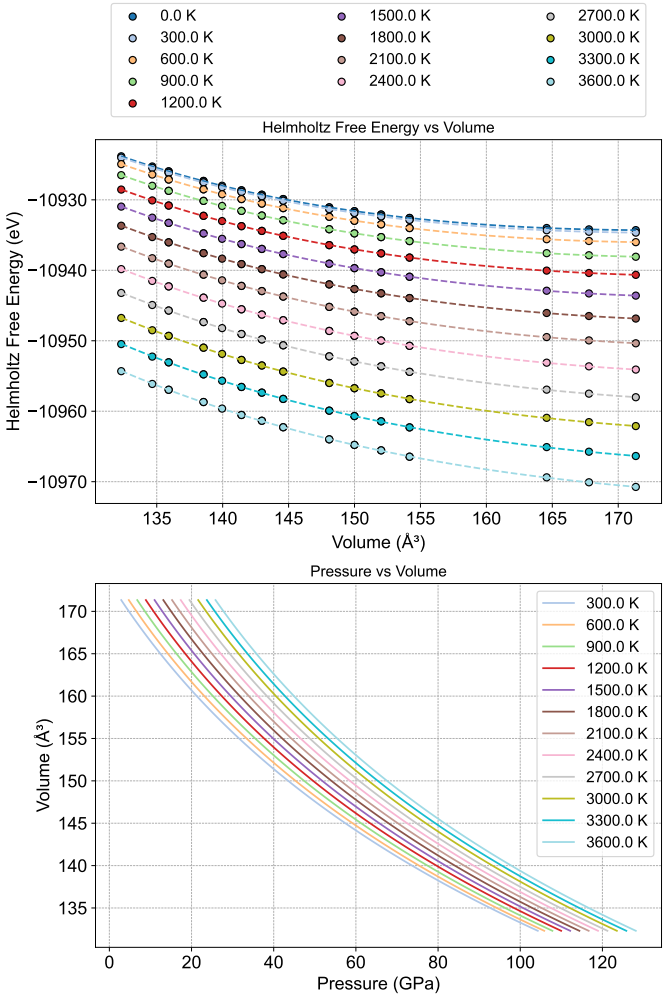

Figure 6.6: Helmholtz free energy and pressure-volume behavior of FeAl50 bridgmanite from 0–3600 K. (Top) $F(V, T)$ curves showing shift in equilibrium volume with temperature. (Bottom) Pressure-volume isotherms derived from BM2 fits to the free energy surface.

6.3.1 Thermoelastic Properties Across Compositions

To quantitatively compare the thermal behavior of bridgmanite across $MgSiO_3$, FeAl25, and FeAl50 compositions, the temperature dependence of the bulk modulus (K_0), thermal expansion coefficient (α), Grüneisen parameter (γ), and thermal pressure (P_{th}) are fitted using empirically constrained, thermodynamically consistent models commonly applied in mantle geophysics to describe anharmonic behavior (Anderson, 1995; Stixrude and Lithgow-Bertelloni, 2005; Boehler,

2000). These functional forms are widely used in lower mantle modeling and high-pressure mineral physics, where they successfully capture anharmonic vibrational effects and thermal trends over broad temperature ranges. These models describe first-order anharmonic trends observed over the full temperature range up to 3600 K. Results are shown in Figure 6.7 and summarized in Table 6.4.

Table 6.4: Fitted parameters and 1σ uncertainties for thermoelastic properties as functions of temperature T. Units: K_0 in GPa, α in 1/K, P_{th} in GPa.

Property	Fit Function	Composition	Fit Parameters (with 1σ)
$K_0(T)$	$aT + b$	$MgSiO_3$	$a = -0.0240 \pm 0.0003$, $b = 235.33 \pm 0.6$
		FeAl25	$a = -0.0184 \pm 0.0002$, $b = 230.54 \pm 0.5$
		FeAl50	$a = -0.0222 \pm 0.0002$, $b = 228.49 \pm 0.4$
$\alpha(T)$	$a(1 - e^{-bT}) + c$	$MgSiO_3$	$a = 3.84\times10^{-5} \pm 2\times10^{-6}$, $b = 0.00153 \pm 0.0002$, $c = 4.29\times10^{-6} \pm 2\times10^{-6}$
		FeAl25	$a = 2.66\times10^{-5} \pm 9\times10^{-7}$, $b = 0.00252 \pm 0.0002$, $c = 5.82\times10^{-6} \pm 8\times10^{-7}$
		FeAl50	$a = 3.26\times10^{-5} \pm 2\times10^{-6}$, $b = 0.00179 \pm 0.0002$, $c = 6.77\times10^{-6} \pm 1\times10^{-6}$
$\gamma(T)$	$a(1 - e^{-bT}) + c$	$MgSiO_3$	$a = 6.90 \pm 0.2$, $b = 0.00281 \pm 0.0002$, $c = 0.65 \pm 0.2$
		FeAl25	$a = 5.04 \pm 0.3$, $b = 0.00365 \pm 0.0005$, $c = 1.29 \pm 0.3$
		FeAl50	$a = 5.90 \pm 0.2$, $b = 0.00318 \pm 0.0003$, $c = 1.35 \pm 0.2$
$P_{\mathrm{th}}(T)$	$aT + b$	$MgSiO_3$	$a = 6.73\times10^{-3} \pm 1\times10^{-4}$, $b = -1.009 \pm 0.2$
		FeAl25	$a = 5.72\times10^{-3} \pm 7\times10^{-5}$, $b = -0.515 \pm 0.1$
		FeAl50	$a = 6.35\times10^{-3} \pm 8\times10^{-5}$, $b = -0.705 \pm 0.2$

The isothermal bulk modulus K_0 decreases approximately linearly with increasing temperature for all compositions at 0 GPa (Figure 6.7a). $MgSiO_3$ maintains the highest K_0 at all temperatures, while FeAl50 exhibits the lowest values and the steepest rate of thermal softening, consistent with enhanced anharmonic effects in more Fe-Al-rich bridgmanite. Interestingly, FeAl25 shows a stiffer response than both $MgSiO_3$ and FeAl50 across the entire temperature range, suggesting a non-monotonic relationship between Fe-Al content and compressibility. The thermal expansion coefficient α shows a characteristic saturation trend at high T. FeAl25 has the lowest asymptotic α values, consistent with its higher stiffness. The Grüneisen parameter γ also saturates with increasing temperature. Its value increases systematically with Fe/Al content, which may influence thermodynamic properties under deep mantle conditions. Thermal pressure P_{th} increases linearly with temperature, with larger slopes in Fe-Al-rich compositions reflecting greater

vibrational energy contributions.

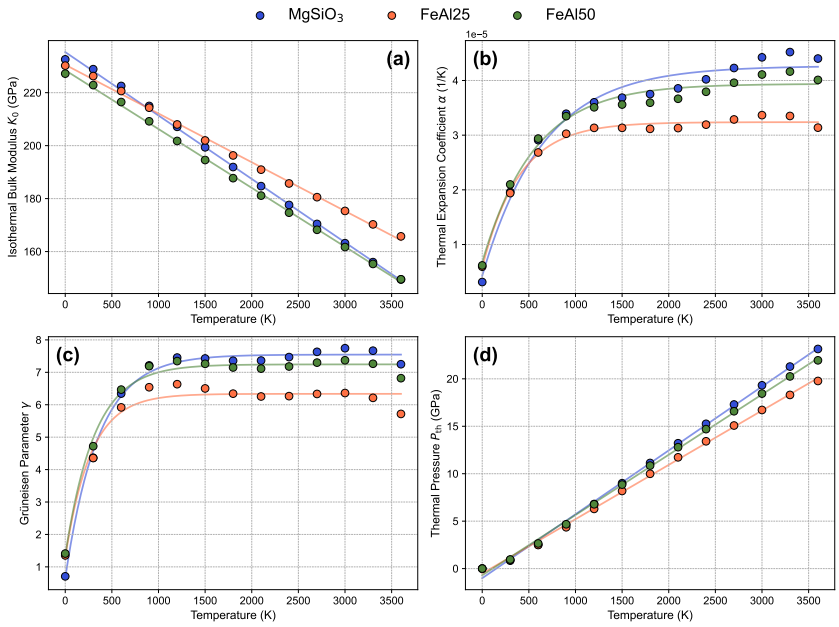

Figure 6.7: Temperature dependence of thermoelastic properties of bridgmanite at 0 GPa. (a) isothermal bulk modulus K_0, (b) thermal expansion coefficient α, (c) Grüneisen parameter γ, and (d) thermal pressure P_{th}. Markers show DFT results and curves show fitted models.

6.4 Discussion

Building on the QHA-DFT thermodynamic calculations for pure $MgSiO_3$, FeAl25 and FeAl50 bridgmanite over 0-140 GPa and 300-3600 K, several key insights emerge regarding their high-temperature behavior under lower-mantle conditions. All three compositions exhibit the expected thermal softening, bulk moduli $K(T)$ decrease monotonically with T, but the magnitude and rate of this softening vary markedly with Fe-Al content (Fig. 6.7).

6.4.1 Bulk Modulus and Thermal Softening

At 0 GPa and 0 K the bulk moduli (K) of all three compositions decreased with increasing pressure. However with increasing temperature, distinct differences emerged when comparing the

bulk moduli, thermal expansion coefficient (α), Grüneisen parameter (γ), and the rate at which the bulk modulus softened. $MgSiO_3$ exhibited the largest thermal expansion and the most consistent decrease in bulk modulus with temperature, indicating relatively uniform anharmonic behavior and minimal variation in structural rigidity. In contrast, FeAl50, which contains higher Fe and Al substitution than FeAl25, showed the largest softening in K above $\sim$1000 K, suggesting that these substitutions can significantly influence the material's high-temperature response depending on their atomic positions and bond lengths. FeAl25 displayed a unique behavior, maintaining a higher bulk modulus throughout the temperature range than both $MgSiO_3$ and FeAl50, suggesting that its structural rigidity is greater, potentially due to the specific cation arrangement (Figure 6.7).

6.4.2 Thermal Expansion and Grüneisen Parameter Behavior

To quantify the temperature-dependent thermal properties of bridgmanite, the thermal expansion coefficient (α), Grüneisen parameter (γ), and other thermoelastic parameters were derived. The results of these fits are summarized in Table 6.4 and presented in Figure 6.7. These quantities capture the anharmonic behavior and the coupling between vibrational modes and thermal pressure as a function of temperature, providing insight into the thermodynamic behavior of $MgSiO_3$, FeAl25, and FeAl50 under high-pressure, high-temperature conditions relevant to the lower mantle.

The thermal expansion coefficient (α) and Grüneisen parameter (γ) both increase with temperature, though the magnitude and curvature of these trends vary among compositions. For $MgSiO_3$ and FeAl50, $\alpha(T)$ and $\gamma(T)$ rise steeply at low temperature and gradually approach near-constant values above 1500–2000 K, consistent with the partial saturation of vibrational contributions at high T. In contrast, FeAl25 shows a more subdued, nearly linear increase in both parameters, reflecting a weaker temperature dependence overall. This behavior likely arises

from the increased stiffness of the FeAl25 lattice, where stronger Fe–O and Al–O bonds restrict vibrational amplitude and reduce lattice anharmonicity, resulting in limited thermal expansion and vibrational coupling. Such compositional stiffening effects are consistent with the higher bulk modulus (K_0) observed for FeAl25.

The thermal expansion coefficient α increases with temperature as the atoms vibrate more intensely, leading to overall lattice expansion. Similarly, the Grüneisen parameter, which reflects the coupling between vibrational modes and thermal pressure, also increases with temperature, indicating stronger vibrational coupling under thermal excitation. Among the compositions, $\mathrm{MgSiO_3}$ exhibits the highest asymptotic α values but the lowest γ values, suggesting a relatively harmonic lattice with lower sensitivity to thermal pressure. FeAl25 maintains the lowest α across all temperatures, consistent with its rigidity, whereas FeAl50 shows intermediate α and γ values, indicating a moderate degree of anharmonicity and thermal expansion.

Overall, $\gamma(T)$ increases systematically with Fe–Al substitution, with FeAl50 exhibiting the highest values. This trend reflects enhanced anharmonic effects and stronger coupling between vibrational modes and thermal pressure in Fe–Al-bearing bridgmanite, particularly at higher substitution levels. Since γ governs how efficiently thermal energy is converted into thermal pressure, higher γ values amplify the thermal pressure contribution for a given temperature. This leads to steeper adiabatic gradients and greater thermal expansivity at depth, which modify buoyancy forces and density contrasts within the mantle. As a result, regions rich in Fe–Al-bearing bridgmanite with elevated γ are predicted to exhibit altered convective behavior and seismic velocity structure compared to closer $\mathrm{MgSiO_3}$-dominated assemblages. These effects collectively influence the dynamics and thermal evolution of the Earth's deep interior.

At high temperatures, the partial saturation of α and γ observed in $\mathrm{MgSiO_3}$ and FeAl50 is

consistent with quasi-harmonic approximation predictions, where most phonon modes are thermally populated. However, the systematic compositional differences among the three bridgmanite compositions indicate that Fe and Al substitutions alter the phonon density of states and modify the degree of lattice anharmonicity, influencing the thermoelastic response under lower-mantle conditions.

6.4.3 Cation Arrangement and Bulk Modulus in Fe-Al-Bridgmanite

The anomalously high isothermal bulk modulus (K_0) observed in FeAl25, when compared to both pure $\mathrm{MgSiO_3}$ and the more heavily substituted FeAl50 at temperatures above $\sim$1000 K, can be attributed to the specific cation configuration present in the FeAl25 structure. In this composition, a single Fe^{3+} and Al^{3+} pair occupy adjacent A- and B-site positions (A_4 and B_4) with a moderate interatomic separation (see Tables 5.1 and B.8). This proximity between Fe^{3+} and Al^{3+} enables localized charge compensation, where the trivalent cations balance each other within a shared polyhedral neighborhood. The close pairing of Fe and Al cations minimizes electrostatic repulsion and avoids the need for extended lattice distortions to screen the substituted charges. This configuration is energetically favorable, as it allows the perovskite framework to maintain its local bonding topology with minimal distortion. As a result, the mechanical rigidity of the structure is preserved, contributing to the higher K_0 observed in FeAl25.

In contrast, the FeAl50 structure features two Fe-Al substitution pairs that are more geometrically dispersed in comparison to the arrangement in FeAl25 (see Table B.8 and Table B.9). These larger separations deviate from the idealized local coordination necessary for effective charge compensation. Such a configuration can disrupt the cooperative tilting of the perovskite octahedra and affect the connectivity of the lattice, resulting in increased local strain (Woodward, 1997). This

strain leads to the necessity for long-range lattice relaxation to stabilize the structure, and as a result, the overall bulk modulus is reduced. The higher amount of Fe-Al substitution in FeAl50 increases lattice distortion and site disorder, reducing structural coherence and contributing to elastic softening (Boström and Kieslich, 2021). This softening is consistent with the decreased bulk modulus observed in FeAl50, highlighting the influence of cation arrangement on the material's overall mechanical properties.

This interpretation aligns with prior DFT studies, which have demonstrated that defect clustering, charge distribution, and local elastic relaxations significantly impact the elastic properties of bridgmanite and other perovskites (Dou *et al.*, 2025; Zhang *et al.*, 2025; Oganov *et al.*, 2001b; Muir and Brodholt, 2020; Geng and Jónsson, 2019; Criniti *et al.*, 2024; Karki and Crain, 1998; Wan *et al.*, 2024; Grüninger *et al.*, 2019; Baktash *et al.*, 2021; Criniti *et al.*, 2021). These studies have shown that such local structural variations can substantially affect the overall mechanical response of perovskites under high-pressure conditions.

These findings emphasize that the spatial arrangement of substituted cations, rather than their concentration alone, plays a critical role in controlling the thermoelastic response of Fe-Al-bearing bridgmanite. In cases like FeAl25, where Fe^{3+} and Al^{3+} form well-paired substitutions in the crystal lattice, the material accommodates defects with minimal energetic cost, maintaining structural integrity and high bulk modulus. However, in FeAl50, the more dispersed Fe-Al substitutions generate structural distortions, leading to reduced lattice efficiency and softening of the material. This suggests that localized cation configurations should be considered when modeling the thermoelastic properties of complex silicate perovskites in deep Earth conditions.

6.4.4 Implications for Lower Mantle Modeling

The compositional and thermal trends observed in Fe-Al-bearing bridgmanite have significant implications for the interpretation of the thermoelastic behavior of the lower mantle. As the most abundant mineral in Earth's interior, bridgmanite plays a central role in mantle dynamics, influencing seismic wave propagation, density profiles, and thermal conductivity (Murakami *et al.*, 2012; Irifune *et al.*, 2010; Lin *et al.*, 2013; Huang *et al.*, 2021b; Zhu *et al.*, 2020). Its thermal properties govern mantle behavior under extreme conditions of temperature and pressure, directly impacting seismic observations and the interpretation of mantle convection.

The observed increase in the thermal expansion coefficient (α) and Grüneisen parameter (γ) with Fe-Al content indicates that Fe and Al substitutions enhance the anharmonicity of the crystal lattice, especially at high temperatures (Wolf *et al.*, 2015; Shukla *et al.*, 2016). This results in greater sensitivity to thermal excitation and an increase in thermal pressure, which can lower the material's elastic stiffness (Fu *et al.*, 2023; Nakatsuka *et al.*, 2021; Edmund *et al.*, 2024). Specifically, Nakatsuka *et al.* (2021) noted that Fe and Al substitution induces structural distortions due to the tilting of BO_6 octahedra, which enhances the flexibility of A-O bonds, further reducing elastic stiffness under thermal excitation and pressure.

These changes in thermoelastic properties significantly affect the behavior of Fe-rich regions within the mantle. The reduction in elastic stiffness in Fe-rich bridgmanite compositions, such as FeAl50, could contribute to lower seismic wave velocities in Fe-enriched mantle regions (Kurnosov *et al.*, 2017; Zhang, 2022; Wolf *et al.*, 2015). This observation aligns with earlier studies showing that Fe incorporation in mantle minerals alters seismic properties, notably reducing both shear (V_S) and compressional (V_P) wave velocities. For example, Fu *et al.* (2023) observed that V_S and

V_P increase monotonically with pressure up to 82 GPa, but remain lower than in pure $MgSiO_3$ bridgmanite. Similarly, Fukui *et al.* (2016) found that Fe and Al substitution in bridgmanite decreases elastic moduli and seismic velocities, a trend attributed to increased anharmonicity in the crystal lattice.

Moreover, the enhanced anharmonicity in Fe–Al-bearing bridgmanite likely contributes to reduced thermal conductivity in these regions, primarily by increasing phonon scattering and reducing the mean free path of heat-carrying lattice vibrations (Hsieh *et al.*, 2017, 2018; Murakami *et al.*, 2022). Lower thermal conductivity limits the efficiency of conductive heat transport, causing steeper local temperature gradients and promoting stronger thermal buoyancy contrasts. As a result, heat is more effectively transferred by advection rather than conduction, potentially enhancing convective vigor in Fe-rich mantle domains. Conversely, the reduced ability to dissipate heat can also stabilize long-lived thermal anomalies by slowing lateral heat diffusion. Fe enrichment further modifies the density and thermal expansivity of bridgmanite, producing compositional and thermal buoyancy contrasts that influence the stability and ascent of thermal plumes, thereby affecting the geometry and dynamics of large-scale mantle convection (Ballmer *et al.*, 2017; Beier *et al.*, 2008; Guerrero *et al.*, 2024; Le Bars and Davaille, 2004).

The non-linear dependence of the bulk modulus (K_0) on composition, with FeAl25 exhibiting unexpectedly high stiffness relative to both pure $MgSiO_3$ and FeAl50, highlights the critical role of local atomic configurations in determining macroscopic elasticity. This finding challenges the assumption that Fe and Al substitution always results in a softer material. In the case of FeAl25, the more compact Fe-Al cation arrangement preserves higher rigidity, suggesting that moderate Fe-Al substitutions may not necessarily weaken the mantle (Huang *et al.*, 2021a; Fu *et al.*, 2023; Criniti *et al.*, 2024; Ballaran *et al.*, 2012). These results emphasize the need for more nuanced,

compositionally resolved models of mantle behavior, accounting for the effects of local cation arrangements and atomic environments rather than relying on simple linear mixing models for solid solutions (Zhang *et al.*, 2016; Criniti *et al.*, 2024).

Variations in the Grüneisen parameter (γ) across compositions have important implications for the calculation of adiabatic gradients and thermal expansivity in mantle convection models (Oganov *et al.*, 2001a). Higher γ values, as seen in FeAl50, lead to greater thermal pressure contributions, enhancing the material's ability to store thermal energy (Edmund *et al.*, 2024; Criniti *et al.*, 2024). This, in turn, affects the buoyancy and stability of Fe-rich heterogeneities, influencing the dynamics of thermal plumes. In contrast, the lower γ in $\mathrm{MgSiO_3}$ indicates a more harmonic vibrational response with reduced sensitivity to temperature-induced elastic softening. As a result, regions with lower Fe/Al content are expected to show more stable thermoelastic behavior with temperature, whereas Fe–Al-rich domains are more prone to thermally driven changes in compressibility and structure that can influence mantle convection dynamics (Wang, 2000; Wang *et al.*, 1991; Christensen, 1995; Huang *et al.*, 2021b; Oganov and Ono, 2004).

These compositional variations in thermal properties also have implications for seismic tomography. Seismic wave speeds are highly sensitive to changes in elastic moduli and density profiles, and the compositional sensitivity observed in this study suggests that Fe/Al variations at depth could contribute to seismic anomalies in the lower mantle (Schouten *et al.*, 2024; Zhang *et al.*, 2016; Fu *et al.*, 2018; Vilella *et al.*, 2021; Huang *et al.*, 2021a; Wu, 2016). Specifically, the reduced K_0 and elevated γ in FeAl50 would manifest as slower bulk-sound velocities (V_ϕ), detectable in seismic tomography studies. Conversely, the higher stiffness of FeAl25 could produce comparatively higher seismic velocities in regions with moderate Fe–Al enrichment, potentially explaining some velocity anomalies observed in the mid-to-lower mantle (Zeng and Sasselov, 2013;

Fu *et al.*, 2018; Garnero *et al.*, 2016). Direct computation of V_P and V_S requires the shear modulus G and is beyond the scope of this study. However, since $V_\phi = \sqrt{K_S/\rho}$ with $K_S = K_T(1 + \alpha\gamma T)$, the higher stiffness of FeAl25 relative to FeAl50 implies a correspondingly higher bulk-sound speed under comparable conditions. These effects are particularly relevant when interpreting structures such as Large Low Shear Velocity Provinces (LLSVPs) and chemically distinct mantle domains, which remain a focal point of debate in the geophysical community (Garnero *et al.*, 2016; Vilella *et al.*, 2021).

Finally, the fitted equations of state (EOS) parameters and their temperature dependence provide a quantitative foundation for incorporating compositional variability into 1-D and 3-D geophysical models (Connolly, 2009; Fichtner *et al.*, 2024).

6.5 Conclusion

This study examined the high-temperature behavior of Fe-Al-bearing bridgmanite, using *ab initio* density functional theory (DFT) calculations combined with lattice dynamics within the quasi-harmonic approximation (QHA) covering a temperature range of 0–3600 K and pressures up to 140 GPa.

The calculations show temperature-dependent trends in the thermoelastic properties of pure $\mathrm{MgSiO_3}$, FeAl25, and FeAl50 bridgmanite compositions. Notably, the bulk modulus (K_0) of all compositions decreases with increasing temperature, reflecting thermal softening, yet significant differences emerge in the rate of softening. FeAl50 exhibits the largest softening, indicative of a greater impact from the Fe-Al substitutions on the material's rigidity. In contrast, FeAl25 maintains a higher bulk modulus across all temperatures above $\sim$1000 K, suggesting that the specific cation arrangement in this composition enhances the stability of the structure.

The thermal expansion coefficient (α) and Grüneisen parameter (γ) exhibit characteristic behavior with increasing temperature, showing saturation trends. These parameters capture the material's anharmonicity and its response to thermal excitation. $MgSiO_3$ exhibits the highest values for both α and γ, suggesting a more anharmonic vibrational response.

In contrast, FeAl25 shows the lowest values for both α and γ, indicating that the substitution of Fe and Al into their specific atomic positions reduces the material's thermal expansion and anharmonicity. This is likely due to the more compact and well-ordered Fe-Al cation arrangement in FeAl25, which limits the flexibility of the crystal lattice and suppresses the thermal vibrations. As a result, FeAl25 displays lower thermal expansion and anharmonicity compared to both $MgSiO_3$ and FeAl50. FeAl50 lies between the two, exhibiting intermediate values due to its higher degree of Fe-Al substitution, which leads to increased anharmonic effects.

Furthermore, the research highlights significant implications for seismic tomography and mantle dynamics. Variations in K_0 and γ across compositions suggest that Fe/Al variations at depth could contribute to seismic anomalies in the lower mantle. The lower K_0 and higher γ in FeAl50 suggest that even high Fe-rich regions may exhibit slower seismic velocities, while the higher stiffness of FeAl25 could lead to unexpectedly higher velocities in regions with moderate Fe-Al content. These effects are used for interpreting structures such as Large Low Shear Velocity Provinces (LLSVPs), where seismic tomography reveals lower shear wave velocities (V_S) and slower compressional wave velocities (V_P) in these regions compared to surrounding mantle areas. The variations in K_0 and γ suggest that compositional differences in Fe-Al-bearing bridgmanite could contribute to these velocity anomalies, with regions of lower K_0 and higher γ corresponding to slower seismic velocities in Fe-rich domains within the LLSVPs.

Chapter 7
Discussion

This discussion chapter brings together the three complementary approaches: (i) laboratory measurements that capture the messiness of real samples (Chapters 3 and 4), (ii) first-principles calculations that isolate intrinsic lattice physics (Chapters 5 and 6), and (iii) thermodynamic forward models that embed both into whole-mantle petrology presented in the discussion.

High-pressure X-ray diffraction (XRD) experiments (Chapters 3 and 4) probe sintered polycrystalline samples in a diamond-anvil cell, capturing the full complexity of real materials. Grain boundaries, residual stresses, minor secondary phases and local compositional heterogeneity can all influence the measured bulk modulus (K_0). These extrinsic features can mask or even invert the intrinsic elastic trends expected from ideal crystals, making the experimental K_0 appear stiffer than the zero-Kelvin lattice prediction.

By contrast, density functional theory (DFT) (Chapters 5 and 6) treats a perfectly periodic bridgmanite crystal at 0 K, using the PBEsol exchange–correlation functional to isolate intrinsic lattice physics. In this idealized framework, Fe-Al substitution produces a systematic softening (i.e. a decrease in K_0). However, fixed cation ordering and the neglect of temperature-induced cation redistribution or spin transitions that can happen during laser-heating mean that DFT calculations cannot capture extrinsic microstructural or thermal effects.

The different approaches of DFT and XRD give rise to divergent compressibility trends in this work. At ambient temperature, DFT predicts that increasing Fe and Al content lowers K_0, consistent with the expected softening effect of Fe–Al substitution. In contrast, the experimental data show a more complex, non-monotonic behavior, with moderate substitution levels (e.g.,

FeAl25) appear anomalously stiff relative to both $MgSiO_3$ and FeAl50, even though higher Fe–Al contents ultimately lead to lower K_0. Thus, while the stiffening is not linear with composition, the overall experimental trend still places Fe-rich bridgmanite as stiffer than the pure $MgSiO_3$ endmember, differing from the DFT prediction of continuous softening.

Several factors contribute to this discrepancy. First, the DFT calculations are idealized, sampling only the most stable atomic configurations within a 20-atom cell and neglecting possible site disorder and microstructural effects that may occur in experiments and within the lower mantle. They also omit the effects of the high-spin to low-spin (HS-LS) transition of Fe^{2+} and Fe^{3+}, since Fe and Al are fixed to specific sites, which can significantly influence compressibility at lower-mantle pressures (Lin *et al.*, 2013; Catalli *et al.*, 2011). Additionally, DFT relies on the quasi-harmonic approximation (QHA) to include thermal effects, which assumes that anharmonic contributions are captured indirectly through volume-dependent phonons. In contrast, the experimental data inherently include these anharmonic and defect-related effects, as well as grain-boundary compliance and potential residual stress within polycrystalline samples. Taken together, these methodological differences, composition, spin state, thermal treatment, and microstructural effects likely explain much of the observed divergence between experimental and computational results.

To consider the high Fe-Al-bridgmanite compositions into a mantle-scale context (including the influence of Ca), Perple_X is employed to minimize Gibbs free energy across 25–140 GPa and 300–4000 K. Bulk compositions were derived from a pyrolitic mantle reference model (Anderson, 1989), with additional variants adjusted to reproduce the Fe–Al bridgmanite compositions (F1A1 and F3A3) characterized in Chapter 3. Using the `stx21ver.dat` database from Stixrude and Lithgow-Bertelloni (2022), these forward models generate phase assemblages, densities and seismic velocities that synthesize the softening from DFT with the stiffening evident in XRD.

By weaving together experimental measurements, first-principles predictions and thermodynamic modeling, this chapter demonstrates how intrinsic lattice physics and real-sample effects combine within realistic lower-mantle mineralogy, and why both experimental and computational approaches are essential for accurate predictions of mantle elasticity and seismic structure.

7.1 Experimental and Theoretical Constraints on Fe-Al-Bridgmanite

The experimental and computational work presented in this thesis are integrated to analyze iron and aluminum substitution in bridgmanite (Figure 7.1, Table 7.1).

The sintered polycrystalline bridgmanite samples used in Chapter 3 were synthesized at 1650°C (1923 K) for five minutes in a large-volume press prior to XRD experiments (see Section 2.1). Although short, even brief heating can promote cation redistribution or local ordering, affecting mechanical properties. Fe and Al may segregate or concentrate at specific lattice sites (see Figures A.4 and A.5 SEM-EDS), producing a microstructure more resistant to compression than the homogeneous distribution that can be explicitly chosen in DFT.

DFT calculations indicate that the bulk modulus (K_0) decreases with increasing Fe and Al substitution at ambient conditions (0 GPa and 300 K), suggesting that these substitutions lead to an inherently softer (more compressible) lattice. From an ideal-crystal perspective, incorporating these cations weakens the bonding network, likely through changes in bond lengths and strengths that reduce resistance to compression (Bosi, 2014).

From 0 to 1000 K, DFT results consistently show lower K_0 as Fe and Al content increases. However, above 1000 K FeAl25 becomes stiffer than both $MgSiO_3$ and FeAl50. This reversal arises from the specific Fe/Al arrangement in FeAl25 (see Chapter 6.4.3), indicating that substitution and thermal effects together induce fundamental changes in bonding. By obtaining finite temperature-dependent properties obtained from lattice-dynamics calculations carried out within the quasi-

harmonic approximation, results no longer follow the simple softening trend that emerges at 300 K.

The high-pressure XRD measurements collected at 300 K on sintered polycrystalline bridgmanite presented in Chapter 3, demonstrate that K_0 increases non-monotonically with Fe-Al substitution when analyzed using higher-order equations of state (BM3 and Vinet) (Figure 3.14, Table 3.7). Although this appears inconsistent with the softening predicted by the presented DFT calculations and other experimental studies (Ballaran *et al.*, 2012; Catalli *et al.*, 2011), pre-synthesized sintered polycrystalline samples can exhibit structural or chemical heterogeneities, compositional gradients, or minor secondary phases that result in apparent stiffening, differing from single-crystal and powder samples. Substitution driven changes in grain size or boundary character may also alter how grains pack and transfer stress, overshadowing the computational trend below 1000 K.

Table 7.1: [
Fitted EOS parameters from experimental and DFT data with literature.]Fitted EOS parameters for experimental (XRD) and computational (DFT) data with reference literature, as reported in Chapter 3 and Chapter 6.

Composition		V_0 (Å^3)	K_0 (GPa)	K_0'	**Study**
$MgSiO_3$	(DFT)	162.37	257	3.93	This Study
M-brg	(XRD)	162.30(40)	254(20)	4.49(99)	This Study
$MgSiO_3$	(XRD)	162.36(5)	251(1)	4.12(10)	Ballaran *et al.* (2012)
F1A1-brg	(XRD)	164.84(37)	304(14)	3.05(30)	This Study
$Mg_{0.88}Fe_{0.13}Si_{0.88}Al_{0.11}O_3$ (F1A1-brg)	(XRD)	165.04(39)	243(8)	3.72(20)	Catalli *et al.* (2011)
FeAl25	(DFT)	168.50	238	3.97	This Study
F3A3-brg, Ne	(XRD)	168.42(30)	287(12)	3.13(40)	This Study
F3A3-brg, Ar	(XRD)	168.87(28)	288(13)	2.72(40)	This Study
FeAl50	(DFT)	171.35	234	3.97	This Study

The opposing compressibility trends between experiments and DFT highlight the complex interplay of intrinsic chemical effects and extrinsic sample-related factors, and the difficulty of capturing both within a single model.

For example, rapid quenching after heating can trap residual stresses and distortions in

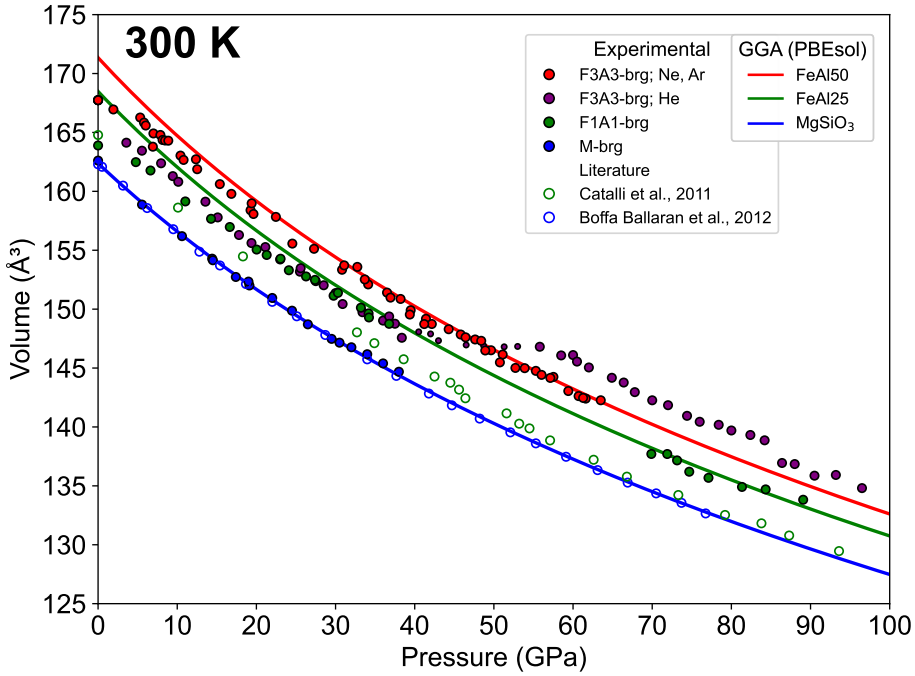

Figure 7.1: Pressure-Volume relationship for 300 K data of Fe-Al-bearing bridgmanite. Experimental data (symbols) are shown for F3A3-brg (red and purple), F1A1-brg (green), and M-brg (blue), with literature data from Catalli *et al.* (2011) and Ballaran *et al.* (2012). Third-order Birch-Murnaghan Equation of State (EOS) curves (solid lines) are fitted to computational (DFT: GGA-PBEsol) composition results for FeAl50 (red), FeAl25 (green), and $MgSiO_3$ (blue). A pressure correction was applied to the DFT data for all three datasets. The pressure offset (P_offset) was calculated by evaluating the Birch-Murnaghan EOS at the reference volume at 300 K for each dataset. The resulting pressure value was subtracted from the DFT-calculated pressures, ensuring that the corrected pressures yield 0 GPa at the experimental volume, thus aligning the DFT results with the experimental data.

the lattice, as atoms lack time to reach thermodynamic equilibrium (Prevey, 1986). These non-equilibrium features, frozen into the structure, increase resistance to compression during subsequent DAC experiments. By contrast, annealing prior to XRD relieves residual stresses and allows cations to migrate toward equilibrium sites, sharpening XRD peaks and yielding K_0 values that better reflect intrinsic lattice properties (Wang *et al.*, 2022). Annealing "heals" grain-boundary defects, reduces strain fields, and, after slow cooling, yields a bulk modulus in closer agreement with DFT predictions (Dorfman *et al.*, 2012). Laser heating in a DAC can nearly eliminate macroscopic deviatoric stress during heating, but upon thermal quench stress is reintroduced (Kavner and Duffy, 2001). Consequently, pre-compression annealing may not completely remove non-equilibrium stresses, and some discrepancy with DFT may still persist.

During high-pressure XRD at 300 K (Chapter 3), applied pressure itself can drive changes in cation distribution and bonding that lower-temperature DFT models do not capture. At these conditions, new cation arrangements may become thermodynamically favorable, but atomic diffusion is sluggish at 300 K, preventing equilibration. As a result, the sample may remain in a metastable configuration that appears stiffer than its fully equilibrated state. Slight non-hydrostatic stress and residual strain in the DAC can also bias K_0 upward when fitting EOS to limited pressure-volume data.

Defects in synthesized samples, such as cation vacancies or minor phases, can change the overall rigidity measured by XRD. Slight deviations from ideal stoichiometry, combined with variations in the local coordination of Fe and Al, may lead to mixed oxidation or spin states that are not fully captured by simplified computational models. Details of the iron spin transition are discussed in Chapter 1.3.2, and the limitations of the DFT approach in representing these effects arising from the fixed atomic placement of Fe and Al in the model are outlined in Chapter 5.1.

Slight differences in pressure-transmitting medium, calibration procedures, and diamond quality (e.g., new vs. used diamonds)could also influence the apparent K_0 in the F3A3-brg sample (Chapter 3). Additionally, data in Chapter 4 on majorite highlight that some phases may persist despite metastability, resulting in elastic properties that differ from equilibrium mantle values.

A pressure correction was applied to the DFT data for all three datasets presented in Chapter 6. This correction is justified because energy derivatives at a given volume (i.e., compressibility) are generally more reliable in DFT than the precise equilibrium volume (Vanderbilt, 1998; Oganov *et al.*, 2001a). The the pressure offset was calculated, P_{offset}, by evaluating the Birch-Murnaghan EOS the experimental reference volume for $MgSiO_3$ (300 K) and applied to Fe-Al composition. Subtracting this offset from the DFT pressures ensures that the corrected DFT curve passes through 0 GPa at the experimental volume, allowing direct comparison with XRD results.

Furthermore, standard DFT functionals typically assume idealized conditions and may under represent strong-correlation effects that arise in Fe-bearing systems with certain atomic arrangements (e.g., FeAl25; Figure 5.8). Additionally, the DFT models presented in Chapters 5 and 6, placed all iron as Fe^{3+} on the A-site, despite Fe^{3+} preferentially occupying B-site octahedra (see Chapter 1.3.2). These site occupancies can influence the bonding environments and, thus, impact the bulk modulus and thermoelastic properties under mantle conditions.

7.2 Thermodynamic Modeling using Perple_X

As previously noted throughout this thesis, bridgmanite dominates the lower mantle and its behavior depends on Fe and Al. Accordingly, phase stability and seismic properties must be evaluated for bulk lower-mantle compositions.

Stable mineral assemblages were calculated with Perple_X (Middelburg, 2024) by minimizing

Gibbs free energy on a two-dimensional pressure–temperature (P–T) grid. Pressures range from 25 to 140 GPa and temperatures from 300 to 4000 K, encompassing lower-mantle conditions and the P–T space of the X-ray diffraction and DFT experiments reported here.

Calculations employed the `stx21ver.dat` thermodynamic database, the update of `stx11ver.dat` (Stixrude and Lithgow-Bertelloni, 2011, 2022), whose bridgmanite solution model explicitly includes coupled Fe–Al substitution. A closed, anhydrous system was assumed, with volatile-bearing components omitted to mimic nominally dry lower-mantle conditions (Evans *et al.*, 2014; Ohtani, 2005, 2020; Bouhifd *et al.*, 2013; Racioppi *et al.*, 2023; Wang and Xu, 2024).

Bulk compositions were based on the pyrolite reference of Anderson (1989) and adjusted to reflect the higher Fe and Al contents measured in the experimental bridgmanite samples (Chapter 3; Table 7.2). This strategy ties the modeled phase relations directly to the experimental starting materials and permits Perple_X to predict the composition of the bridgmanite that forms at each P–T point. Because lower-mantle bridgmanite commonly deviates in Fe-Mg-Al ratios from its bulk source, both the input bulk and the calculated bridgmanite compositions are reported.

A potential objection is that Perple_X draws thermoelastic parameters from a community database rather than from the new elasticity measurements presented in this thesis. Two considerations mitigate this concern. First, the current `stx21ver.dat` release does not yet support composition-dependent elastic moduli, so the new bridgmanite bulk modulus (K) cannot be incorporated without modifying the source code and retuning the entire dataset. Second, retaining the standard dataset allows mismatches between predicted and measured moduli to be attributed unambiguously to specific database entries, clarifying where future revisions are required.

In this sense, the present modeling constitutes a forward testbed that illustrates how strongly phase equilibria and seismic velocities are expected to shift once forthcoming database updates

integrate the new Fe–Al elasticity constraints.

The oxide totals in Table 7.2 are slightly below 100 wt% due to minor analytical artifacts such as surface topography, beam interaction effects, or sample contamination during EPMA analysis. The original analytical ratios were retained rather than renormalized to preserve the measured Fe-Al proportions. Perple_X internally rescales each bulk composition to 100 wt% while keeping CaO fixed, as CaO is essential for stabilizing Ca-perovskite and garnet.

Running the models after the experimental and DFT chapters enables a direct, composition-matched comparison between intrinsic lattice behavior (DFT), sample-specific extrinsic effects (XRD), and whole-rock phase equilibria (this section).

Table 7.2: Bulk oxide compositions (wt%) entered into Perple_X. Totals are not normalized, and therefore, sum to $>$ 100 wt% because trace-element fractions are retained. Perple_X rescales each bulk to 100 wt% internally while preserving CaO, which is required to stabilize Ca-perovskite and garnet.

Oxide (wt%)	**Pyrolite**	**F1A1-PX**	**F3A3-PX**
SiO_2	45.10	52.10	39.05
MgO	38.10	31.89	25.44
FeO	7.80	11.64	21.34
Al_2O_3	4.60	4.38	14.19
CaO	3.10	3.00	3.00

At each grid point the calculation returns (i) the modal proportions of all stable phases and (ii) the composition of every phase. The bridgmanite chemistry predicted at depth can therefore be compared directly with the experimental and *ab initio* compositions presented earlier in this thesis. Using these compositions allows the new elasticity data to expose, rather than mask, any shortcomings of the current thermodynamic database. Such iterative coupling of experiment, *ab initio* theory, and forward phase-equilibrium modeling forms the foundation for next-generation models of the lower mantle.

Phase Stability Trends

In the pyrolite model (Anderson, 1989), the dominant assemblage in the lower mantle consists of bridgmanite, ferropericlase, and Ca-perovskite (Pv + Wus + Ca-Pv; Figure 7.2a). With increasing Fe-Al content in the bulk compositions, bridgmanite becomes more stable across P–V space.

In the F3A3-PX model, ferropericlase is notably suppressed over most of the P–T range (Figure 7.2c), while F1A1-PX retains a broader stability field for ferropericlase (Figure 7.2b). Part of this difference may reflect the slightly higher CaO content in F3A3-PX, as each mole of CaO consumes a mole of SiO_2 to form Ca-silicates, leaving less Si available for bridgmanite and less (Mg,Fe)O to form ferropericlase. Nevertheless, the overall trend that Fe- and Al-rich compositions stabilize bridgmanite at the expense of ferropericlase remains consistent with experimental observations and supports the hypothesis that Fe-Al-rich bridgmanite may dominate in certain deep-mantle regions (Kurnosov *et al.*, 2017; Ismailova *et al.*, 2016; Dorfman and Duffy, 2014; Wang *et al.*, 2021).

The modal abundance of bridgmanite is sensitive to the bulk Fe-Al content. Figures 7.3a and 7.3b show the bridgmanite mode fraction for the F1A1-PX and F3A3-PX models, respectively. In the F1A1-PX system, bridgmanite dominates over most of the P–T space, often exceeding 80–90%, with a modest decrease around 60–80 GPa at intermediate temperatures.

In contrast, the F3A3-PX model exhibits an extended region of reduced bridgmanite (Pv) stability between 60 and 80 GPa, primarily reflecting its higher FeO and Al_2O_3 contents. The difference map in Figure 7.4 shows that F1A1-PX generally maintains a higher bridgmanite mode across most P–T conditions, whereas F3A3-PX stabilizes more bridgmanite only at higher temperatures near 120 GPa. These results suggest that F3A3 does not represent a compositionally stable single-phase bridgmanite, but rather one that partitions into multiple coexisting phases under

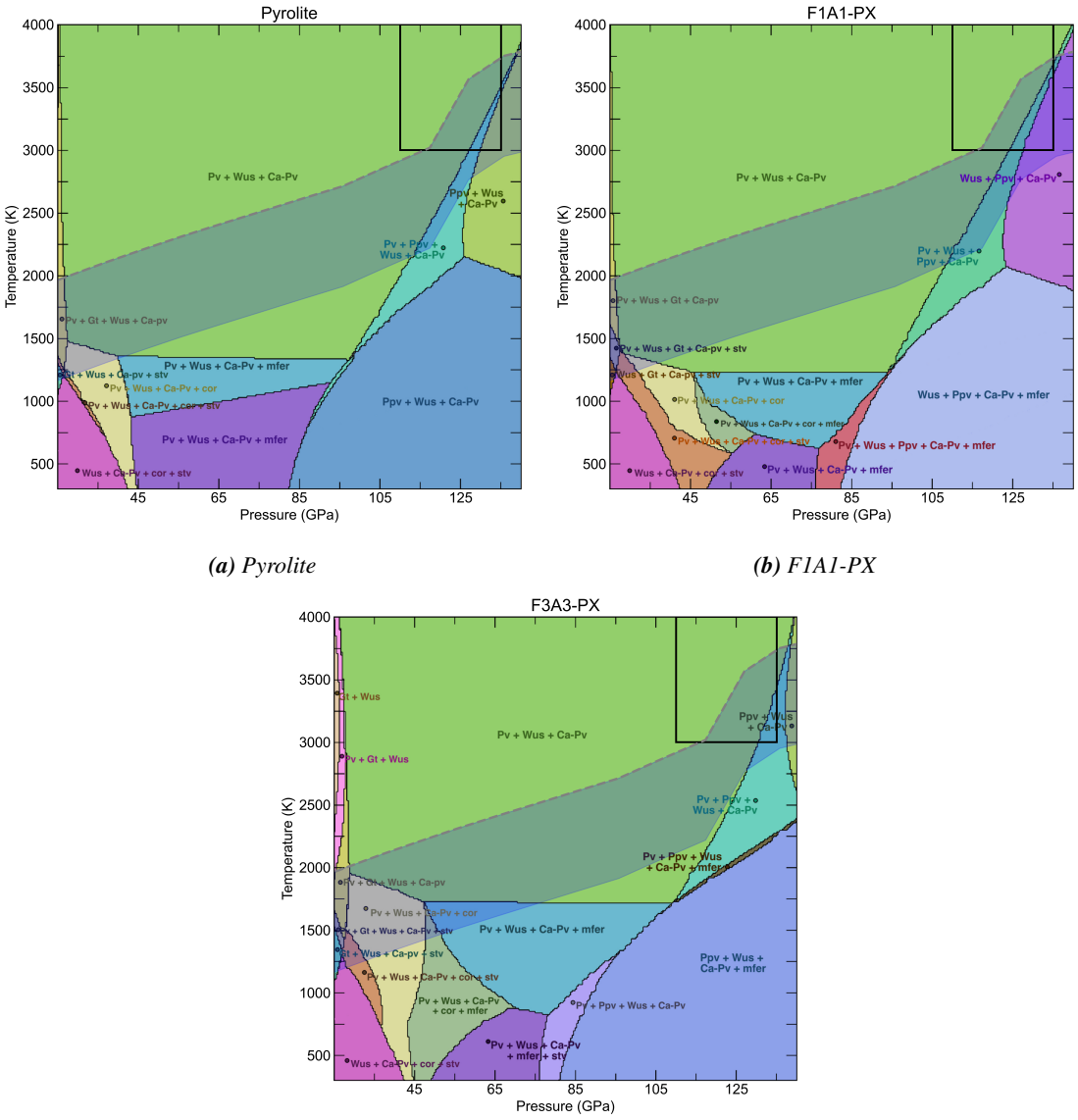

(a) *Pyrolite*

(b) *F1A1-PX*

(c) *F3A3-brg*

Figure 7.2: Phase assemblage diagrams for (a) Pyrolite, (b) F1A1-PX, and (c) F3A3-PX compositions (Table 7.2), modeled with Perple_X. The dashed gray line marks a lower mantle geotherm, and the shaded region below represents colder slab conditions. The black box indicates a pressure-temperature window consistent with large low shear velocity provinces (LLSVPs). Bridgmanite (Pv) dominates across all models, while increased Fe and Al shift the Pv-Ppv boundary to lower temperatures and produce more complex multiphase fields in the transition zone and upper lower mantle.

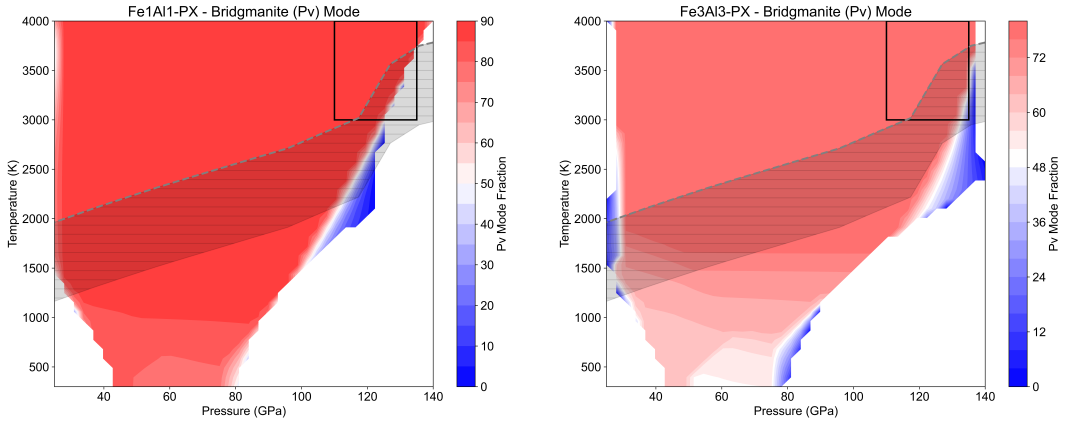

(a) *F1A1-PX* ***(b)*** *F3A3-PX*

Figure 7.3: Perple_X thermodynamic modeling of bridgmanite (Pv) mode color maps showing the modal abundance of bridgmanite over a range of temperatures (up to 4000 K) and pressures (up to 140 GPa). Warmer colors (red) correspond to higher bridgmanite mode, while cooler colors (blue) denote a lower fraction. (a) Bridgmanite (Pv) mode for F1A1-PX, (b) Bridgmanite (Pv) mode for the F3A3-PX. The black boxes highlight regions of notable phase behavior, illustrating how compositional variations influence the stability of bridgmanite in the mantle-like pressure-temperature regime.

most mantle conditions.

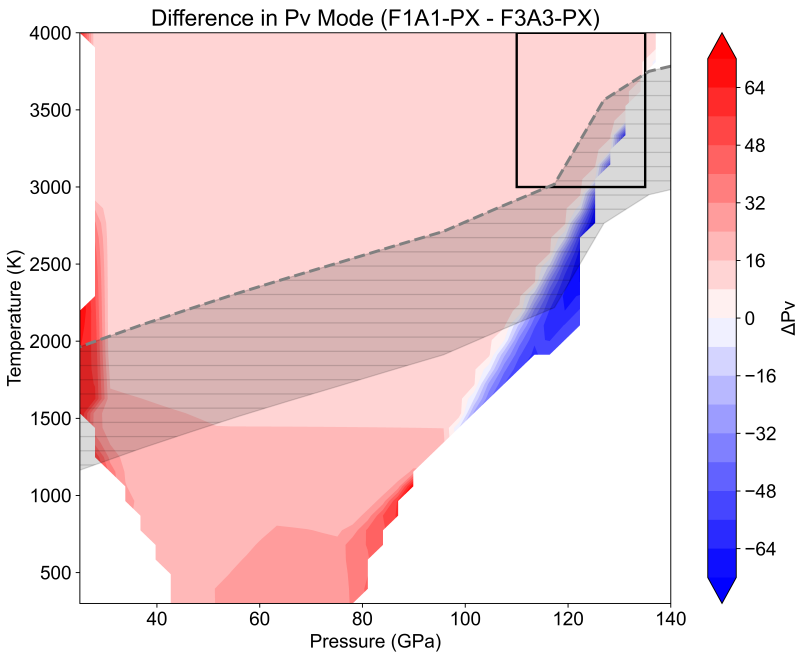

Figure 7.4: Difference in perovskite (Pv) mode between the F1A1-PX and F3A3-PX compositions as predicted by Perple_X thermodynamic modeling. The color map illustrates the variation in Pv mode over a range of pressure and temperature conditions. Positive values (red) indicate domains where the F1A1-PX composition exhibits a higher Pv mode relative to the F3A3-PX composition, while negative values (blue) reflect the opposite trend.

7.3 Density, Bulk Modulus, and Seismic Property Variations

Fe and Al substitutions in bridgmanite lead to an increase in density due to the incorporation of higher atomic mass cations and potential distortions in the octahedral sites. Charge-coupled substitution mechanisms, such as $FeAlO_3$, lead to anisotropic increases in B–O bond distances, resulting in more distorted octahedral B-sites and an expansion of the unit cell along the c-axis (Huang *et al.*, 2021b). These structural changes contribute to the observed increase in density. Variations in substitution influence the electronic structure, affecting both the atomic packing and bulk properties of the mineral. These changes in structure and composition are well-documented, with studies showing how such substitutions can affect the physical properties of bridgmanite, including its elasticity and compressibility (Mao *et al.*, 2011; Fukui *et al.*, 2016).

Figure 7.5 presents the pressure dependence of density, compressional wave velocity (V_p), and shear wave velocity (V_s) for three bridgmanite compositions at 2482 K. The results indicate that while density increases with Fe-Al substitution, the effects on seismic velocities are impacted non-linearly.

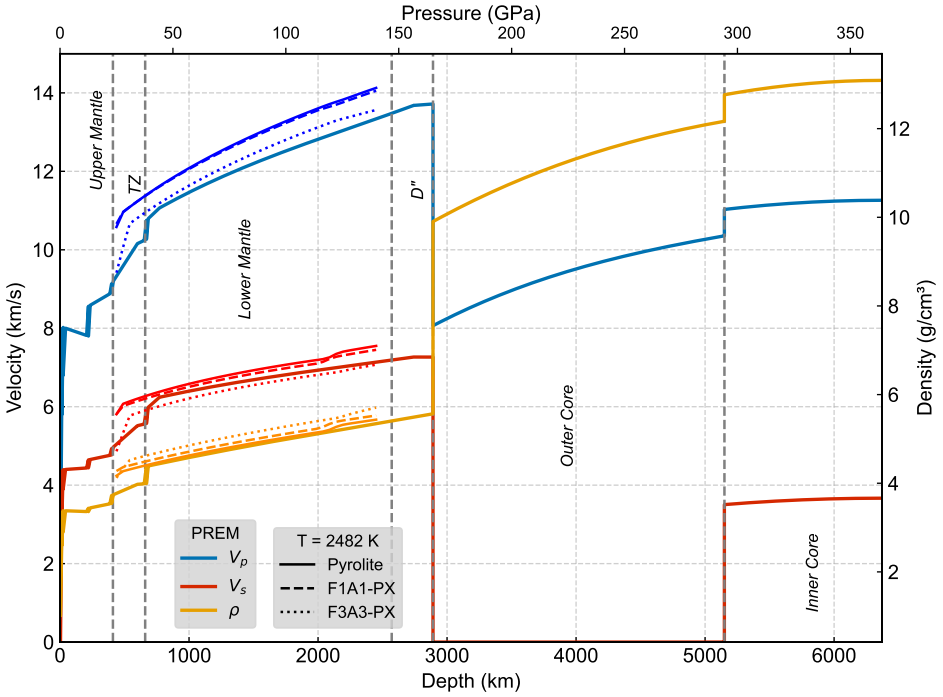

Figure 7.5: Pressure-depth profile of seismic velocities (V_p, V_s) and density for the earth's interior. The plot includes the PREM model (Dziewonski and Anderson, 1981) (blue for V_p, red for V_s, and orange for density ρ) alongside experimental data for different compositions (F1A1-PX, F3A3-PX, and Pyrolite). The different lifestyles indicate the different compositions' profiles, demonstrating the variations with respect to pressure. The right axis shows density in g/cm^3, while the left axis shows seismic velocity in km/s.

Lin and Tsuchiya (2008) reported significant softening of the bulk modulus during the spin transition of iron at 300 K. Their study demonstrated that the spin-transition of iron in ferropericlase leads to a reduction in the bulk modulus (K) at lower temperatures, while the shear modulus (G) remains largely unaffected. This softening is attributed to the change in iron's electronic

configuration, which alters the bond stiffness and compressibility. At higher temperatures, the effect of the spin-transition on the bulk modulus diminishes, suggesting that thermal motion alleviates some of the strain induced by the electronic transition. This phenomenon has been observed in other iron-bearing minerals, including bridgmanite, where similar transitions in iron lead to changes in elastic properties (Mohn and Trønnes, 2016).

The effect of increasing Fe-Al content on the density and stiffness of bridgmanite is generally characterized by an increase in density and moderate reductions in stiffness. This trend is observed across a range of compositions and is driven by the larger ionic radii of Fe and Al relative to Mg, as well as the changes in the crystal structure associated with their substitution (Fiquet *et al.*, 2000). These substitutions affect the mineral's elastic properties by altering the atomic packing, leading to variations in compressibility, and thus, seismic velocity.

The adiabatic bulk modulus (K_s), shown in Figure 7.6 for Perple_X modeling, also does not vary linearly with Fe-Al content. Instead, it reflects contributions from multiphase assemblages and the interactions between various mineral phases in the lower mantle. This is particularly important in understanding how these substitutions affect the overall elasticity of the mantle. Although the K_s trend is not directly calculated for the experimental and computational data in this thesis, the results are consistent with trends observed for the adiabatic bulk modulus (K_T). These findings suggest that, in addition to the direct effects of composition, the phase assemblages play a crucial role in determining the bulk mantle's overall elasticity.

For instance, the intermediate F1A1-PX model, yields the largest K_s above 85 GPa at both 300 K and 2482 K when compared to pyrolite and F3A3-PX. This is in agreement with the findings for K_T, where the "intermediate" Fe-Al-bearing compositions presented in this thesis– such as F1A1-brg (from experiments) and FeAl25 (from computations)–exhibit a higher modulus than the

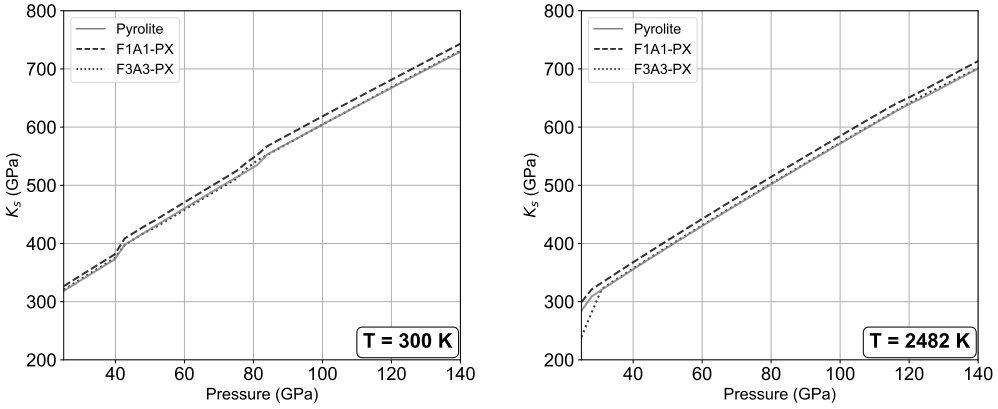

(a) 300 K *(b) 2482 K*

Figure 7.6: Adiabatic bulk modulus K_s (GPa) for Pyrolite (solid), F1A1-PX (dashed), F3A3-PX (dotted) from Perple_X modeling plotted against pressure at constant temperature (a) 300 K, (b) 2482 K.

$MgSiO_3$ end-member and the high Fe-Al compositions (F3A3-brg and FeAl50) at high pressure. These results suggest that intermediate Fe-Al-bearing compositions may exhibit enhanced stiffness relative to the more iron- and aluminum-rich compositions. This enhancement is likely due to a balance between the effects of increased atomic mass and the structural distortions caused by the substitution of larger cations (Shukla *et al.*, 2016, 2015; Fiquet *et al.*, 2000; Fukui *et al.*, 2016).

DFT calculations indicate that the zero-pressure bulk modulus decreases with increasing Fe and Al substitution, suggesting that these substitutions soften the lattice. However, at high-temperatures (>1000 K), DFT calculations within the quasi-harmonic approximation (QHA) show that this trend diminishes above approximately 1000 K. This implies that the softening associated with Fe and Al substitution is most pronounced under static or low-temperature conditions, while at higher temperatures, thermal expansion and vibrational contributions reduce the relative contrast among compositions.

The static high-pressure X-ray diffraction (XRD) measurements show an increase in K_0 with Fe and Al substitution, contrary to DFT calculations at 300 K and other experimental studies

(Table 3.1). This discrepancy suggests extrinsic factors dominate experimental observations. For instance, bridgmanite in this study are of sintered polycrystalline samples which may exhibit structural or chemical heterogeneities, local compositional gradients, or partial secondary phase formation that contribute to apparent stiffening. Other factors such as sample imperfections, grain size, boundary characteristics, non-hydrostatic stresses, and data fitting nuances may also lead to overestimation of K_0 in the XRD results.

Thus, while DFT predicts intrinsic softening from Fe and Al substitution at static conditions, experimental stiffening is likely driven by extrinsic factors such as sample imperfections and environmental variations not fully captured in simplified computational models.

7.4 Geophysical Implications

High-pressure X-ray diffraction (XRD), density functional theory (DFT), and Perple_X modeling were used to quantify how Fe-Al substitution in bridgmanite modifies its elastic and seismic properties under lower-mantle conditions. These findings are interpreted in the context of existing mineral physics and deep Earth geophysical observations to better understand the compositional origin of seismic anomalies such as Large Low Shear Velocity Provinces (LLSVPs) and Ultra-Low Velocity Zones (ULVZs).

The substitution of iron and aluminum in bridgmanite has significant implications for mantle seismic properties (Marquardt and Thomson, 2020; Ishii *et al.*, 2022). The increased density and variation in bulk modulus trends from Fe-Al substitutions suggest that these compositional variations may contribute to observed seismic anomalies in the lower mantle (Garnero and McNamara, 2008; Cottaar and Lekic, 2016). Specifically, Fe-Al-rich domains could cause variations in seismic wave velocities and V_p/V_s ratios. Perple_X modeling indicates that increasing Fe-Al content shifts V_p/V_s

ratios, with lateral variations potentially contributing to distinct seismic signatures (Trampert *et al.*, 2004; Deschamps *et al.*, 2012). Subtle differences in V_p/V_s ratios between F1A1-PX and F3A3-PX highlight the importance of considering compositional heterogeneity in interpreting large-scale seismic data, such as those associated with LLSVPs and other deep mantle anomalies (Vilella *et al.*, 2021; Su *et al.*, 1994; Dziewonski *et al.*, 2010; Garnero *et al.*, 2016).

Phase changes from Fe and Al substitution modify seismic velocities and the V_p/V_s ratio (Wang *et al.*, 2021). Figure 7.7 shows the V_p/V_s ratio fields for pyrolite, F1A1-PX, and F3A3-PX. In the pyrolite model (Figure 7.7a), the V_p/V_s ratio increases smoothly with pressure and temperature, from $\sim$1.65 to 1.98. In Fe-Al-rich systems (Figures 7.7b and 7.7c), the overall range remains similar but with shifted ratios.

High-spin iron influences the elastic moduli and atomic configurations of cations, thereby modifying the bulk physical properties of the mineral. As demonstrated by the DFT calculations on FeAl25 presented in this thesis (Chapter 6), under lower-mantle–like high-pressure and high-temperature conditions, the resulting atomic arrangement produces a measurable stiffening relative to $MgSiO_3$ and FeAl50 (Figure 6.7a). At the macroscopic scale, this behavior is reflected in the modeled seismic velocity ratios: Figure 7.8 shows that the F1A1-PX composition generally yields lower V_p/V_s ratios than F3A3-PX across most of the pressure–temperature range. When uncertainties associated with the effective bulk and shear moduli of the modeled mineral assemblages are propagated through the V_p/V_s calculations (Figure 7.9), only a small fraction of the pressure–temperature grid exceeds the 2σ significance threshold. These results suggest that lateral variations in Fe and Al content could contribute to weak, spatially localized seismic anomalies, consistent with the small scale heterogeneities observed in large low-shear-velocity provinces (LLSVPs) (Ballmer *et al.*, 2017; McNamara, 2019; Trampert *et al.*, 2004; Deschamps and Trampert,

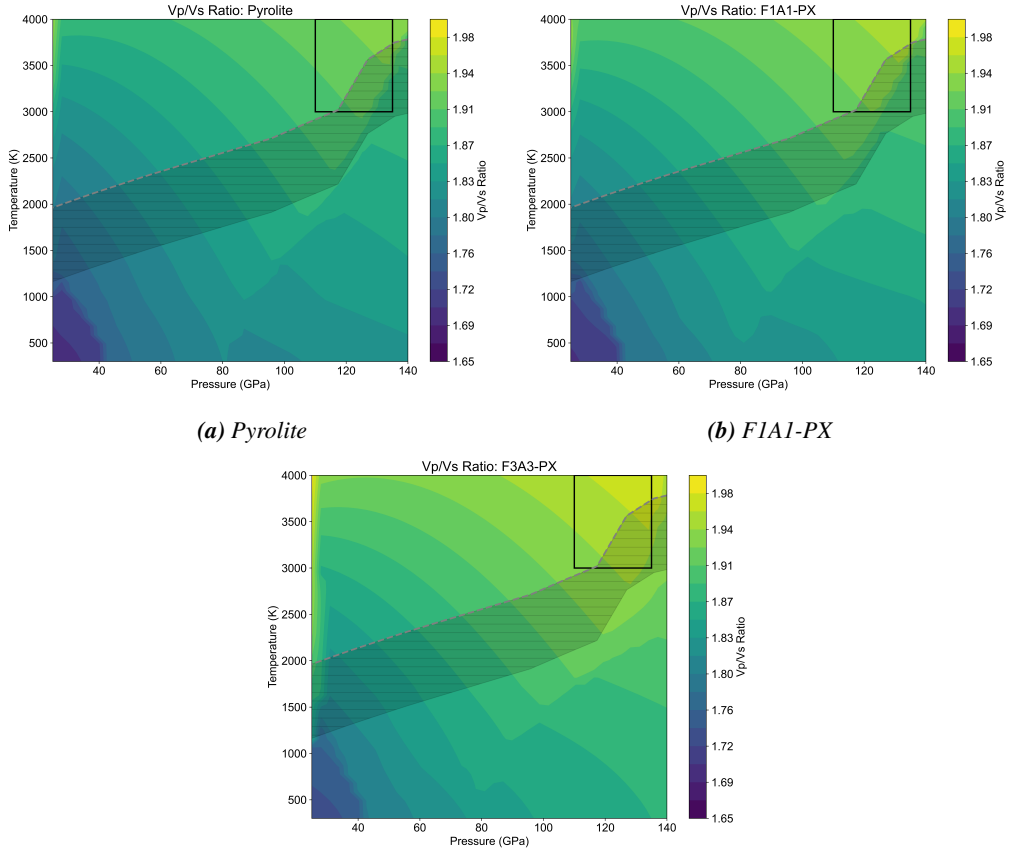

(a) *Pyrolite*

(b) *F1A1-PX*

(c) *F3A3-PX*

Figure 7.7: V_p/V_s ratio as a function of pressure (0–140 GPa) and temperature (300–4000 K) based on Perple_X modeling for (a) Pyrolite, (b) F1A1-PX, and (c) F3A3-PX. The color scale depicts the ratio between compressional wave velocity (V_p) and shear wave velocity (V_s). Higher values (yellow) indicate a larger V_p/V_s ratio, while lower values (green to blue) indicate a smaller ratio. The black boxes highlights the P–T range of LLSVPs.

2003; Vilella *et al.*, 2021).

Garnero and McNamara (2008) suggested that a 1.5–3% density increase relative to the surrounding mantle may reflect Fe enrichment, affecting V_s and V_p/V_s. Bridgmanite's density increases with Fe-Al substitution, potentially contributing to the formation and stabilization of LLSVPs in the lower mantle (Trampert *et al.*, 2004). The suppression of ferropericlase, combined with the addition of denser bridgmanite, creates localized compositional domains that are seismically distinct (Trampert *et al.*, 2004; Vilella *et al.*, 2021). These findings align with geodynamic models

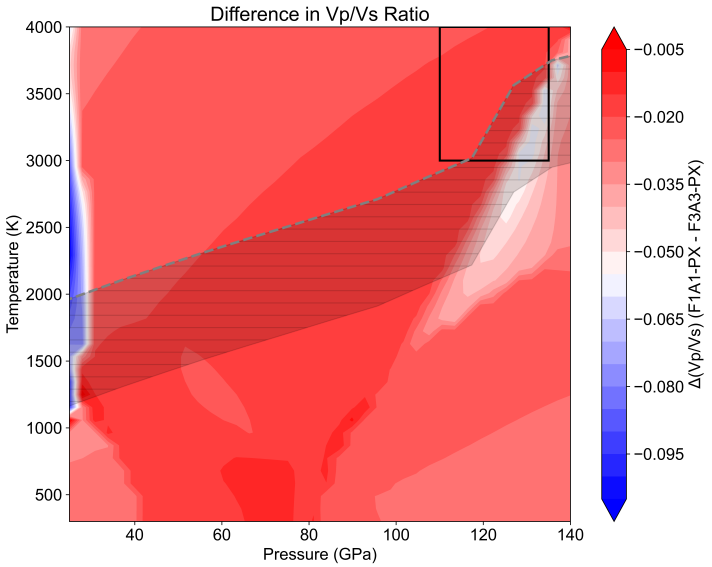

Figure 7.8: Variation in $\Delta(V_p/V_s)$ between the F1A1-PX and F3A3-PX compositions, plotted as a function of pressure (0–140 GPa) and temperature (300–4000 K). Red regions represent higher V_p/V_s values for F1A1-PX than for F3A3-PX, whereas blue regions mark the opposite. The black boxes highlights the P–T range of LLSVPs.

that view LLSVPs as chemically distinct reservoirs.

An example bulk composition for LLSVPs, modified from Ballmer *et al.* (2016) and Trampert *et al.* (2004), is shown in Table 7.4. This composition assumes a significant increase in FeO relative to the pyrolite reference.

Understanding Fe and Al substitution in bridgmanite is crucial for interpreting seismological observations and improving mineralogical models (Anderson, 1983; Karki *et al.*, 1997; Hummer and Fei, 2012). The decrease in bulk modulus suggests that regions enriched with some amount of Fe and Al, such as LLSVPs, are more compressible than surrounding mantle material, contributing to slower seismic wave velocities, particularly compressional waves (V_p), in these areas. These slower velocities likely correspond to higher Fe and Al concentrations or higher temperuatures (Garnero and McNamara, 2008).

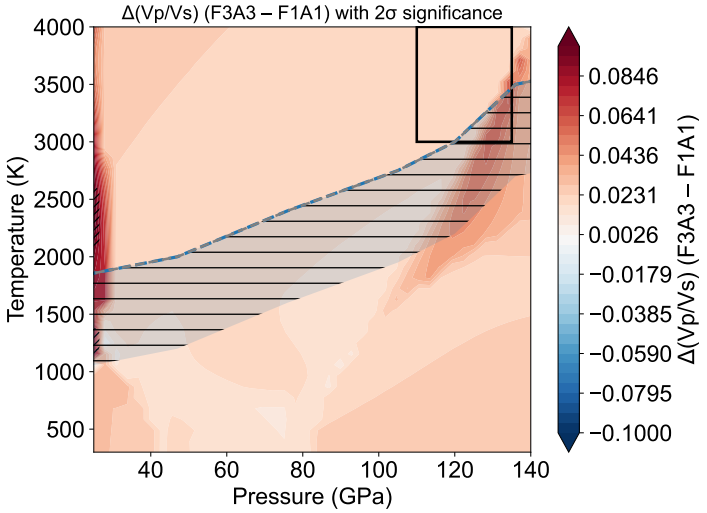

Figure 7.9: Difference in modeled seismic velocity ratio ($\Delta V_p/V_s$) between F3A3-PX and F1A1-PX bulk compositions from Perple_X calculations. Warm colors indicate higher V_p/V_s ratios relative to F1A1. Hatched regions at low pressures mark where $|\Delta V_p/V_s|$ exceeds the propagated 2σ uncertainty, denoting conditions where compositional effects may be seismically resolvable. The dashed line shows the lower-mantle geotherm, and the black box outlines the approximate pressure–temperature range of large low-shear-velocity provinces (LLSVPs).

Seismologically, the reduced shear wave velocity (V_s) and lower V_p/V_s ratios in these regions indicate compositional and structural differences within the mantle. The increased density, coupled with reduced bulk modulus due to Fe-Al substitution, results in a seismically distinct material, which may explain the persistent presence of LLSVPs in seismic tomography.

Minor anisotropy in bridgmanite, especially if a crystallographic preferred orientation develops during mantle flow, could influence seismic anisotropy (Bull *et al.*, 2010). Variations in axial compressibility in Fe-Al-bearing compositions suggest that chemical heterogeneity affects mantle convection and slab stagnation in subduction zones (Ismailova *et al.*, 2016).

Further investigations should focus on the distribution of Fe and Al within the bridgmanite structure. In samples with high iron content (i.e., $>$ 15-25%), understanding the location of Fe and its proximity to Al could provide important insights into lower mantle anomalies.

Table 7.3: LLSVP compositional models compared to pyrolite reference from the literature.

Reference & Model	**SiO_2** (wt%)	**MgO** (wt%)	**FeO** (wt%)	**Al_2O_3** (wt%)	**CaO** (wt%)	
Pyrolite Reference[a]	44–45	37–38	7–8	4–5	3–4	Baseline "average mantle" composition commonly used for modeling.
Ishii and Tromp (1999) *"Dense Pile" Hypothesis*	40–42	32–35	10–12	4–5	4–5	Normal-mode seismology and gravity suggest a 1–2% denser LLSVP, implying significant Fe-enrichment (+1–3 wt% FeO above pyrolite).
Trampert *et al.* (2004) *Modestly Fe-Enriched LM*	44–45	36–37	8–10	4–5	3–4	Seismic tomography and mineral physics indicate a slightly Fe-rich lower mantle, with Fe/(Fe+Mg) $\approx$ 0.10–0.12. Other oxides remain near pyrolitic values.
McNamara and Zhong (2004) *Thermochemical Convection Models*	40–45	32–38	8–12	3–5	3–5	Numerical simulations of superplumes/piles show a range from mild to strong Fe-enrichment. Stabilized "piles" can match seismic and geodynamic observations.
Ballmer *et al.* (2017) *Basaltic/Eclogitic Piles*	50–51	6–10	8–10	15–17	10–12	Argue for recycled oceanic crust in the deep mantle. Basaltic domains are SiO_2-, Al_2O_3-, and CaO-rich relative to pyrolite.

[a] E.g., Ringwood (1975), Anderson (1989), McDonough and Sun (1995).

At the core-mantle boundary (CMB), disproportionation reactions, such as $3\,Fe^{2+} \longrightarrow Fe^0 + 2\,Fe^{3+}$ (Frost and Myhill, 2016; McCammon, 2005), may occur, leading to increased Fe^{3+} abundances and the formation of metallic Fe^0. Additionally, Fe^0 can react with bridgmanite and ferropericlase, as seen in the reactions: $Fe^0 + SiO_2 \longrightarrow Fe^{2+} + Si$ and $Fe^0 + Fe^{3+}$-bearing minerals $\longrightarrow Fe^{2+}$. These reactions could promote the breakdown of silicon into the metallic core (Gessmann

Table 7.4: Example LLSVP bulk composition that is a hypothetical Fe-enriched peridotite modified from Ballmer *et al.* (2016) and Trampert *et al.* (2004).

Oxides(Wt%)	LLSVP	**Compared to Pyrolite**
SiO_2	44.5	slightly high
MgO	32.0	lower than pyrolite
FeO	15.0	significantly higher
Al_2O_3	4.5	similar to pyrolite
CaO	3.5	normal
Na_2O	0.3	trace

et al., 2001) and facilitate redox buffering through multi-mixed valence state iron oxides (Frost *et al.*, 2008; Kulka, 2021).

Experimental data presented in Chapter 3 suggests that He might potentially influencing its elastic properties. Additionally, Fe^0 could host hydrogen in Fe-H alloys, which might affect deep-Earth water storage (He *et al.*, 2023; Kawano *et al.*, 2024; Yang *et al.*, 2022; Lai *et al.*, 2022b). Under inner core conditions, light elements such as H, O, and C may enter a "superionic" state characterized by extremely low velocities and high density, diffusing within a solid iron lattice (Wu *et al.*, 2024; Liu and Cohen, 2025; Zhang *et al.*, 2024).

The presence of Fe-Al substitutions in bridgmanite also likely contributes to the formation of Ultra-Low Velocity Zones (ULVZs) near the CMB, regions where additional seismic anomalies have been observed (Zhang *et al.*, 2016). These substitutions can lead to reduced seismic wave velocities (Muir and Brodholt, 2020; Garnero and McNamara, 2008), which aligns with characteristics commonly seen in ULVZs (Williams and Garnero, 1996). Fe-Al-rich regions are likely to cause slower seismic wave propagation, explaining the ultra-low velocities observed in certain ULVZs (Garnero and McNamara, 2008).

ULVZ formation near the core–mantle boundary is often associated with partial melting or strong compositional contrasts, both of which can be enhanced in Fe-rich environments (Kawano

et al., 2024; Williams and Garnero, 1996). As the dominant mineral of the lower mantle, bridgmanite therefore plays a central role in understanding the formation and persistence of ULVZs (Brodholt, 2000; Murakami *et al.*, 2004; Kawai and Tsuchiya, 2009; Tsuchiya *et al.*, 2004). The elastic properties of bridgmanite, when modulated by Fe-Al substitution, can produce modest reductions in seismic velocities relative to $MgSiO_3$, potentially contributing to weak velocity anomalies in compositionally heterogeneous regions of the lower mantle (Mao *et al.*, 2017; Nakatsuka *et al.*, 2021; Huang *et al.*, 2015). However, achieving ULVZ-like seismic properties likely requires either partial melting or the presence of Fe-enriched secondary phases such as ferropericlase, FeO, or metallic iron, rather than solely Fe substitution within the bridgmanite structure. Nevertheless, Fe-Al-bearing bridgmanite may contribute to the seismic heterogeneity surrounding ULVZs by acting as a chemically distinct, elastically weaker component within the deep-mantle assemblage.

Studies have shown that iron and aluminum substitutions in bridgmanite can suppress phase transitions, such as the transformation to post-perovskite (Pv-Ppv) at the CMB. The Clapeyron slope associated with this transition can shift based on compositional factors, such as elevated Fe and Al content, potentially suppressing or expanding the Pv stability field (Dubrovinsky *et al.*, 2001; Huang *et al.*, 2021b; Kurnosov *et al.*, 2017). This is particularly relevant for ULVZs at the edges of Large Low Shear Velocity Provinces (LLSVPs), where temperature and compositional anomalies are believed to influence mantle dynamics.

Moreover, the presence of iron in ULVZs may promote the formation of hydrous phases or metallic Fe^0, which would further alter the region's seismic properties (He *et al.*, 2023; Ohtani, 2020; Kawano *et al.*, 2024). For example, in cooler thermal regimes the formation of a Pv-Ppv double-crossing could result in the generation of thin post-perovskite layers within bridgmanite-dominated assemblages (Dubrovinsky *et al.*, 2001; Huang *et al.*, 2021b). This interaction between composition

and temperature could lead to complex mineralogical layering within ULVZs, complicating seismic data interpretation.

These mineralogical transitions and compositional variations are essential for understanding the persistent seismic anomalies associated with ULVZs. The increased Fe and Al content in bridgmanite can influence the mantle's rheology, potentially slowing mantle convection and altering deep-mantle dynamics. The presence of enriched domains at the base of the mantle could also impact core-mantle heat and mass exchange, affecting global mantle circulation and core dynamics. Investigating the role of Fe-Al substitution in bridgmanite is crucial not only for understanding seismic properties in the lower mantle but also for linking LLSVPs, ULVZs, and the broader thermochemical structure of Earth's interior (Lai *et al.*, 2022a). Additional experimental and computational studies are needed to fully explore these effects, particularly under the extreme conditions of the lower mantle and core-mantle boundary. This work provides quantitative constraints on how Fe-Al chemistry influences bridgmanite's elastic behavior, offering a basis for interpreting seismic features in the deep mantle.

Chapter 8
Conclusion

This thesis set out to investigate how iron (Fe) and aluminum (Al) substitution influences the structural, elastic, and thermodynamic properties of bridgmanite under lower mantle conditions (Irifune *et al.*, 2010; Murakami *et al.*, 2012; Huang *et al.*, 2021a; Zhu *et al.*, 2020). The overarching aim was to quantify how Fe-Al chemistry affects bridgmanite's elastic behavior, and to explore the implications of these effects on the deep-mantle. These objectives were addressed through a combined approach using high-pressure X-ray diffraction (XRD), density functional theory (DFT) calculations, and thermodynamic modeling with Perple_X.

The findings demonstrate that Fe-Al substitution exerts complex, pressure- and temperature-dependent effects on bridgmanite's elasticity and density. DFT calculations indicate that at 0 K, the substitution leads to a decrease in bulk modulus (K_0), suggesting greater compressibility. However, at elevated temperatures, particularly in the FeAl25 composition, thermal effects counteract this softening, leading instead to a stiffening response. This contrast highlights the importance of incorporating temperature-dependent atomic behavior into models of lower-mantle mineral physics.

Experimental XRD results show an apparent stiffening with increasing Fe-Al content at 300 K, diverging from the presented DFT predictions. This likely reflects sample-related factors such as grain size, residual stress, and chemical heterogeneity in sintered polycrystalline samples, effects not captured in the computational models. Together, these findings highlight the value of integrating both theoretical and experimental perspectives to gain a complete understanding of mineral behavior at extreme conditions.

Thermodynamic modeling further supports the effect of Fe and Al on bridgmanite, such as

the expansion of its stability field and the suppression of the formation of other mantle phases such as ferropericlase. These results align with experimental observations and suggest that Fe-Al-rich bridgmanite may dominate in certain deep mantle regions, particularly at the base of Large Low Shear Velocity Provinces (LLSVPs) (Wang *et al.*, 2021; Sun *et al.*, 2018). The modeling also shows that Fe-Al substitution increases density and reduces both compressional (V_p) and shear (V_s) wave velocities, resulting in lower V_p/V_s ratios, features that correlate with observed seismic anomalies in both LLSVPs and Ultra-Low Velocity Zones (ULVZs) (Shukla *et al.*, 2016; Vilella *et al.*, 2021).

Altogether, this thesis provides new constraints on how compositional variability in bridgmanite influences lower mantle seismic structure and reinforces the need to include chemical heterogeneity in geophysical models.

Several future directions emerge from this study. If given access to a laboratory and an additional few years of research time, the next steps would focus on both experimental and computational developments. First, *in situ* high-pressure, high-temperature XRD experiments using laser-heated diamond anvil cells (LHDACs) should be performed on these sintered polycrystalline Fe-Al-bearing bridgmanite to directly measure thermal EOS parameters at lower mantle conditions (30–100 GPa, 1500–3000 K). These data would bridge the gap between static DFT predictions and ambient-temperature experiments. Second, synchrotron-based Mössbauer spectroscopy or X-ray emission spectroscopy (XES) could be used to track spin transitions and valance states of iron under varying pressures and temperatures. Since spin state has a major influence on compressibility and elasticity, this would clarify its seismic relevance in Fe-rich bridgmanite.

On the computational side, advanced DFT methods such as GGA+U or hybrid functionals should be employed to improve the treatment of strongly correlated Fe $3d$ electrons and to better capture spin-state transitions and electronic structure under compression. Atomistic modeling tech-

niques, including Monte Carlo simulations, could be used to investigate Fe and Al site occupancy in the A- and B-sites across a range of compositions and pressures, including potential short-range ordering.

Another direction involves exploring the energetics and structural consequences of H and He incorporation into Fe-Al-rich bridgmanite, using both DFT and targeted high-pressure experiments. The influence of the pressure-transmitting medium on sintered polycrystalline bridgmanite in particular warrants further investigation, drawing on insights from materials-science studies on perovskites (Racioppi *et al.*, 2023). These investigations could provide critical insights into the role of bridgmanite in deep Earth volatile storage.

Finally, the compositional and elastic parameters developed in this thesis should be incorporated into seismic waveform modeling and geodynamic simulations. This would enable an assessment of how Fe-Al-rich bridgmanite domains influence mantle convection, slab stagnation, and core-mantle boundary processes.

Collectively, these future steps would significantly expand upon the contributions of this thesis and help resolve the complex interplay between bridgmanite composition, seismic anomalies, and mantle dynamics.

BIBLIOGRAPHY

Ammann, M., J. Brodholt and D. Dobson, 'Ferrous iron diffusion in ferro-periclase across the spin transition", Earth and Planetary Science Letters **302**, 3-4, 393–402 (2011).

Anderson, D. L., 'The anelasticity of the mantle", Geophysical Journal International **14**, 1-4, 135–163 (1967).

Anderson, D. L., 'Composition of the mantle and core", In: Annual review of earth and planetary sciences. Volume 5.(A77-38469 17-46) Palo Alto, Calif., Annual Reviews, Inc., 1977, p. 179-202. **5**, 179–202 (1977).

Anderson, D. L., 'Chemical composition of the mantle", Journal of Geophysical Research: Solid Earth **88**, S01, B41–B52 (1983).

Anderson, D. L., 'Composition of the earth", Science **243**, 4889, 367–370 (1989).

Anderson, O. L., *Equations of state of solids for geophysics and ceramic science* (Oxford university press, 1995).

Anderson, O. L. and Y. Sumino, 'The thermodynamic properties of the earth's lower mantle", Physics of the Earth and Planetary Interiors **23**, 4, 314–331 (1980).

Andrault, D., N. Bolfan-Casanova and N. Guignot, 'Equation of state of lower mantle (al, fe)-mgsio $_3$ perovskite", Earth and Planetary Science Letters **193**, 3-4, 501–508 (2001).

Angel, R. J., 'Equations of state", Reviews in mineralogy and geochemistry **41**, 1, 35–59 (2000).

Badro, J., G. Fiquet, F. Guyot, J.-P. Rueff, V. V. Struzhkin, G. Vanko and G. Monaco, 'Iron partitioning in earth's mantle: Toward a deep lower mantle discontinuity", Science **300**, 5620, 789–791 (2003).

Badro, J., J.-P. Rueff, G. Vanko, G. Monaco, G. Fiquet and F. Guyot, 'Electronic transitions in perovskite: Possible nonconvecting layers in the lower mantle", Science **305**, 5682, 383–386 (2004).

Baktash, A., B. Demir, Q. Yuan and D. J. Searles, 'Effect of defects and defect distribution on li-diffusion and elastic properties of anti-perovskite li3ocl solid electrolyte", Energy Storage Materials **41**, 614–622 (2021).

Ballaran, T. B., A. Kurnosov, K. Glazyrin, D. J. Frost, M. Merlini, M. Hanfland and R. Caracas, 'Effect of chemistry on the compressibility of silicate perovskite in the lower mantle", Earth and Planetary Science Letters **333**, 181–190 (2012).

Ballmer, M. D., C. Houser, J. W. Hernlund, R. M. Wentzcovitch and K. Hirose, 'Persistence of strong silica-enriched domains in the earth's lower mantle", Nature Geoscience **10**, 3, 236–240 (2017).

Ballmer, M. D., L. Schumacher, V. Lekic, C. Thomas and G. Ito, 'Compositional layering within the large low shear-wave velocity provinces in the lower mantle", Geochemistry, Geophysics, Geosystems **17**, 12, 5056–5077 (2016).

Baroni, S., S. De Gironcoli, A. Dal Corso and P. Giannozzi, 'Phonons and related crystal properties from density-functional perturbation theory", Reviews of modern Physics **73**, 2, 515 (2001).

Beier, C., T. Rushmer and S. Turner, 'Heat sources for mantle plumes", Geochemistry, Geophysics, Geosystems **9**, 6 (2008).

Bina, C. R. and G. Helffrich, 'Phase transition clapeyron slopes and transition zone seismic discontinuity topography", Journal of Geophysical Research: Solid Earth **99**, B8, 15853–15860 (1994).

Bindi, L., S.-H. Shim, T. G. Sharp and X. Xie, 'Evidence for the charge disproportionation of iron in extraterrestrial bridgmanite", Science Advances **6**, 2, eaay7893 (2020).

Birch, F., 'Finite elastic strain of cubic crystals", Physical review **71**, 11, 809 (1947).

Boehler, R., 'High-pressure experiments and the phase diagram of lower mantle and core materials", Reviews of Geophysics **38**, 2, 221–245 (2000).

Boggs, P. T. and J. E. Rogers, 'Orthogonal distance regression", Tech. Rep. NISTIR 89-4197, U.S. Department of Commerce, National Institute of Standards and Technology, Gaithersburg, MD, revised July 1990 (1989).

Boioli, F., P. Carrez, P. Cordier, A. Goryaeva, K. Gouriet, P. Hirel, A. Kraych, S. Mahendran, A. Mussi, B. C. Nzogang *et al.*, *Multiscale modeling of the mantle rheology* (Cordier Patrick et AM Goryaeva, 2018).

Bolfan-Casanova, N., H. Keppler and D. C. Rubie, 'Water partitioning at 660 km depth and evidence for very low water solubility in magnesium silicate perovskite", Geophysical Research Letters **30**, 17 (2003).

Bonsor, A., Z. M. Leinhardt, P. J. Carter, T. Elliott, M. J. Walter and S. T. Stewart, 'A collisional origin to earth's non-chondritic composition?", Icarus **247**, 291–300 (2015).

Bosi, F., 'Mean bond-length variation in crystal structures: a bond-valence approach", Structural Science **70**, 4, 697–704 (2014).

Boström, H. L. and G. Kieslich, 'Influence of metal defects on the mechanical properties of abx3 perovskite-type metal-formate frameworks", The Journal of Physical Chemistry C **125**, 2, 1467–1471 (2021).

Bouhifd, M. A., A. P. Jephcoat, V. S. Heber and S. P. Kelley, 'Helium in earth's early core", Nature Geoscience **6**, 11, 982–986 (2013).

Bower, D. J., M. Gurnis, J. M. Jackson and W. Sturhahn, 'Enhanced convection and fast plumes in the lower mantle induced by the spin transition in ferropericlase", Geophysical Research Letters **36**, 10 (2009).

Bragg, W. H. and W. L. Bragg, 'The reflection of x-rays by crystals", Proceedings of the Royal Society of London. Series A, Containing Papers of a Mathematical and Physical Character **88**, 605, 428–438 (1913).

Brodholt, J. P., 'Pressure-induced changes in the compression mechanism of aluminous perovskite in the earth's mantle", Nature **407**, 6804, 620–622 (2000).

Bull, A., A. McNamara, T. Becker and J. Ritsema, 'Global scale models of the mantle flow field predicted by synthetic tomography models", Physics of the Earth and Planetary Interiors **182**, 3-4, 129–138 (2010).

Burns, R. G., *Mineralogical applications of crystal field theory*, no. 5 in 5 (Cambridge university press, 1993).

Callister Jr, W. D. and D. G. Rethwisch, *Materials science and engineering: an introduction* (John wiley & sons, 2020).

Canup, R. M., 'Accretion of the earth", Philosophical Transactions of the Royal Society A: Mathematical, Physical and Engineering Sciences **366**, 1883, 4061–4075 (2008).

Car, R. and M. Parrinello, 'Unified approach for molecular dynamics and density-functional theory", Physical review letters **55**, 22, 2471 (1985).

Carter, P. J., Z. M. Leinhardt, T. Elliott, M. J. Walter and S. T. Stewart, 'Compositional evolution during rocky protoplanet accretion", The Astrophysical Journal **813**, 1, 72 (2015).

CASTEP Developers Group, 'Geometry optimization convergence thresholds (coarse/medium/fine/ultra-fine) – castep", `https://www.tcm.phy.cam.ac.uk/castep/documentation/WebHelp/content/modules/castep/dlgcastepgeomoptmin.htm`, accessed: 2025-10-27 (2024).

Catalli, K., S. Shim, V. B. Prakapenka, J. Zhao, W. Sturhahn, P. Chow, Y. Xiao, H. Liu, H. Cynn and W. J. Evans, 'Spin transition in ferric iron in mgsio3 perovskite and its effect on elastic properties", Earth Planet. Sci. Lett (2009a).

Catalli, K., S.-H. Shim, P. Dera, V. B. Prakapenka, J. Zhao, W. Sturhahn, P. Chow, Y. Xiao, H. Cynn and W. J. Evans, 'Effects of the fe3+ spin transition on the properties of aluminous perovskite—new insights for lower-mantle seismic heterogeneities", Earth and Planetary Science Letters **310**, 3-4, 293–302 (2011).

Catalli, K., S.-H. Shim and V. Prakapenka, 'Thickness and clapeyron slope of the post-perovskite boundary", Nature **462**, 7274, 782–785 (2009b).

Catalli, K., S.-H. Shim, V. B. Prakapenka, J. Zhao, W. Sturhahn, P. Chow, Y. Xiao, H. Liu, H. Cynn and W. J. Evans, 'Spin state of ferric iron in mgsio$_3$ perovskite and its effect on elastic properties", Earth and Planetary Science Letters **289**, 1-2, 68–75 (2010).

Cesare, B., F. Nestola, T. Johnson, E. Mugnaioli, G. Della Ventura, L. Peruzzo, O. Bartoli, C. Viti and T. Erickson, 'Garnet, the archetypal cubic mineral, grows tetragonal", Scientific Reports **9**, 1, 14672 (2019).

Chai, M. and J. Michael Brown, 'Effects of static non-hydrostatic stress on the r lines of ruby single crystals", Geophysical research letters **23**, 24, 3539–3542 (1996).

Chandler, B. C., L.-W. Chen, M. Li, B. Romanowicz and H.-R. Wenk, 'Seismic anisotropy, dominant slip systems and phase transitions in the lowermost mantle", Geophysical Journal International **227**, 3, 1665–1681 (2021).

Chantel, J., D. J. Frost, C. A. McCammon, Z. Jing and Y. Wang, 'Acoustic velocities of pure and iron-bearing magnesium silicate perovskite measured to 25 gpa and 1200 k", Geophysical Research Letters **39**, 19 (2012).

Christensen, U., 'Effects of phase transitions on mantle convection", Annual Review Of Earth And Planetary Sciences, Volume 23, pp. 65-88. **23**, 65–88 (1995).

Christensen, U. R. and A. W. Hofmann, 'Segregation of subducted oceanic crust in the convecting mantle", Journal of Geophysical Research: Solid Earth **99**, B10, 19867–19884 (1994).

Clark, S. J., M. D. Segall, C. J. Pickard, P. J. Hasnip, M. J. Probert, K. Refson and M. Payne, 'First principles methods using CASTEP", Z. Kristall. **220**, 567–570 (2005).

Cohen, R. E., 'Elasticity and equation of state of mgsio3 perovskite", Geophysical Research Letters **14**, 10, 1053–1056 (1987).

Connolly, J., 'The geodynamic equation of state: what and how", Geochemistry, geophysics, geosystems **10**, 10 (2009).

Connolly, J. A. D., 'Multivariable phase diagrams: an algorithm based on generalized thermodynamics", American Journal of Science **290**, 6, 666–718 (1990).

Connolly, J. A. D., 'Computation of phase equilibria by linear programming: A tool for geodynamic modeling and its application to subduction zone decarbonation", Earth and Planetary Science Letters **236**, 1-2, 524–541 (2005).

Cottaar, S. and V. Lekic, 'Morphology of seismically slow lower-mantle structures", Geophysical Supplements to the Monthly Notices of the Royal Astronomical Society **207**, 2, 1122–1136 (2016).

Cottaar, S. and B. Romanowicz, 'An unsually large ulvz at the base of the mantle near hawaii", Earth and Planetary Science Letters **355**, 213–222 (2012).

Couper, S., S. Speziale, H. Marquardt, H.-P. Liermann and L. Miyagi, 'Does heterogeneous strain act as a control on seismic anisotropy in earth's lower mantle?", Frontiers in Earth Science **8**, 540449 (2020).

Courtillot, V., A. Davaille, J. Besse and J. Stock, 'Three distinct types of hotspots in the earth's mantle", Earth and Planetary Science Letters **205**, 3-4, 295–308 (2003).

Criniti, G., T. Boffa Ballaran, A. Kurnosov, Z. Liu, K. Glazyrin, M. Merlini, M. Hanfland and D. J. Frost, 'Thermal equation of state and structural evolution of al-bearing bridgmanite", Journal of Geophysical Research: Solid Earth **129**, 1, e2023JB026879 (2024).

Criniti, G., A. Kurnosov, T. Boffa Ballaran and D. J. Frost, 'Single-crystal elasticity of $mgsio_3$ bridgmanite to mid-lower mantle pressure", Journal of Geophysical Research: Solid Earth **126**, 5, e2020JB020967 (2021).

CrystalMaker, S. L., 'Crystalmaker x (version 10.8.1)", Software, URL https://www.crystalmaker.com, software for crystal and molecular modeling. (2023).

Cullity, B. D. B. D. and S. R. Stock, *Elements of X-ray diffraction*, Always learning (Pearson, Harlow, Essex, 2014), third, pearson new international edition. edn.

Dannberg, J., K. Chotalia and R. Gassmöller, 'How lowermost mantle viscosity controls the chemical structure of earth's deep interior", Communications Earth & Environment **4**, 1, 493 (2023).

Debye, P. and P. Scherrer, 'Interferenzen an regellos orientierten teilchen im röntgenlicht. i.", Nachrichten von der Gesellschaft der Wissenschaften zu Göttingen, Mathematisch-Physikalische Klasse **1916**, 1–15, URL http://eudml.org/doc/58947 (1916).

Demouchy, S., 'Diffusion of hydrogen in olivine grain boundaries and implications for the survival of water-rich zones in the earth's mantle", Earth and Planetary Science Letters **295**, 1-2, 305–313 (2010).

Dennis, J. G. and C. T. Walker, 'Earthquakes resulting from metastable phase transitions", Tectonophysics **2**, 5, 401–407 (1965).

Deschamps, F., L. Cobden and P. J. Tackley, 'The primitive nature of large low shear-wave velocity provinces", Earth and Planetary Science Letters **349**, 198–208 (2012).

Deschamps, F. and J. Trampert, 'Mantle tomography and its relation to temperature and composition", Physics of the Earth and Planetary Interiors **140**, 4, 277–291 (2003).

Dewaele, A., P. Loubeyre and M. Mezouar, 'Equations of state of six metals above 94 gpa", Physical Review B—Condensed Matter and Materials Physics **70**, 9, 094112 (2004).

Dewaele, A., P. Loubeyre, F. Occelli, M. Mezouar, P. I. Dorogokupets and M. Torrent, 'Quasihydrostatic equation of state of iron above 2 mbar", Physical Review Letters **97**, 21, 215504 (2006).

Dewaele, A., M. Torrent, P. Loubeyre and M. Mezouar, 'Compression curves of transition metals in the mbar range: Experiments and projector augmented-wave calculations", Physical Review B—Condensed Matter and Materials Physics **78**, 10, 104102 (2008).

Dohmen, R. and R. Milke, 'Diffusion in polycrystalline materials: grain boundaries, mathematical models, and experimental data", Reviews in Mineralogy and Geochemistry **72**, 1, 921–970 (2010).

Dong, W., K. Glazyrin, S. Khandarkhaeva, T. Fedotenko, J. Bednarčík, E. Greenberg, L. Dubrovinsky, N. Dubrovinskaia and H.-P. Liermann, 'Fe0. 79si0. 07b0. 14 metallic glass gaskets for high-pressure research beyond 1 mbar", Synchrotron Radiation **29**, 5, 1167–1179 (2022).

Dorfman, S. M. and T. S. Duffy, 'Effect of fe-enrichment on seismic properties of perovskite and post-perovskite in the deep lower mantle", Geophysical Journal International **197**, 2, 910–919 (2014).

Dorfman, S. M., S. R. Shieh, Y. Meng, V. B. Prakapenka and T. S. Duffy, 'Synthesis and equation of state of perovskites in the (mg, fe) 3al2si3o12 system to 177 gpa", Earth and Planetary Science Letters **357**, 194–202 (2012).

Dou, P., J. Brodholt, L. Vočadlo, H. Ni and Y. Li, 'Ab initio evaluation of point defects in bridgmanite under lower mantle conditions", Journal of Geophysical Research: Solid Earth **130**, 5, e2025JB031147 (2025).

Dove, M. T., *Introduction to lattice dynamics*, no. 4 in Cambridge Topics in Mineral Physics and Chemistry, Series Number 4 (Cambridge university press, 1993).

Downs, R. T., C.-S. Zha, T. S. DuFFY and L. W. Finger, 'The equation of state of forsterite to 17.2 gpa and effects of pressure media", American Mineralogist **81**, 1-2, 51–55 (1996).

Dubrovinsky, L., H. Annersten, N. Dubrovinskaia, F. Westman, H. Harryson, O. Fabrichnaya and S. Carlson, 'Chemical interaction of fe and al2o3 as a source of heterogeneity at the earth's core–mantle boundary", Nature **412**, 6846, 527–529 (2001).

Dziewonski, A. M. and D. L. Anderson, 'Preliminary reference earth model", Physics of the earth and planetary interiors **25**, 4, 297–356 (1981).

Dziewonski, A. M., V. Lekic and B. A. Romanowicz, 'Mantle anchor structure: an argument for bottom up tectonics", Earth and Planetary Science Letters **299**, 1-2, 69–79 (2010).

Edmund, E., I. Chuvashova, Z. Konôpková, R. Husband, C. Strohm, K. Appel, C. Bähtz, O. Ball, V. Bouffetier, K. Brugman *et al.*, 'The thermal conductivity of bridgmanite at lower mantle conditions using a multi-technique approach", Journal of Geophysical Research: Solid Earth **129**, 6, e2024JB028823 (2024).

Eremets, M., *High pressure experimental methods* (Oxford University Press, 1996).

Errandonea, D., R. Boehler, S. Japel, M. Mezouar and L. Benedetti, 'Structural transformation of compressed solid ar: An x-ray diffraction study to 114 gpa", Physical Review B—Condensed Matter and Materials Physics **73**, 9, 092106 (2006).

Etter, M. and R. E. Dinnebier, 'Direct parameterization of the pressure-dependent volume by using an inverted approximate vinet equation of state", Applied Crystallography **47**, 1, 384–390 (2014).

Evans, A., M. Zuber, B. Weiss and S. Tikoo, 'A wet, heterogeneous lunar interior: Lower mantle and core dynamo evolution", Journal of Geophysical Research: Planets **119**, 5, 1061–1077 (2014).

Ewald, P. and P. Ewald, 'Über röntgenstrahlen", Kristalle und Röntgenstrahlen pp. 52–66 (1923).

Farver, J. R. and R. A. Yund, 'Silicon diffusion in forsterite aggregates: Implications for diffusion accommodated creep", Geophysical Research Letters **27**, 15, 2337–2340 (2000).

Farver, J. R., R. A. Yund and D. C. Rubie, 'Magnesium grain boundary diffusion in forsterite aggregates at 1000–1300 c and 0.1 mpa to 10 gpa", Journal of Geophysical Research: Solid Earth **99**, B10, 19809–19819 (1994).

Faust, J. and E. Knittle, 'The stability and equation of state of majoritic garnet synthesized from natural basalt at mantle conditions", Geophysical research letters **23**, 23, 3377–3380 (1996).

Fei, H., Z. Liu, R. Huang, S. Kamada, N. Hirao, S. Kawaguchi, C. McCammon and T. Katsura, 'Pressure destabilizes oxygen vacancies in bridgmanite", Journal of Geophysical Research: Solid Earth **126**, 12, e2021JB022437 (2021).

Fei, H., Y. Lyu, F. Wang, C. McCammon and T. Katsura, 'The effects of trivalent cations (al and fe) on the grain growth rates of bridgmanite", Earth and Planetary Science Letters **646**, 118983 (2024).

Fichtner, A., B. L. Kennett, V. C. Tsai, C. H. Thurber, A. J. Rodgers, C. Tape, N. Rawlinson, R. D. Borcherdt, S. Lebedev, K. Priestley *et al.*, 'Seismic tomography 2024", Bulletin of the Seismological Society of America **114**, 3, 1185–1213 (2024).

Finger, L., R. Hazen, G. Zou, H. Mao and P. Bell, 'Structure and compression of crystalline argon and neon at high pressure and room temperature", Applied Physics Letters **39**, 11, 892–894 (1981).

Fiquet, G., D. Andrault, A. Dewaele, T. Charpin, M. Kunz and D. Haüsermann, 'Pvt equation of state of mgsio3 perovskite", Physics of the Earth and Planetary Interiors **105**, 1-2, 21–31 (1998).

Fiquet, G., A. Dewaele, D. Andrault, M. Kunz and T. Le Bihan, 'Thermoelastic properties and crystal structure of mgsio3 perovskite at lower mantle pressure and temperature conditions", Geophysical Research Letters **27**, 1, 21–24 (2000).

Fitzgerald, R., K. Keil and K. F. Heinrich, 'Solid-state energy-dispersion spectrometer for electron-microprobe x-ray analysis", Science **159**, 3814, 528–530 (1968).

Foley, B. J., D. Bercovici and L. T. Elkins-Tanton, 'Initiation of plate tectonics from post-magma ocean thermochemical convection", Journal of Geophysical Research: Solid Earth **119**, 11, 8538–8561 (2014).

Frost, D., U. Mann, Y. Asahara and D. Rubie, 'The redox state of the mantle during and just after core formation", Philosophical Transactions of the Royal Society A: Mathematical, Physical and Engineering Sciences **366**, 1883, 4315–4337 (2008).

Frost, D. J., 'The upper mantle and transition zone", Elements **4**, 3, 171–176 (2008).

Frost, D. J. and R. Myhill, 'Chemistry of the lower mantle", Deep Earth: Physics and Chemistry of the Lower Mantle and Core pp. 225–240 (2016).

Fu, S., J. Yang, N. Tsujino, T. Okuchi, N. Purevjav and J.-F. Lin, 'Single-crystal elasticity of (al, fe)-bearing bridgmanite and seismic shear wave radial anisotropy at the topmost lower mantle", Earth and Planetary Science Letters **518**, 116–126 (2019).

Fu, S., J. Yang, Y. Zhang, T. Okuchi, C. McCammon, H.-I. Kim, S. K. Lee and J.-F. Lin, 'Abnormal elasticity of fe-bearing bridgmanite in the earth's lower mantle", Geophysical Research Letters **45**, 10, 4725–4732 (2018).

Fu, S., Y. Zhang, T. Okuchi and J.-F. Lin, 'Single-crystal elasticity of (al, fe)-bearing bridgmanite up to 82 gpa", American Mineralogist: Journal of Earth and Planetary Materials **108**, 4, 719–730 (2023).

Fujino, K., D. Nishio-Hamane, Y. Kuwayama, N. Sata, S. Murakami, M. Whitaker, A. Shinozaki, H. Ohfuji, Y. Kojima, T. Irifune *et al.*, 'Spin transition and substitution of fe3+ in al-bearing post-mg-perovskite", Physics of the Earth and Planetary Interiors **217**, 31–35 (2013).

Fukui, H., A. Yoneda, A. Nakatsuka, N. Tsujino, S. Kamada, E. Ohtani, A. Shatskiy, N. Hirao, S. Tsutsui, H. Uchiyama *et al.*, 'Effect of cation substitution on bridgmanite elasticity: A key to interpret seismic anomalies in the lower mantle", Scientific reports **6**, 1, 33337 (2016).

Funamori, N., T. Yagi, W. Utsumi, T. Kondo, T. Uchida and M. Funamori, 'Thermoelastic properties of mgsio3 perovskite determined by in situ x ray observations up to 30 gpa and 2000 k", Journal of Geophysical Research: Solid Earth **101**, B4, 8257–8269 (1996).

Gardés, E., B. Wunder, K. Marquardt and W. Heinrich, 'The effect of water on intergranular mass transport: new insights from diffusion-controlled reaction rims in the mgo–sio2 system", Contributions to Mineralogy and Petrology **164**, 1, 1–16 (2012).

Garnero, E. J., 'Heterogeneity of the lowermost mantle", Annual Review of Earth and Planetary Sciences **28**, 1, 509–537 (2000).

Garnero, E. J. and A. K. McNamara, 'Structure and dynamics of earth's lower mantle", science **320**, 5876, 626–628 (2008).

Garnero, E. J., A. K. McNamara and S.-H. Shim, 'Continent-sized anomalous zones with low seismic velocity at the base of earth's mantle", Nature Geoscience **9**, 7, 481–489 (2016).

Gasc, J., C. Daigre, A. Moarefvand, D. Deldicque, J. Fauconnier, B. Gardonio, C. Madonna, P. Burnley and A. Schubnel, 'Deep-focus earthquakes: From high-temperature experiments to cold slabs", Geology **50**, 9, 1018–1022 (2022).

Gasparik, T., 'Evidence for immiscibility in majorite garnet from experiments at 13–15 gpa", Geochimica et Cosmochimica Acta **64**, 9, 1641–1650 (2000).

Geng, M. and H. Jónsson, 'Density functional theory calculations and thermodynamic analysis of bridgmanite surface structure", Physical Chemistry Chemical Physics **21**, 3, 1009–1013 (2019).

German, R. M., *Sintering Theory and Practice* (Wiley-Interscience, 1996), 1st edn., provided by the SAO/NASA Astrophysics Data System.

Gessmann, C., B. Wood, D. Rubie and M. Kilburn, 'Solubility of silicon in liquid metal at high pressure: implications for the composition of the earth's core", Earth and Planetary Science Letters **184**, 2, 367–376 (2001).

Grüninger, H., Z. Liu, R. Siegel, T. Boffa Ballaran, T. Katsura, J. Senker and D. J. Frost, 'Oxygen vacancy ordering in aluminous bridgmanite in the earth's lower mantle", Geophysical Research Letters **46**, 15, 8731–8740 (2019).

Guerrero, J. M., F. Deschamps, W.-P. Hsieh and P. J. Tackley, 'The combined effect of heterogeneous thermal conductivity, chemical density contrast, and heat-producing element enrichment on the stability of primordial reservoirs above the core-mantle boundary", Earth and Planetary Science Letters **637**, 118699 (2024).

Guo, Q., H. Hou, K. Wang, M. Li, P. K. Liaw and Y. Zhao, 'Coalescence of al0. 3cocrfeni polycrystalline high-entropy alloy in hot-pressed sintering: a molecular dynamics and phase-field study", Npj Computational Materials **9**, 1, 185 (2023).

Hacker, B. R., G. A. Abers and S. M. Peacock, 'Subduction factory 1. theoretical mineralogy, densities, seismic wave speeds, and h2o contents", Journal of Geophysical Research: Solid Earth **108**, B1 (2003).

Hacker, B. R. and G. Bebout, 'Eclogite formation and the rheology, buoyancy, seismicity, and h˜ 2o content of oceanic crust", Geophysical Monograph-American Geophysical Union **96**, 337–346 (1996).

Hager, B. H., R. W. Clayton, M. A. Richards, R. P. Comer and A. M. Dziewonski, 'Lower mantle heterogeneity, dynamic topography and the geoid", Nature **313**, 6003, 541–545 (1985).

Halliday, A. N. and R. M. Canup, 'The accretion of planet earth", Nature Reviews Earth & Environment **4**, 1, 19–35 (2023).

Halliday, D., R. Resnick and J. Walker, *Fundamentals of physics* (John Wiley & Sons, 2013).

Hama, J. and K. Suito, 'The search for a universal equation of state correct up to very high pressures", Journal of Physics: Condensed Matter **8**, 1, 67 (1996).

Hayden, L. A. and E. B. Watson, 'Grain boundary mobility of carbon in earth's mantle: A possible carbon flux from the core", Proceedings of the National Academy of Sciences **105**, 25, 8537–8541 (2008).

Hazen, R., R. Downs, P. Conrad, L. Finger and T. Gasparik, 'Comparative compressibilities of majorite-type garnets", Physics and Chemistry of Minerals **21**, 344–349 (1994).

He, Y., D. Y. Kim, V. V. Struzhkin, Z. M. Geballe, V. Prakapenka and H.-k. Mao, 'The stability of fehx and hydrogen transport at earth's core mantle boundary", Science Bulletin **68**, 14, 1567–1573 (2023).

Hernlund, J., A. McNamara and G. Schubert, '7.11: The core–mantle boundary region", Treatise on geophysics **2**, 7, 461–519 (2015).

Hernlund, J. W. and I. Bonati, 'Modeling ultralow velocity zones as a thin chemically distinct dense layer at the core-mantle boundary", Journal of Geophysical Research: Solid Earth **124**, 8, 7902–7917 (2019).

Hernlund, J. W. and C. Houser, 'On the statistical distribution of seismic velocities in earth's deep mantle", Earth and Planetary Science Letters **265**, 3-4, 423–437 (2008).

Hirose, K., 'Phase transitions in pyrolitic mantle around 670-km depth: Implications for upwelling of plumes from the lower mantle", Journal of Geophysical Research: Solid Earth **107**, B4, ECV–3 (2002).

Hirose, K., 'Phase transition and melting in the deep lower mantle", Deep Earth: Physics and Chemistry of the Lower Mantle and Core pp. 209–224 (2016).

Hirose, K., R. Sinmyo, N. Sata and Y. Ohishi, 'Determination of post-perovskite phase transition boundary in mgsio3 using au and mgo pressure standards", Geophysical Research Letters **33**, 1 (2006).

Hofmann, A. W., 'Mantle geochemistry: the message from oceanic volcanism", Nature **385**, 6613, 219–229 (1997).

Hofmeister, A. M., 'Interatomic potentials calculated from equations of state: Limitation of finite strain to moderate k′", Geophysical Research Letters **20**, 7, 635–638 (1993).

Hohenberg, P. and W. Kohn, 'Inhomogeneous electron gas", Phys. Rev. **136**, B864–B871 (1964).

Hohenberg, P., W. Kohn and L. Sham, 'The beginnings and some thoughts on the future", in 'Advances in Quantum Chemistry", vol. 21, pp. 7–26 (Elsevier, 1990).

Holland, T. and R. Powell, 'An improved and extended internally consistent thermodynamic dataset for phases of petrological interest, involving a new equation of state for solids", Journal of metamorphic Geology **29**, 3, 333–383 (2011).

Holmes, N., J. Moriarty, G. Gathers and W. Nellis, 'The equation of state of platinum to 660 gpa (6.6 mbar)", Journal of Applied Physics **66**, 7, 2962–2967 (1989).

Horiuchi, H., M. Hirano, E. Ito and Y. Matsui, 'Mgsio3 (ilmenite-type): single crystal x-ray diffraction study", American Mineralogist **67**, 7-8, 788–793 (1982).

Hsieh, W.-P., F. Deschamps, T. Okuchi and J.-F. Lin, 'Reduced lattice thermal conductivity of fe-bearing bridgmanite in earth's deep mantle", Journal of Geophysical Research: Solid Earth **122**, 7, 4900–4917 (2017).

Hsieh, W.-P., F. Deschamps, T. Okuchi and J.-F. Lin, 'Effects of iron on the lattice thermal conductivity of earth's deep mantle and implications for mantle dynamics", Proceedings of the National Academy of Sciences **115**, 16, 4099–4104 (2018).

Hsu, H., P. Blaha, M. Cococcioni and R. M. Wentzcovitch, 'Spin-state crossover and hyperfine interactions of ferric iron in $mgsio_3$ perovskite", Physical Review Letters **106**, 11, 118501 (2011).

Hsu, H., G. Y. Yonggang and R. M. Wentzcovitch, 'Spin crossover of iron in aluminous mgsio3 perovskite and post-perovskite", Earth and Planetary Science Letters **359**, 34–39 (2012).

Huang, C., W. Leng and Z. Wu, 'Iron-spin transition controls structure and stability of llsvps in the lower mantle", Earth and Planetary Science Letters **423**, 173–181 (2015).

Huang, R., T. B. Ballaran, C. A. McCammon, N. Miyajima, D. Dolejš and D. J. Frost, 'The composition and redox state of bridgmanite in the lower mantle as a function of oxygen fugacity", Geochimica et Cosmochimica Acta **303**, 110–136 (2021a).

Huang, R., T. Boffa Ballaran, C. A. McCammon, N. Miyajima and D. J. Frost, 'The effect of fe-al substitution on the crystal structure of mgsio$_3$ bridgmanite", Journal of Geophysical Research: Solid Earth **126**, 9, e2021JB021936 (2021b).

Hummer, D. R. and Y. Fei, 'Synthesis and crystal chemistry of fe^{3+}-bearing (mg, fe^{3+})(si, fe^{3+}) o$_3$ perovskite", American Mineralogist **97**, 11-12, 1915–1921 (2012).

Irifune, T., 'An experimental investigation of the pyroxene-garnet transformation in a pyrolite composition and its bearing on the constitution of the mantle", Physics of the Earth and Planetary Interiors **45**, 4, 324–336 (1987).

Irifune, T., 'Kawai-type multianvil ultrahigh-pressure technology", Proceedings of the Japan Academy, Series B **100**, 3, 149–164 (2024).

Irifune, T. and A. Ringwood, 'Phase transformations in subducted oceanic crust and buoyancy relationships at depths of 600–800 km in the mantle", Earth and Planetary Science Letters **117**, 1-2, 101–110 (1993).

Irifune, T., A. Ringwood and W. Hibberson, 'Subduction of continental crust and terrigenous and pelagic sediments: an experimental study", Earth and Planetary Science Letters **126**, 4, 351–368 (1994).

Irifune, T., T. Shinmei, C. A. McCammon, N. Miyajima, D. C. Rubie and D. J. Frost, 'Iron partitioning and density changes of pyrolite in earth's lower mantle", Science **327**, 5962, 193–195 (2010).

Ishii, M. and J. Tromp, 'Normal-mode and free-air gravity constraints on lateral variations in velocity and density of earth's mantle", Science **285**, 5431, 1231–1236 (1999).

Ishii, T., E. Ohtani and A. Shatskiy, 'Aluminum and hydrogen partitioning between bridgmanite and high-pressure hydrous phases: Implications for water storage in the lower mantle", Earth and Planetary Science Letters **583**, 117441 (2022).

Ishii, T., L. Shi, R. Huang, N. Tsujino, D. Druzhbin, R. Myhill, Y. Li, L. Wang, T. Yamamoto, N. Miyajima *et al.*, 'Generation of pressures over 40 gpa using kawai-type multi-anvil press with tungsten carbide anvils", Review of Scientific Instruments **87**, 2 (2016).

Ismailova, L., E. Bykova, M. Bykov, V. Cerantola, C. McCammon, T. Boffa Ballaran, A. Bobrov, R. Sinmyo, N. Dubrovinskaia, K. Glazyrin *et al.*, 'Stability of fe, al-bearing bridgmanite in the lower mantle and synthesis of pure fe-bridgmanite", Science Advances **2**, 7, e1600427 (2016).

Ito, E. and E. Takahashi, 'Postspinel transformations in the system mg2sio4-fe2sio4 and some geophysical implications", Journal of Geophysical Research: Solid Earth **94**, B8, 10637–10646 (1989).

Jackson, I. and S. M. Rigden, 'Analysis of pvt data: constraints on the thermoelastic properties of high-pressure minerals", Physics of the earth and planetary interiors **96**, 2-3, 85–112 (1996).

Jeanloz, R., 'Finite-strain equation of state for high-pressure phases", Geophysical Research Letters **8**, 12, 1219–1222 (1981a).

Jeanloz, R., 'Majorite: Vibrational and compressional properties of a high-pressure phase", Journal of Geophysical Research: Solid Earth **86**, B7, 6171–6179 (1981b).

Jephcoat, A. P., 'Rare-gas solids in the earth's deep interior", Nature **393**, 6683, 355–358 (1998).

Juhin, A., G. Morin, E. Elkaïm, D. J. Frost, M. Fialin, F. Juillot and G. Calas, 'Structure refinement of a synthetic knorringite, mg3 (cr0. 8mg0. 1si0. 1) 2 (sio4) 3", American Mineralogist **95**, 1, 59–63 (2010).

Karato, S.-i., D. Wang *et al.*, *Physics and Chemistry of the Deep Earth* (Wiley Online Library, 2013).

Karki, B., L. Stixrude, S. Clark, M. Warren, G. Ackland and J. Crain, 'Elastic properties of orthorhombic mgsio$_3$ perovskite at lower mantle pressures", American Mineralogist **82**, 5-6, 635–638 (1997).

Karki, B. B. and J. Crain, 'First-principles determination of elastic properties of casio3 perovskite at lower mantle pressures", Geophysical research letters **25**, 14, 2741–2744 (1998).

Kavner, A. and T. S. Duffy, 'Pressure–volume–temperature paths in the laser-heated diamond anvil cell", Journal of Applied Physics **89**, 3, 1907–1914 (2001).

Kawai, K. and T. Tsuchiya, 'Temperature profile in the lowermost mantle from seismological and mineral physics joint modeling", Proceedings of the National Academy of Sciences **106**, 52, 22119–22123 (2009).

Kawano, K., M. Nishi, H. Kuwahara, S. Kakizawa, T. Inoue and T. Kondo, 'Extensive iron–water exchange at earth's core–mantle boundary can explain seismic anomalies", Nature Communications **15**, 1, 8701 (2024).

King, S. D., D. J. Frost and D. C. Rubie, 'Why cold slabs stagnate in the transition zone", Geology **43**, 3, 231–234 (2015).

Kirby, S. H., S. Stein, E. A. Okal and D. C. Rubie, 'Metastable mantle phase transformations and deep earthquakes in subducting oceanic lithosphere", Reviews of geophysics **34**, 2, 261–306 (1996).

Kiseeva, E. S., D. M. Vasiukov, B. J. Wood, C. McCammon, T. Stachel, M. Bykov, E. Bykova, A. Chumakov, V. Cerantola, J. W. Harris *et al.*, 'Oxidized iron in garnets from the mantle transition zone", Nature Geoscience **11**, 2, 144–147 (2018).

Klotz, S., J. Chervin, P. Munsch and G. Le Marchand, 'Hydrostatic limits of 11 pressure transmitting media", Journal of Physics D: Applied Physics **42**, 7, 075413 (2009).

Knittle, E. and R. Jeanloz, 'Synthesis and equation of state of (mg, fe) sio3 perovskite to over 100 gigapascals", Science **235**, 4789, 668–670 (1987).

Kohn, W. and L. J. Sham, 'Self-consistent equations including exchange and correlation effects", Physical review **140**, 4A, A1133 (1965).

Komabayashi, T., K. Hirose, E. Sugimura, N. Sata, Y. Ohishi and L. S. Dubrovinsky, 'Simultaneous volume measurements of post-perovskite and perovskite in mgsio3 and their thermal equations of state", Earth and Planetary Science Letters **265**, 3-4, 515–524 (2008).

Konôpková, Z., A. Rothkirch, A. K. Singh, S. Speziale and H.-P. Liermann, 'In situ x-ray diffraction of fast compressed iron: Analysis of strains and stress under non-hydrostatic pressure", Physical Review B **91**, 14, 144101 (2015).

Korenaga, J., 'Scaling of plate tectonic convection with pseudoplastic rheology", Journal of Geophysical Research: Solid Earth **115**, B11 (2010).

Kubo, T., E. Ohtani, T. Kondo, T. Kato, M. Toma, T. Hosoya, A. Sano, T. Kikegawa and T. Nagase, 'Metastable garnet in oceanic crust at the top of the lower mantle", Nature **420**, 6917, 803–806 (2002).

Kudoh, Y., E. Ito and H. Takeda, 'Effect of pressure on the crystal structure of perovskite-type mgsio 3", Physics and chemistry of minerals **14**, 350–354 (1987).

Kulka, B. L., *Possible Control of Redox Conditions in the Laser-Heated Diamond Anvil Cell*, Master's thesis, Arizona State University (2021).

Kulka, B. L., J. D. Dolinschi, K. D. Leinenweber, V. B. Prakapenka and S.-H. Shim, 'The bridgmanite–akimotoite–majorite triple point determined in large volume press and laser-heated diamond anvil cell", Minerals **10**, 1, 67 (2020).

Kunimoto, T., T. Irifune, Y. Tange and K. Wada, 'Pressure generation to 50 gpa in kawai-type multianvil apparatus using newly developed tungsten carbide anvils", High Pressure Research **36**, 2, 97–104 (2016).

Kupenko, I., C. McCammon, R. Sinmyo, C. Prescher, A. Chumakov, A. Kantor, R. Rüffer and L. Dubrovinsky, 'Electronic spin state of fe, al-containing mgsio3 perovskite at lower mantle conditions", Lithos **189**, 167–172 (2014).

Kurnosov, A., H. Marquardt, D. J. Frost, T. B. Ballaran and L. Ziberna, 'Evidence for a fe3+-rich pyrolitic lower mantle from (al, fe)-bearing bridgmanite elasticity data", Nature **543**, 7646, 543–546 (2017).

Kuzmann, E., Z. Homonnay, Z. Klencsár and R. Szalay, '57fe mössbauer spectroscopy as a tool for study of spin states and magnetic interactions in inorganic chemistry", Molecules **26**, 4, 1062 (2021).

Lai, V. H., D. V. Helmberger, V. V. Dobrosavljevic, W. Wu, D. Sun, J. M. Jackson and M. Gurnis, 'Strong ulvz and slab interaction at the northeastern edge of the pacific llsvp favors plume generation", Geochemistry, Geophysics, Geosystems **23**, 2, e2021GC010020 (2022a).

Lai, X., F. Zhu, J. Gao, E. Greenberg, V. B. Prakapenka, Y. Meng and B. Chen, 'Melting of the fe-c-h system and earth's deep carbon-hydrogen cycle", Geophysical Research Letters **49**, 13, e2022GL098919 (2022b).

Le Bail, A., H. Duroy and J. L. Fourquet, 'Ab-initio structure determination of lisbwo6 by x-ray powder diffraction", Materials Research Bulletin **23**, 3, 447–452 (1988).

Le Bars, M. and A. Davaille, 'Whole layer convection in a heterogeneous planetary mantle", Journal of Geophysical Research: Solid Earth **109**, B3 (2004).

Li, B., C. Ji, W. Yang, J. Wang, K. Yang, R. Xu, W. Liu, Z. Cai, J. Chen and H.-k. Mao, 'Diamond anvil cell behavior up to 4 mbar", Proceedings of the National Academy of Sciences **115**, 8, 1713–1717 (2018).

Li, J., D. Tian, M. Li, D. Sun, Z. Mao and V. V. Dobrosavljevic, 'Ultralow velocity zones at the core-mantle boundary near the caroline hotspot", Journal of Geophysical Research: Solid Earth **130**, 7, e2024JB030763 (2025).

Li, L., J. P. Brodholt, S. Stackhouse, D. J. Weidner, M. Alfredsson and G. D. Price, 'Elasticity of (mg, fe)(si, al) o_3-perovskite at high pressure", Earth and Planetary Science Letters **240**, 2, 529–536 (2005).

Li, Z., K. Leng, J. Jenkins and S. Cottaar, 'Kilometer-scale structure on the core–mantle boundary near hawaii", Nature Communications **13**, 1, 2787 (2022).

Liang, H., N. Min, D. Wang, X. Song, P. Gao and Q. Li, 'Unexpected strength of noble gas solids in diamond anvil cells", The Journal of Physical Chemistry C **128**, 11, 4839–4847 (2024).

Liebermann, R. C., 'Multi-anvil, high pressure apparatus: a half-century of development and progress", High Pressure Research **31**, 4, 493–532 (2011).

Lin, J.-F., S. Speziale, Z. Mao and H. Marquardt, 'Effects of the electronic spin transitions of iron in lower mantle minerals: Implications for deep mantle geophysics and geochemistry", Reviews of Geophysics **51**, 2, 244–275 (2013).

Lin, J.-F., V. V. Struzhkin, S. D. Jacobsen, M. Y. Hu, P. Chow, J. Kung, H. Liu, H.-k. Mao and R. J. Hemley, 'Spin transition of iron in magnesiowüstite in the earth's lower mantle", Nature **436**, 7049, 377–380 (2005).

Lin, J.-F. and T. Tsuchiya, 'Spin transition of iron in the earth's lower mantle", Physics of the Earth and Planetary Interiors **170**, 3-4, 248–259 (2008).

Lin, J.-F., G. Vankó, S. D. Jacobsen, V. Iota, V. V. Struzhkin, V. B. Prakapenka, A. Kuznetsov and C.-S. Yoo, 'Spin transition zone in earth's lower mantle", Science **317**, 5845, 1740–1743 (2007).

Liu, C. and R. Cohen, 'Electrical resistivity, thermal conductivity, and viscosity of fe-h alloys at earth's core conditions", Physical Review B **111**, 9, 094101 (2025).

Liu, J., S. M. Dorfman, F. Zhu, J. Li, Y. Wang, D. Zhang, Y. Xiao, W. Bi and E. E. Alp, 'Valence and spin states of iron are invisible in earth's lower mantle", Nature Communications **9**, 1, 1284 (2018).

Liu, L.-g., 'Bulk moduli of mgsio3-perovskite", Physics of the earth and planetary interiors **72**, 1-2, 12–20 (1992).

Lou, Y., S. Stackhouse, A. M. Walker and Z. Zhang, 'Thermoelastic properties of mgsio3-majorite at high temperatures and pressures: A first principles study", Physics of the Earth and Planetary Interiors **303**, 106491 (2020).

Lundin, S., K. Catalli, J. Santillan, S.-H. Shim, V. Prakapenka, M. Kunz and Y. Meng, 'Effect of fe on the equation of state of mantle silicate perovskite over 1 mbar", Physics of the Earth and Planetary Interiors **168**, 1-2, 97–102 (2008).

Lyubutin, I. S., V. V. Struzhkin, A. Mironovich, A. G. Gavriliuk, P. G. Naumov, J.-F. Lin, S. G. Ovchinnikov, S. Sinogeikin, P. Chow, Y. Xiao *et al.*, 'Quantum critical point and spin fluctuations in lower-mantle ferropericlase", Proceedings of the National Academy of Sciences **110**, 18, 7142–7147 (2013).

Mao, H., R. Hemley, Y. Fei, J. Shu, L. Chen, A. Jephcoat, Y. Wu and W. Bassett, 'Effect of pressure, temperature, and composition on lattice parameters and density of (fe, mg) sio3-perovskites to 30 gpa", Journal of Geophysical Research: Solid Earth **96**, B5, 8069–8079 (1991).

Mao, Z., J. Lin, H. Scott, H. Watson, V. Prakapenka, Y. Xiao, P. Chow and C. McCammon, 'Iron-rich perovskite in the earth's lower mantle", Earth and Planetary Science Letters **309**, 3-4, 179–184 (2011).

Mao, Z., J.-F. Lin, J. Yang, T. Inoue and V. B. Prakapenka, 'Effects of the fe^{3+} spin transition on the equation of state of bridgmanite", Geophysical Research Letters **42**, 11, 4335–4342 (2015).

Mao, Z., F. Wang, J.-F. Lin, S. Fu, J. Yang, X. Wu, T. Okuchi, N. Tomioka, V. B. Prakapenka, Y. Xiao *et al.*, 'Equation of state and hyperfine parameters of high-spin bridgmanite in the earth's lower mantle by synchrotron x-ray diffraction and mössbauer spectroscopy", American Mineralogist **102**, 2, 357–368 (2017).

Marquardt, H. and A. R. Thomson, 'Experimental elasticity of earth's deep mantle", Nature Reviews Earth & Environment **1**, 9, 455–469 (2020).

Marquardt, K. and U. H. Faul, 'The structure and composition of olivine grain boundaries: 40 years of studies, status and current developments", Physics and Chemistry of Minerals **45**, 2, 139–172 (2018).

Marquardt, K., E. Petrishcheva, E. Gardés, R. Wirth, R. Abart and W. Heinrich, 'Grain boundary and volume diffusion experiments in yttrium aluminium garnet bicrystals at 1,723 k: a miniaturized study", Contributions to Mineralogy and Petrology **162**, 739–749 (2011a).

Marquardt, K., Q. M. Ramasse, C. Kisielowski and R. Wirth, 'Diffusion in yttrium aluminium garnet at the nanometer-scale: Insight into the effective grain boundary width", American Mineralogist **96**, 10, 1521–1529 (2011b).

McAneney, J., *Characteristics of Thin and Ultrathin Film Ferroelectric Capacitor Structures*, Ph.D. thesis, Queen's University of Belfast (2006).

McCammon, C., ‘Perovskite as a possible sink for ferric iron in the lower mantle”, Nature **387**, 6634, 694–696 (1997).

McCammon, C., ‘The paradox of mantle redox”, Science **308**, 5723, 807–808 (2005).

McCammon, C., S. Lauterbach, F. Seifert, F. Langenhorst and P. Van Aken, ‘Iron oxidation state in lower mantle mineral assemblages: I. empirical relations derived from high-pressure experiments”, Earth and Planetary Science Letters **222**, 2, 435–449 (2004).

McDonough, W. F. and S.-S. Sun, ‘The composition of the earth”, Chemical geology **120**, 3-4, 223–253 (1995).

McNamara, A. K., ‘A review of large low shear velocity provinces and ultra low velocity zones”, Tectonophysics **760**, 199–220 (2019).

McNamara, A. K. and S. Zhong, ‘The influence of thermochemical convection on the fixity of mantle plumes”, Earth and Planetary Science Letters **222**, 2, 485–500 (2004).

Middelburg, J. J., ‘The gibbs free energy”, in ‘Thermodynamics and Equilibria in Earth System Sciences: An Introduction”, pp. 35–46 (Springer, 2024).

Milke, R., R. Dohmen, H.-W. Becker and R. Wirth, ‘Growth kinetics of enstatite reaction rims studied on nano-scale, part i: Methodology, microscopic observations and the role of water”, Contributions to Mineralogy and Petrology **154**, 519–533 (2007).

Milke, R., M. Wiedenbeck and W. Heinrich, ‘Grain boundary diffusion of si, mg, and o in enstatite reaction rims: a sims study using isotopically doped reactants”, Contributions to Mineralogy and Petrology **142**, 15–26 (2001).

Mills, R., D. Liebenberg, J. Bronson and L. Schmidt, ‘Procedure for loading diamond cells with high-pressure gas”, Review of Scientific Instruments **51**, 7, 891–895 (1980).

Mohn, C. E. and R. G. Trønnes, ‘Iron spin state and site distribution in fealo3-bearing bridgmanite”, Earth and Planetary Science Letters **440**, 178–186 (2016).

Monkhorst, H. J. and J. D. Pack, ‘Special points for brillouin-zone integrations”, Physical review B **13**, 12, 5188 (1976).

Muir, J. M. and J. P. Brodholt, ‘Ferrous iron partitioning in the lower mantle”, Physics of the Earth and Planetary Interiors **257**, 12–17 (2016).

Muir, J. M. and J. P. Brodholt, ‘Ferric iron in bridgmanite and implications for ulvzs”, Physics of the Earth and Planetary Interiors **306**, 106505 (2020).

Murakami, M., A. F. Goncharov, N. Miyajima, D. Yamazaki and N. Holtgrewe, ‘Radiative thermal conductivity of single-crystal bridgmanite at the core-mantle boundary with implications for thermal evolution of the earth”, Earth and Planetary Science Letters **578**, 117329 (2022).

Murakami, M., K. Hirose, K. Kawamura, N. Sata and Y. Ohishi, ‘Post-perovskite phase transition in mgsio3”, Science **304**, 5672, 855–858 (2004).

Murakami, M., K. Hirose, N. Sata and Y. Ohishi, 'Post-perovskite phase transition and mineral chemistry in the pyrolitic lowermost mantle", Geophysical Research Letters **32**, 3 (2005).

Murakami, M., Y. Ohishi, N. Hirao and K. Hirose, 'A perovskitic lower mantle inferred from high-pressure, high-temperature sound velocity data", Nature **485**, 7396, 90–94 (2012).

Murnaghan, F. D., 'The compressibility of media under extreme pressures", Proceedings of the National Academy of Sciences **30**, 9, 244–247 (1944).

Nakagawa, T. and P. J. Tackley, 'Influence of combined primordial layering and recycled morb on the coupled thermal evolution of earth's mantle and core", Geochemistry, Geophysics, Geosystems **15**, 3, 619–633 (2014).

Nakajima, Y., D. J. Frost and D. C. Rubie, 'Ferrous iron partitioning between magnesium silicate perovskite and ferropericlase and the composition of perovskite in the earth's lower mantle", Journal of Geophysical Research: Solid Earth **117**, B8 (2012).

Nakatsuka, A., H. Fukui, S. Kamada, N. Hirao, M. Ohkawa, K. Sugiyama and T. Yoshino, 'Incorporation mechanism of fe and al into bridgmanite in a subducting mid-ocean ridge basalt and its crystal chemistry", Scientific reports **11**, 1, 22839 (2021).

Nakatsuka, A., A. Yoshiasa, T. Yamanaka and O. Ohtaka, 'Symmetry change of majorite solid-solution in the system mg3al2si3o12-mgsio3", American Mineralogist **84**, 7-8, 1135–1143 (1999).

Nishio-Hamane, D., T. Nagai, K. Fujino, Y. Seto and N. Takafuji, 'Fe3+ and al solubilities in mgsio3 perovskite: implication of the fe3+ alo3 substitution in mgsio3 perovskite at the lower mantle condition", Geophysical research letters **32**, 16 (2005).

Nishio-Hamane, D., Y. Seto, K. Fujino and T. Nagai, 'Effect of fealo3 incorporation into mgsio3 on the bulk modulus of perovskite", Physics of the Earth and Planetary Interiors **166**, 3-4, 219–225 (2008).

Oganov, A. R., J. P. Brodholt and G. D. Price, 'Ab initio elasticity and thermal equation of state of mgsio3 perovskite", Earth and Planetary Science Letters **184**, 3-4, 555–560 (2001a).

Oganov, A. R., J. P. Brodholt and G. D. Price, 'The elastic constants of mgsio3 perovskite at pressures and temperatures of the earth's mantle", Nature **411**, 6840, 934–937 (2001b).

Oganov, A. R. and S. Ono, 'Theoretical and experimental evidence for a post-perovskite phase of mgsio3 in earth's d "layer", Nature **430**, 6998, 445–448 (2004).

Ohtani, E., 'Water in the mantle", Elements **1**, 1, 25–30 (2005).

Ohtani, E., 'The role of water in earth's mantle", National Science Review **7**, 1, 224–232 (2020).

Okuda, Y., K. Ohta, R. Sinmyo, K. Hirose, T. Yagi and Y. Ohishi, 'Effect of spin transition of iron on the thermal conductivity of (fe, al)-bearing bridgmanite", Earth and Planetary Science Letters **520**, 188–198 (2019).

Okuda, Y., K. Ohta, T. Yagi, R. Sinmyo, T. Wakamatsu, K. Hirose and Y. Ohishi, 'The effect of iron and aluminum incorporation on lattice thermal conductivity of bridgmanite at the earth's lower mantle", Earth and Planetary Science Letters **474**, 25–31 (2017).

Panero, W. R., S. Akber-Knutson and L. Stixrude, 'Al2o3 incorporation in mgsio3 perovskite and ilmenite", Earth and Planetary Science Letters **252**, 1-2, 152–161 (2006).

Parlinski, K., Z. Li and Y. Kawazoe, 'First-principles determination of the soft mode in cubic zro_2", Phys. Rev. Lett. **78**, 21, 4063–4066, original finite-displacement phonon paper (1997).

Pauling, L., 'The influence of relative ionic sizes on the properties of ionic compounds", Journal of the American Chemical Society **50**, 4, 1036–1045 (1928).

Pawley, G., 'Unit-cell refinement from powder diffraction scans", Applied Crystallography **14**, 6, 357–361 (1981).

Perdew, J. P., 'Climbing the ladder of density functional approximations", MRS bulletin **38**, 9, 743–750 (2013).

Perdew, J. P., K. Burke and M. Ernzerhof, 'Generalized gradient approximation made simple", Physical review letters **77**, 18, 3865 (1996).

Perdew, J. P., A. Ruzsinszky, G. I. Csonka, O. A. Vydrov, G. E. Scuseria, L. A. Constantin, X. Zhou and K. Burke, 'Restoring the density-gradient expansion for exchange in solids and surfaces", Physical review letters **100**, 13, 136406 (2008).

Poirier, J.-P., *Introduction to the Physics of the Earth's Interior* (Cambridge University Press, 2000).

Porcelli, D. and A. Halliday, 'The core as a possible source of mantle helium", Earth and Planetary Science Letters **192**, 1, 45–56 (2001).

Powell, R. and T. Holland, 'On thermobarometry", Journal of Metamorphic Geology **26**, 2, 155–179 (2008).

Prakapenka, V. B., G. Shen, M. L. Rivers, S. R. Sutton and L. Dubrovinsky, 'Grain-size control in situ at high pressures and high temperatures in a diamond-anvil cell", Synchrotron Radiation **12**, 5, 560–565 (2005).

Prescher, C. and V. B. Prakapenka, 'Dioptas: a program for reduction of two-dimensional x-ray diffraction data and data exploration", High Pressure Research **35**, 3, 223–230 (2015).

Prevey, P. S., 'X-ray diffraction residual stress techniques", in 'ASM Handbook", edited by R. E. Whan, vol. 10 of *Materials Characterization*, pp. 380–392 (ASM International, Materials Park, OH, 1986).

Putz, H. and K. Brandenburg, 'Match! - phase analysis using powder diffraction", `https://www.crystalimpact.de/match`, accessed: 2025-04-04 (2025).

Racioppi, S., M. Miao and E. Zurek, 'Intercalating helium into a-site vacant perovskites", Chemistry of Materials **35**, 11, 4297–4310 (2023).

Rahaman, M. N., *Ceramic processing and sintering* (CRC press, 2017).

Refson, K., S. J. Clark, J. A. Spencer and F. Cora, 'Phonons and thermodynamic properties with castep", J. Phys.: Condens. Matter **33**, 46, 464002 (2021).

Richards, A., 'University of oxford advanced research computing", Zenodo **10**, 5281 (2015).

Rietveld, H. M., 'A profile refinement method for nuclear and magnetic structures", Applied Crystallography **2**, 2, 65–71 (1969).

Ringwood, A., 'A model for the upper mantle", Journal of Geophysical Research **67**, 2, 857–867 (1962).

Ringwood, A. E., 'Composition and petrology of the earth's mantle", MacGraw-Hill **618** (1975).

Ringwood, A. E., 'Phase transformations and their bearing on the constitution and dynamics of the mantle", Geochimica et Cosmochimica Acta **55**, 8, 2083–2110 (1991).

Ross, N. L. and R. M. Hazen, 'High-pressure crystal chemistry of mgsio3 perovskite", Physics and Chemistry of Minerals **17**, 3, 228–237 (1990).

Rubie, D. C., D. J. Frost, U. Mann, Y. Asahara, F. Nimmo, K. Tsuno, P. Kegler, A. Holzheid and H. Palme, 'Heterogeneous accretion, composition and core–mantle differentiation of the earth", Earth and Planetary Science Letters **301**, 1-2, 31–42 (2011).

Saha, S., A. Bengtson, K. L. Crispin, J. A. Van Orman and D. Morgan, 'Effects of spin transition on diffusion of fe 2+ in ferropericlase in earth's lower mantle", Physical Review B—Condensed Matter and Materials Physics **84**, 18, 184102 (2011).

Sahni, V., K.-P. Bohnen and M. K. Harbola, 'Analysis of the local-density approximation of density-functional theory", Physical Review A **37**, 6, 1895 (1988).

Saikia, A., T. B. Ballaran and D. J. Frost, 'The effect of fe and al substitution on the compressibility of mgsio3-perovskite determined through single-crystal x-ray diffraction", Physics of the Earth and Planetary Interiors **173**, 1-2, 153–161 (2009).

Samuel, H. and N. Tosi, 'The influence of post-perovskite strength on the earth's mantle thermal and chemical evolution", Earth and Planetary Science Letters **323**, 50–59 (2012).

Sans, J. A., F. J. Manjón, C. Popescu, V. P. Cuenca-Gotor, O. Gomis, A. Muñoz, P. Rodríguez-Hernández, J. Pellicer-Porres, A. L. d. J. Pereira, D. Santamaría-Pérez *et al.*, 'Helium ordered trapping in arsenolite under compression: Synthesis of he2as4o6", arXiv preprint arXiv:1502.04279 (2015).

Sato, T., N. Funamori and T. Yagi, 'Helium penetrates into silica glass and reduces its compressibility", Nature Communications **2**, 1, 345 (2011).

Savitzky, A. and M. J. Golay, 'Smoothing and differentiation of data by simplified least squares procedures.", Analytical chemistry **36**, 8, 1627–1639 (1964).

Saxena, S. K., L. S. Dubrovinsky, F. Tutti and T. Le Bihan, 'Equation of state of mgsio3 with the perovskite structure based on experimental measurement", American Mineralogist **84**, 3, 226–232 (1999).

Schouten, T. L., L. Gebraad, S. Noe, A. J. Gülcher, S. Thrastarson, D.-P. van Herwaarden and A. Fichtner, 'Full-waveform inversion reveals diverse origins of lower mantle positive wave speed anomalies", Scientific Reports **14**, 1, 26708 (2024).

Segall, M., P. J. Lindan, M. a. Probert, C. J. Pickard, P. J. Hasnip, S. Clark and M. Payne, 'First-principles simulation: ideas, illustrations and the castepcode", Journal of physics: condensed matter **14**, 11, 2717 (2002).

Shahnas, M., R. Pysklywec, J. Justo and D. Yuen, 'Spin transition-induced anomalies in the lower mantle: implications for mid-mantle partial layering", Geophysical Journal International **210**, 2, 765–773 (2017).

Sharp, T. G., C. M. Lingemann, C. Dupas and D. Stoffler, 'Natural occurrence of mgsio3-ilmenite and evidence for mgsio3-perovskite in a shocked l chondrite", Science **277**, 5324, 352–355 (1997).

Shcheka, S. S. and H. Keppler, 'The origin of the terrestrial noble-gas signature", Nature **490**, 7421, 531–534 (2012).

Shen, G., Q. Mei, V. B. Prakapenka, P. Lazor, S. Sinogeikin, Y. Meng and C. Park, 'Effect of helium on structure and compression behavior of sio2 glass", Proceedings of the National Academy of Sciences **108**, 15, 6004–6007 (2011).

Shim, S., 'Peakpo: A python software for x-ray diffraction analysis at high pressure and high temperature", Zenodo: Meyrin, Switzerland (2017).

Shindo, D., T. Oikawa, D. Shindo and T. Oikawa, 'Energy dispersive x-ray spectroscopy", Analytical electron microscopy for materials science pp. 81–102 (2002).

Sholl, D. S. and J. A. Steckel, *Density functional theory: a practical introduction* (John Wiley & Sons, 2022).

Shukla, G., M. Cococcioni and R. M. Wentzcovitch, 'Thermoelasticity of fe3+-and al-bearing bridgmanite: Effects of iron spin crossover", Geophysical Research Letters **43**, 11, 5661–5670 (2016).

Shukla, G. and R. M. Wentzcovitch, 'Spin crossover in (mg, fe3+)(si, fe3+) o3 bridgmanite: Effects of disorder, iron concentration, and temperature", Physics of the Earth and Planetary Interiors **260**, 53–61 (2016).

Shukla, G., Z. Wu, H. Hsu, A. Floris, M. Cococcioni and R. M. Wentzcovitch, 'Thermoelasticity of fe2+-bearing bridgmanite", Geophysical Research Letters **42**, 6, 1741–1749 (2015).

Singh, A. K., 'The lattice strains in a specimen (cubic system) compressed nonhydrostatically in an opposed anvil device", Journal of Applied Physics **73**, 9, 4278–4286 (1993).

Sinmyo, R., Y. Nakajima, C. A. McCammon, N. Miyajima, S. Petitgirard, R. Myhill, L. Dubrovinsky and D. J. Frost, 'Effect of fe3+ on phase relations in the lower mantle: Implications for redox melting in stagnant slabs", Journal of Geophysical Research: Solid Earth **124**, 12, 12484–12497 (2019).

Sinogeikin, S. V., J. Zhang and J. D. Bass, 'Elasticity of single crystal and polycrystalline mgsio3 perovskite by brillouin spectroscopy", Geophysical Research Letters **31**, 6 (2004).

Stacey, F. and D. Isaak, 'Anharmonicity in mineral physics: A physical interpretation", Journal of Geophysical Research: Solid Earth **108**, B9 (2003).

Steinberger, B. and T. H. Torsvik, 'A geodynamic model of plumes from the margins of large low shear velocity provinces", Geochemistry, Geophysics, Geosystems **13**, 1 (2012).

Stixrude, L. and C. Lithgow-Bertelloni, 'Thermodynamics of mantle minerals—i. physical properties", Geophysical Journal International **162**, 2, 610–632 (2005).

Stixrude, L. and C. Lithgow-Bertelloni, 'Thermodynamics of mantle minerals-ii. phase equilibria", Geophysical Journal International **184**, 3, 1180–1213 (2011).

Stixrude, L. and C. Lithgow-Bertelloni, 'Thermal expansivity, heat capacity and bulk modulus of the mantle", Geophysical Journal International **228**, 2, 1119–1149 (2022).

Su, W.-j., R. L. Woodward and A. M. Dziewonski, 'Degree 12 model of shear velocity heterogeneity in the mantle", Journal of Geophysical Research: Solid Earth **99**, B4, 6945–6980 (1994).

Sun, N., W. Wei, S. Han, J. Song, X. Li, Y. Duan, V. B. Prakapenka and Z. Mao, 'Phase transition and thermal equations of state of (fe, al)-bridgmanite and post-perovskite: Implication for the chemical heterogeneity at the lowermost mantle", Earth and Planetary Science Letters **490**, 161–169 (2018).

Tackley, P. J., 'Dynamics and evolution of the deep mantle resulting from thermal, chemical, phase and melting effects", Earth-Science Reviews **110**, 1-4, 1–25 (2012).

Takemura, K., 'Evaluation of the hydrostaticity of a helium-pressure medium with powder x-ray diffraction techniques", Journal of applied physics **89**, 1, 662–668 (2001).

Takemura, K., 'Pressure scales and hydrostaticity", High Pressure Research **27**, 4, 465–472 (2007).

Tange, Y., Y. Kuwayama, T. Irifune, K.-i. Funakoshi and Y. Ohishi, 'P-v-t equation of state of mgsio3 perovskite based on the mgo pressure scale: A comprehensive reference for mineralogy of the lower mantle", Journal of Geophysical Research: Solid Earth **117**, B6 (2012).

Tateno, S., K. Hirose, N. Sata and Y. Ohishi, 'Phase relations in mg3al2si3o12 to 180 gpa: Effect of al on post-perovskite phase transition", Geophysical Research Letters **32**, 15 (2005).

Thomas, E. L., *Crystal growth and the search for highly correlated ternary intermetallic antimonides and stannides*, Doctoral dissertation, Louisiana State University (2006).

Thompson, P., D. Cox and J. Hastings, 'Rietveld refinement of debye–scherrer synchrotron x-ray data from al2o3", Applied Crystallography **20**, 2, 79–83 (1987).

Trampert, J., F. Deschamps, J. Resovsky and D. Yuen, 'Probabilistic tomography maps chemical heterogeneities throughout the lower mantle", Science **306**, 5697, 853–856 (2004).

Tschauner, O., C. Ma, J. R. Beckett, C. Prescher, V. B. Prakapenka and G. R. Rossman, 'Discovery of bridgmanite, the most abundant mineral in earth, in a shocked meteorite", Science **346**, 6213, 1100–1102 (2014).

Tsuchiya, T., 'First-principles prediction of the p-v-t equation of state of gold and the 660-km discontinuity in earth's mantle", Journal of Geophysical Research: Solid Earth **108**, B10 (2003).

Tsuchiya, T. and J. Tsuchiya, 'Effect of impurity on the elasticity of perovskite and postperovskite: Velocity contrast across the postperovskite transition in (mg, fe, al)(si, al) o3", Geophysical Research Letters **33**, 12 (2006).

Tsuchiya, T., J. Tsuchiya, K. Umemoto and R. M. Wentzcovitch, 'Phase transition in mgsio3 perovskite in the earth's lower mantle", Earth and Planetary Science Letters **224**, 3-4, 241–248 (2004).

Tsujino, N., Y. Nishihara, D. Yamazaki, Y. Seto, Y. Higo and E. Takahashi, 'Mantle dynamics inferred from the crystallographic preferred orientation of bridgmanite", Nature **539**, 7627, 81–84 (2016).

Utsumi, W., N. Funamori, T. Yagi, E. Ito, T. Kikegawa and O. Shimomura, 'Thermal expansivity of mgsio3 perovskite under high pressures up to 20 gpa", Geophysical Research Letters **22**, 9, 1005–1008 (1995).

Van der Hilst, R. D., S. Widiyantoro and E. Engdahl, 'Evidence for deep mantle circulation from global tomography", Nature **386**, 6625, 578–584 (1997).

van Mierlo, W. L., F. Langenhorst, D. J. Frost and D. C. Rubie, 'Stagnation of subducting slabs in the transition zone due to slow diffusion in majoritic garnet", Nature Geoscience **6**, 5, 400–403 (2013).

Vanderbilt, D., 'First-principles theory of structural phase transitions in cubic perovskites", JOURNAL-KOREAN PHYSICAL SOCIETY **32**, S103–S106 (1998).

Vanpeteghem, C., J. Zhao, R. Angel, N. Ross and N. Bolfan-Casanova, 'Crystal structure and equation of state of mgsio3 perovskite", Geophysical Research Letters **33**, 3 (2006a).

Vanpeteghem, C. B., R. Angel, N. Ross, S. Jacobsen, D. Dobson, K. Litasov and E. Ohtani, 'Al, fe substitution in the mgsio3 perovskite structure: A single-crystal x-ray diffraction study", Physics of the Earth and Planetary Interiors **155**, 1-2, 96–103 (2006b).

Vilella, K., T. Bodin, C.-E. Boukaré, F. Deschamps, J. Badro, M. D. Ballmer and Y. Li, 'Constraints on the composition and temperature of llsvps from seismic properties of lower mantle minerals", Earth and Planetary Science Letters **554**, 116685 (2021).

Vinet, P., J. Ferrante, J. H. Rose and J. R. Smith, 'Compressibility of solids", Journal of Geophysical Research: Solid Earth **92**, B9, 9319–9325 (1987).

Vinet, P., J. H. Rose, J. Ferrante and J. R. Smith, 'Universal features of the equation of state of solids", Journal of Physics: Condensed Matter **1**, 11, 1941 (1989).

Wallace, D. C. and H. Callen, 'Thermodynamics of crystals", American Journal of Physics **40**, 11, 1718–1719 (1972).

Wan, T., C. Luo, Y. Sun and R. M. Wentzcovitch, 'Thermoelastic properties of bridgmanite using deep-potential molecular dynamics", Physical Review B **109**, 9, 094101 (2024).

Wang, K., X. Lu, X. Liu and K. Yin, 'Noble gas (he, ne, and ar) solubilities in high-pressure silicate melts calculated based on deep-potential modeling", Geochimica et Cosmochimica Acta **350**, 57–68 (2023).

Wang, L., G. Liu, X. Xi, G. Yang, L. Hu, B. Zhu, Y. He, Y. Liu, H. Qian, S. Zhang *et al.*, 'Annealing engineering in the growth of perovskite grains", Crystals **12**, 7, 894 (2022).

Wang, W., J. Liu, F. Zhu, M. Li, S. M. Dorfman, J. Li and Z. Wu, 'Formation of large low shear velocity provinces through the decomposition of oxidized mantle", Nature communications **12**, 1, 1911 (2021).

Wang, Y., 'Phase transformations: Implications for mantle structure", Geophysical Monograph **1**, 17 (2000).

Wang, Y., T. Uchida, J. Zhang, M. L. Rivers and S. R. Sutton, 'Thermal equation of state of akimotoite mgsio3 and effects of the akimotoite–garnet transformation on seismic structure near the 660 km discontinuity", Physics of the Earth and Planetary Interiors **143**, 57–80 (2004).

Wang, Y., D. J. Weidner, R. C. Liebermann, X. Liu, J. Ko, M. T. Vaughan, Y. Zhao, A. Yeganeh-Haeri and R. E. Pacalo, 'Phase transition and thermal expansion of mgsio3 perovskite", Science **251**, 4992, 410–413 (1991).

Wang, Y. and Y.-G. Xu, 'Volatiles in the mantle transition zone and their effects on big mantle wedge systems", National Science Review **11**, 6, nwae136 (2024).

Warren, M. and G. Ackland, 'Ab initio studies of structural instabilities in magnesium silicate perovskite", Physics and Chemistry of Minerals **23**, 2, 107–118 (1996).

Warren, M. C., G. J. Ackland, B. B. Karki and S. J. Clark, 'Phase transitions in silicate perovskites from first principles", Mineralogical Magazine **62**, 5, 585–598 (1998).

Wehinger, B., A. Bosak, S. Nazzareni, D. Antonangeli, A. Mirone, S. L. Chaplot, R. Mittal, E. Ohtani, A. Shatskiy, S. Surendra *et al.*, 'Lattice dynamics of mgsio _3 perovskite (bridgmanite) studied by inelastic x-ray scattering and ab initio calculations", arXiv preprint arXiv:1509.06164 (2015).

Wentzcovitch, R., J. Justo, Z. Wu, C. R. da SILVA, D. Yuen and D. Kohlstedt, 'Anomalous compressibility of ferropericlase throughout the iron spin cross-over", Proceedings of the National Academy of Sciences **106**, 21, 8447–8452 (2009).

Wentzcovitch, R. M., J. J. Valencia-Cardona, J. Zhuang, G. Shukla and K. Sarkar, 'The post-perovskite transition in fe-and al-bearing bridgmanite: Effects on seismic observables", Journal of Geophysical Research: Solid Earth **128**, 3, e2022JB025475 (2023).

Williams, Q. and E. J. Garnero, 'Seismic evidence for partial melt at the base of earth's mantle", Science **273**, 5281, 1528–1530 (1996).

Wilson, A. J., C. J. Davies, A. M. Walker, M. Pozzo, D. Alfè and A. Deuss, 'The formation and evolution of the earth's inner core", Nature Reviews Earth & Environment **6**, 2, 140–154 (2025).

Wolf, A. S., J. M. Jackson, P. Dera and V. B. Prakapenka, 'The thermal equation of state of (mg, fe) sio3 bridgmanite (perovskite) and implications for lower mantle structures", Journal of Geophysical Research: Solid Earth **120**, 11, 7460–7489 (2015).

Wood, B. J., M. J. Walter and J. Wade, 'Accretion of the earth and segregation of its core", Nature **441**, 7095, 825–833 (2006).

Woodward, P. M., 'Octahedral tilting in perovskites. i. geometrical considerations", Structural Science **53**, 1, 32–43 (1997).

Workman, R. K. and S. R. Hart, 'Major and trace element composition of the depleted morb mantle (dmm)", Earth and Planetary Science Letters **231**, 1-2, 53–72 (2005).

Wu, Z., 'Velocity structure and composition of the lower mantle with spin crossover in ferropericlase", Journal of Geophysical Research: Solid Earth **121**, 4, 2304–2314 (2016).

Wu, Z., C. Gao, F. Zhang, S. Wu, K.-M. Ho, R. M. Wentzcovitch and Y. Sun, 'Ab initio superionic-liquid phase diagram of $Fe_{1-x}O_x$ under Earth's inner core conditions", arXiv preprint arXiv:2410.23557 (2024).

Xu, S., S.-H. Shim and D. Morgan, 'Origin of fe3+ in fe-containing, al-free mantle silicate perovskite", Earth and Planetary Science Letters **409**, 319–328 (2015).

Yagi, T., H. Mao and P. Bell, 'Hydrostatic compression of perovskite-type mgsio3", in 'Advances in Physical Geochemistry", pp. 317–325 (Springer, 1982).

Yagi, T., H.-K. Mao and P. M. Bell, 'Structure and crystal chemistry of perovskite-type mgsio3", Physics and Chemistry of Minerals **3**, 2, 97–110 (1978).

Yagi, T., Y. Uchiyama, M. Akaogi and E. Ito, 'Isothermal compression curve of mgsio3 tetragonal garnet", Physics of the Earth and Planetary Interiors **74**, 1-2, 1–7 (1992).

Yang, H., J. M. Muir and F. Zhang, 'Iron hydride in the earth's inner core and its geophysical implications", Geochemistry, Geophysics, Geosystems **23**, 12, e2022GC010620 (2022).

Ye, Y., V. Prakapenka, Y. Meng and S.-H. Shim, 'Intercomparison of the gold, platinum, and mgo pressure scales up to 140 gpa and 2500 k", Journal of Geophysical Research: Solid Earth **122**, 5, 3450–3464 (2017).

Yeganeh-Haeri, A., 'Synthesis and re-investigation of the elastic properties of single-crystal magnesium silicate perovskite", Physics of the Earth and Planetary Interiors **87**, 1-2, 111–121 (1994).

Yoshioka, S., R. Daessler and D. A. Yuen, 'Stress fields associated with metastable phase transitions in descending slabs and deep-focus earthquakes", Physics of the earth and planetary interiors **104**, 4, 345–361 (1997).

Young, R. A., *The rietveld method*, vol. 5 (International union of crystallography, 1993).

Zeng, L. and D. Sasselov, 'A detailed model grid for solid planets from 0.1 through 100 earth masses", Publications of the Astronomical Society of the Pacific **125**, 925, 227 (2013).

Zhang, L., 'Bridgmanite across the lower mantle", Nature Geoscience **15**, 12, 964–964 (2022).

Zhang, L., Y. Meng, W. Yang, L. Wang, W. L. Mao, Q.-S. Zeng, J. S. Jeong, A. J. Wagner, K. A. Mkhoyan, W. Liu *et al.*, 'Disproportionation of (mg, fe) sio3 perovskite in earth's deep lower mantle", Science **344**, 6186, 877–882 (2014).

Zhang, L., H. Yuan, Y. Meng and H.-K. Mao, 'Development of high-pressure multigrain x-ray diffraction for exploring the earth's interior", Engineering **5**, 3, 441–447 (2019).

Zhang, S., S. Cottaar, T. Liu, S. Stackhouse and B. Militzer, 'High-pressure, temperature elasticity of fe-and al-bearing mgsio3: Implications for the earth's lower mantle", Earth and Planetary Science Letters **434**, 264–273 (2016).

Zhang, Y., J. Tsuchiya, C. Li, Z. Ye, W. Yan, T. Okuchi, S.-i. Karato, J. Kung and J.-F. Lin, 'Hydrogen dissolution mechanisms in bridgmanite by first-principles calculations and infrared spectroscopy", Journal of Geophysical Research: Solid Earth **130**, 1, e2024JB030403 (2025).

Zhang, Y., W. Wang, Y. Li and Z. Wu, 'Superionic iron hydride shapes ultralow-velocity zones at earth's core–mantle boundary", Proceedings of the National Academy of Sciences **121**, 35, e2406386121 (2024).

Zhao, Y., Z. Wu, S. Hao, W. Wang, X. Deng and J. Song, 'Elastic properties of fe-bearing akimotoite at mantle conditions: Implications for composition and temperature in lower mantle transition zone", Fundamental Research **2**, 4, 570–577 (2022).

Zhu, F., J. Liu, X. Lai, Y. Xiao, V. Prakapenka, W. Bi, E. E. Alp, P. Dera, B. Chen and J. Li, 'Synthesis, elasticity, and spin state of an intermediate mgsio3-fealo3 bridgmanite: Implications for iron in earth's lower mantle", Journal of Geophysical Research: Solid Earth **125**, 7, e2020JB019964 (2020).

Ziesche, P., S. Kurth and J. P. Perdew, 'Density functionals from lda to gga", Computational materials science **11**, 2, 122–127 (1998).

Appendix A: Additional Figures

A.1 Chapter 2: Materials and Methodology

Figure A.1: A short symmetric DAC (right) and a standard symmetric DAC (left) in the opened piston-and-cylinder configuration. Although the closed cell (right) is shorter, both have the same basic setup.

A.2 Chapter 3: Elastic Behavior of Sintered Polycrystalline Fe-Al-bearing Bridgmanite at High-Pressures

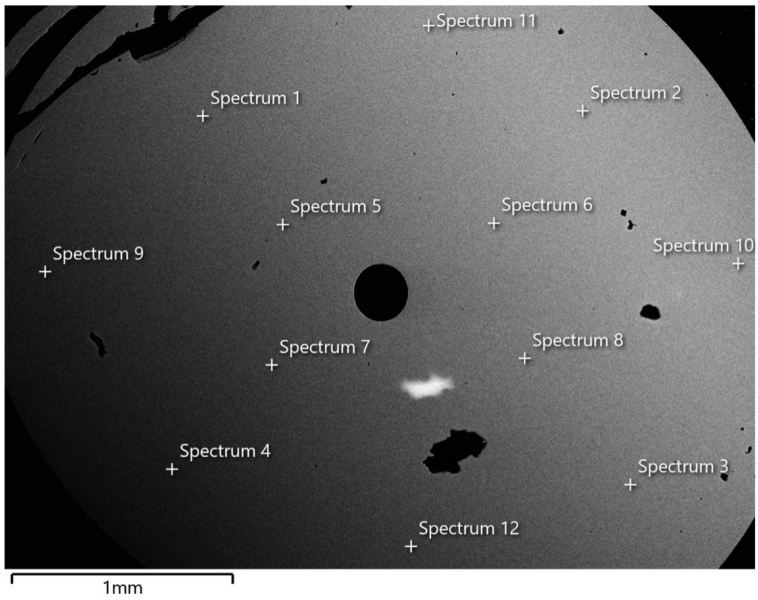

Figure A.2: SEM-EDS image of the $MgSiO_3$ glass pellet with spots of collected spectrum. Spectrum information can be found in Table B.2.

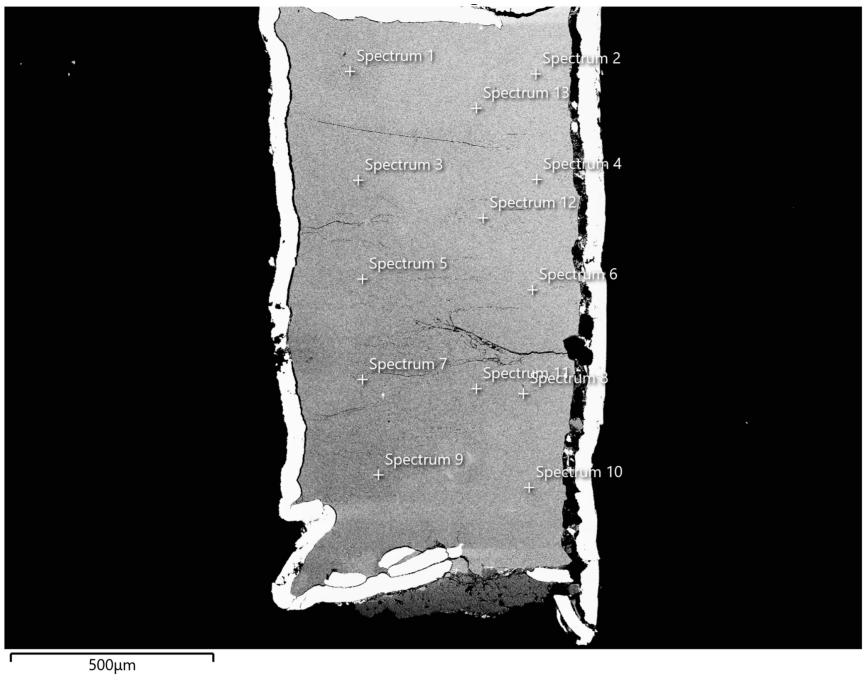

Figure A.3: SEM-EDS image of the recovered synthesized $MgSiO_3$ bridgmanite LVP sample that has been cut, polished and embedded into epoxy. Spectrum information can be found in Table B.3.

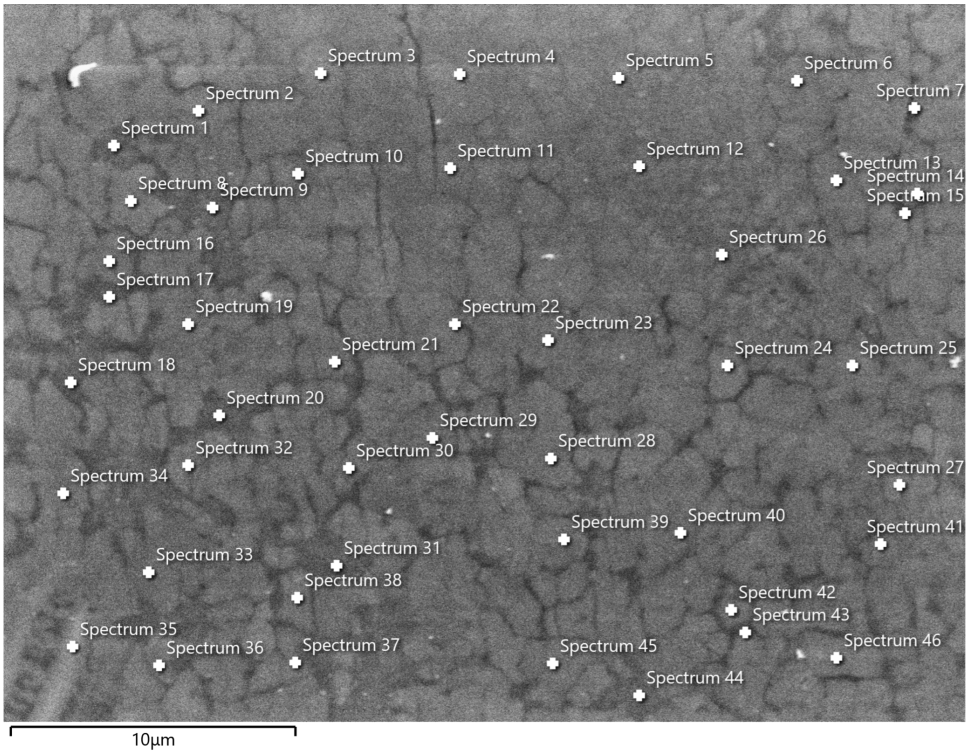

Figure A.4: SEM-EDS image of the recovered synthesized of F1A1-brg LVP sample that has been cut and polished. Spectrum information can be found in Table B.5.

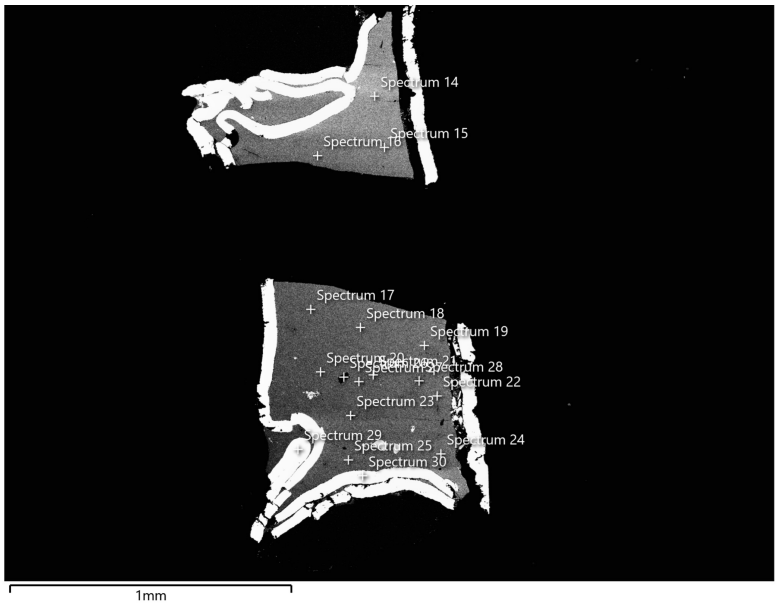

Figure A.5: SEM-EDS image of the recovered synthesized Fe-Al-bearing bridgmanite F3A3-brg LVP sample that has been cut and polished. Spectrum information can be found in Table B.5.

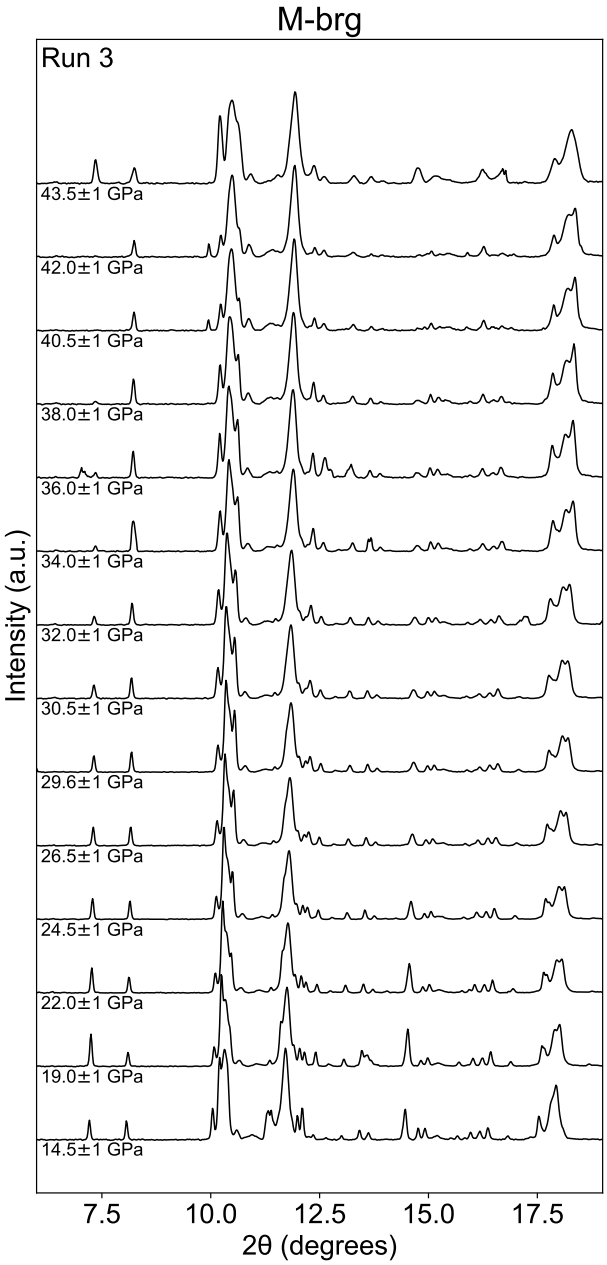

Figure A.6: Waterfall plot of X-ray diffraction patterns for M-brg at pressures ranging from 14.5 to 43.5 GPa at 300 K. Diffraction intensity (arbitrary units) is plotted as a function of 2θ. Data show the evolution of peak positions and XRD quality with increasing pressure.

A.3 Chapter 4: Elastic Properties of Metastable Fe-Al Majoritic Garnet up to 83 GPa at 300 K

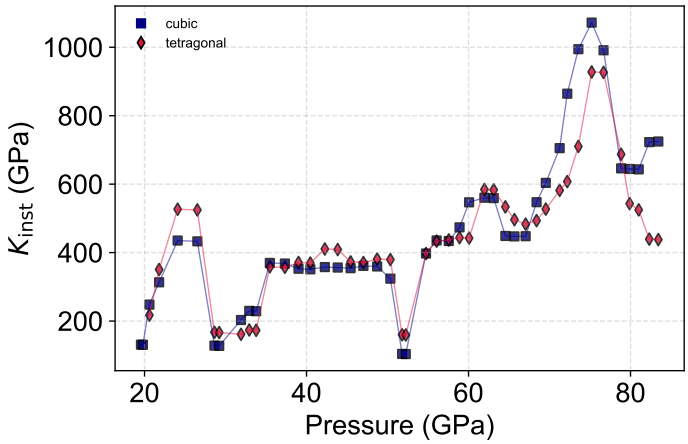

Figure A.7: Instantaneous bulk modulus K_{inst} (GPa) for cubic (blue squares) and tetragonal (red diamonds) garnet structures. Data points were obtained by finite-difference differentiation of the measured P-V data after Savitzky-Golay smoothing (Savitzky and Golay, 1964).

A.4 Chapter 5 & 6: *Ab Initio* Density Functional Theory Calculations on Fe-Al-Bridgmanite

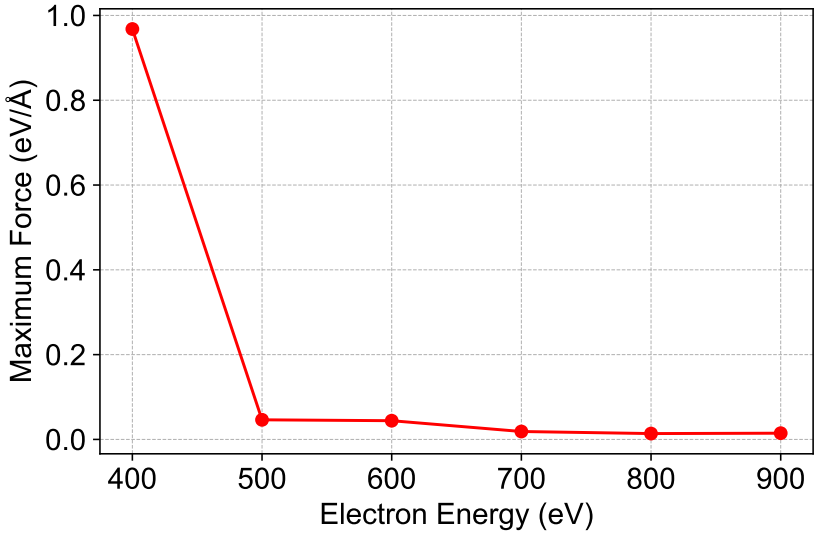

Figure A.8: Convergence of maximum force (eV/Å) with respect to plane-wave cutoff energy for $MgSiO_3$.

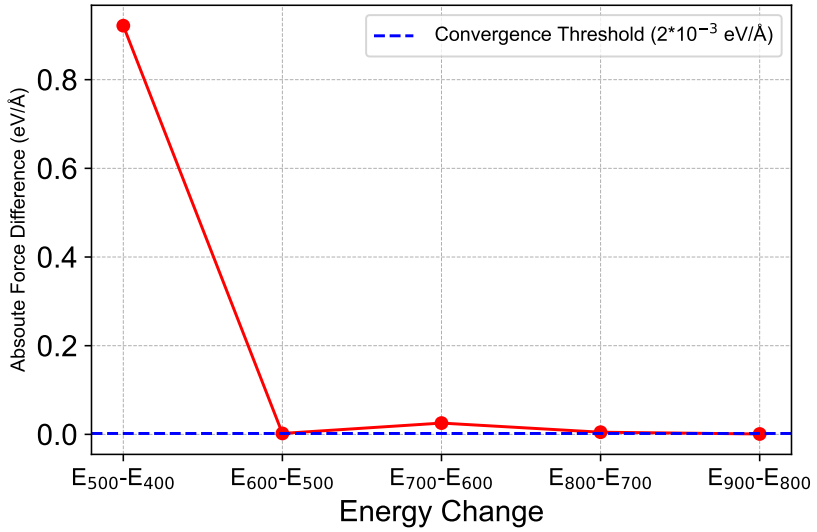

Figure A.9: Absolute force differences between successive plane-wave cutoff energies for $MgSiO_3$, showing convergence behavior. The force difference drops sharply between 400 eV and 500 eV, then fluctuates within the convergence threshold of 2×10^{-3} eV/Å (dashed blue line), indicating that a cutoff energy of 800 eV ensures stable and reliable force calculations.

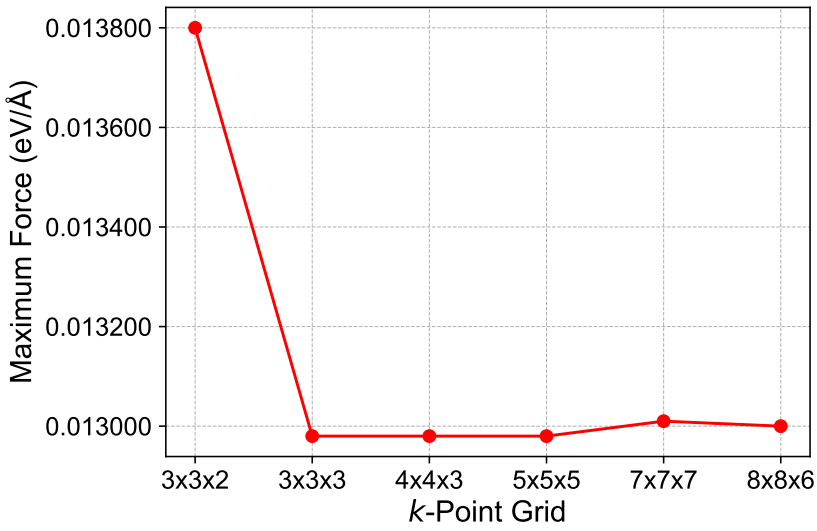

Figure A.10: Convergence of maximum force (in eV/Å) with respect to k-point grid density for $MgSiO_3$. The maximum force stabilizes after a $3 \times 3 \times 3$ grid, with negligible changes for denser grids, indicating that a $4 \times 4 \times 3$ k-point mesh is sufficient for accurate force calculations in this system.

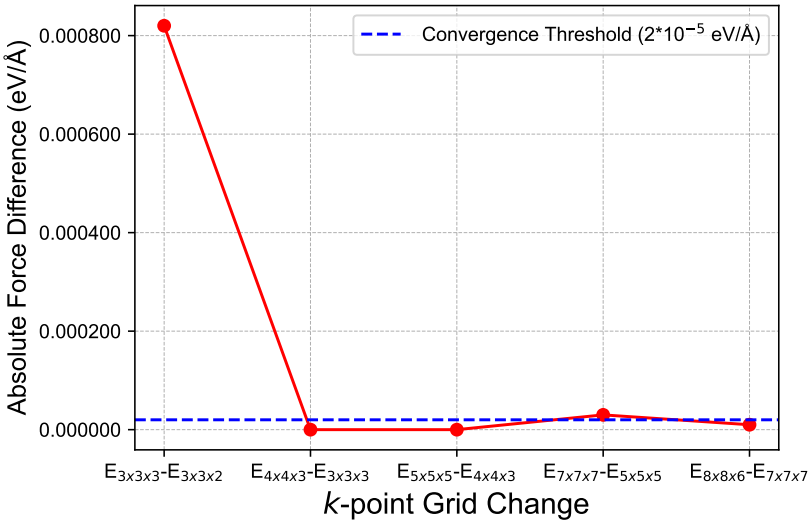

Figure A.11: Absolute force differences between successive k-point grids for $MgSiO_3$, assessing convergence behavior. A significant drop is observed between $3 \times 3 \times 2$ and $3 \times 3 \times 3$, after which all differences remain well below the convergence threshold of 2×10^{-5} eV/Å (dashed blue line), confirming that a $4 \times 4 \times 3$ grid or denser is sufficient for accurate force calculations.

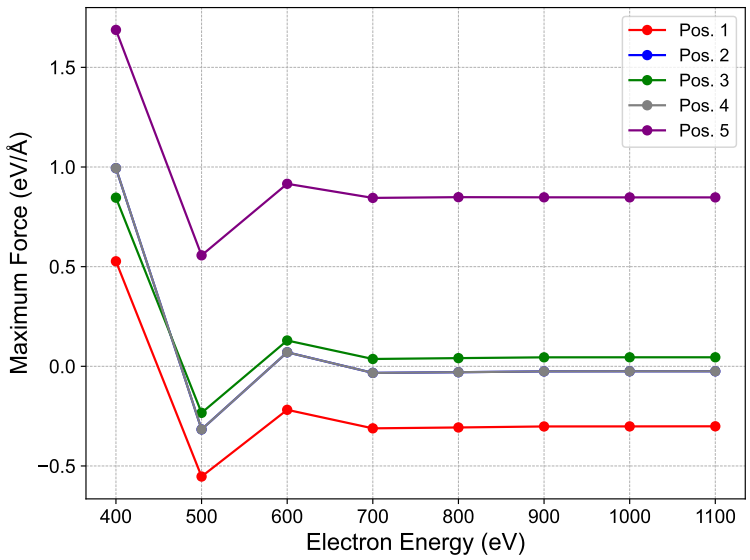

Figure A.12: Energy cutoff convergence test for all five atomic arrangements for FeAl25. The plotted arrangements correspond with information in Table B.8. There is slight numerical variation between Position 2 and Position 4, although it is difficult to see visually as it appears they are plotted directly on top of each other.

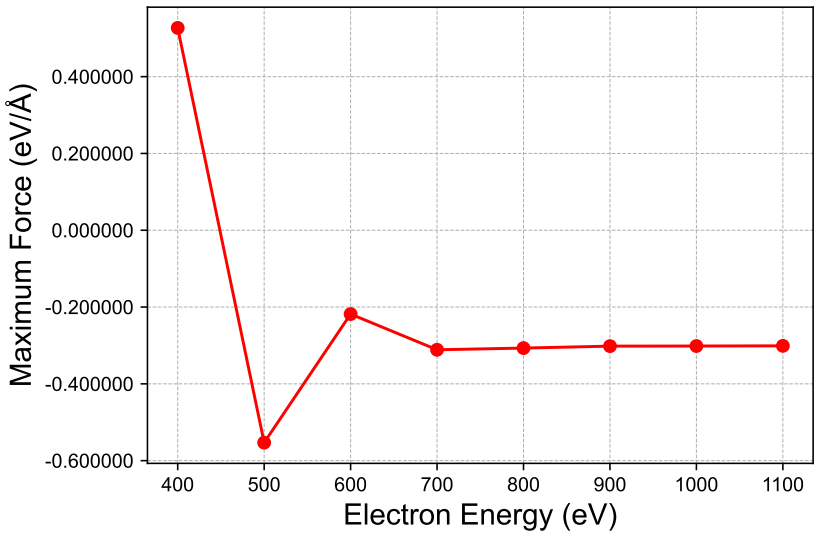

Figure A.13: Convergence of maximum force (eV/Å) with respect to plane-wave cutoff energy for FeAl25.

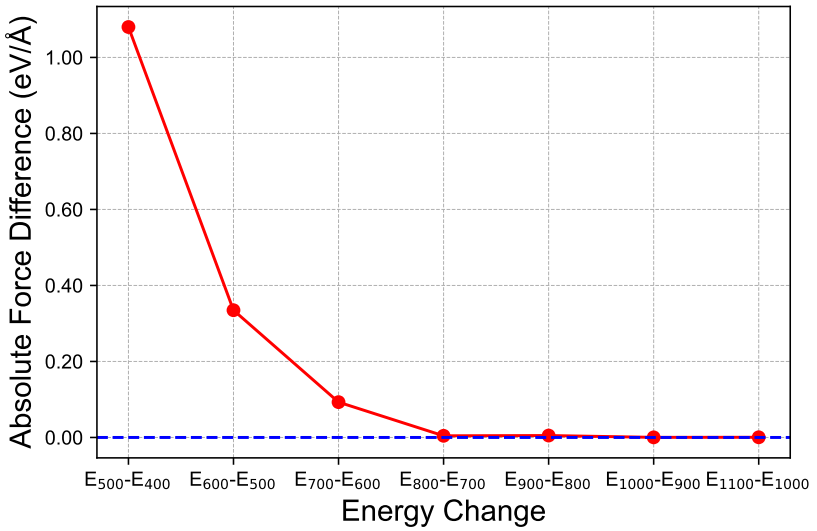

Figure A.14: Absolute force differences between successive plane-wave cutoff energies for FeAl25, showing convergence behavior. The force difference meets the convergence threshold of $2 \times 10^{-5}\,\mathrm{eV/Å}$ (dashed blue line) at a cutoff energy of 900 eV ensures stable and reliable force calculations.

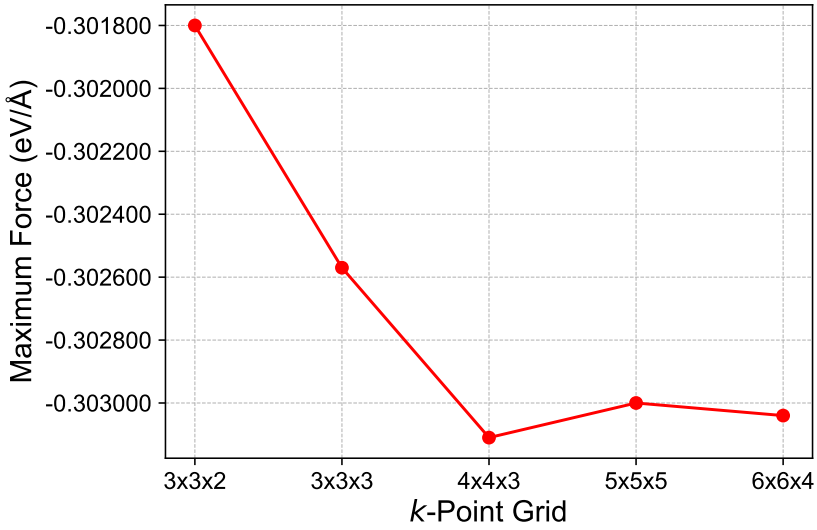

Figure A.15: Convergence of maximum force (in eV/Å) with respect to k-point grid density for FeAl25. The maximum force stabilizes after a $4 \times 4 \times 3$ grid, with negligible changes for denser grids, indicating that a $5 \times 5 \times 5$ k-point mesh is sufficient for accurate force calculations in this system without excessive computational time.

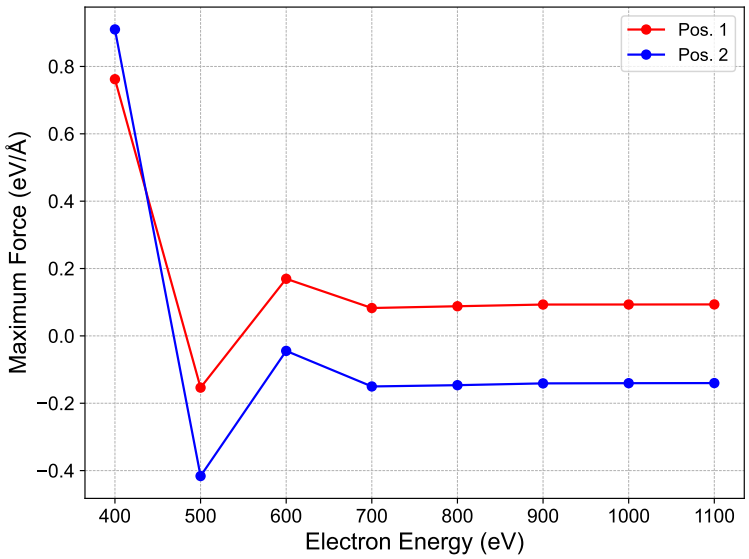

Figure A.16: Energy cutoff convergence test for all five atomic arrangements for FeAl50. The plotted arrangements correspond with information in Table B.9.

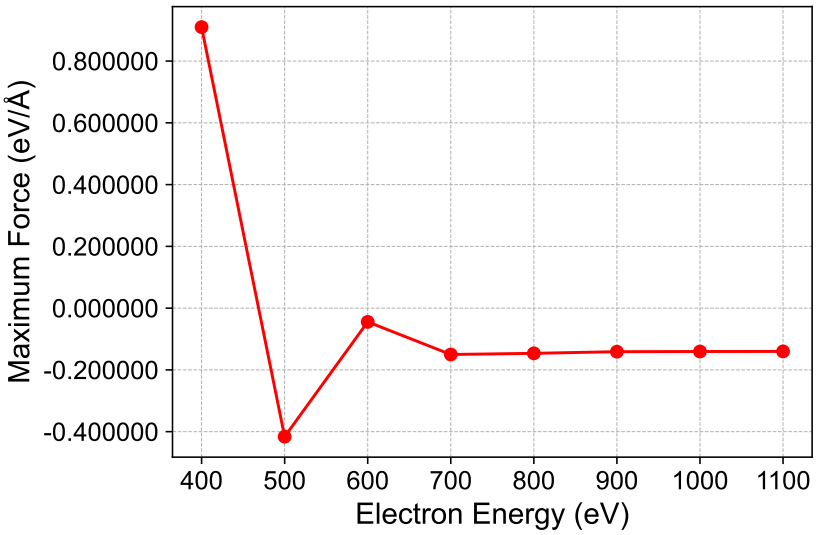

Figure A.17: Convergence of maximum force (eV/Å) with respect to plane-wave cutoff energy for FeAl50.

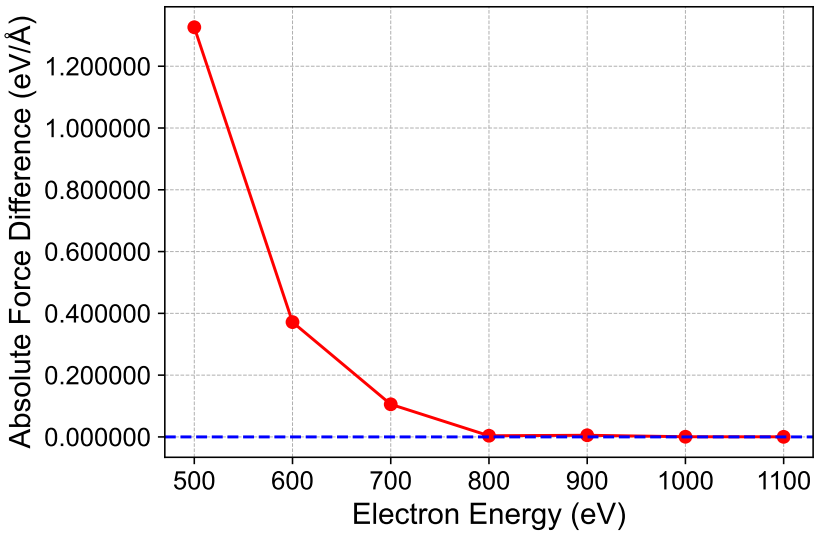

Figure A.18: Absolute force differences between successive plane-wave cutoff energies for FeAl50, showing convergence behavior. The force difference meets the convergence threshold of $2 \times 10^{-5}\,\mathrm{eV/Å}$ (dashed blue line) at a cutoff energy of 900 eV ensures stable and reliable calculations.

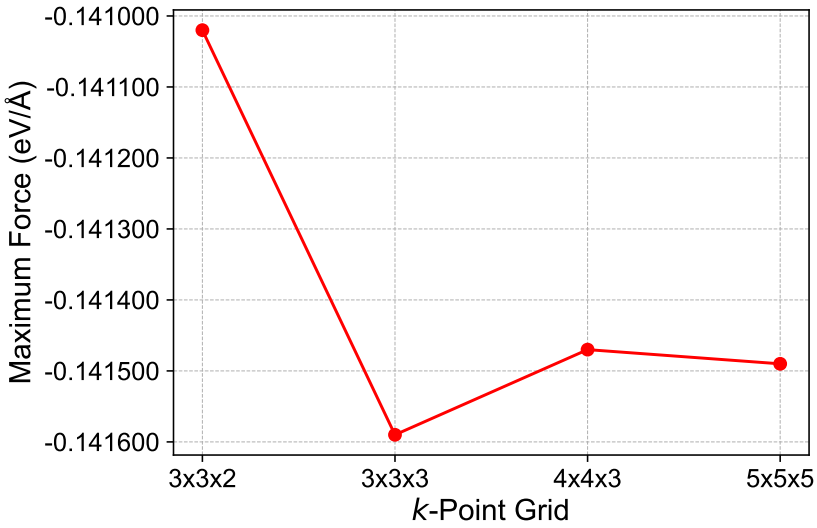

Figure A.19: Convergence of maximum force (in eV/Å) with respect to k-point grid density for FeAl50. The maximum force stabilizes after a $4 \times 4 \times 3$ grid, with negligible changes for denser grids, indicating that a $5 \times 5 \times 5$ k-point mesh is sufficient for accurate force calculations in this system without excessive computational time.

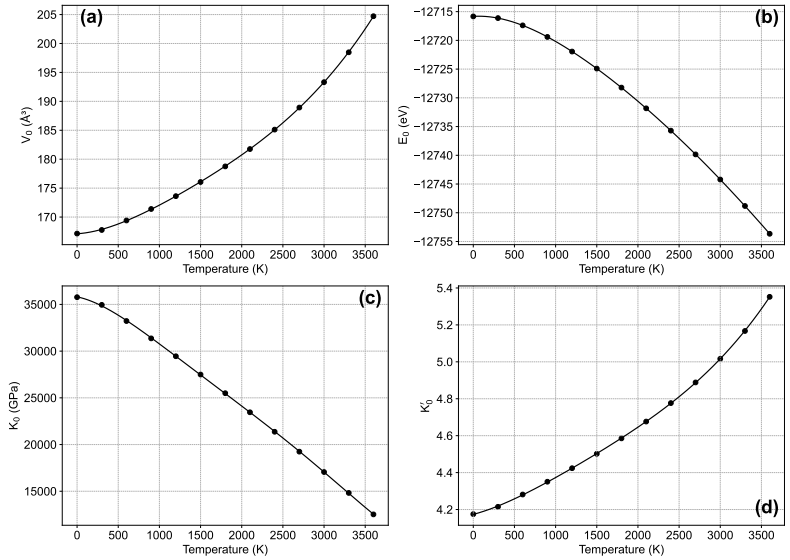

Figure A.20: Temperature dependence of thermodynamic and elastic parameters for $\mathrm{MgSiO_3}$ bridgmanite at 0 GPa based on *ab initio* DFT calculations using BM3-EOS. (a) The unit cell volume (V_0) shows nonlinear thermal expansion with increasing temperature. (b) The static internal energy (E_0) becomes less negative with temperature, reflecting the contribution of thermal energy. (c) The isothermal bulk modulus (K_0) decreases linearly as temperature increases, consistent with the thermal softening of bridgmanite. (d) The first pressure derivative of the bulk modulus (K_0) for the studied temperature range.

Appendix B: Additional Tables

B.1 Chapter 2: Materials and Methodology

Table B.1: Values for the anvil cubes used for LVP synthesis, from Ishii *et al.* (2016).

Company	**Grade**	**Vickers hardness (MPa)**	**Rockwell hardness A**	**Compressional strength (GPa)**
Hawedia	HA06	2040	94.5	>7.0
Fujiloy	TF05	2280	>94	6.7

B.2 Chapter 3: Elastic Behavior of Sintered Polycrystalline Fe-Al-bearing Bridgmanite at High-Pressures

Table B.2: SEM-EDS spectrum data for $MgSiO_3$ glass.

Spectrum	**O** (at%)	**Mg** (at%)	**Si** (at%)	**O** (wt%)	**Mg** (wt%)	**Si** (wt%)
1	59.99	20.03	19.98	44.49	28.96	26.55
2	59.99	20.04	19.97	44.49	28.98	26.53
3	60.01	19.97	20.02	44.55	28.92	26.53
4	60.04	19.89	20.07	44.65	28.80	26.55
5	59.99	20.03	19.98	44.49	28.96	26.55
6	60.01	19.97	20.02	44.55	28.92	26.53
7	59.99	20.03	19.98	44.49	28.96	26.55
8	60.02	19.93	20.05	44.57	28.89	26.54
9	60.02	19.95	20.03	44.57	28.91	26.52
10	59.96	20.13	19.92	44.43	29.05	26.52
11	59.99	20.04	19.97	44.49	28.98	26.53
12	60.01	19.98	20.01	44.55	28.94	26.51
Max	60.04	20.13	20.07	44.65	29.05	26.55
Min	59.96	19.89	19.92	44.43	28.80	26.51
Average	60.00	20.00	20.00	44.53	28.94	26.54
SD	0.02	0.06	0.04	0.06	0.07	0.01

Table B.3: SEM-EDS spectrum data for the synthesized $MgSiO_3$ bridgmanite (M-brg).

Spectrum	O (at%)	Mg (at%)	Si (at%)	O (wt%)	Mg (wt%)	Si (wt%)
1	59.97	20.08	19.95	44.49	28.97	26.54
2	59.91	20.27	19.82	44.45	29.11	26.44
3	60.22	19.34	20.44	44.64	28.41	26.95
4	59.98	20.06	19.96	44.49	28.96	26.55
5	59.95	20.15	19.90	44.48	29.02	26.50
6	59.92	20.25	19.83	44.47	29.09	26.44
7	60.31	19.08	20.61	44.69	28.30	27.01
8	59.92	20.24	19.84	44.47	29.08	26.45
9	59.90	20.29	19.80	44.47	29.13	26.40
10	59.92	20.24	19.84	44.47	29.08	26.45
11	59.88	20.37	19.76	44.44	29.19	26.37
12	59.95	20.15	19.90	44.48	29.02	26.50
13	59.95	20.16	19.89	44.48	29.03	26.49
Max	60.31	20.37	20.61	44.69	29.19	27.01
Min	59.88	19.08	19.76	44.44	28.30	26.37
Average	59.99	20.16	20.05	44.52	28.94	26.53
SD	0.11	0.38	0.28	0.07	0.22	0.18

Table B.4: SEM-EDS spectrum data for the synthesized $(Mg_{0.83}, Fe_{0.17})(Si_{0.91}, Al_{0.09})O_3$ (F1A1-brg) composition. The spectrum correlated with those on Figure A.4.

Spectrum	Mg (at%)	Al (at%)	Si (at%)	Fe (at%)	Mg (wt%)	Al (wt%)	Si (wt%)	Fe (wt%)
1	35.01	5.20	52.22	7.58	35.01	5.20	52.22	7.58
2	35.24	5.03	52.40	7.33	35.24	5.03	52.40	7.33
3	35.40	5.31	52.17	7.12	35.40	5.31	52.17	7.12
4	34.95	4.68	52.63	7.74	34.95	4.68	52.63	7.74
5	34.86	5.21	52.65	7.28	34.86	5.21	52.65	7.28
6	35.43	5.20	52.21	7.15	35.43	5.20	52.21	7.15
7	35.39	5.15	52.27	7.18	35.39	5.15	52.27	7.18
8	34.66	5.36	52.56	7.42	34.66	5.36	52.56	7.42
9	35.33	5.35	52.45	6.86	35.33	5.35	52.45	6.86
10	34.95	5.03	52.72	7.30	34.95	5.03	52.72	7.30
11	34.82	4.93	52.80	7.45	34.82	4.93	52.80	7.45
12	34.99	4.87	52.74	7.40	34.99	4.87	52.74	7.40
13	34.89	5.22	52.76	7.24	34.89	5.22	52.76	7.24
14	35.06	4.99	52.62	7.33	35.06	4.99	52.62	7.33
15	34.78	5.20	52.55	7.47	34.78	5.20	52.55	7.47

Continued on the next page...

Table B.4 – continued from previous page.

Spectrum	Mg (at%)	Al (at%)	Si (at%)	Fe (at%)	Mg (wt%)	Al (wt%)	Si (wt%)	Fe (wt%)
16	35.22	5.12	52.50	7.15	35.22	5.12	52.50	7.15
17	35.05	5.05	52.60	7.30	35.05	5.05	52.60	7.30
18	34.80	5.15	52.68	7.37	34.80	5.15	52.68	7.37
19	35.19	4.95	52.43	7.43	35.19	4.95	52.43	7.43
20	35.11	5.00	52.46	7.43	35.11	5.00	52.46	7.43
21	34.99	4.90	52.59	7.52	34.99	4.90	52.59	7.52
22	34.78	4.98	52.75	7.49	34.78	4.98	52.75	7.49
23	34.87	5.14	52.65	7.34	34.87	5.14	52.65	7.34
24	35.25	5.07	52.38	7.30	35.25	5.07	52.38	7.30
25	34.95	5.00	52.51	7.54	34.95	5.00	52.51	7.54
26	34.89	5.15	52.58	7.38	34.89	5.15	52.58	7.38
27	34.90	5.20	52.52	7.38	34.90	5.20	52.52	7.38
28	35.18	5.10	52.50	7.22	35.18	5.10	52.50	7.22
29	35.14	5.08	52.49	7.29	35.14	5.08	52.49	7.29
30	34.87	5.18	52.70	7.25	34.87	5.18	52.70	7.25
31	34.95	4.98	52.57	7.50	34.95	4.98	52.57	7.50
32	34.99	5.03	52.57	7.41	34.99	5.03	52.57	7.41
33	35.08	5.17	52.48	7.27	35.08	5.17	52.48	7.27
34	34.99	5.01	52.53	7.47	34.99	5.01	52.53	7.47
35	35.19	5.15	52.32	7.34	35.19	5.15	52.32	7.34
36	35.15	5.08	52.50	7.27	35.15	5.08	52.50	7.27
37	35.17	4.90	52.62	7.31	35.17	4.90	52.62	7.31
38	35.43	4.88	52.53	7.16	35.43	4.88	52.53	7.16
39	37.17	4.88	50.51	7.44	37.17	4.88	50.51	7.44
40	34.76	5.26	52.45	7.53	34.76	5.26	52.45	7.53
41	34.49	4.98	53.11	7.42	34.49	4.98	53.11	7.42
42	35.22	4.93	52.99	6.87	35.22	4.93	52.99	6.87
43	34.85	4.84	52.43	7.88	34.85	4.84	52.43	7.88
44	35.27	5.25	52.33	7.15	35.27	5.25	52.33	7.15
45	35.29	4.76	52.06	7.90	35.29	4.76	52.06	7.90
46	35.26	4.78	53.08	6.88	35.26	4.78	53.08	6.88
Max	40.05	5.91	53.50	7.97	40.05	5.91	53.50	7.97
Min	32.66	3.72	49.87	6.36	32.66	3.72	49.87	6.36
Average	35.24	5.08	52.53	7.15	35.24	5.08	52.53	7.15
SD	0.98	0.36	0.64	0.40	0.98	0.36	0.64	0.40

Table B.5: SEM-EDS spectrum data for the synthesized F3A3-brg bridgmanite, normalized to exclude oxygen.

Spectrum	**Mg (at%)**	**Al (at%)**	**Si (at%)**	**Fe (at%)**	**Mg (wt%)**	**Al (wt%)**	**Si (wt%)**	**Fe (wt%)**
14	34.92	14.29	32.97	17.82	15.72	7.14	17.16	18.44
15	34.71	14.40	34.40	16.50	15.67	7.21	17.94	17.11
16	34.73	14.81	34.66	15.80	15.71	7.44	18.12	16.43
17	34.19	14.59	35.55	15.66	15.44	7.32	18.55	16.25
18	33.69	15.44	35.37	15.51	15.21	7.74	18.45	16.09
19	33.74	14.92	35.47	15.87	15.27	7.58	18.54	16.09
20	35.91	14.12	32.45	17.52	15.81	6.90	16.52	19.76
21	33.78	14.68	35.85	15.69	15.11	7.29	18.53	16.73
22	34.25	14.95	35.17	15.62	15.34	7.43	18.01	17.09
23	34.20	14.73	35.40	15.67	15.47	7.42	18.48	16.18
24	34.47	15.10	35.09	15.34	15.57	7.63	18.26	16.09
25	34.51	15.10	35.19	15.20	15.65	7.64	18.34	15.86
26	34.00	14.30	35.39	16.30	15.19	7.10	17.87	17.86
27	34.50	15.00	35.29	15.21	15.76	7.57	18.36	15.77
28	34.44	14.88	35.31	15.37	15.69	7.51	18.34	15.97
29	34.17	14.98	35.33	15.52	15.51	7.52	18.30	16.27
30	34.68	14.76	35.05	15.52	15.86	7.44	18.20	16.09
Max	35.91	15.44	35.85	17.52	15.86	7.74	18.55	19.76
Min	33.69	14.12	32.45	15.20	15.11	6.90	16.52	15.77
Average	34.38	14.78	34.94	15.89	15.53	7.40	18.11	16.71
SD	0.62	0.38	1.05	0.63	0.24	0.22	0.54	1.07

Table B.6: Unit-cell lattice parameters and uncertainties for M-brg, F1A1-brg, and F3A3-brg obtained from analysis of all *in situ* X-ray diffraction data on bridgmanite in this study. The ambient conditions lattice parameters and the volume without uncertainties and were calculated from Rietveld refinement. Match! did not give uncertainties, therefore none are reported. $\mathbf{P}_m$ is pressure medium and $\mathbf{P}_s$ is pressure scale. For Au, pressures were calculated using the Au scale from Tsuchiya (2003). Pressure calculations from ruby shift are from Dewaele *et al.* (2008). For Ar, pressures were calculated using Errandonea *et al.* (2006). Pressure was measured *in situ* using an online ruby fluorescence system. Due to the absence of ruby spectra for post-experiment analysis, pressures are reported as noted during the experiment, with a conservative estimated uncertainty of ± 1 GPa. Asterisk (*) next to the **Run**, indicates runs using metallic glass gasket inserts (Dong *et al.*, 2022). Exclamation mark (!) next to the **Run**, indicate datasets with anomalous data discussed in later text.

P (GPa)	$\mathbf{P}_m$	$\mathbf{P}_s$	a **(Å)**	b **(Å)**	c **(Å)**	**V (Å^3)**	ρ **(g/cm^3)**
				M-brg			
Run 1							
0.0001	–	–	4.7779(20)	4.9345(21)	6.8970(30)	162.610(82)	4.100
			4.7778	4.9328	6.8917	162.42	4.105
Run 2							
5.55(17)	He	Au	4.7445(26)	4.8914(24)	6.8459(39)	158.88(15)	4.197
10.60(4)	He	Au	4.7176(62)	4.8683(58)	6.8011(95)	156.20(46)	4.269
14.41(14)	He	Au	4.6962(45)	4.8504(42)	6.7733(65)	154.28(25)	4.322
17.40(50)	He	Au	4.6795(70)	4.8353(64)	6.7500(98)	152.73(10)	4.366
19.12(11)	He	Au	4.6724(56)	4.8273(64)	6.7395(99)	152.01(6)	4.387
Run 3[!]							
14.5(100)	He	ruby	4.6800(9)	4.8656(10)	6.7697(16)	154.15(56)	4.326
19.0(100)	He	ruby	4.6638(6)	4.8336(7)	6.7577(11)	152.34(40)	4.377
22.0(100)	He	ruby	4.6546(2)	4.8241(2)	6.7226(4)	150.95(13)	4.417
24.5(100)	He	ruby	4.6430(3)	4.8102(3)	6.7104(5)	149.87(17)	4.449
26.5(100)	He	ruby	4.6323(2)	4.8018(3)	6.6856(4)	148.71(14)	4.484
29.5(100)	He	ruby	4.6150(2)	4.7920(3)	6.6687(4)	147.48(8)	4.521
30.5(100)	He	ruby	4.6098(2)	4.7903(2)	6.6640(3)	147.15(2)	4.531
32.0(100)	He	ruby	4.6029(4)	4.7867(4)	6.6612(6)	146.77(5)	4.543
34.0(100)	He	ruby	4.5922(4)	4.7683(4)	6.6299(7)	146.17(2)	4.561
36.0(100)	He	ruby	4.5846(10)	4.7672(11)	6.6525(18)	145.39(4)	4.586
38.0(100)	He	ruby	4.5758(2)	4.7714(2)	6.6270(3)	144.69(2)	4.609
40.5(100)	He	ruby	4.5742(3)	4.7644(3)	6.6210(3)	144.29(2)	4.621
42.0(100)	He	ruby	4.5792(11)	4.7696(10)	6.6073(17)	144.31(3)	4.621
43.5(100)	He	ruby	4.5772(5)	4.7549(5)	6.6232(8)	144.15(1)	4.626
				F1A1-brg			
Run 1[!]							
0.0001	–	–	4.7848(203)	4.9462(229)	6.9250(341)	163.89(13)	4.282

Continued on next page...

Table B.6 – continued from previous page.

P (GPa)	$\mathbf{P}_m$	$\mathbf{P}_s$	a **(Å)**	b **(Å)**	c **(Å)**	**V (Å^3)**	ρ **(g/cm^3)**
			4.7826	4.9480	6.9234	163.83	4.283
Run 2							
21.3(100)	He	ruby	4.6897(30)	4.8615(32)	6.7810(47)	154.60(18)	4.539
24.1(100)	He	ruby	4.8620(38)	4.8534(41)	6.7552(60)	153.30(23)	4.578
27.4(100)	He	ruby	4.6697(44)	4.8493(41)	6.7337(52)	152.48(23)	4.602
30.3(100)	He	ruby	4.6554(53)	4.8318(53)	6.7299(77)	151.38(30)	4.636
33.2(100)	He	ruby	4.6477(59)	4.8212(62)	6.6996(88)	150.12(34)	4.675
Run 3*							
4.77(4)	He	Au	4.7688(56)	4.9379(51)	6.9001(77)	162.48(31)	4.319
6.62(184)	He	Au	4.7674(74)	4.9257(63)	6.8889(96)	161.77(40)	4.338
11.02(56)	He	Au	4.7333(83)	4.9022(87)	6.8585(115)	159.14(48)	4.410
14.27(47)	He	Au	4.7191(70)	4.8907(66)	6.8316(99)	157.67(39)	4.451
16.64(35)	He	Au	4.7148(51)	4.8765(49)	6.8273(72)	156.97(28)	4.471
20.03(40)	He	Au	4.6860(45)	4.8648(49)	6.8019(71)	155.06(27)	4.526
23.05(27)	He	Au	4.6775(57)	4.8661(62)	6.7782(88)	154.28(34)	4.549
26.27(5)	He	Au	4.6511(67)	4.8629(72)	6.7547(103)	152.78(39)	4.593
27.5(35)	He	Au	4.6567(76)	4.8498(81)	6.7471(117)	152.38(44)	4.605
29.75(31)	He	Au	4.6427(52)	4.8339(56)	6.7344(80)	151.14(30)	4.643
34.17(148)	He	Au	4.6298(35)	4.8186(38)	6.7075(55)	149.64(20)	4.690
34.22(35)	He	Au	4.6286(67)	4.8094(74)	6.7067(106)	149.29(40)	4.700
36.77(51)	He	Au	4.6227(72)	4.8076(78)	6.6935(111)	148.75(41)	4.718
Run 4*							
69.89(185)	He	Au	4.5068(109)	4.6700(94)	6.5429(123)	137.71(51)	5.096
71.90(150)	He	Au	4.4934(80)	4.6710(74)	6.5608(98)	137.70(39)	5.096
73.14(319)	He	Au	4.4883(109)	4.6751(96)	6.5366(119)	137.16(50)	5.116
74.68(489)	He	Au	4.4742(96)	4.6697(90)	6.5188(112)	136.20(46)	5.152
77.11(382)	He	Au	4.4700(103)	4.6632(91)	6.5093(112)	135.68(47)	5.172
81.34(312)	He	Au	4.4717(87)	4.6428(76)	6.4982(99)	134.91(40)	5.202
84.33(310)	He	Au	4.4511(82)	4.6583(90)	6.4964(116)	134.70(43)	5.210
89.07(383)	He	Au	4.4580(87)	4.6306(78)	6.4827(100)	133.82(40)	5.244
				F3A3-brg			
Run 1							
0.0001	–	–	4.8076(32)	4.9954(35)	6.9845(43)	167.74(19)	4.362
			4.8054	4.9934	6.9764	167.40	4.371
Run 2$^!$							
5.54(5)	He	Au	4.7710(69)	4.9600(68)	6.9071(104)	163.45(29)	4.476
7.96(67)	He	Au	4.7694(22)	4.9409(24)	6.8909(35)	162.38(22)	4.506
9.44(176)	He	Au	4.7665(55)	4.9347(59)	6.8574(90)	161.29(36)	4.536
13.56(67)	He	Au	4.7419(42)	4.9105(45)	6.8337(67)	159.12(21)	4.598
17.80(64)	He	Au	4.7027(69)	4.8857(64)	6.8025(98)	156.29(27)	4.681

Continued on next page...

Table B.6 – continued from previous page.

P (GPa)	$\mathbf{P}_m$	$\mathbf{P}_s$	a **(Å)**	b **(Å)**	c **(Å)**	**V (Å^3)**	ρ **(g/cm^3)**
19.38(79)	He	Au	4.7027(48)	4.8757(55)	6.7865(84)	155.61(17)	4.702
23.0(100)	He	ruby	4.6934(75)	4.8645(72)	6.7549(117)	154.22(40)	4.744
25.5(100)	He	ruby	4.6792(34)	4.8536(41)	6.7448(60)	153.18(57)	4.776
28.5(100)	He	ruby	4.6681(43)	4.8384(51)	6.7310(75)	152.03(51)	4.813
30.0(100)	He	ruby	4.6510(59)	4.8287(71)	6.7397(105)	151.36(26)	4.834
33.4(100)	He	ruby	4.6281(57)	4.8260(70)	6.7042(113)	149.74(51)	4.886
36.0(100)	He	ruby	4.6276(38)	4.8199(46)	6.6816(67)	149.03(36)	4.909
37.5(100)	He	ruby	4.6143(95)	4.8091(91)	6.7039(157)	148.76(34)	4.918
40.5(100)	He	ruby	4.6162(31)	4.8024(29)	6.6793(50)	148.07(16)	4.941
42.0(100)	He	ruby	4.6184(125)	4.8064(119)	6.6628(187)	147.90(43)	4.947
43.0(100)	He	ruby	4.6052(102)	4.7940(107)	6.6732(162)	147.33(50)	4.966
46.5(100)	He	ruby	4.6033(56)	4.7898(64)	6.6652(99)	146.960(43)	4.978
48.7(100)	He	ruby	4.5994(38)	4.7973(38)	6.6577(53)	146.900(64)	4.981
51.3(100)	He	ruby	4.5987(60)	4.7895(61)	6.6656(83)	146.803(29)	4.984
53.0(100)	He	ruby	4.5940(97)	4.8101(94)	6.6448(130)	146.834(62)	4.983
55.8(100)	He	ruby	4.5866(84)	4.7962(90)	6.6737(140)	146.808(12)	4.984
58.5(100)	He	ruby	4.5995(69)	4.7989(81)	6.6179(85)	146.072(29)	5.009
60.0(100)	He	ruby	4.5829(226)	4.7817(254)	6.6671(415)	146.102(49)	5.008
60.5(100)	He	ruby	4.5690(154)	4.8211(169)	6.6075(206)	145.549(25)	5.027
62.0(100)	He	ruby	4.5925(108)	4.7948(116)	6.5872(181)	145.049(20)	5.045
64.9(100)	He	ruby	4.5792(56)	4.7879(65)	6.5759(99)	144.173(43)	5.075
66.4(100)	He	ruby	4.5757(116)	4.7798(126)	6.5736(185)	143.770(46)	5.089
67.8(100)	He	ruby	4.5736(171)	4.7625(175)	6.5630(264)	142.955(39)	5.118
70.0(100)	He	ruby	4.5626(58)	4.7667(64)	6.5412(95)	142.263(12)	5.143
72.0(100)	He	ruby	4.5554(72)	4.7650(76)	6.5347(115)	141.847(27)	5.158
74.4(100)	He	ruby	4.5159(115)	4.7676(127)	6.5464(190)	140.944(70)	5.191
76.0(100)	He	ruby	4.5251(61)	4.7707(68)	6.5559(103)	140.439(15)	5.210
78.4(100)	He	ruby	4.5253(62)	4.7588(67)	6.5095(102)	140.182(32)	5.219
80.0(100)	He	ruby	4.5081(47)	4.7548(43)	6.5173(49)	139.700(46)	5.237
82.4(100)	He	ruby	4.5054(60)	4.7424(65)	6.5204(92)	139.318(75)	5.252
84.2(100)	He	ruby	4.5154(69)	4.7336(74)	6.4970(119)	138.866(94)	5.269
86.4(100)	He	ruby	4.4886(160)	4.7245(148)	6.4576(207)	136.942(17)	5.343
88.0(100)	He	ruby	4.4697(51)	4.7285(51)	6.4750(77)	136.849(70)	5.346
90.5(100)	He	ruby	4.4616(78)	4.7153(91)	6.4580(124)	135.864(97)	5.385
93.2(100)	He	ruby	4.4835(81)	4.7054(86)	6.4429(94)	135.925(47)	5.383
96.5(100)	He	ruby	4.4652(70)	4.6986(56)	6.4255(92)	134.808(29)	5.427
Run 3							
3.57(134)	He	Au	4.7784(33)	4.9571(29)	6.9290(53)	164.13(80)	4.458
10.13(9)	He	Au	4.7414(47)	4.9266(51)	6.8843(83)	160.81(10)	4.550
15.11(10)	He	Au	4.7209(29)	4.8974(35)	6.8248(52)	157.79(87)	4.637
21.13(17)	He	Au	4.6943(43)	4.8700(47)	6.7918(69)	155.27(94)	4.712

Continued on next page...

Table B.6 – continued from previous page.

P (GPa)	$\mathbf{P}_m$	$\mathbf{P}_s$	a **(Å)**	b **(Å)**	c **(Å)**	**V (Å^3)**	ρ **(g/cm^3)**
25.59(38)	He	Au	4.6722(67)	4.8540(64)	6.7675(98)	153.48(40)	4.767
30.89(28)	He	Au	4.6420(23)	4.8305(27)	6.7089(40)	150.44(34)	4.863
36.77(116)	He	Au	4.6241(85)	4.8057(77)	6.7220(153)	149.38(60)	4.898
38.37(122)	He	Au	4.6041(79)	4.7952(74)	6.6843(116)	147.57(43)	4.958
Run 4*							
1.93(38)	Ne	Au	4.8305(97)	5.0013(101)	6.9105(146)	166.95(59)	4.382
5.32(74)	Ne	Au	4.8209(79)	4.9816(82)	6.9231(122)	166.27(49)	4.400
6.92(77)	Ne	Au	4.8040(72)	4.9241(75)	6.9241(111)	163.79(44)	4.467
10.41(85)	Ne	Au	4.7892(80)	4.9596(83)	6.8639(121)	163.03(48)	4.488
12.36(89)	Ne	Au	4.7685(104)	4.9636(111)	6.8749(161)	162.72(64)	4.496
15.38(96)	Ne	Au	4.7551(56)	4.9242(59)	6.8595(87)	160.61(34)	4.555
19.26(57)	Ne	Au	4.7380(85)	4.9089(89)	6.8103(130)	158.40(51)	4.619
19.63(55)	Ne	Au	4.7330(76)	4.9046(79)	6.8098(117)	158.08(45)	4.628
24.54(100)	Ne	Au	4.7115(104)	4.8838(113)	6.7607(160)	155.56(62)	4.703
30.82(112)	Ne	Au	4.6607(62)	4.8762(69)	6.7473(100)	153.34(37)	4.771
34.12(118)	Ne	Au	4.6687(58)	4.8524(61)	6.7139(90)	152.10(34)	4.810
36.50(193)	Ne	Au	4.6365(165)	4.8830(200)	6.6875(202)	151.41(94)	4.832
38.21(49)	Ne	Au	4.6538(62)	4.8400(62)	6.6979(81)	150.87(33)	4.850
39.49(69)	Ne	Au	4.6512(49)	4.8315(53)	6.6709(75)	149.91(28)	4.881
41.42(56)	Ne	Au	4.6388(69)	4.8296(73)	6.6587(105)	149.18(39)	4.904
42.16(71)	Ne	Au	4.6259(72)	4.8238(72)	6.6657(97)	148.74(39)	4.919
45.81(62)	Ne	Au	4.6125(78)	4.8178(79)	6.6532(107)	147.85(42)	4.949
47.63(65)	Ne	Au	4.6211(74)	4.7986(80)	6.6484(113)	147.43(42)	4.963
48.40(81)	Ne	Au	4.6123(66)	4.8050(68)	6.6470(101)	147.31(37)	4.967
49.64(152)	Ne	Au	4.6086(64)	4.7963(68)	6.6281(98)	146.51(36)	4.994
51.11(94)	Ne	Au	4.6036(59)	4.7917(62)	6.6254(90)	146.15(33)	5.006
52.72(125)	Ne	Au	4.5801(61)	4.7920(66)	6.6070(95)	145.01(35)	5.045
53.89(94)	Ne	Au	4.5800(62)	4.7929(67)	6.6050(96)	144.99(35)	5.046
55.30(98)	Ne	Au	4.5767(47)	4.7954(51)	6.5958(73)	144.76(27)	5.054
57.52(78)	Ne	Au	4.5750(66)	4.7826(71)	6.5927(102)	144.25(37)	5.072
60.70(113)	Ne	Au	4.5533(72)	4.7756(68)	6.5588(99)	142.62(37)	5.130
61.60(70)	Ne	Au	4.5471(63)	4.7730(62)	6.5615(89)	142.41(33)	5.138
63.50(119)	Ne	Au	4.5404(70)	4.7789(68)	6.5566(100)	142.27(37)	5.143
Run 5*							
5.40(100)	Ar	Ar	4.7902(17)	4.9781(0016)	6.9543(23)	165.83(10)	4.412
6.02(14)	Ar	Ar	4.7887(25)	4.9795(0023)	6.9442(38)	165.59(15)	4.418
6.99(14)	Ar	Ar	4.7817(39)	4.9760(0037)	6.9309(60)	164.91(23)	4.436
7.87(15)	Ar	Ar	4.7850(38)	4.9689(0027)	6.9307(59)	164.79(21)	4.440
8.15(17)	Ar	Ar	4.7770(47)	4.9677(0030)	6.9260(62)	164.36(24)	4.451
8.46(15)	Ar	Ar	4.7667(54)	4.9717(0057)	6.9336(94)	164.32(34)	4.453
8.87(16)	Ar	Ar	4.7693(45)	4.9775(0047)	6.9211(70)	164.30(28)	4.453

Continued on next page...

Table B.6 – continued from previous page.

P (GPa)	$\mathbf{P}_m$	$\mathbf{P}_s$	a **(Å)**	b **(Å)**	c **(Å)**	**V (Å^3)**	ρ **(g/cm^3)**
10.80(6)	Ar	Ar	4.7600(39)	4.9525(0037)	6.9003(52)	162.67(22)	4.498
12.52(11)	Ar	Ar	4.7463(67)	4.9386(0068)	6.9059(93)	161.88(39)	4.520
16.84(14)	Ar	Ar	4.7306(0045)	4.9290(52)	6.8528(70)	159.79(28)	4.579
19.40(14)	Ar	Ar	4.7182(0079)	4.9141(87)	6.8568(105)	158.98(46)	4.602
22.46(17)	Ar	Ar	4.6997(0100)	4.8974(119)	6.8574(134)	157.83(60)	4.636
27.28(22)	Ar	Ar	4.6841(0044)	4.8731(44)	6.7958(69)	155.12(26)	4.717
31.09(27)	Ar	Ar	4.6659(0024)	4.8701(22)	6.7647(37)	153.72(14)	4.760
32.75(31)	Ar	Ar	4.6709(0052)	4.8649(48)	6.7590(71)	153.59(28)	4.764
33.69(5)	Ar	Ar	4.6607(0048)	4.8572(46)	6.7374(68)	152.52(26)	4.797
36.94(1)	Ar	Ar	4.6407(0041)	4.8385(40)	6.7194(63)	150.98(23)	4.846
39.38(3)	Ar	Ar	4.6193(0048)	4.8266(51)	6.7045(75)	149.54(28)	4.892
41.20(4)	Ar	Ar	4.6037(0049)	4.8286(53)	6.6909(85)	148.73(30)	4.919
44.29(5)	Ar	Ar	4.5952(0043)	4.8252(47)	6.6881(68)	148.29(25)	4.934
46.42(6)	Ar	Ar	4.5971(0066)	4.8146(57)	6.6691(914)	147.61(34)	4.957
48.91(3)	Ar	Ar	4.5744(0063)	4.8082(63)	6.6604(93)	146.49(35)	4.994
50.76(1)	Ar	Ar	4.5716(0062)	4.7896(61)	6.6440(89)	145.48(33)	5.029
56.02(11)	Ar	Ar	4.5614(0053)	4.7736(52)	6.6326(77)	144.42(29)	5.066
57.13(9)	Ar	Ar	4.5602(0064)	4.7767(63)	6.6182(92)	144.16(34)	5.075
59.40(6)	Ar	Ar	4.5441(0051)	4.7609(55)	6.6123(83)	143.05(29)	5.115
61.27(245)	Ar	Ar	4.5392(0047)	4.7589(51)	6.5952(74)	142.47(26)	5.136

B.3 Chapter 4: Elastic Properties of Metastable Fe-Al Majoritic Garnet up to 83 GPa at 300 K

Table B.7: Lattice parameter a_{cubic} Å and unit-cell volume V_{cubic} Å^3 of cubic garnet and a_{tet} and c_{tet} Å and unit-cell volume V_{tet} Å^3 of tetragonal garnet. Values and uncertainties are given.

P (GPa)	a_{cubic} (Å)	V_{cubic} (Å^3)	a_{tet} (Å)	c_{tet} (Å)	V_{tet} (Å^3)
19.56(0.31)	11.122(1.50)	1375.84(3.15)	11.129(1.50)	11.109(1.50)	1375.862(3.15)
19.80(1.00)	11.114(0.15)	1372.74(3.10)	11.123(0.15)	11.103(0.15)	1373.660(3.10)
20.60(1.00)	11.109(1.40)	1370.90(2.57)	11.098(1.40)	11.077(1.40)	1364.211(2.57)
21.80(1.00)	11.083(1.70)	1361.37(4.85)	11.081(1.70)	11.061(1.70)	1358.227(4.85)
24.09(0.14)	11.065(1.70)	1354.69(4.60)	11.056(1.70)	11.036(1.70)	1349.088(4.60)
26.52(0.60)	11.042(1.10)	1346.23(1.44)	11.067(1.10)	11.047(1.10)	1352.990(1.44)
28.63(0.59)	11.029(1.20)	1341.45(1.53)	11.049(1.20)	11.029(1.20)	1346.400(1.53)
29.22(0.36)	11.019(1.70)	1337.99(4.61)	11.012(1.70)	10.992(1.70)	1332.876(4.61)
32.93(0.14)	10.975(1.60)	1322.01(4.11)	10.993(1.60)	10.973(1.60)	1326.012(4.11)
31.91(0.11)	10.980(1.70)	1323.65(4.58)	10.998(1.70)	10.978(1.70)	1327.737(4.58)
33.78(0.16)	10.969(1.60)	1319.62(4.36)	10.961(1.60)	10.941(1.60)	1314.327(4.36)
35.47(0.24)	10.935(2.10)	1307.42(8.84)	10.941(2.10)	10.921(2.10)	1307.274(8.84)
37.33(0.22)	10.937(1.60)	1308.16(3.97)	10.915(1.60)	10.895(1.60)	1307.274(3.97)
39.01(0.17)	10.899(1.70)	1294.50(5.18)	10.911(1.70)	10.891(1.70)	1296.468(5.18)
40.47(0.12)	10.898(1.70)	1294.43(5.05)	10.895(1.70)	10.875(1.70)	1290.900(5.05)
42.26(0.21)	10.871(1.30)	1284.62(2.10)	10.874(1.30)	10.854(1.30)	1283.322(2.10)
43.85(0.20)	10.864(1.50)	1282.14(3.53)	10.870(1.50)	10.850(1.50)	1282.041(3.53)
45.44(0.19)	10.846(1.50)	1275.81(3.54)	10.852(1.50)	10.832(1.50)	1275.746(3.54)
47.02(0.25)	10.835(1.50)	1271.94(3.42)	10.828(1.50)	10.808(1.50)	1267.143(3.42)
48.72(0.23)	10.808(1.00)	1262.37(1.06)	10.818(1.00)	10.798(1.00)	1263.731(1.06)
50.35(0.24)	10.799(1.40)	1259.44(2.56)	10.806(1.40)	10.786(1.40)	1259.488(2.56)
51.80(0.24)	10.770(1.50)	1249.24(3.08)	10.785(1.50)	10.765(1.50)	1252.149(3.08)
52.25(0.21)	10.771(1.50)	1249.65(3.24)	10.774(1.50)	10.754(1.50)	1248.280(3.24)
54.75(0.18)	10.745(1.60)	1240.54(4.40)	10.776(1.60)	10.757(1.60)	1249.155(4.40)
56.06(0.16)	10.727(1.60)	1234.46(4.16)	10.750(1.60)	10.730(1.60)	1239.900(4.16)
57.56(0.16)	10.716(1.70)	1230.54(4.92)	10.738(1.70)	10.719(1.70)	1235.975(4.92)
58.89(0.18)	10.700(1.80)	1224.98(5.62)	10.732(1.80)	10.713(1.80)	1233.931(5.62)
60.07(0.27)	10.711(0.96)	1228.68(0.89)	10.712(0.96)	10.692(0.96)	1227.090(0.89)
61.96(0.21)	10.697(1.20)	1223.86(1.53)	10.711(1.20)	10.691(1.20)	1226.368(1.53)
63.11(0.22)	10.673(1.60)	1215.85(4.09)	10.676(1.60)	10.657(1.60)	1223.978(4.09)
64.55(0.20)	10.682(1.50)	1218.90(3.14)	10.657(1.50)	10.638(1.50)	1221.943(3.14)
65.67(0.22)	10.667(1.30)	1213.74(2.33)	10.640(1.30)	10.621(1.30)	1215.569(2.33)
67.05(0.21)	10.643(1.70)	1205.53(5.30)	10.676(1.70)	10.656(1.70)	1213.259(5.30)
68.40(0.20)	10.651(1.20)	1208.46(1.65)	10.658(1.20)	10.638(1.20)	1214.596(1.65)
69.54(0.50)	10.631(1.60)	1201.55(4.29)	10.640(1.60)	10.621(1.60)	1208.354(4.29)
71.25(0.48)	10.621(1.60)	1198.21(4.39)	10.636(1.60)	10.617(1.60)	1202.487(4.39)
72.19(0.30)	10.619(1.60)	1197.58(4.44)	10.636(1.60)	10.618(1.60)	1200.870(4.44)
73.56(0.30)	10.623(0.94)	1198.88(0.83)	10.638(0.94)	10.619(0.94)	1201.409(0.83)
75.20(0.44)	10.614(1.00)	1195.67(0.99)	10.631(1.00)	10.611(1.00)	1199.099(0.99)
76.67(0.58)	10.609(0.95)	1194.18(0.87)	10.629(0.95)	10.609(0.95)	1198.503(0.87)

Continued on next page...

P (GPa)	a_{cubic} (Å)	V_{cubic} (Å^3)	a_{tet} (Å)	c_{tet} (Å)	V_{tet} (Å^3)
78.84(0.31)	10.601(1.10)	1191.27(1.49)	10.613(1.10)	10.594(1.10)	1193.406(1.49)
79.89(0.34)	10.594(1.00)	1189.12(1.05)	10.608(1.00)	10.588(1.00)	1192.130(1.05)

B.4 Chapter 5 & Chapter 6: *Ab Initio* Density Functional Theory Calculations on Fe-Al-Bridgmanite

Table B.8: Atomic position arrangements for Fe and Al in Fe-Al-bearing perovskite (FeAl25). Position # was assigned arbitrarily. A_x and B_x refer to the corresponding cation fraction coordination from Table 5.1. Distance (Å) refers to the distance between the Fe and Al cations within the structure in real space.

Position	Fe	Al	Dist. (Å)
1	A_4: (0.9859, 0.0560, 0.2500)	B_4: (0.0000, 0.5000, 0.0000)	2.786
2	A_2: (0.0141, 0.9440, 0.7500)	B_1: (0.5000, 0.0000, 0.5000)	3.139
3	A_2: (0.0141, 0.9440, 0.7500)	B_2: (0.0000, 0.5000, 0.5000)	2.877
4	A_2: (0.0141, 0.9440, 0.7500)	B_3: (0.5000, 0.0000, 0.0000)	3.139
5	A_1: (0.5141, 0.5560, 0.2500)	B_2: (0.0000, 0.5000, 0.5000)	3.030

Table B.9: Atomic position arrangements for Fe and Al in Fe-Al-bearing perovskite (FeAl50). Position # was assigned arbitrarily. $\mathbf{A_x}$ and $\mathbf{B_x}$ refer to the corresponding cation fraction coordination from Table 5.1. Distance (Å) refers to the distance between the Fe and Al cations within the structure in real space.

Position	Fe	Al	Dist. (Å)
1			
d_1	A_1: (0.5141, 0.5560, 0.2500)	B_1: (0.5000, 0.0000, 0.5000)	3.318
d_2	A_3: (0.4859, 0.4440, 0.7500)	B_3: (0.5000, 0.0000, 0.0000)	2.877
2			
d_1	A_2: (0.0141, 0.9440, 0.7500)	B_1: (0.5000, 0.0000, 0.5000)	3.139
d_2	A_4: (0.9859, 0.0560, 0.2500)	B_3: (0.5000, 0.0000, 0.0000)	3.030

Table B.10: Convergence settings for the static calculations.

Composition	Cut-off / eV	k-mesh
$MgSiO_3$	800	$4 \times 4 \times 3$
FeAl25	900	$5 \times 5 \times 5$
FeAl50	900	$5 \times 5 \times 5$

Table B.11: Unit cell volumes V_{0K} (Å^3), density ρ (g/cm^3), and lattice parameters a, b, and c (Å) for $MgSiO_3$, FeAl25, and FeAl50 at 0 K across a pressure range of 0—140 GPa, obtained from *ab initio* calculations.

P (GPa)	**a** (Å)	**b** (Å)	**c** (Å)	$\mathbf{V_{0K}}$ **(Å^3)**	ρ (g/cm^3)
			$MgSiO_3$		
0	4.802469	4.952185	6.924516	164.684	4.662
5	4.770158	4.923532	6.877519	161.526	4.754
10	4.739225	4.895427	6.834262	158.559	4.843
15	4.710821	4.870606	6.793174	155.866	4.927
20	4.680752	4.849489	6.755223	153.339	5.008
25	4.653973	4.828032	6.720726	151.012	5.085
30	4.629648	4.807989	6.686849	148.945	5.155
35	4.605172	4.790086	6.655387	146.812	5.230
40	4.583686	4.771898	6.625461	144.918	5.299
45	4.561632	4.755384	6.596904	143.102	5.366
50	4.541119	4.739785	6.570164	141.416	5.430
55	4.520679	4.725072	6.544098	139.785	5.493
60	4.501494	4.710894	6.519812	138.260	5.554
65	4.480824	4.698895	6.495659	136.766	5.615
70	4.463479	4.685725	6.472708	135.374	5.672
75	4.444537	4.674012	6.451342	134.019	5.730
80	4.428078	4.668040	6.430377	132.919	5.777
85	4.410945	4.651006	6.410186	131.507	5.839
90	4.394532	4.640225	6.390634	130.315	5.892
95	4.378624	4.629759	6.372010	129.173	5.945
100	4.362866	4.619999	6.353731	128.069	5.996
105	4.347522	4.610349	6.336199	127.000	6.046
110	4.332441	4.601265	6.319100	125.969	6.096
115	4.317435	4.592850	6.302299	124.970	6.144
120	4.303205	4.583969	6.286512	124.006	6.192
125	4.288327	4.575959	6.271208	123.061	6.240
130	4.275188	4.567869	6.255977	122.170	6.285
135	4.261166	4.559835	6.241893	121.281	6.331
140	4.248250	4.553260	6.225548	120.423	6.377
			FeAl25		
0	4.810837	5.003458	6.998741	168.465	4.258
5	4.777237	4.973984	6.944551	165.016	4.347
10	4.745980	4.946998	6.895842	161.903	4.431
15	4.716748	4.922125	6.851580	159.069	4.510
20	4.688966	4.899413	6.810587	156.461	4.585
25	4.662654	4.878139	6.772614	154.044	4.657

Continued on next page...

Table B.11 – continued from previous page.

P (GPa)	**a** (Å)	**b** (Å)	**c** (Å)	$\mathbf{V}_{0K}$ (**Å**^{3})	ρ (g/cm^3)
30	4.637579	4.858319	6.737182	151.794	4.726
35	4.613373	4.839552	6.703950	149.677	4.793
40	4.590269	4.822185	6.672856	147.705	4.857
45	4.568057	4.806126	6.643453	145.855	4.918
50	4.547367	4.790026	6.615330	144.095	4.978
55	4.526382	4.775950	6.587755	142.413	5.037
60	4.506592	4.761890	6.563175	140.845	5.093
65	4.488376	4.747483	6.538770	139.331	5.148
70	4.469870	4.734602	6.515483	137.888	5.202
75	4.451958	4.722391	6.493054	136.509	5.255
80	4.434528	4.710756	6.471102	135.181	5.306
85	4.417672	4.699539	6.451016	133.930	5.356
90	4.400982	4.688731	6.430846	132.701	5.406
95	4.384811	4.678443	6.411552	131.527	5.454
100	4.369083	4.668553	6.392926	130.398	5.501
105	4.353913	4.658990	6.374690	129.310	5.547
110	4.338627	4.649823	6.357512	128.255	5.593
115	4.323703	4.641161	6.340238	127.223	5.638
120	4.309380	4.632438	6.323852	126.243	5.682
125	4.294858	4.624355	6.308266	125.288	5.726
130	4.280998	4.616218	6.292694	124.356	5.768
135	4.267103	4.608589	6.277797	123.455	5.811
140	4.253342	4.601141	6.262823	122.565	5.853
			FeAl50		
0	4.832604	5.022253	7.059550	171.339	4.482
5	4.797493	4.994550	7.002318	167.785	4.577
10	4.764658	4.969364	6.950778	164.576	4.666
15	4.733944	4.946239	6.903813	161.654	4.750
20	4.704877	4.924897	6.860702	158.970	4.830
25	4.677243	4.905110	6.820777	156.485	4.907
30	4.650955	4.886520	6.783832	154.176	4.981
35	4.626028	4.869188	6.748900	152.019	5.051
40	4.602406	4.852884	6.715634	149.993	5.119
45	4.577974	4.837648	6.686538	148.084	5.185
50	4.556156	4.823320	6.657172	146.297	5.249
55	4.534729	4.809597	6.629524	144.591	5.311
60	4.513991	4.796538	6.603286	142.971	5.371
65	4.493908	4.784253	6.578015	141.427	5.430
70	4.474358	4.772590	6.554017	139.956	5.487
75	4.455272	4.761095	6.531656	138.549	5.542

Continued on next page...

Table B.11 – continued from previous page.

P (GPa)	**a** (Å)	**b** (Å)	**c** (Å)	$\mathbf{V}_{0K}$ (Å^3)	ρ (g/cm^3)
80	4.437676	4.749396	6.509661	137.199	5.597
85	4.420349	4.738532	6.488350	135.905	5.650
90	4.402014	4.729679	6.467822	134.661	5.702
95	4.385793	4.719003	6.448983	133.472	5.753
100	4.369027	4.710026	6.429506	132.308	5.804
105	4.352455	4.701806	6.411122	131.120	5.856
110	4.336499	4.693180	6.393536	130.121	5.901
115	4.320821	4.684856	6.376580	129.077	5.949
120	4.305349	4.677023	6.360015	128.067	5.996
125	4.290014	4.669645	6.343993	127.088	6.042
130	4.275062	4.662373	6.328425	126.138	6.088
135	4.260278	4.655401	6.313226	125.212	6.133
140	4.245568	4.648715	6.298570	124.311	6.177

Table B.12: Compressibility calculations for the lattice parameters a, b and c for $MgSiO_3$, FeAl25, and FeAl50 at 0 K.

P (GPa)	$\kappa_a\|_{T=0}$ (GPa^{-1})	$\kappa_b\|_{T=0}$ (GPa^{-1})	$\kappa_c\|_{T=0}$ (GPa^{-1})
$MgSiO_3$			
0	1.384e-3	1.181e-3	1.346e-3
5	1.325e-3	1.110e-3	1.279e-3
10	1.268e-3	1.042e-3	1.214e-3
15	1.214e-3	9.770e-4	1.152e-3
20	1.162e-3	9.160e-4	1.093e-3
25	1.112e-3	8.580e-4	1.036e-3
30	1.065e-3	8.040e-4	9.831e-4
35	1.021e-3	7.534e-4	9.329e-4
40	9.809e-4	7.070e-4	8.859e-4
45	9.431e-4	6.644e-4	8.422e-4
50	9.084e-4	6.259e-4	8.019e-4
55	8.769e-4	5.915e-4	7.651e-4
60	8.487e-4	5.613e-4	7.319e-4
65	8.239e-4	5.354e-4	7.024e-4
70	8.025e-4	5.139e-4	6.765e-4
75	7.846e-4	4.967e-4	6.544e-4
80	7.703e-4	4.840e-4	6.366e-4
85	7.596e-4	4.757e-4	6.219e-4
90	7.525e-4	4.719e-4	6.115e-4
95	7.492e-4	4.728e-4	6.051e-4
100	7.496e-4	4.782e-4	6.027e-4

Continued on next page...

Table B.12 – continued from previous page.

P (GPa)	κ_a	κ_b	κ_c
105	6.890e-4	3.924e-4	5.359e-4
110	6.812e-4	3.835e-4	5.252e-4
115	6.758e-4	3.771e-4	5.171e-4
120	6.729e-4	3.734e-4	5.117e-4
125	6.724e-4	3.722e-4	5.090e-4
130	6.745e-4	3.736e-4	5.091e-4
135	6.791e-4	3.776e-4	5.118e-4
140	6.863e-4	3.843e-4	5.174e-4
FeAl25			
0	1.342e-3	1.102e-3	1.414e-3
5	1.294e-3	1.049e-3	1.348e-3
10	1.246e-3	9.977e-4	1.284e-3
15	1.200e-3	9.481e-4	1.221e-3
20	1.156e-3	9.002e-4	1.161e-3
25	1.113e-3	8.539e-4	1.103e-3
30	1.072e-3	8.095e-4	1.047e-3
35	1.033e-3	7.668e-4	9.933e-4
40	9.948e-4	7.261e-4	9.423e-4
45	9.589e-4	6.874e-4	8.938e-4
50	9.249e-4	6.506e-4	8.480e-4
55	8.929e-4	6.160e-4	8.049e-4
60	8.629e-4	5.834e-4	7.647e-4
65	8.349e-4	5.530e-4	7.273e-4
70	8.090e-4	5.248e-4	6.930e-4
75	7.853e-4	4.988e-4	6.616e-4
80	7.638e-4	4.751e-4	6.334e-4
85	7.446e-4	4.537e-4	6.083e-4
90	7.276e-4	4.346e-4	5.865e-4
95	7.130e-4	4.179e-4	5.678e-4
100	7.007e-4	4.036e-4	5.525e-4
105	6.908e-4	3.916e-4	5.405e-4
110	6.834e-4	3.821e-4	5.318e-4
115	6.785e-4	3.751e-4	5.266e-4
120	6.760e-4	3.705e-4	5.248e-4
125	6.761e-4	3.683e-4	5.265e-4
130	6.788e-4	3.687e-4	5.317e-4
135	6.841e-4	3.716e-4	5.405e-4
140	6.920e-4	3.771e-4	5.528e-4
FeAl50			
0	1.400e-3	1.024e-3	1.486e-3

Continued on next page...

Table B.12 – continued from previous page.

P (GPa)	κ_a	κ_b	κ_c
5	1.350e-3	9.744e-4	1.415e-3
10	1.301e-3	9.263e-4	1.345e-3
15	1.253e-3	8.798e-4	1.277e-3
20	1.208e-3	8.349e-4	1.212e-3
25	1.163e-3	7.915e-4	1.148e-3
30	1.121e-3	7.499e-4	1.088e-3
35	1.080e-3	7.099e-4	1.030e-3
40	1.041e-3	6.718e-4	9.743e-4
45	1.004e-3	6.355e-4	9.217e-4
50	9.693e-4	6.011e-4	8.720e-4
55	9.364e-4	5.687e-4	8.254e-4
60	9.056e-4	5.382e-4	7.819e-4
65	8.769e-4	5.097e-4	7.416e-4
70	8.505e-4	4.833e-4	7.045e-4
75	8.263e-4	4.589e-4	6.708e-4
80	8.045e-4	4.367e-4	6.406e-4
85	7.850e-4	4.165e-4	6.137e-4
90	7.680e-4	3.986e-4	5.904e-4
95	7.534e-4	3.828e-4	5.707e-4
100	7.413e-4	3.692e-4	5.547e-4
105	7.318e-4	3.579e-4	5.422e-4
110	7.248e-4	3.487e-4	5.336e-4
115	7.205e-4	3.419e-4	5.286e-4
120	7.189e-4	3.373e-4	5.275e-4
125	7.199e-4	3.350e-4	5.302e-4
130	7.237e-4	3.350e-4	5.368e-4
135	7.302e-4	3.373e-4	5.473e-4
140	7.396e-4	3.420e-4	5.618e-4